The influence of thermal plasma profiles on low-frequency Alfvén eigenmode dynamics in a tokamak

Diarmuid B. Curran

Department of Physics,
University College Cork

Supervisor: Dr. Patrick J. McCarthy
Head of department: Prof. John McInerney

Thesis submitted for the degree of Doctor of Philosophy to the
National University of Ireland, Cork
March 2014

Contents

Declaration

I hereby declare that this thesis, submitted in March 2014 for the degree of Doctor of Philosophy to the National University of Ireland, Cork, is my own work and has not been submitted for another degree, either at University College Cork or elsewhere.

Diarmuid B. Curran

Abstract

The confinement of fast particles, present in a tokamak plasma as nuclear fusion products and through external heating, will be essential for any future fusion reactor. Fast particles can be expelled from the plasma through their interaction with Alfvén eigenmode (AE) instabilities. AEs can exist in gaps in the Alfvén continuum created by plasma equilibrium non-uniformities. In the ASDEX Upgrade tokamak, low-frequency modes in the frequency range from $f \approx 10 - 90$kHz, including beta-induced Alfvén eigenmodes (BAEs) and lower frequency modes with mixed Alfvén and acoustic polarisations, have been observed. These exist in gaps in the Alfvén continuum opened up by geodesic curvature and finite plasma compressibility.

In this thesis, a kinetic dispersion relation is solved numerically to investigate the influence of thermal plasma profiles on the evolution of these low-frequency modes during the sawtooth cycle. Using information gained from various experimental sources to constrain the equilibrium reconstructions, realistic safety factor profiles are obtained for the analysis using the CLISTE code. The results for the continuum accumulation point evolution are then compared with experimental results from ASDEX Upgrade during periods of ICRH only as well as for periods with both ICRH and ECRH applied simultaneously. It is found that the diamagnetic frequency plays an important role in influencing the dynamics of BAEs and low-frequency acoustic Alfvén eigenmodes, primarily through the presence of gradients in the thermal plasma profiles.

Different types of modes that are observed during discharges heated almost exclusively by ECRH were also investigated. These include electron internal transport barrier (eITB) driven modes, which are observed to coincide with the occurrence of an eITB in the plasma during the low-density phase of the discharge. Also observed are BAE-like modes and edge-TAEs, both of which occur during the H-mode phase of the discharge.

Chapter 1

Introduction

1.1 Nuclear fusion

Nuclear fusion is the process by which two light nuclei combine to form a nucleus heavier than that of the original individual nuclei.

$$\begin{aligned}
&{}^{2}_{1}D + {}^{3}_{1}T \rightarrow {}^{4}_{2}He + {}^{1}_{0}n + 17.6MeV \\
&{}^{2}_{1}D + {}^{2}_{1}D \rightarrow {}^{3}_{1}He + {}^{1}_{0}n + 3.27MeV \\
&{}^{2}_{1}D + {}^{2}_{1}D \rightarrow {}^{3}_{1}T + {}^{1}_{1}H + 4.03MeV \\
&{}^{2}_{1}D + {}^{3}_{2}He \rightarrow {}^{4}_{2}He + {}^{1}_{1}H + 18.3MeV
\end{aligned} \tag{1.1.1}$$

The total mass of the resultant nuclear products is slightly less than the combined mass of the two original nuclei. This mass deficit Δm is converted into energy, in accordance with the principle of mass-energy equivalence $E = \Delta mc^2$, where E is the energy and c is the speed of light in a vacuum. This energy takes the form of the kinetic energy imparted to the resultant nuclear products.

The primary goal of nuclear fusion research is the efficient harnessing of the energy released during nuclear fusion reactions for the purpose of generating electricity in a commercially viable power plant. Equation 1.1.1 presents a number of possible fusion reactions, with the corresponding plots of the fusion reaction cross-sections versus the relative energies of the reactants shown in figure 1.1. For the purpose of fuelling an electrical power station the most promising of these reactions is that between deuterium and tritium, both of which are isotopes of hydrogen. The result of this reaction is a helium nucleus, known as an α-particle, and a neutron, as well as 17.6MeV of energy. The majority of this energy, 14.1MeV, is imparted to the neutron and the remaining 3.5MeV to the α-particle. This reaction is the most favourable due to the fact that its maximum fusion cross-section occurs at an energy of 100keV, which is accessible to particles in the high energy tail of the distribution function for current fusion relevant machines [1].

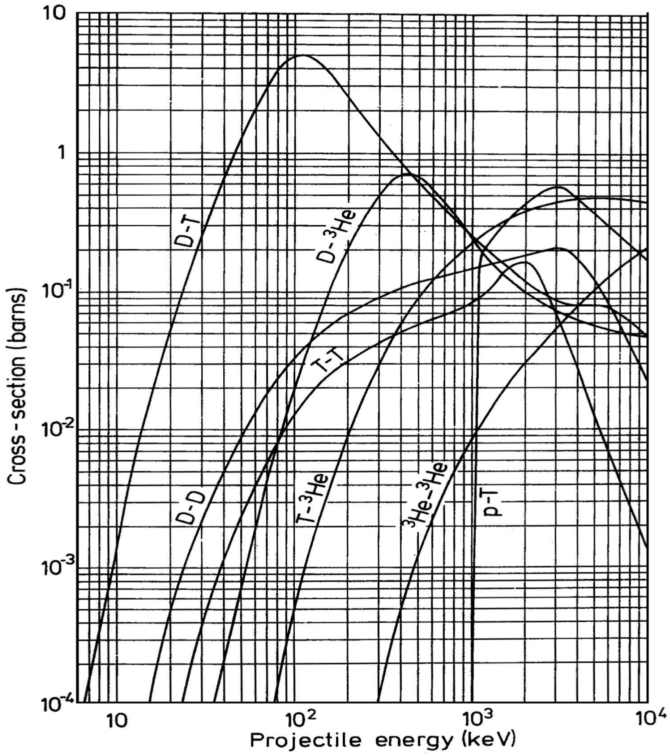

Figure 1.1. Cross-sections of potential nuclear fusion reactions as a function of the relative energies of the reactants [1].

1.2 Why is nuclear fusion important?

The population of the Earth has increased substantially since the middle of the twentieth century, rising from approximately 2.5 billion in 1950 to nearly 7.2 billion in 2013. Employing a set of assumptions that lie between the most conservative and the most extreme cases, the population is projected to rise to almost 11 billion by the end of the century [2]. A result of this growth has been a dramatic increase in the global demand for energy. Compounding the increase in energy demand due to this population rise has been the increase in the energy demand per person in developed nations as well as that resulting from the rapid industrialisation of highly populous nations such as China. Currently, the majority of global energy is obtained through the burning of fossil fuels such as coal and oil. The energy yield and expected lifetime of the global reserves of these resources are shown in figure 1.2, with oil in particular expected to see currently viable reserves depleted within the next 40 years.

Resources	GJ	Life-Time
Coal	10^{14}	300 years
Oil	1.2×10^{13}	40 years
Natural Gas	1.4×10^{13}	50 years
^{235}U (fission reactors)	10^{13}	30 years
^{238}U and ^{232}Th (breeder reactors)	10^{16}	30000 years
Lithium (D-T fusion reactors):		
Land	10^{16}	30000 years
Oceans	10^{19}	$3 \cdot 10^{7}$ years
Present world annual		
primary energy consumption	3×10^{11}	

Figure 1.2. Energy yield and expected lifetime of global reserves of fossil fuels, uranium and lithium [1].

While it is true that improvements in technology and the adjustment of consumer sentiment to accept higher energy prices could lead to an extension of these estimates, several factors make the search for alternative sources of energy of vital importance. These include the impact of the burning of fossil fuels on the environment, possible interruption of supply due to political instability in the nations that possess the greatest fossil fuel reserves, as well as the cost and difficulty of locating and accessing as yet undiscovered reserves. Many potential solutions to the problem of sustainable energy have been proposed, but each is accompanied by a host of problems. Proponents of renewable energy technologies such as wind and solar power have found it difficult to implement schemes sufficient to consistently generate energy on a large scale, while nuclear fission is accompanied by the inherent risk of potentially devastating runaway nuclear chain reactions, as well as the necessity of storing nuclear waste from the fission process which has an extremely long half-life.

Nuclear fusion possesses many of the benefits of renewable energy technologies but is not accompanied by the same degree of risk associated with nuclear fission. The fuels for nuclear fusion are abundant and, after undergoing certain processing techniques, readily available. Deuterium occurs naturally in seawater, with a mean abundance of approximately 0.015% of the atoms per sample [1]. This translates to a supply that is essentially limitless for all practical purposes, given the vast volume of seawater constituting the Earth's oceans. Tritium, while it does not exist in nature, is obtainable through the reaction between a lithium nucleus and a neutron. As can be seen in figure 1.2, lithium is itself extremely abundant on Earth, and it is conceived that the tritium could be bred within a fusion reactor using neutrons from fusion reactions. The radioactive waste material from a nuclear fusion reactor would have a half life far shorter than that produced by a fission reactor. The chance of an uncontrolled fusion reaction is also negated by the fact that the amount of deuterium and tritium fuel in a reactor at any given time is kept below potentially dangerous levels.

1.3 Harnessing energy from nuclear fusion

Sections 1.3 and 1.4 follow primarily the descriptions given in [1,3]. At temperatures close to the atomic ionisation energy, atoms decompose into negatively charged electrons and positively charged ions. While no longer bound, these particles are influenced by electromagnetic fields. This new arrangement, known as a plasma, is characterised by the excitation of a wide variety of collective dynamical modes [3]. As such, when considering the behaviour of a plasma we assume that it consists of an equal number of electrons and ions with charge $-e$ and $+e$ respectively, where e is the elementary charge. The resulting state, in which the plasma is macroscopically neutral, is called quasi-neutrality, meaning that $n_e \simeq n_i \equiv n$, where n_e and n_i are the electron and ion number densities respectively.

In order for a fusion reaction to occur, the mutual Coulomb repulsion between the positively charged deuterium and tritium nuclei must be overcome. In fact, the Coulomb barrier itself does not need to be fully surmounted. If sufficient heating is provided particles in the high energy tail of the Maxwellian distribution can overcome the repulsion at small distances through quantum mechanical tunnelling.

At the predicted 10keV operational temperature of a fusion reactor, the deuterium and tritium fuels become fully ionised, forming a plasma. Initially, external heating of the fuel must be provided so that the inevitable energy losses to the surroundings during the fusion process can be compensated for. When the energy of the charged fusion products is confined to a sufficient degree, this external heating can be removed. At this point the plasma heating becomes self-sustaining as the fusion born α-particles impart much of their energy to the plasma through collisions. A statement of the conditions necessary for this to occur is given by the Lawson Criterion, which can be stated by the following equation

$$\hat{n}\hat{T}\tau_E > 5 \times 10^{21} m^{-3} skeV \tag{1.3.1}$$

where $\hat{n}$ and $\hat{T}$ are the peak density and temperature values, τ_E is the energy confinement time, and temperatures of $10-20$keV must be reached in conjunction with the conditions laid out by equation 1.3.1 for the reaction to become self-sustaining [1]. This attainment of a so-called "burning plasma" is known as ignition.

1.4 The tokamak concept

The most promising design for a nuclear fusion power plant is based on the tokamak concept. The word "tokamak" is derived from the Russian words **to**roidalnaya **ka**mera and **ma**gnitnymi **k**atushkami, meaning "toroidal chamber" and "magnetic coil" [1]. An example of the configuration of a typical tokamak is given in figure 1.3. As suggested by the name, a tokamak consists of a toroidally shaped vessel, with magnetic field coils surrounding it in the toroidal and poloidal directions. A solenoid runs vertically through the centre of the vessel, and the magnetic flux through this solenoid is varied in time. This induces a toroidal electric field in the vessel, which in turn drives a toroidal current that ionises the deuterium and tritium fuel through Ohmic heating, forming a plasma. Current flowing through the toroidal field coils induces a toroidal magnetic field in the vessel, while the toroidal plasma current induces a smaller poloidal magnetic field. These combine to form a magnetic field that twists through the vessel and plasma.

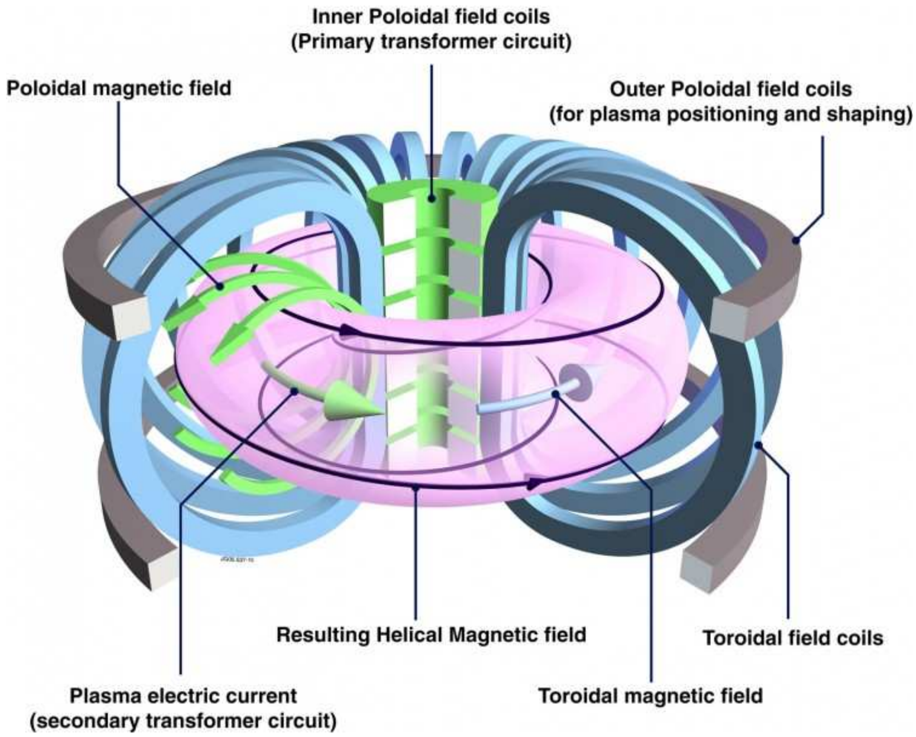

Figure 1.3. Configuration of primary toroidal and poloidal field coils in a tokamak, as well as the induced magnetic fields and current [4].

The plasma assumes a toroidal shape, resulting from the topology of the magnetic field that confines its constituent particles, and is shown in pink in figure 1.3.

Major radius	R_0	1.65m
Minor vertical/horizontal plasma radius	b/a	0.8m/0.5m
Plasma volume	V_p	$14m^3$
Maximum plasma current	I_p	1.6MA
Maximum toroidal field	B_0	3.9T
Discharge duration	t	$< 10s$

Table 1.1. Main plasma parameters of ASDEX Upgrade [5, 6].

The results utilised during this work were obtained from measurements carried out at the ASDEX Upgrade tokamak in Garching, Germany. ASDEX is an acronym for Axial Symmetric Divertor EXperiment and the tokamak was designed as a fusion experiment with a reactor relevant plasma cross section, divertor and poloidal field coil arrangement [6]. The typical plasma parameters of ASDEX Upgrade are presented in table 1.1.

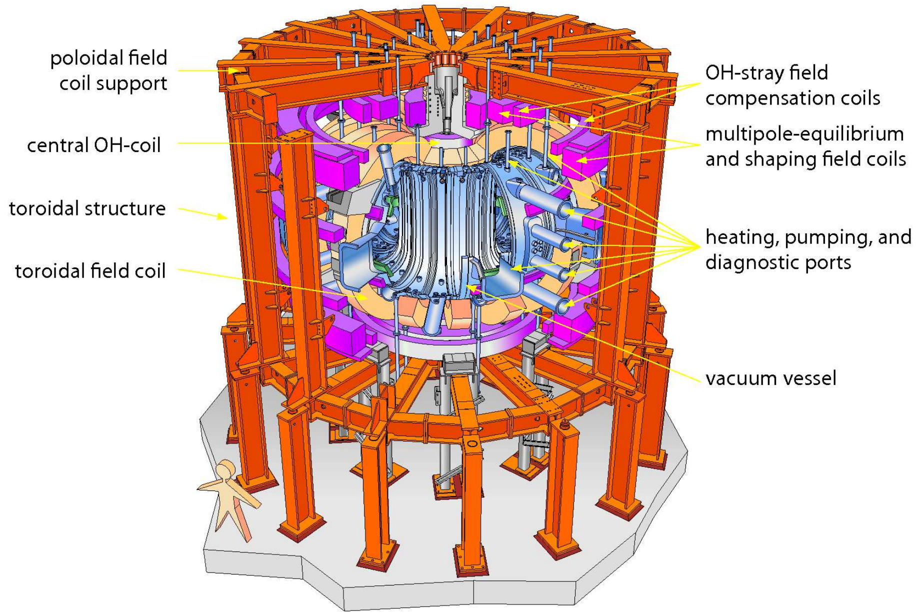

Figure 1.4. Configuration of the main components of the ASDEX Upgrade tokamak [5].

1.5 Thesis outline

A tokamak plasma can play host to a myriad of instabilities that degrade the confinement of fusion born α-particles, and thus prevent the plasma from reaching ignition. One family of instabilities is known as an Alfvén eigenmode, which at the most fundamental level arises from an oscillatory exchange of energy between the plasma and the magnetic field. A detailed discussion of the properties of Alfvén eigenmodes is presented in chapter 3. These instabilities are important due to the fact that energy can be transferred between them and energetic particles present in the plasma, with the potential for a deleterious redistribution of the energetic particle population. This can seriously degrade the energy confinement of the plasma and even lead to the outer vessel being damaged if the α-particles are expelled from the plasma with sufficient energy. Alfvén eigenmodes can be subdivided into several different types, each resulting from a particular characteristic of the plasma, such as its geometry or current profile. During the course of this thesis, the focus will primarily be on two particular types of Alfvén eigenmode: The beta-induced Alfvén eigenmode (BAE) and the acoustic Alfvén eigenmode. These arise from the presence of finite plasma compressibility and geodesic curvature in the plasma, as well as from the coupling between shear Alfvén waves and sound waves [7].

Chapter 2 introduces the fundamental concepts of plasma physics and the main plasma instabilities of interest in the context of this work. It also presents the primary diagnostics used for investigating a tokamak plasma and the methods by which the plasma is heated. Chapter 3 gives an outline of the physics governing Alfvén eigenmode instabilities, starting with the ideal magnetohydrodynamics description and progressing to the more complete kinetic description.

Chapter 4 details the experimental and numerical analysis procedure used in the investigation of the Alfvén eigenmodes. Chapter 5 presents results obtained from the application of the analysis procedure described in chapter 4 to low-frequency Alfvén eigenmodes during the ICRH only phase of different discharges. Experimental observations of the BAE and acoustic Alfvén eigenmodes are analysed and compared with the results from a numerical analysis of low-frequency Alfvén eigenmodes. Chapter 6 extends the analysis conducted in chapter 5 to modes observed during periods of additional heating provided by ECRH. It also includes a series of parameter sensitivity scans used to investigate the response of low-frequency Alfvén eigenmode activity to different parameter regimes. Chapter 7 investigates three different types of mode that exhibit characteristics similar to Alfvén eigenmode but that are observed during discharges heated almost exclusively via ECRH. This is followed by the conclusion, outlook, and appendices.

Chapter 2

Theoretical and experimental overview of tokamak physics

2.1 Fundamentals of plasma physics

This chapter begins with a discussion of the basic concepts and parameters needed to describe a fusion plasma. This is followed by an overview of charged particle motion in a magnetic field, in particular the types of particle drift that occur. Finally, the ideal magnetohydrodynamic (MHD) description of a plasma is introduced. An understanding of ideal MHD is important as it provides the most intuitive description of a fusion plasma. The treatment of the concepts in sections 2.1.1, 2.1.2 and 2.1.3 primarily follows those given in [1,3,8].

2.1.1 Basic concepts and parameters

The definition of a plasma has been given in chapter 1. In this section, the main parameters characterising a plasma are presented. The kinetic temperature T_s of a plasma species s is a measure of its average kinetic energy and is measured in electron-volts (eV) [3]. The typical particle speed of a particular species, of mass m_s, is estimated by the thermal speed, defined as

$$v_{ts} = \sqrt{2T_s/m_s} \tag{2.1.1}$$

The plasma frequency ω_{ps}, is given by

$$\omega_{ps}^2 = n_s e^2/\epsilon_0 m_s \tag{2.1.2}$$

for a species s, where n_s is the number density of species s, ϵ_0 is the vacuum permittivity and e is the elementary charge. This describes an electrostatic oscillation frequency brought about in the plasma due to small amounts of local charge separation. Clearly the electron plasma frequency is far greater than that of the ions due to the much smaller mass of the electron, and in general when the term plasma frequency is used it refers to the electron plasma frequency. Thus, species subscripts will be suppressed in the remaining definitions in this section. The plasma frequency in turn defines a fundamental time-scale for the plasma [3]

$$\tau_p = 1/\omega_p \tag{2.1.3}$$

as well as a corresponding fundamental length scale called the Debye length

$$\lambda_D \equiv \tau_p \sqrt{T/m} = \sqrt{\epsilon_0 T/ne^2} \tag{2.1.4}$$

Phenomena occurring at time-scales faster than τ_p or at length scales shorter than λ_D can no longer usefully be considered a plasma. Thus, two of the conditions determining whether a system is a plasma can be summarised as follows

$$\lambda_D/L \ll 1 \tag{2.1.5}$$

$$\tau_p/\tau \ll 1 \tag{2.1.6}$$

where L and τ represent the typical length and time-scales of the system under investigation [3]. A third fundamental parameter, known as the plasma parameter, is defined as follows

$$\Lambda = 4\pi\epsilon_0^{3/2} T^{3/2}/e^3 n^{1/2} \tag{2.1.7}$$

and equals the typical number of particles within a Debye sphere. $\Lambda \ll 1$ corresponds to a cold, dense plasma which is said to be strongly coupled. $\Lambda \gg 1$ corresponds to a warm, diffuse plasma which is said to be weakly coupled. Plasmas of fusion interest are weakly coupled and only these are treated in this work [3].

While the parameters discussed thus far describe the essential conditions under which a particular system can be considered a plasma, it is instructive to introduce a number of further parameters that help to describe the characteristics of a given plasma. The first is the collisionality of a plasma. The collision frequency ν is defined as the inverse of the typical time needed for a particle to undergo enough collisions to be scattered through a 90 degree angle. Following from this, the mean free path of the particle can be defined as [3]

$$\lambda_{mfp} = v_t/\nu \tag{2.1.8}$$

This defines the average distance travelled by the particle in a single scattering time. A plasma can be said to be collisionless in the limit where $\lambda_{mfp} \gg L$.

A plasma is said to be magnetised if the introduction of a magnetic field significantly alters the particle trajectories. Particles in a magnetic field experience the Lorentz force given by

$$\mathbf{F} = q\mathbf{v} \times \mathbf{B} \tag{2.1.9}$$

As a result of this, the particles will stream freely in the direction of the magnetic field while gyrating about it in a direction dependant on the sign of their charge. The frequency at which this occurs is called the cyclotron frequency and is defined as

$$\Omega_c = eB/m \tag{2.1.10}$$

The corresponding radius of this motion is known as the gyro-radius or Larmor radius and is given by

$$r_L = v_t/\Omega_c \tag{2.1.11}$$

A measure of the magnetisation of a plasma is given by the magnetisation parameter

$$\delta = r_L/L \tag{2.1.12}$$

A plasma can be said to be strongly magnetised if $\delta \ll 1$, indicating that the Larmor radius is much smaller than the typical length scale of the plasma [3]. The magnetisation parameter is the fundamental measure of the magnetic field's effect on the plasma.

One of the most important parameters describing a plasma is the plasma β. This is defined as the ratio of the plasma kinetic pressure to the magnetic pressure. For each species s it is defined as

$$\beta_s = 2\mu_0 p_s / B^2 \tag{2.1.13}$$

where p_s is the scalar pressure for species s, μ_0 the vacuum permeability, B the magnetic field and where the total plasma β for all plasma species s is given by

$$\beta = \sum_s \beta_s \tag{2.1.14}$$

2.1.2 Particle drifts and orbits

Particle drifts The macroscopic behaviour of a plasma is determined by the motion of its constituent particles. Thus, before considering the plasma as a whole, it is instructive to consider how these particles behave in the presence of finite electro-magnetic fields. This is done by considering a magnetised, collisionless plasma where the particles are confined to orbits about the magnetic field and where this motion dominates that resulting from collisions. The dynamical equations for an individual particle are given by

$$\frac{d\mathbf{r}}{dt} = \mathbf{v} \tag{2.1.15}$$

$$m\frac{d\mathbf{v}}{dt} = e(\mathbf{E} + \mathbf{v} \times \mathbf{B}) \tag{2.1.16}$$

In a uniform electromagnetic field this motion takes the form of free-streaming parallel to the magnetic field lines, gyration about the magnetic field with frequency $\Omega = \Omega_c$ and a steady drift at velocity

$$\mathbf{v}_E = \frac{\mathbf{E} \times \mathbf{B}}{B^2} \tag{2.1.17}$$

This is termed the *E-cross-B drift* and is in the same direction for both electrons and ions as it is independent of the sign of their charge. This drift can be eliminated by transforming to an inertial frame with $\mathbf{E}_\perp = 0$, which moves with the velocity $\mathbf{v}_E$ relative to the lab frame, and can be regarded as the rest frame of the plasma. Note that the parallel electric field $E_\parallel$ is very small or vanishing for a plasma close to equilibrium [3]. The guiding centre is the gyrocentre of the gyrating particle motion. This is shown in figure 2.1.

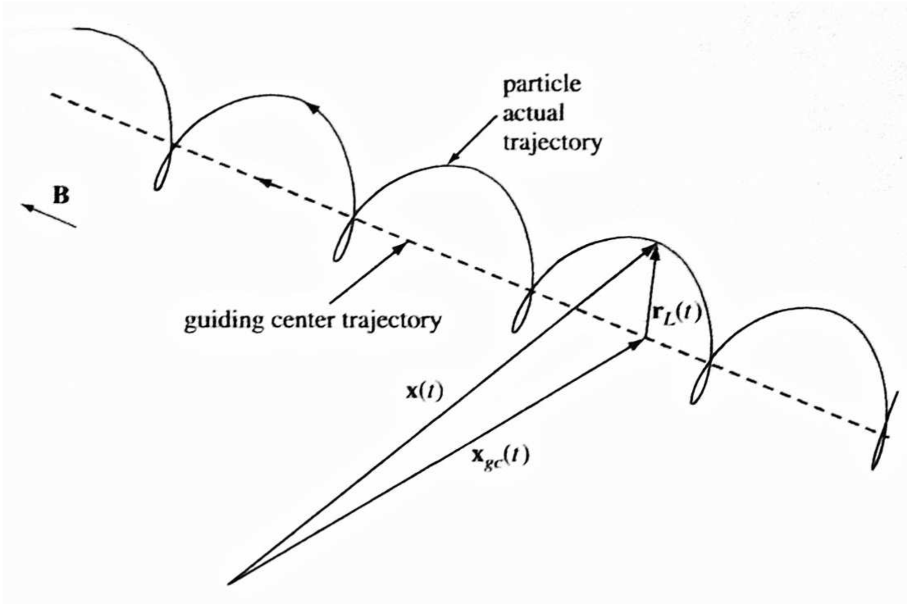

Figure 2.1. Relationship between guiding centre trajectory and actual trajectory of a particle in the presence of a magnetic field [9].

We next consider particle trajectories in electric and magnetic fields that are no longer spatially or temporally uniform. The magnetic field is assumed to not vary much over a gyro-period or gyro-radius. This assumption can be stated as follows

$$r_L \nabla B \ll B \tag{2.1.18}$$

$$\frac{1}{\Omega}\frac{\partial B}{\partial t} \ll B \tag{2.1.19}$$

The electric field is assumed to be comparable to the magnetic field. The particle position can be written in terms of its radius of gyration r_L and guiding centre radius x_{gc} as

$$\mathbf{x}(t) = \mathbf{r}_L(t) + \mathbf{x}_{gc}(t) \tag{2.1.20}$$

This rapid gyrating motion can be averaged out and only the motion of the guiding centre considered. The velocity can be divided into the guiding centre velocity $\mathbf{U}$ and gyration velocity $\mathbf{u}$ as $\mathbf{v} = \mathbf{U} + \mathbf{u}$. Taking the gyrophase average of equation 2.1.16, the first order guiding centre equation of motion is recovered

$$m\frac{d\mathbf{U}_0}{dt} = eE_\parallel \mathbf{b} + e\mathbf{U}_1 \times \mathbf{B} - \mu \nabla B \tag{2.1.21}$$

where $\mu = mu_\perp^2/2B$ is the magnetic moment, which is found to be an invariant of the system, and $u_\perp$ is the perpendicular velocity of the particle. From this equation the first order perpendicular drift velocity can be recovered. Thus, the motion of a charged particle in spatially and temporally varying electric and magnetic fields is found to consist of gyration about the guiding centre with a velocity $u_\perp$ determined by the magnetic moment, and a perpendicular drift consisting of the $E \times B$ drift and a first order perpendicular drift. The $E \times B$ drift and the magnetic drift component of the first order perpendicular drift are demonstrated in figure 2.2 (a) and (b) respectively.

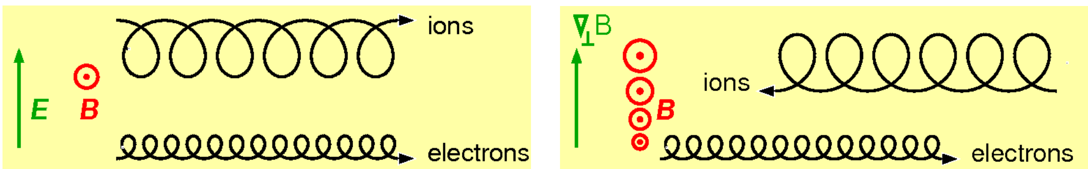

(a) (b)

Figure 2.2. (a) The perpendicular $E \times B$ drift originates from the alternating acceleration and deceleration of particles in the presence of an electric field, resulting in a changing gyro-radius. (b) The magnetic drift results from the variation of the gyro-radius in the presence of a finite magnetic field gradient [10].

The parallel motion of the particle is determined by taking the parallel component of the first order guiding centre equation of motion. The first order perpendicular drift velocity takes the following form [3]

$$\mathbf{U}_{1\perp} = \frac{\mu}{m\Omega}\mathbf{b} \times \nabla B + \frac{U_{0\parallel}}{\Omega}\mathbf{b} \times \frac{d\mathbf{b}}{dt} + \frac{\mathbf{b}}{\Omega} \times \frac{d\mathbf{v}_E}{dt} \tag{2.1.22}$$

This expression can be simplified and three physically distinct drifts identified. The first is called the magnetic drift and has the following form

$$\mathbf{U}_{mag} = \frac{\mu}{m\Omega}\mathbf{b} \times \nabla B \tag{2.1.23}$$

This results from the particle gyrating in a region with a finite magnetic field gradient. As the particle moves into a region with a higher magnetic field, the radius of gyration will decrease as $r_L \propto 1/B$.

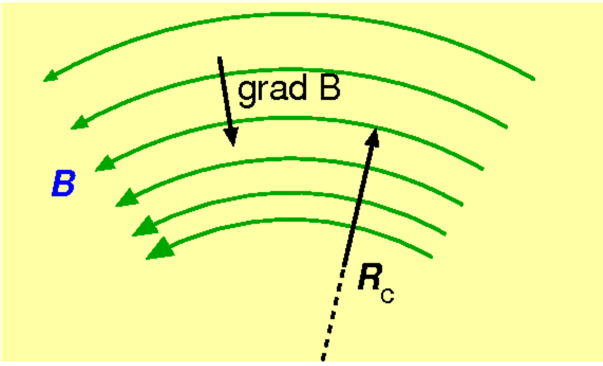

Figure 2.3. The magnetic curvature drift originates from particles following curved magnetic field lines and experiencing a centrifugal force as a result [10].

Thus the orbit will not fully close and the particle guiding centre will drift in a direction perpendicular to the magnetic field gradient and the local magnetic field direction [3], as demonstrated in figure 2.2 (b). Upon simplification, the most important contribution to the second term in equation 2.1.22 is found to be

$$\mathbf{U}_{curv} = \frac{U_{0\|}^2}{\Omega}\mathbf{b} \times (\mathbf{b} \cdot \nabla)\mathbf{b} \tag{2.1.24}$$

This is called the magnetic curvature drift, as demonstrated in figure 2.3. This nomenclature arises from the $(\mathbf{b} \cdot \nabla)\mathbf{b}$ terms which can be identified as a vector, known as the radius of curvature, pointing towards the centre of a circle approximated by the local magnetic field line, and with a magnitude inversely proportional to the radius of this circle [3]. The centripetal acceleration caused by the magnetic field curvature gives rise to a drift velocity perpendicular to the radius of curvature and the direction of the local magnetic field. The final term in equation 2.1.22 can be simplified to

$$\mathbf{U}_{polz} = \frac{1}{\Omega}\frac{d}{dt}(\frac{\mathbf{E}_{\perp}}{B}) \tag{2.1.25}$$

This describes a drift due to a constant change in the polarisation of the plasma caused by a continuous change in the perpendicular electric field in time, known as the polarisation drift. This is independent of the parallel electric field and is much greater for ions than for electrons due to the Ω^{-1} term preceding it [3].

Particle orbits In a tokamak, the magnetic field has a $1/R$ dependence, where R is the plasma major radius. Particles with sufficient parallel velocity will be able to circulate around the torus freely.

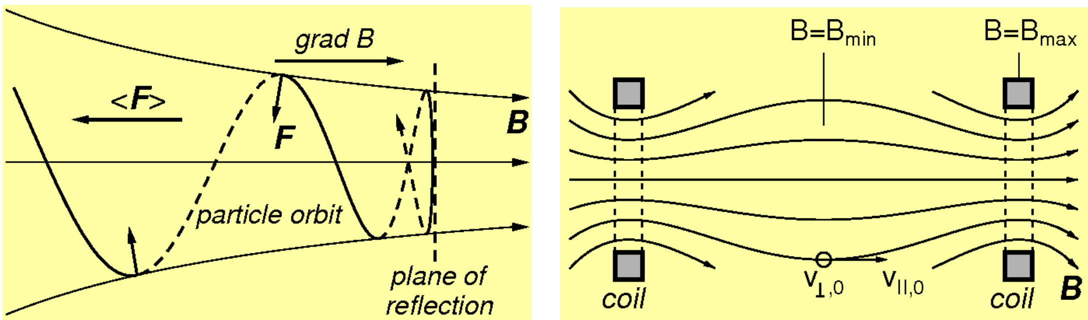

(a) (b)

Figure 2.4. (a) Parallel magnetic field gradient results in Lorentz force reducing $v_{\|}$ component of velocity, eventually reversing its sign at the reflection point. The magnetic moment μ is conserved as magnetic field strength increases. (b) This velocity behaviour leads to the mirror principle of magnetic confinement [10].

These are known as *passing particles*. Those with insufficient parallel velocity will be trapped on the outer side of the torus as they are unable to overcome the mirror force resulting from the poloidal variation of the magnetic field. These are known as *trapped particles* and they will bounce between turning points [1], as demonstrated in figures 2.4 and 2.5.

The magnetic moment $\mu = mv_{\perp}^2/2B$ is a constant of motion to the lowest order, that is $d\mu/dt = 0$. The mirror force that causes the particle trapping can be thought of as a force $\mathbf{F} = -\mu\nabla_{\|}B$ on the magnetic moment and is demonstrated in figures 2.4 (a) and (b). The minimum magnetic field B_{min} experienced in a particle orbit will occur at the median plane [1]. From the constancy of the magnetic moment μ, the following is found to be true

$$\frac{v_\perp^2}{B} = \frac{v_{\perp 0}^2}{B_{min}} \tag{2.1.26}$$

where $v_{\perp 0}^2$ is the perpendicular velocity at the median plane. At the mirror point, the trapped particle will have $v_\parallel = 0$. From the conservation of energy, this leads to [10]

$$\frac{1}{2}mv^2 = \frac{1}{2}mv_{\parallel 0}^2 + \frac{1}{2}mv_{\perp 0}^2 \leq \mu B_{max} \tag{2.1.27}$$

The maximum magnetic field at the bounce point B_{max} is recovered by combining these two equations, and the trapping condition is given by [1]

$$\frac{v_{\parallel 0}}{v_{\perp 0}} \leq (\frac{B_{max}}{B_{min}} - 1)^{1/2} \tag{2.1.28}$$

Thus, any particles at the median plane satisfying this condition will be trapped, while the rest will pass unobstructed around the torus.

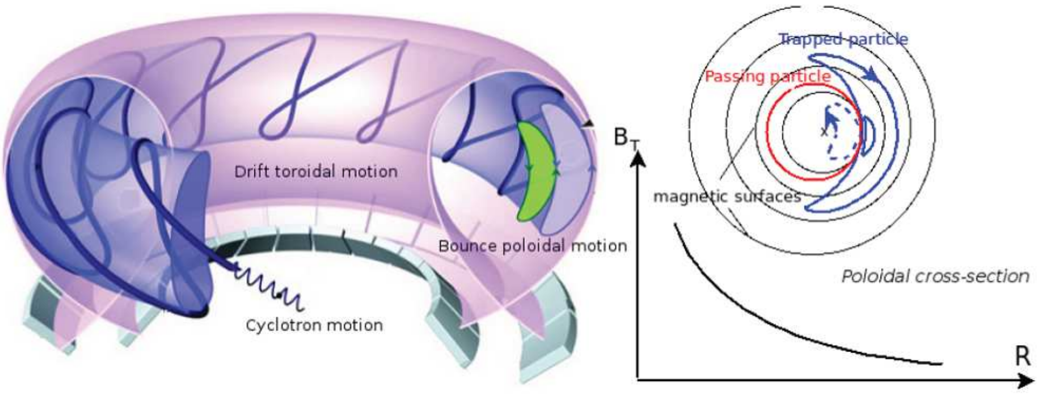

Figure 2.5. Demonstration of different components of particle motion in a tokamak plasma, including bounce motion in the poloidal direction, drift toroidal motion and cyclotron motion. Passing particle orbits, as well as the dependence of the turning points of the different types of trapped particle orbits on the toroidal magnetic field are also shown [11].

2.1.3 Ideal magnetohydrodynamics (MHD)

It is desirable to work in a system that can describe the macroscopic behaviour of a plasma. This is provided by ideal magnetohydrodynamics (MHD), in which the plasma is treated as a perfectly conducting fluid which can be described by a few local variables such as the mass density, kinetic temperature and fluid velocity [3].

The evolution of these variables is governed by a set of equations similar to those of hydrodynamics, but with the effects of electromagnetic forces included. The pre-Maxwellian equations are also included in the set of ideal MHD equations 2.1.29-2.1.35, which provides a single fluid, long-wavelength, low-frequency description of the macroscopic plasma behaviour [8].

$$\frac{d\rho}{dt} = -\rho\nabla \cdot \mathbf{v} \tag{2.1.29}$$

$$\rho\frac{d\mathbf{v}}{dt} = \mathbf{J} \times \mathbf{B} - \nabla p \tag{2.1.30}$$

$$\frac{dp}{dt} = -\gamma p\nabla \cdot \mathbf{v} \tag{2.1.31}$$

$$\nabla \times \mathbf{B} = \mu_0\mathbf{J} \tag{2.1.32}$$

$$\frac{\partial\mathbf{B}}{\partial t} = -\nabla \times \mathbf{E} \tag{2.1.33}$$

$$\mathbf{E} + \mathbf{v} \times \mathbf{B} = 0 \tag{2.1.34}$$

$$\nabla \cdot \mathbf{B} = 0 \tag{2.1.35}$$

Here, $\mathbf{E}$ and $\mathbf{B}$ are the electric and magnetic fields, $\mathbf{J}$ is the current density, ρ the mass density, $\mathbf{v}$ is the fluid velocity, p is the pressure and γ is the ratio of specific heats. $d/dt = \partial/\partial t + \mathbf{v} \cdot \nabla$ is the convective derivative.

Ideal MHD equilibrium The discussions in the following sections concern the properties of ideal MHD equilibrium, the plasma safety factor and plasma diamagnetism and follow primarily the discussions in [1, 3, 8, 12]. In order to facilitate a sustained fusion reaction it is necessary that the plasma achieve a stable, stationary configuration. This is to ensure that it does not come into contact with the surrounding surfaces, leading to a disruption of the plasma. These conditions are also necessary so that a large enough β value can be achieved in order to output sufficient energy to operate a viable fusion power plant, while maintaining the stability of the plasma [8].

The subject of tokamak equilibrium can be divided into two main aspects. Firstly, the pressure of the plasma and the forces due to the magnetic field must be balanced. Secondly, the shape and position of the plasma must be controlled. This is achieved via currents in the external coils surrounding the plasma, as has been described in section 1.4. A stationary, perfectly conducting plasma can be described by the following set of reduced ideal MHD equations

$$\nabla p = \mathbf{J} \times \mathbf{B} \tag{2.1.36}$$

$$\nabla \times \mathbf{B} = \mu_0 \mathbf{J} \tag{2.1.37}$$

$$\nabla \cdot \mathbf{B} = 0 \tag{2.1.38}$$

where p is the total scalar pressure, $\mathbf{J}$ is the current density, $\mathbf{B}$ is the magnetic field and μ_0 is the vacuum permeability. Assuming a right-handed, cylindrical coordinate system, described by the coordinates R, ϕ, Z, with $\partial/\partial\phi = 0$ from toroidal axisymmetry, an equation describing an axisymmetric toroidal plasma equilibrium can be derived. This equation, known as the Grad-Shafranov equation (GSE) [13, 14], is a two-dimensional, non-linear, elliptic partial differential equation, and is stated as follows

$$-(\frac{\partial^2\psi}{\partial R^2} - \frac{1}{R}\frac{\partial\psi}{\partial R} + \frac{\partial^2\psi}{\partial Z^2}) = \mu_0 R^2 p'(\psi) + FF'(\psi) = \mu_0 R j_\phi \tag{2.1.39}$$

where j_ϕ is the toroidal current density and ψ is the poloidal magnetic flux per radian. $F = RB_\phi = \mu_0 I_{pol}/2\pi$, where $I_{pol}(\psi)$ is the poloidal current unique to every point on the flux surface labelled by the poloidal flux value ψ [8, 12]. $p'(\psi) = dp/d\psi$ and $FF'(\psi)$ are arbitrary functions of ψ [12]. The left hand side of the equation includes the elliptic operator $-\Delta^*$, and is given by [8]

$$-\Delta^*\psi = -(\frac{\partial^2\psi}{\partial R^2} - \frac{1}{R}\frac{\partial\psi}{\partial R} + \frac{\partial^2\psi}{\partial Z^2}) \tag{2.1.40}$$

which is almost identical to the Laplacian operator in cylindrical coordinates, save for the minus sign before the $1/R$ term. The stability of ideal MHD equilibria is discussed in section 3.2.1 in the context of ideal MHD wave theory.

Safety factor The safety factor q is so called because of the role it plays in determining plasma stability. In general, higher q values will lead to greater stability. In an axisymmetric tokamak equilibrium, each magnetic field line has a q value associated with it. This gives a measure of the helicity of the field line. If at some toroidal angle ϕ the field line has a certain position in the poloidal plane, it will return to that position in the poloidal plane after a change of $\Delta\phi$ in the toroidal angle. The q-value of this field line is then defined by [1]

$$q = \frac{\Delta\phi}{2\pi} \tag{2.1.41}$$

Rational values of q play an important role in stability, and their significance in the context of the analysis conducted in this work will become clear in later chapters. Again, following the description given in [1], if $q = m/n$, where m and n are integers, then the magnetic field line will join up on itself after m toroidal and n poloidal rotations around the torus. The radial q-profile usually has its minimum value at, or close to, the magnetic axis and increases outwards. In the case of a large aspect-ratio and circular cross section plasma, the behaviour of q is simply determined by the toroidal current density profile $j(r)$, where r is the radius of the plasma [1]. From Ampére's law, an expression for the q value at a certain radial position in terms of the total current $I(r)$ at that position and the toroidal magnetic field B_ϕ is given by [1]

$$q(r) = \frac{2\pi r^2 B_\phi}{\mu_0 I(r) R} \tag{2.1.42}$$

Plasma diamagnetism Upon considering the momentum equation 2.1.30 in the drift limit, the perpendicular velocity for both the ions and electrons can be written in terms of the $E\times B$ velocity v_E and a second drift term v_{ds} resulting from an additional, non-magnetic force on the particles. The perpendicular velocity is given by

$$\mathbf{v}_{\perp s} = \mathbf{v}_E + \mathbf{v}_{ds} \tag{2.1.43}$$

where $\mathbf{v}_E = \mathbf{E} \times \mathbf{B}/B^2$, $\mathbf{v}_d = -\nabla p \times \mathbf{B}/nqB^2$ and s is the particle species. $\mathbf{v}_d$ is known as the diamagnetic drift velocity. As described in [3], this name stems from the fact that the diamagnetic current

$$\mathbf{j}_d = -en(\mathbf{v}_{de} - \mathbf{v}_{di}) = -\frac{\nabla p \times \mathbf{B}}{B^2} \tag{2.1.44}$$

generally acts to reduce the magnetic field inside the plasma. Physically, the drift arises from the presence of gradients in the temperature and density.

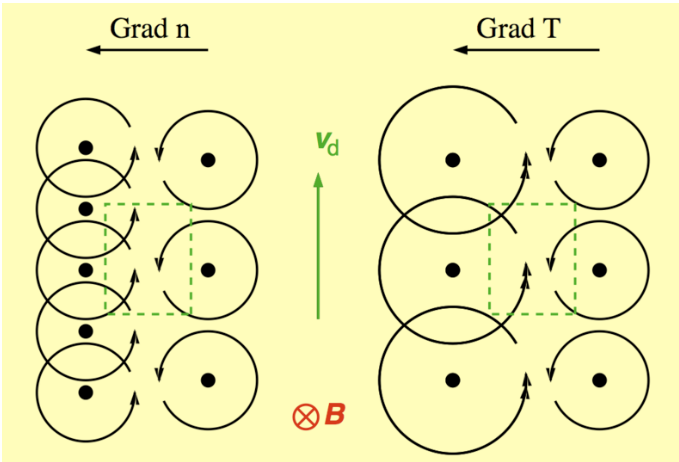

Figure 2.6. Demonstration of the origin of the diamagnetic drift velocity v_d in the presence of finite density and temperature gradients [10].

At a given point on the plasma radius, the presence of a density gradient means that a net particle flux will exist in a given direction, giving rise to a drift velocity. This process is demonstrated in figure 2.6. It should be pointed out that the diamagnetic flows represent fluid flows for which there is no corresponding motion of the particle guiding centres but which nevertheless stem from real fluid velocities. The ion and electron diamagnetic drifts will be of similar magnitudes but in opposite directions [3].

2.2 Plasma heating

There are a number of plasma heating methods available at ASDEX Upgrade. One of these is through Ohmic heating, which results from current flowing through a plasma of finite resistivity. However, the plasma can also be heated via a number of external sources. These include injecting neutral ions into the plasma to heat it through collisions, a method known as neutral beam injection (NBI), and the introduction of radio frequency waves into the plasma to heat it through resonant absorption, known as radio frequency (RF) heating. RF heating can be sub-divided into ion cyclotron resonance heating (ICRH) and electron cyclotron resonance heating (ECRH), that preferentially heat the ions and electrons respectively. The basic theory and implementation of these systems is described in this section, following the descriptions given in [1, 5, 6].

2.2.1 Ohmic heating

As has been described in section 1.3, the poloidal magnetic field in a tokamak is induced by a toroidal plasma current, which is itself a result of the varying in time of the magnetic flux through the central solenoid. The toroidal current will result in the plasma being heated in the presence of finite resistivity, a results of collisions between electrons and ions. This is known as Ohmic heating and its heating power density is given by $P_\Omega = \eta j^2$, where η is the plasma resistivity and j is the current density [1]. As $\eta \propto T_e^{-3/2}$, the efficiency of the Ohmic heating power falls off rapidly with increasing T_e. At ASDEX Upgrade approximately 1MW of Ohmic heating power is available. Thus, Ohmic heating alone is not sufficient to achieve the temperatures necessary to reach ignition, motivating the usage of external heating sources.

2.2.2 Ion cyclotron resonance heating (ICRH)

ICRH power can be launched into the plasma and be absorbed by either ions or electrons, thereby heating the plasma. Direct absorption by the ions occurs at specific locations R where the frequency ω matches the local cyclotron frequency of the ions ω_{ci}, i.e. where $\omega = \omega_{ci}(R)$. The resonance is subject to Doppler broadening, resulting in a resonance width $\delta x = (k_\parallel v_{ti}/\omega_{ci})R$, where $k_\parallel$ is the parallel wavenumber and v_{ti} is the thermal ion velocity. This resonance is achieved by using a small concentration of the resonating species in a majority of non-resonating ions, in a scenario known as minority heating. The wave can also be absorbed at the harmonics of the cyclotron resonances of the ions, if their Larmor radius is large enough [1, 6]. At ASDEX Upgrade, ICRH power can be launched into the plasma by four antennas, as shown in figure 2.7 (a). These are powered by four generators, each with an output power of 2MW.

2.2.3 Electron cyclotron resonance heating (ECRH)

ECRH power is absorbed by electrons when $\omega = n\omega_{ce}$, where n is an integer and indicates the harmonic number. Since $\omega_{ce} \geq \omega_{pe}$, only electrons respond to electron cyclotron waves and only they are heated directly. Up to 4MW of ECRH power can be launched into the plasma at ASDEX Upgrade [1].

2.2.4 Neutral beam injection heating (NBI)

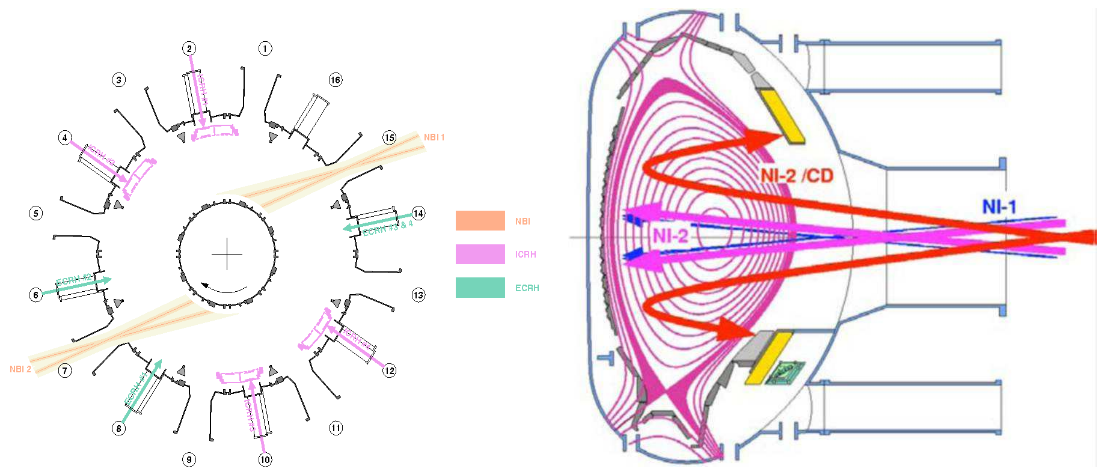

(a) (b)

Figure 2.7. (a) Direction of NBI beam sources and locations of ECRH/ICRH launchers in toroidal plane. (b) Typical path of NBI beams in poloidal plane [5].

Neutral atoms injected into a tokamak plasma travel in straight lines as they are unaffected by the magnetic field. The atoms become ionised through collisions with the particles that form the plasma and the resulting ions and electrons are subject to confinement by the magnetic field due to their charge. Since the ions and electrons have the same velocity, the energy is carried almost entirely by the more massive ions. Once ionised, the ions have orbits determined by their energy, angle of injection and point of deposition. The energy of the injected ions is gradually transferred to the plasma electrons and ions through Coulomb collisions. Thus, the injected ions are initially slowed and eventually thermalised [1].

At ASDEX upgrade, the NBI system consists of two injectors, each equipped with four ion sources. These are capable of injecting up to 20MW into the plasma. The ion sources are arranged in a rectangle, with one pair of beams injecting more normal and the other more tangential to the plasma [6]. The positioning of these sources as well as those of the ECRH and ECRH systems is demonstrated in figure 2.7.

2.3 Plasma diagnostics

An extensive suite of diagnostics is available at ASDEX Upgrade in order to measure different plasma parameters. For this work, the most important diagnostics are those that measure the electron and ion temperatures and densities, and those that provide information concerning the frequency and amplitude of different types of mode activity. Measurements of the temperature and density are provided by the electron cyclotron emission (ECE), Thomson scattering, interferometry, lithium beam (LIB) and charge exchange recombination spectroscopy (CXRS) diagnostics. Measurements of the mode activity are provided by the Mirnov coil, soft x-ray (SXR) and 2D electron cyclotron emission imaging (ECEI) diagnostics. A short description of each is presented in the following sections. The discussions in sections 2.3.1-2.3.9 primarily follow those given in [15–18], [1], [21, 22], [23] and [24].

2.3.1 Mirnov coils

Information about the characteristics of modes in a tokamak plasma can normally be obtained through observations of the magnetic field perturbations that these modes cause. This information includes the frequency at which the modes rotate, the poloidal and toroidal mode numbers, as well as the magnetic perturbation amplitude. From Faraday's law 2.3.1, it is known that a magnetic field that changes in time induces an electric field

$$V = \oint_C \mathbf{E} \cdot d\mathbf{l} = -\frac{\partial}{\partial t} \int_S \mathbf{B} \cdot d\mathbf{S} \qquad (2.3.1)$$

In the presence of a conducting loop, a voltage is induced in this loop due to the magnetic field changing in time, as presented in equation 2.3.1 [15]. By measuring the amplitude of this voltage, the degree to which the magnetic field changes in time can be recovered. At ASDEX Upgrade many such coils, known as Mirnov coils, are positioned about the plasma in both the poloidal and toroidal planes, as demonstrated in figure 2.8. From these arrays of Mirnov coils, information about magnetic perturbations resulting from modes can be obtained [15].

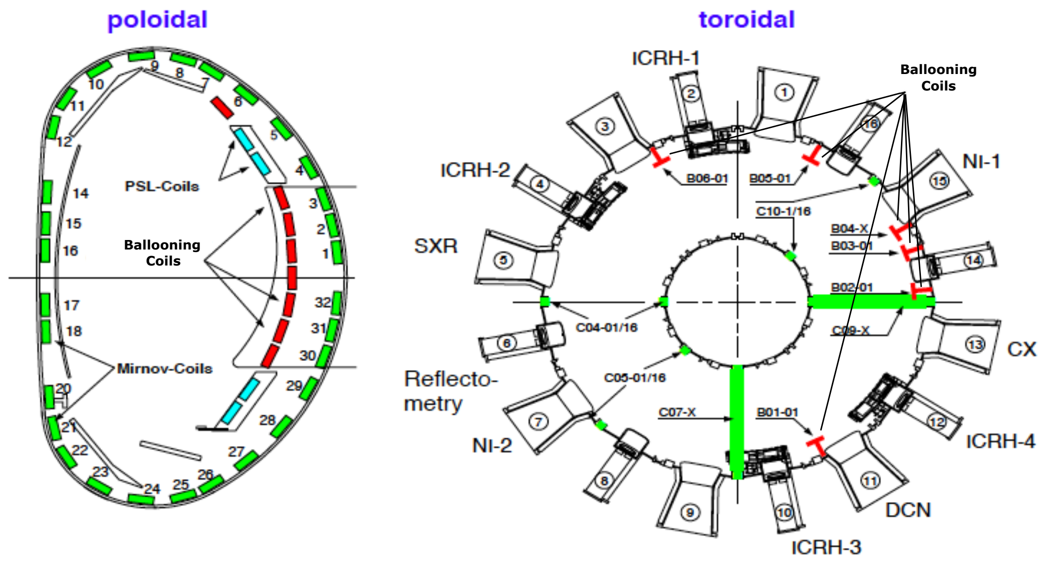

(a) (b)

Figure 2.8. Mirnov coil arrays at ASDEX Upgrade in (a) poloidal and (b) toroidal planes [6].

2.3.2 Soft X-ray (SXR)

Soft x-ray cameras are one of the main plasma diagnostics utilised in current fusion research. The plasma temperature in tokamaks has its maximum in the soft x-ray spectral region (100eV to 10keV). The detection of soft x-ray radiation from a fusion plasma allows the investigation of various MHD instabilities and provides information on equilibrium data [16]. The soft x-ray diagnostic at ASDEX Upgrade provides 208 lines of sight of the plasma, 128 of which have a fast sampling rate of 2MHz [16]. The orientations of these lines of sight are demonstrated in figure 2.9 (a).

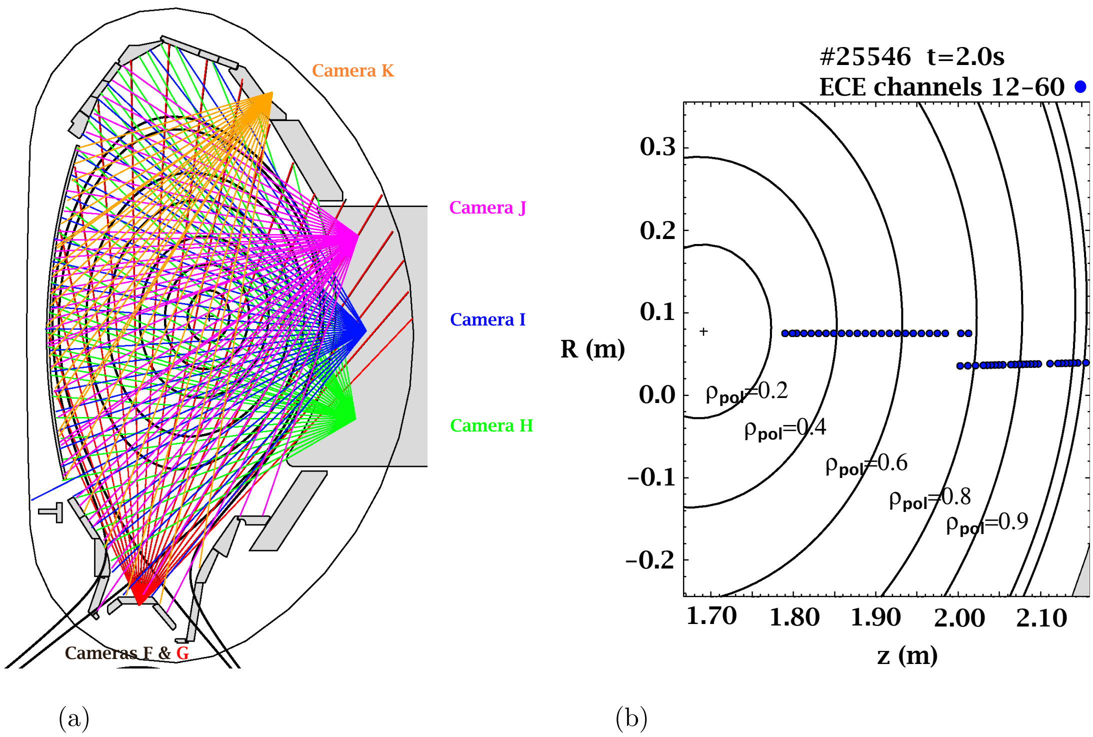

Figure 2.9. (a) Lines of sight of soft x-ray cameras K, J, I, H, F and G at ASDEX Upgrade. (b) Example of ECE channel positions at ASDEX Upgrade for discharge 25546 at $t = 2.0$s.

2.3.3 Electron cyclotron emission (ECE)

The electron cyclotron emission (ECE) diagnostic provides a measures of the electron temperature. In a hot, magnetised plasma, electrons gyrate around magnetic field lines. Because of this accelerated motion they emit electromagnetic radiation at discrete angular frequencies $\omega = n\omega_{ce}$ where n is the harmonic number and the electron cyclotron resonance angular frequency is given by

$$\omega_{ce} = \frac{eB}{m_e} \tag{2.3.2}$$

Here, B is the total magnetic field, e is the elementary charge and m_e the electron mass in the laboratory frame, at low harmonics of the cyclotron frequency. Radiometry of electron cyclotron emission (ECE) can be used to determine the electron temperature of the plasma. In a toroidal configuration, the magnetic field is inhomogeneous, so that the spectral resolution of ECE measurements translates into spatial resolution. For example, in a tokamak the major magnetic field component is the toroidal field $B_t = B_t(R) \propto 1/R$ generated by external coils, where R is the major radius. Spectrally resolved ECE measurements along one single radial line of sight yield a radial T_e profile [1, 17].

2.3.4 Electron cyclotron emission imaging (ECEI)

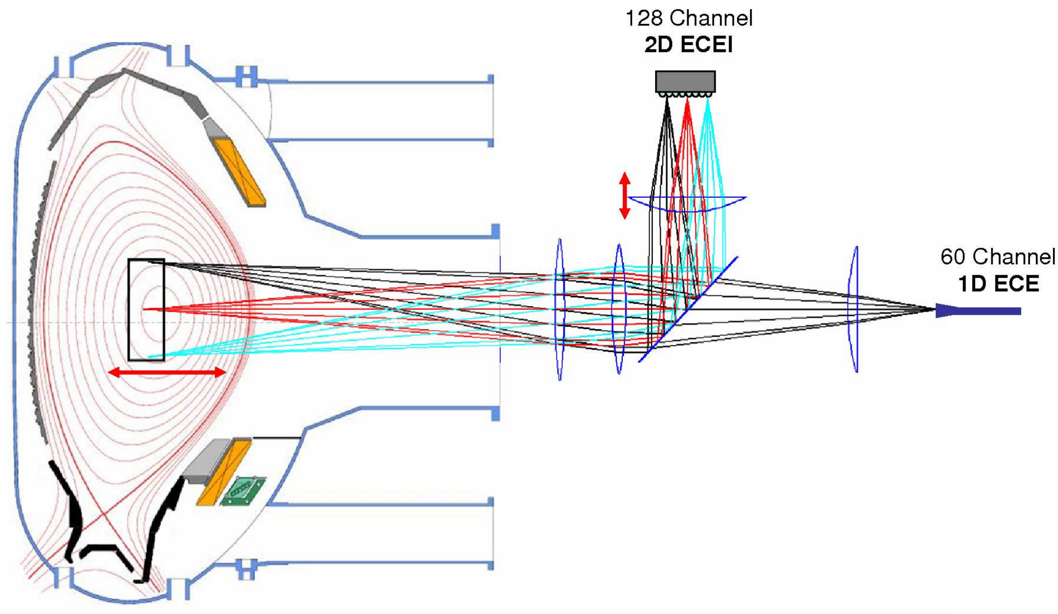

Figure 2.10. Schematic demonstrating operation of 2D ECEI system at ASDEX Upgrade [18].

The principles governing the 1D ECE diagnostic have been described in section 2.3.3. At ASDEX Upgrade, a 2D electron cyclotron emission imaging (ECEI) system is available for the investigation of the 2D electron temperature dynamics of reactor relevant instabilities. The same principles employed in the 1D ECE diagnostic are used for 2D ECEI, except that multiple lines of sight are simultaneously quasioptically imaged onto a linear array of diode detectors. Each of the lines of sight is treated as a 1D ECE radiometer. This gives direct 2D measurements of the electron temperature, radially resolved due to the frequency resolved measurement of the ECE intensity along each line of sight, vertically resolved due to the multiple lines of sight corresponding to the detectors on the array [18]. A schematic demonstrating the operation of the 2D ECEI system is shown in figure 2.10.

2.3.5 Interferometry

The line integrated electron density at different radial locations can be obtained at ASDEX Upgrade from the interferometry diagnostic. At frequencies that are large compared to the plasma frequency, the change in the phase of a beam of coherent radiation passing through a plasma compared to that of a reference beam is proportional to the electron density integrated along the beam probing the plasma. This phase difference can be measured by a Mach-Zehnder interferometer arrangement which causes one of the beams to be shifted in frequency. Upon recombining the reference beam with the frequency shifted radiation, a beat signal at the difference frequency $\Delta\omega_0$ is produced. From the variation in phase of the probing beat signals with respect to the reference beat signals, the line integral of the density may be deduced [1].

2.3.6 Thomson scattering

The electron temperature can be determined at ASDEX Upgrade using the Thomson scattering diagnostic which measures the scattering of light from free electrons. The electron temperature is determined from the degree of broadening of the spectrum of the scattered laser radiation [1].

2.3.7 Lithium beam

The lithium beam diagnostic provides a measure of the electron density in a tokamak plasma. High energy Li atoms are injected into the plasma and from observing the resonant line radiation of the injected Li-beam, it is possible to deduce the electron density profile [21, 22].

2.3.8 Integrated data analysis (IDA)

In nuclear fusion, different measurement techniques for the same physical quantity often provide complementary and redundant information. At ASDEX Upgrade, the concept of integrated data analysis (IDA) within the framework of Bayesian theory has been applied to the combined analysis of lithium beam emission spectroscopy (LIB), deuterium cyanide laser interferometry, electron cyclotron emission (ECE), and Thomson scattering spectroscopy. These four heterogeneous diagnostics enable the simultaneous estimation of the electron density and temperature profiles with high spatial and temporal resolution [23].

2.3.9 Charge exchange recombination spectroscopy (CXRS)

Ion temperature and rotation in a plasma can be measured by an active charge exchange recombination spectroscopy (CXRS). The light emitted due to charge exchange reactions between fully ionised impurity ions and injected neutral atoms yields localised information about the impurity ion temperature and velocity from the Doppler widths and Doppler shifts of the measured spectra. At ASDEX Upgrade, toroidal CXRS systems viewing the core and the edge of the plasma provide temporally and radially resolved CXRS profiles [24].

2.4 Sawtooth instability

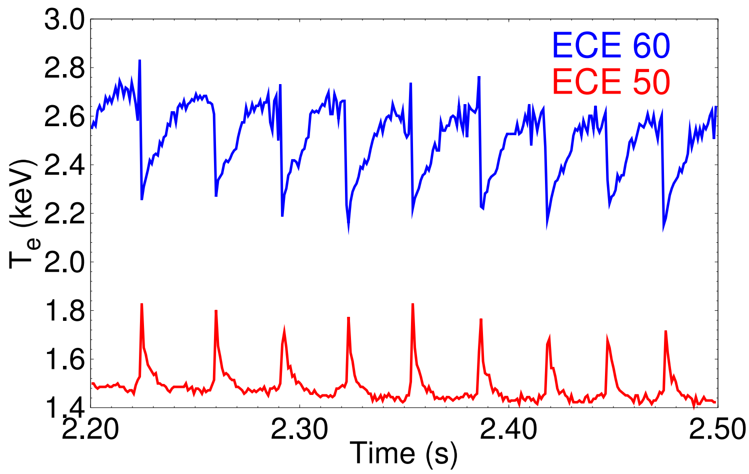

Figure 2.11. Sawtooth activity from $t = 2.20 - 2.50$s during discharge 25546, showing crashes in temperature measured by ECE channel 60 located inside $q = 1$ surface and heat pulses measured by ECE channel 50 located outside $q = 1$ surface.

The sawtooth instability is one of the most important instabilities observed in a tokamak plasma. It is characterised by a repetitive crash of the central electron temperature [25], with figure 2.11 demonstrating this distinctive temporal evolution of the electron temperature T_e from which the instability derives its name.

It can be seen that T_e rises during the stable ramp phase before a collapse in T_e occurs, with the associated thermal energy being released to the outer part of the plasma in the form of a heat pulse [1]. The sawtooth instability is associated with the existence of a kink instability in the plasma, with toroidal and poloidal mode numbers $(m, n) = (1, 1)$. This indicates the existence of a $q = 1$ surface in the plasma.

A model to explain the sawtooth instability has been proposed by Kadomtsev [26] which is based on fast magnetic reconnection. This model proposes that the kink mode would drive magnetic reconnection of the helical flux between the axis and the $q = 1$ surface with an equal and opposite flux outside the $q = 1$ surface. The Kadomtsev model, in which the $(1, 1)$ island results in a new magnetic axis after the crash, provides some insight into the sawtooth instability. However, it has been shown that the model is in contradiction with many experimental observations and cannot explain the measured safety factors nor the existence of the $(1, 1)$ mode after the crash [16]. Thus, it is clear that a revised model is required to fully explain the sawtooth instability. This instability will form a central part of the analysis conducted in this work.

Chapter 3

Theoretical overview of low-frequency Alfvén eigenmodes

In this chapter an overview of the fundamentals of Alfvén eigenmode theory is presented. This overview begins with a discussion of ideal MHD waves before proceeding with a discussion of the kinetic theory of low-frequency Alfvén eigenmodes, including why the kinetic description is necessary to describe these waves accurately.

3.1 Ideal MHD wave theory

The ideal MHD equations can be used to determine a static equilibrium plasma configuration, favourable for the confinement of a tokamak plasma. However, it is also necessary to consider the stability of such a configuration. This can be achieved by linearising the ideal MHD equations and considering the stability of the small-amplitude waves that are recovered from them. These waves can propagate in both homogeneous and inhomogeneous plasma configurations and can couple in the latter, potentially leading to unstable modes.

3.1.1 Ideal MHD waves in a homogeneous plasma

The types of waves that will primarily be considered for the remainder of this work are of small amplitude and exist in the low-frequency regime, well below the ion cyclotron frequency. Essentially, they result from interactions between the magnetic field and plasma fluid.

In sections 3.1 and 3.2 we follow closely the treatment of these waves presented in [8, 27, 28], and begin by considering the ideal MHD equations in an infinite, stationary and homogeneous plasma permeated by an infinite, homogeneous and unidirectional background magnetic field. In this configuration the plasma equilibrium parameters are given by [8]

$$\mathbf{B} = B_0\mathbf{e}_z,\ \rho = \rho_0 \tag{3.1.1}$$

$$\mathbf{J} = 0,\ \mathbf{v} = 0,\ p = p_0 \tag{3.1.2}$$

where B_0, ρ_0 and p_0 are the equilibrium magnetic field, mass density and pressure respectively, with each assumed to be constant. $\mathbf{e}_z$ is the unit vector in the magnetic field direction. In this configuration there are no gradients in the plasma i.e.

$$\nabla p = \nabla \rho = \mathbf{J} = 0 \tag{3.1.3}$$

Linearisation of the ideal MHD equations If we assume an essentially static bulk plasma, with only small magnitude perturbations over the time-scale of interest, then the ideal MHD equations can be linearised by taking each quantity to be the sum of a zeroth order time-independent equilibrium component and a small first order time-dependent perturbation [27]. The linearised ideal MHD equations are then given by equations 3.1.4-3.1.10

$$\frac{\partial \rho_1}{\partial t} + \nabla \cdot (\rho_0 \mathbf{v}_1) = 0 \tag{3.1.4}$$

$$\rho_0 \frac{\partial \mathbf{v}_1}{\partial t} + \nabla p_1 - \mathbf{J}_1 \times \mathbf{B}_0 - \mathbf{J}_0 \times \mathbf{B}_1 = 0 \tag{3.1.5}$$

$$\frac{\partial p_1}{\partial t} + \mathbf{v}_1 \cdot \nabla p_0 + \gamma p_0 \nabla \cdot \mathbf{v}_1 = 0 \tag{3.1.6}$$

$$\nabla \cdot \mathbf{B}_1 = 0 \tag{3.1.7}$$

$$\frac{\partial \mathbf{B}_1}{\partial t} + \nabla \times \mathbf{E}_1 = 0 \tag{3.1.8}$$

$$\nabla \times \mathbf{B}_1 - \mu_0 \mathbf{J}_1 = 0 \tag{3.1.9}$$

$$\mathbf{E}_1 + \mathbf{v}_1 \times \mathbf{B}_0 = 0 \tag{3.1.10}$$

where $\mathbf{B}_1$, $\mathbf{E}_1$, $\mathbf{J}_1$, ρ_1 and p_1 are the perturbed magnetic field, electric field, current density, mass density and pressure respectively and γ is the adiabacity index. [27]. Upon Fourier analysing the above linearised equations, with $\mathbf{k} = k_\perp \mathbf{e}_y + k_\parallel \mathbf{e}_z$, where $k_\perp$ and $k_\parallel$ are the components of the wavevector in the directions perpendicular ($\mathbf{e}_y$) and parallel ($\mathbf{e}_z$) to the equilibrium magnetic field, the relevant perturbed fluid and electromagnetic variables can be written in terms of the perturbed fluid velocity $\mathbf{v}_1$ as follows [8]

$$\omega \rho_1 = -\rho_0 (\mathbf{k} \cdot \mathbf{v}_1) \tag{3.1.11}$$

$$\omega p_1 = -\gamma p_0 (\mathbf{k} \cdot \mathbf{v}_1) \tag{3.1.12}$$

$$\omega \mathbf{B}_1 = \mathbf{k} \times (\mathbf{v}_1 \times \mathbf{B}_0) \tag{3.1.13}$$

$$\omega \mathbf{J}_1 = i\mathbf{k} \times [\mathbf{k} \times (\mathbf{v}_1 \times \mathbf{B}_0)] \tag{3.1.14}$$

Ideal MHD wave dispersion relation Substituting these quantities into the linearised momentum equation 3.1.5 and setting the determinant of the resulting system of linear equations to zero, the following dispersion relation is recovered [8] [27]

$$(\omega^2 - k_\parallel^2 \upsilon_A^2)[\omega^4 - (\upsilon_A^2 + c_s^2)k^2\omega^2 + (\upsilon_A c_s k k_\parallel)^2] = 0 \tag{3.1.15}$$

where $\upsilon_A = B_0/\sqrt{\mu_0 \rho_0}$ is the Alfvén speed, $c_s = \sqrt{\gamma p_0/\rho_0}$ is the sound speed and $k^2 = k_\parallel^2 + k_\perp^2$ [8]. For the remainder of this section we will look in detail at the properties of the solutions to equation 3.1.15 and elucidate their fundamental position within the study of Alfvén eigenmodes in a tokamak plasma.

From the form of equation 3.1.15, three different modes of oscillation of the plasma or waves are expected [27]. The first mode, resulting from the term in parentheses, is known as the shear Alfvén wave and has a dispersion relation given by

$$\omega^2 = k_\parallel^2 v_A^2 \tag{3.1.16}$$

The two remaining modes are known as the fast ω_F and slow ω_S magnetoacoustic waves and result from the positive and negative roots of the quadratic expression in ω^2 in equation 3.1.15 respectively [27]

$$\omega_{F,S}^2 = \frac{k^2}{2}(c_s^2 + v_A^2)\left[1 \pm \sqrt{1 - 4\frac{k_\parallel^2}{k^2}\frac{v_A^2 c_s^2}{(v_A^2 + c_s^2)^2}}\right] \tag{3.1.17}$$

Coordinate system Before discussing the properties of these waves, it is instructive to introduce the following perturbed field variables to describe them

$$\nabla \cdot v_1,\ v_{1z},\ B_{1z},\ J_{1z},\ \rho_1,\ \xi_{1z} \tag{3.1.18}$$

where $\xi_{1z} = (\nabla \times v_1)_z$ is the fluid vorticity in the equilibrium magnetic field direction [28]. These appear in the set of six differential equations that can be formed by manipulating the linearised MHD equations 3.1.4-3.1.10. Two of these equations describe the properties of the shear Alfvén wave while the remaining four describe those of the magnetoacoustic waves [28].

The nature of the coupling of these equations means that some of these variables can be set equal to zero when treating each type of wave. It is also useful to define a number of unit vectors to describe the orientation of the wave-vectors and perturbed variables. As such, $\mathbf{b}$ and $\hat{\mathbf{k}}$ are defined as the unit vectors in the equilibrium magnetic field $\mathbf{B}_0$ and wave-vector $\mathbf{k}$ directions respectively. Finally, we define two further vectors, $\mathbf{a}$ and $\mathbf{t}$, to describe the orientation of the wave polarisations [28]. These are given by the following expressions

$$\mathbf{a} = -\frac{\mathbf{k} \times \mathbf{B}_0}{|\mathbf{k} \times \mathbf{B}_0|} \tag{3.1.19}$$

$$\mathbf{t} = \mathbf{a} \times \hat{\mathbf{k}} \tag{3.1.20}$$

Assuming that the wavevector lies in the x-z plane, the unit vectors assume the following forms [28]

$$\mathbf{b} = (0, 0, 1),\ \hat{\mathbf{k}} = (\sin\theta, 0, \cos\theta) \tag{3.1.21}$$

$$\mathbf{a} = (0, 1, 0),\ \mathbf{t} = (\cos\theta, 0, -\sin\theta) \tag{3.1.22}$$

where θ is the angle between the wavevector $\mathbf{k}$ and the equilibrium magnetic field direction $\mathbf{b}$. Figure 3.1 shows the orientation of the unit vectors defined in equations 3.1.19 - 3.1.22. We begin by considering the properties of these waves in a homogeneous plasma.

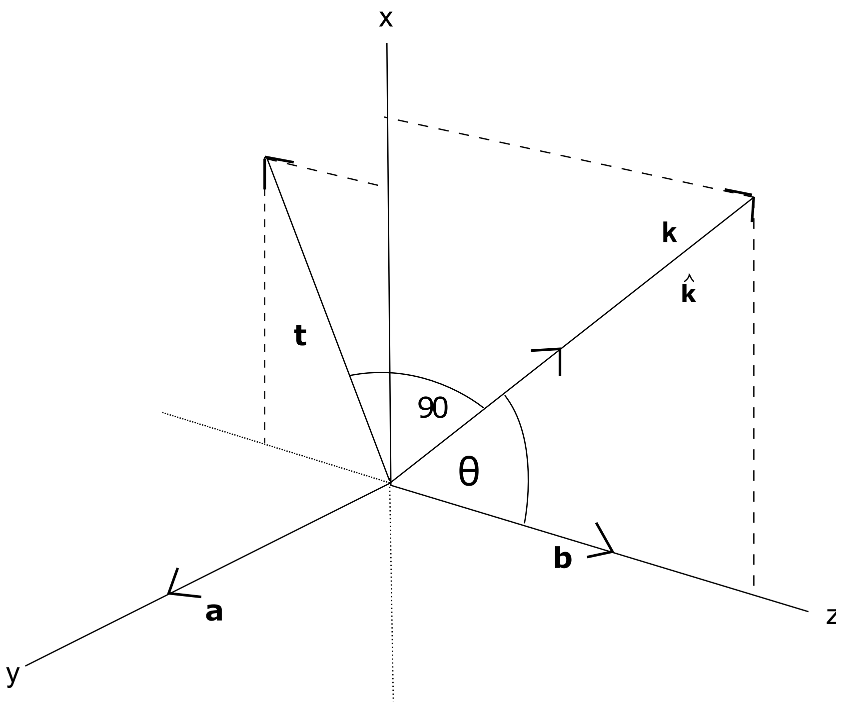

Figure 3.1. Coordinate system and unit vectors for ideal MHD waves in a homogeneous plasma [28].

3.1.2 Shear Alfvén waves

The shear Alfvén wave, with dispersion relation $\omega^2 = k_\parallel^2 v_A^2$, is a transverse electromagnetic wave, meaning that the magnetic field and fluid velocity perturbations,

$\mathbf{B}_1$ and $\mathbf{v}_1$ respectively, are perpendicular to the equilibrium magnetic field direction $\mathbf{b}$. This transverse polarisation will be referred to as Alfvénic polarisation for the remainder of this work. In cylindrical geometry, the shear Alfvén wave is referred to as a torsional wave, with adjacent magnetic surfaces able to shear past one another without coupling [28]. Shear Alfvén waves are incompressible, meaning that they result in no density or pressure perturbations ($\rho_1 = p_1 = 0$). Mathematically, the properties of the shear Alfvén wave can be understood by considering the characteristic variables defined in equation 3.1.18. For a purely Alfvénic wave, only the perturbed field variables ξ_{1z} and J_{1z} are involved and all others can be set equal to zero [28]. Thus, assuming that the wave only propagates in the x-z plane ($k_y = 0$), and with $\mathbf{v}_{1z} = \nabla \cdot \mathbf{v}_1 = ik_x\mathbf{v}_{1x} = 0$, it is found that only $v_{1y} \neq 0$ and the velocity perturbation is purely in the y-direction. Likewise, as $\mathbf{B}_{1z} = \nabla \cdot \mathbf{B}_1 = ik_x\mathbf{B}_{1x} = 0$, only $B_{1y} \neq 0$ and the magnetic field perturbation is also purely in the y-direction, perpendicular to the equilibrium magnetic field and wave-vector directions. Furthermore, as $\nabla \cdot \mathbf{v}_1 = 0$, there are no pressure or density perturbations associated with a purely Alfvénic mode [28]. The field lines are deformed but not compressed by the flow of ions, which is described by the vorticity $\xi_{1z} = (\nabla \times v_1)_z$, resulting in a field aligned current J_{1z} which acts to reduce the field line bending through its induced magnetic field perturbation [28].

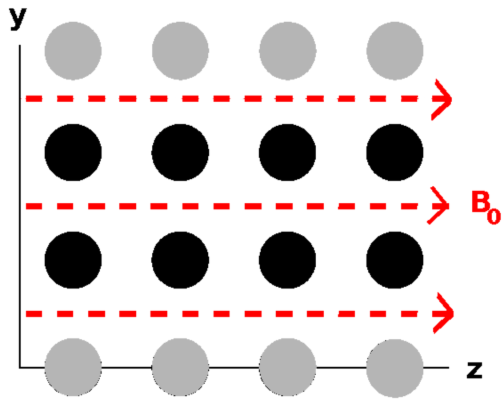

(a)

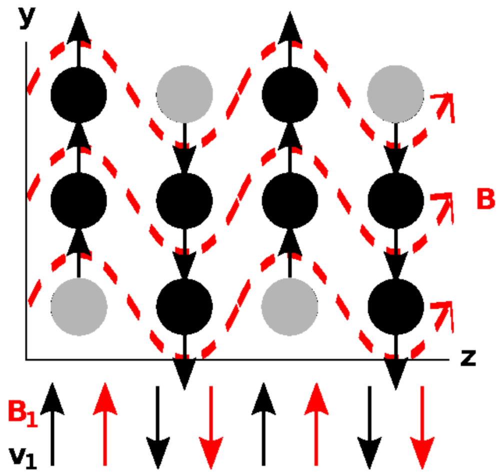

(b)

Figure 3.2. (a) Equilibrium magnetic field configuration with uniform fluid element distribution. (b) Magnetic field and plasma fluid element configuration resulting from the propagation of a shear Alfvén wave in a uniform plasma.

Physically, the shear Alfvén wave describes an oscillatory exchange of energy involving the perpendicular plasma kinetic energy and the potential energy of deformation of the magnetic field lines. From equation 3.1.16 it is clear that the shear Alfvén wave is independent of $k_\perp$, and that it will propagate in the equilibrium magnetic field direction at the Alfvén speed υ_A. The phase velocity of the wave, $\upsilon_A = \omega/k$, is independent of k, meaning that the wave is dispersionless. Figure 3.2 gives a simple illustration of the way in which the plasma and the magnetic field behave in the presence of a shear Alfvén wave. The magnetic field lines will initially not be deformed, and the fluid elements will be stationary in the equilibrium situation, as seen in figure 3.2 (a). However, as presented in figure 3.2 (b), in the presence of a shear Alfvén wave, the magnetic field lines will be perturbed in the the direction perpendicular to that of the equilibrium magnetic field $\mathbf{B}_0$. The fluid will also be displaced in accordance with the ideal MHD principle of flux conservation. The black arrows extending from the fluid elements indicate the direction in which this displacement has taken place. Thus, it is clear that while the individual fluid elements will move relative to one another, the local particle density will remain constant and no density or pressure perturbations will arise.

3.1.3 Fast and slow magnetoacoustic waves

$$\omega_{F,S}^2 = \frac{k^2}{2}(c_s^2 + \upsilon_A^2)\left[1 \pm \sqrt{1 - 4\frac{k_\parallel^2}{k^2}\frac{\upsilon_A^2 c_s^2}{(\upsilon_A^2 + c_s^2)^2}}\right] \tag{3.1.23}$$

Unlike the shear Alfvén wave, the positive and negative roots of equation 3.1.23, known as the fast and slow magnetoacoustic waves respectively, result from the coupling between magnetic compression and fluid compression [27]. The frequencies of the waves are ordered such that $\omega_F > \omega_A > \omega_S$, where $\omega_{F,S}$ are the frequencies of the fast and slow magnetoacoustic waves respectively and ω_A that of the shear Alfvén wave. Both the fast and slow waves possess similar magnetic field polarisations and both are stable in a uniform plasma. This is clear from observing that the term under the square root in equation 3.1.23 never assumes a negative value, ensuring a real solution in all cases. The characteristic variables associated with these waves are $\nabla \cdot \upsilon_1$, υ_{1z}, B_{1z} and ρ_1 [28]. Thus, as suggested by their relation to the compression of the magnetic field and fluid, the latter resulting from the fact that $\nabla \cdot v_1 \neq 0$, both waves will lead to density perturbations ρ_1 and magnetic field perturbations $\mathbf{B}_{1z}$ collinear to the equilibrium magnetic field.

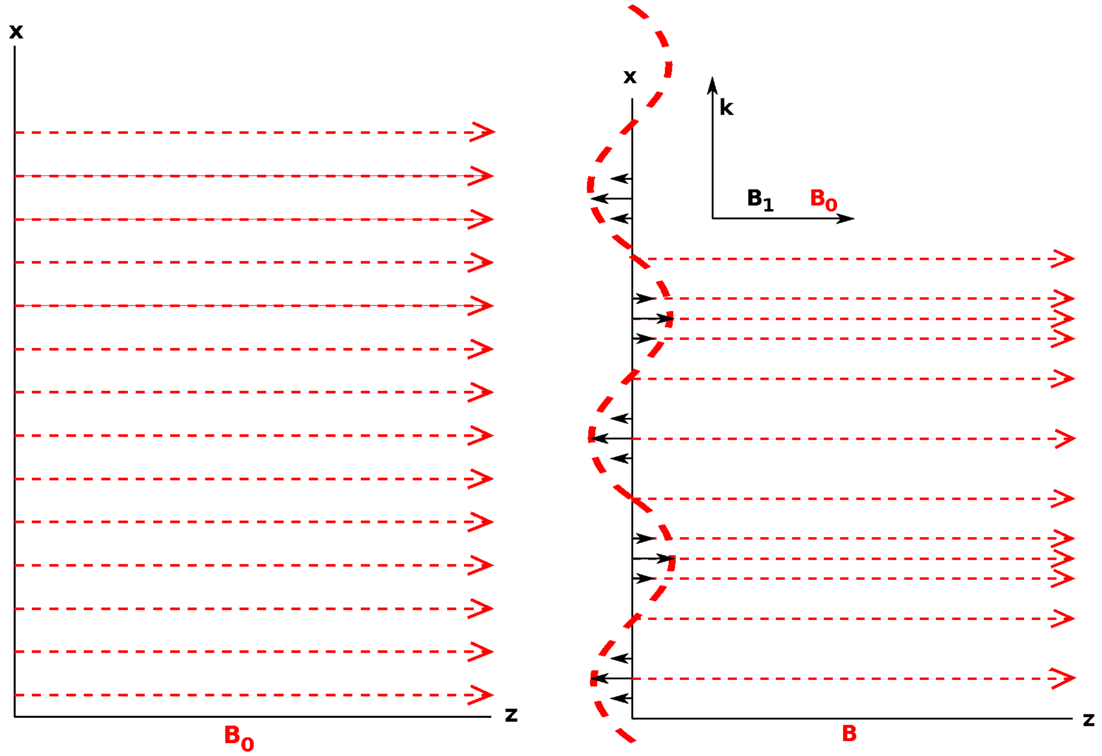

(a) (b)

Figure 3.3. (a) Equilibrium magnetic field line configuration (b) Magnetic field line configuration resulting from presence of a compressional Alfvén wave propagating perpendicular to $\mathbf{B}_0$ in a uniform plasma. The magnetic field perturbation vector is parallel to $\mathbf{B}_0$

The two magnetoacoustic waves can be better understood by considering each separately in the low β regime where $v_A^2 \gg c_s^2$ [8, 27, 28]. In this regime, the fast magnetoacoustic wave reduces to the compressional or fast Alfvén wave, which has a dispersion relation $\omega^2 = k^2 v_A^2$ and which describes the interplay between the energy needed to compress and bend the magnetic field and the perpendicular plasma kinetic energy [27]. As the parallel velocity is of order β compared with the perpendicular energy, the wave is nearly transverse, with $v_{1y} \gg v_{1z}$ [8, 27]. If we assume that the compressional Alfvén wave is propagating perpendicular to the equilibrium magnetic field direction, we find from equation 3.1.19 that the perturbed magnetic field $\mathbf{B}_1 \propto \mathbf{t}$ is parallel to $\mathbf{B}_0$. This will alternately strengthen or weaken the magnetic field spatially, depending on the form of the magnetic field perturbation $\mathbf{B}_{1z}$. This effect of the presence of the compressional Alfvén wave on the equilibrium magnetic field is demonstrated in figure 3.3. In this simple representation, when the magnetic perturbation $\mathbf{B}_1$ is parallel to $\mathbf{B}_0$, hence strengthening it, then the magnetic field lines are closer together. Conversely, when the magnetic perturbation is anti-parallel to $\mathbf{B}_0$, the magnetic field will be weakened and the field lines will be farther apart.

In the case where the direction of propagation is parallel or anti-parallel to the equilibrium magnetic field, the fast wave loses its compressional character and becomes degenerate with the Alfvén wave in the sense that it has a phase velocity v_A and a perturbed magnetic field which is perpendicular to $\mathbf{B}_0$ [28].

In the low β regime, again assuming parallel or anti-parallel propagation, the slow magnetoacoustic wave reduces to a pure sound wave. This possesses a dispersion relation $\omega^2 = k_{\parallel}^2 c_s^2$ and describes a basic oscillation between parallel plasma kinetic energy and plasma internal energy [8]. This wave does not propagate in the perpendicular direction and is nearly longitudinal, with $v_{1z} \gg v_{1y}$ [8, 27].

In an incompressible plasma, where $c_s \to \infty$, the magnetic pressure is no longer dominant and is balanced by the particle pressure [28]. In this case, only the magnetic tension contributes and the dispersion relation reduces to that of the shear Alfvén wave [28]. However, a difference does remain in that the sound wave will have a magnetic field which is polarised in the $\mathbf{t}$ direction, and hence will possess a component in the equilibrium field direction, unlike the pure Alfvén wave [28]. This consideration as to whether a plasma is incompressible or not will become vital when looking at the existence conditions for certain low-frequency Alfvén eigenmodes in the sections that follow.

3.2 Shear Alfvén waves in an inhomogeneous plasma

3.2.1 Stability properties of shear Alfvén spectrum

Before considering the general properties of Alfvén waves in an inhomogeneous plasma it is instructive to briefly consider the stability properties resulting from the ideal MHD description. Following the description given in [8], this can be defined as a normal mode problem and all perturbed quantities written in terms of the vector defined as

$$\mathbf{v}_1 = \frac{\partial \xi}{\partial t} \tag{3.2.1}$$

where ξ represents the plasma displacement away from equilibrium [8]. This gives the following expressions for the perturbed variables

$$\rho_1 = -\nabla \cdot \rho_0 \xi \tag{3.2.2}$$

$$p_1 = -\xi \cdot \nabla p_0 - \gamma p_0 \nabla \cdot \xi \tag{3.2.3}$$

$$\mathbf{B}_1 = \nabla \times (\xi \times \mathbf{B}_0) \tag{3.2.4}$$

Upon substituting these quantities into the linearised momentum balance equation, the following expression is obtained:

$$-\omega^2 \rho_0 \xi = \mathbf{F}(\xi) \tag{3.2.5}$$

where the force operator $\mathbf{F}(\xi)$ is given by

$$\mathbf{F}(\xi) = (\nabla \times \mathbf{B}_1) \times \mathbf{B}_0 + (\nabla \times \mathbf{B}_0) \times \mathbf{B}_1 - \nabla p_1 \tag{3.2.6}$$

Three important results arise from an examination of the properties of the force operator [8]. Firstly, it is found that $\mathbf{F}$ is self-adjoint. Secondly, this self-adjointness means that the eigenvalues of the system ω^2 are purely real. Thus the stability transition occurs when $\omega^2 = 0$, modes with $\omega^2 > 0$ corresponding to oscillating modes and those with $\omega^2 < 0$ corresponding to unstable modes which grow exponentially. Finally, it is found that the frequency spectrum consists not only of discrete modes but also of continua [8]. The existence of these continua drastically affects the frequency evolution and stability of Alfvénic modes in a plasma.

3.2.2 Shear Alfvén continuous spectrum and phase mixing

Up until this point, only ideal MHD waves in a homogeneous plasma have been considered. These are decoupled from one another and are always stable, with $Im(\omega) = 0$. This description changes markedly in the case of an inhomogeneous plasma. Presently, the focus will be on the shear Alfvén wave alone, with considerations of the influence of the magnetoacoustic waves being left to a later section. The reason for this relates to the incompressible nature of the shear Alfvén wave and its significance when considering plasma instabilities.

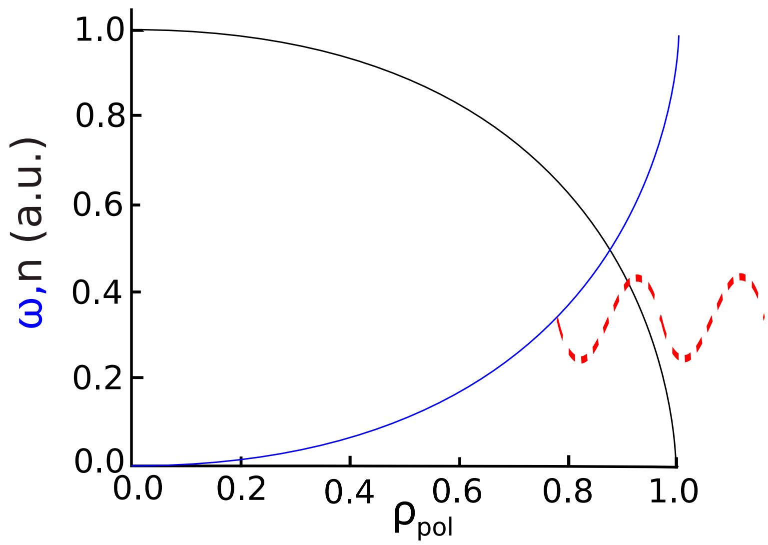

Figure 3.4. Simple illustration of the effect of plasma inhomogeneity on shear Alfvén continuous spectrum and resultant phase mixing. A decrease in the density n will result in an increase in the mode frequency ω due to the fact that $\omega \propto v_A \propto 1/\sqrt{n}$.

In order to compress the plasma and the magnetic field, a certain amount of energy is required. In the case of modes that cause density and pressure perturbations and hence compress the plasma, less energy is consequently available for the excitation of instabilities. However, for shear Alfvén waves energy is not expended in compressing the plasma and the magnetic field due to the wave being incompressible. Thus, the energy remains available to potentially excite instabilities. As such, the most unstable perturbations are almost always coupled with the shear Alfvén wave [27]. This makes a clear understanding of the properties of shear Alfvén waves essential to the interpretation of the low-frequency Alfvén eigenmodes that are the primary focus of this work.

We begin by considering a plasma with non-uniform density profile. It is necessary to alter the shear Alfvén wave dispersion relation to take into account this radial dependence. Thus, the positive dispersion relation is now given by $\omega(r) = k_{\parallel} v_A(r)$, with $v_A(r) = B_0/\sqrt{\mu_0 \rho(r)}$. Figure 3.4 illustrates how the frequency of the shear Alfvén wave will vary radially, depending on the density profile.

The frequencies of the wave at different radii form what is known as the shear Alfvén continuum or continuous Alfvén spectrum. We consider a wave-packet of finite radial extent propagating across the plasma in the presence of this continuum. Due to the fact that sections of the wave-packet at different radial positions will move at different velocities and in different directions, the instability will disperse rapidly in a process known as phase mixing [27, 29–31]. The damping rate γ of the instability is proportional to the gradient of the phase velocity, giving $\gamma \propto -\frac{d}{dr}(k_{\parallel} v_A)$ [27, 31]. Thus, the existence of the shear Alfvén frequency continuum has important consequences for the stability of modes in a plasma.

3.2.3 Shear Alfvén continuum in cylindrical geometry

It is instructive to consider how the perturbation described in the previous section would behave in the more realistic geometry of a cylindrical plasma. We assume an externally applied wave of frequency ω and with axial and azimuthal wavenumbers k_z and m respectively [27]. The radial component of the perturbed plasma displacement is given by

$$\xi_r(r, \theta, z, t) = \sum_m \xi_m(r) e^{i(m\theta + k_z z + \omega t)} \tag{3.2.7}$$

and the equation describing the radial penetration of an externally applied electromagnetic wave into the plasma is given by [27, 32, 33]

$$\frac{d}{dr}r^3(\frac{\omega^2}{v_A^2} - k_\parallel^2)\frac{d\xi_r}{dr} - (m^2 - 1)r(\frac{\omega^2}{v_A^2} - k_\parallel^2)\xi_r = 0 \tag{3.2.8}$$

From this equation the plasma radial displacement is found to possess a singularity at the point r where $\omega = k_\parallel v_A$. In order to resolve this singularity an imaginary component has to be introduced to the solution. This imaginary part represents the resonant absorption of the externally applied wave where its frequency intersects the shear Alfvén continuum. The resultant damping of the wave is known as continuum damping [27, 33]. It should also be noted that equation 3.2.8 is the cylindrical version of the simple shear Alfvén wave dispersion relation $\omega = k_\parallel v_A$ [34].

We can extend this description by introducing an axial current in the cylinder. Whereas previously only an axial component of the equilibrium magnetic field existed, the introduction of the axial current results in an azimuthal component to the magnetic field [31]. This imposes periodicity constraints on the parallel wavevector $k_\parallel$, resulting in the expression

$$k_\parallel = \frac{1}{R}(n - m/q) \tag{3.2.9}$$

where m and n are the poloidal and toroidal mode numbers respectively, q is the safety factor and R is the plasma major radius. The safety factor is usually a function of the plasma radius, meaning that $k_\parallel$ will now possess a radial dependence. This addition of an axial current also alters the form of equation 3.2.8, giving [27, 32, 33]

$$\frac{d}{dr}r^3(\frac{\omega^2}{v_A^2} - k_\parallel^2)\frac{d\xi_r}{dr} - (m^2 - 1)r(\frac{\omega^2}{v_A^2} - k_\parallel^2)\xi_r + (\frac{\omega^2}{v_A^2})'r^2\xi_r = 0 \tag{3.2.10}$$

where the prime denotes differentiation with respect to the radius. This additional term resulting from the current removes the singularity of the eigenfunction. This means that if an externally applied wave is introduced with a frequency just below the continuum such that $\omega \approx \omega_A$, it will at no point be resonant with the Alfvén continuum and thus will be only weakly damped [27]. This occurrence of an extremum in the shear Alfvén continuum results in what is known as a continuum gap, as demonstrated in figure 3.5. This is a generic wave phenomenon observed in numerous physical systems [31]. One such example is an optical fibre with a periodically modulated index of refraction. This spatial modulation results in a band gap at the Bragg frequency with the width of the gap proportional to the amplitude of the modulation [31]. In the case of the gap in the shear Alfvén continuum, the local Alfvén frequency grows as one moves away from the frequency minimum, and the effective refractive index $N_\perp = ck_\perp/\omega$ decreases. Thus, the externally applied wave is reflected by the decreasing $N_\perp$ and is localised in the region close to the continuum minimum [27].

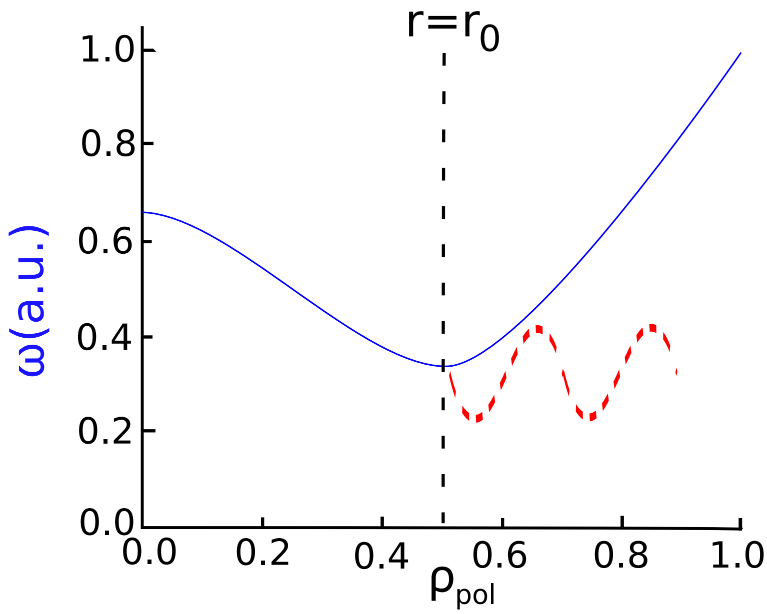

Figure 3.5. Demonstration of the occurence of a gap in the shear Alfvén continuum in the presence of finite axial current in cylindrical geometry.

3.2.4 Shear Alfvén continuum in toroidal geometry

If a magnetic perturbation in the plasma, such as a shear Alfvén wave with poloidal and toroidal mode numbers m and n respectively, is propagating in the magnetic field direction, an individual frequency continuum will be formed for each (m, n) pair. The structure of the continuum will be complicated by the introduction of finite plasma toroidicity. In this case, because of the fact that $B \approx B_0(1 - r/R_0 \cos\theta)$, the magnetic field will now vary with the poloidal angle θ and hence will vary on a magnetic surface [27].

In the toroidal case the parallel component of the wavevector is given by $k_{\|m} = (n - m/q(r))/R$ and the safety factor by $q(r) = \epsilon B_t/B_\theta$, where $\epsilon = r/R_0$ is the inverse aspect ratio, r is the plasma minor radius and B_t and B_θ are the toroidal and poloidal magnetic field components respectively. The fact that $k_{\|m}$ varies over a flux surface means that modes with different m numbers can couple [7] and leads to the opening of a gap in the continuous spectrum. This coupling occurs where the condition $|k_{\|m}| = -|k_{\|m+1}|$ is fulfilled and to the lowest order represents the interaction between two counter propagating waves with adjacent poloidal mode numbers m and $m+1$. The strong interaction between these two waves which occurs due to the toroidal coupling process not only leads to the opening of the continuum gap, but also results in discrete, global, toroidicity-induced shear Alfvén eigenmodes with frequencies inside the continuum gaps [7, 35].
Expanding the toroidicity effect to first order, retaining only two dominant poloidal modes for the toroidicity-induced Alfvén eigenmode (TAE) and neglecting kinetic effects, two coupled second order eigenmode equations for a wave field perturbation of the form $\xi(r,\theta,\phi) = \sum \xi_{m,n}(r)e^{i(n\phi - m\theta - \omega t)}$ can be derived [36]. These are given by

$$\frac{d}{dr}r^3\left(\frac{\omega^2}{\upsilon_A^2} - k_{\|m}^2\right)\frac{d\xi_m}{dr} - (m^2-1)r\left(\frac{\omega^2}{\upsilon_A^2} - k_{\|m}^2\right)\xi_m + \left(\frac{\omega^2}{\upsilon_A^2}\right)' r^2\xi_m + \left(\epsilon\frac{d}{dr}\frac{\omega^2}{\upsilon_A^2}\frac{r^4}{a}\frac{d}{dr}\right)\xi_{m+1} = 0 \quad (3.2.11)$$

$$\frac{d}{dr}r^3\left(\frac{\omega^2}{\upsilon_A^2} - k_{\|m+1}^2\right)\frac{d\xi_{m+1}}{dr} - [(m+1)^2-1]r\left(\frac{\omega^2}{\upsilon_A^2} - k_{\|m+1}^2\right)\xi_{m+1} + \left(\frac{\omega^2}{\upsilon_A^2}\right)' r^2\xi_{m+1} + \left(\epsilon\frac{d}{dr}\frac{\omega^2}{\upsilon_A^2}\frac{r^4}{a}\frac{d}{dr}\right)\xi_m = 0 \quad (3.2.12)$$

where the prime denotes differentiation with respect to the radius and $\epsilon = r/R_0$. The eigenmode equation 3.2.8 for the cylindrical case can be recovered by setting $\epsilon = 0$, i.e. by assuming zero plasma toroidicity. The toroidal shear Alfvén frequency continuum can be obtained by setting the determinant of the coefficients of the two second order derivative terms equal to zero, with the two resulting branches given by the following expression [36]

$$\omega_{\pm}^2 = \frac{k_{\|m}^2 v_A^2 + k_{\|m+1}^2 v_A^2 \pm \sqrt{(k_{\|m}^2 v_A^2 - k_{\|m+1}^2 v_A^2)^2 + 4\epsilon^2 x^2 k_{\|m}^2 v_A^2 k_{\|m+1}^2 v_A^2}}{2(1-\epsilon^2 x^2)} \tag{3.2.13}$$

where $x = r/a$.

3.3 Low-frequency beta-induced gap in continuous spectrum

3.3.1 Eigenmode equation for coupled shear Alfvén and sound waves

In the situations considered so far it has been assumed that Alfvénic waves are decoupled from sound waves in the plasma. In section 3.3, the effects of coupling between these two waves are presented, following primarily the treatments given in [7,38,41]. As considered in section 3.1.3, the dispersion relation for a pure sound wave is given by $\omega = k_{\|} c_s$ and that for a shear Alfvén wave by $\omega = k_{\|} v_A$. In a low-β plasma, where $c_s \ll v_A$, a sound wave with high $k_{\|}$ can potentially couple to an Alfvénic wave with low $k_{\|}$ in the presence of finite geodesic curvature [7]. It has been demonstrated that this results in the opening of a new gap beneath the frequency continuum [7]. It is this gap that will be the primary focus of the investigations in this work. Thus, an exposition of its basic features is outlined in the sections which follow.

The ideal MHD eigenmode equations describing this coupling between the shear Alfvén waves and the sound waves on a flux surface are derived from the ideal MHD equations 3.1.5, 3.1.6 and 3.1.9 and are given by equations 3.3.1 and 3.3.2 [7,35]

$$\omega^2 \rho \frac{|\nabla\psi|^2}{B^2}\xi_s + (\mathbf{B}\cdot\nabla)\frac{|\nabla\psi|^2}{B^2}(\mathbf{B}\cdot\nabla)\xi_s + \gamma p k_s \nabla\cdot\vec{\xi} = 0 \tag{3.3.1}$$

$$(\frac{\gamma p}{B^2}+1)\nabla\cdot\vec{\xi} + \frac{\gamma p}{\omega^2\rho}(\mathbf{B}\cdot\nabla)\frac{\mathbf{B}\cdot\nabla}{B^2}\nabla\cdot\vec{\xi} + k_s\xi_s = 0 \tag{3.3.2}$$

where ψ is the poloidal magnetic flux, p and ρ are the plasma equilibrium pressure and density, γ is the specific heat ratio, $\xi_s \equiv \vec{\xi} \cdot [\mathbf{B} \times \nabla\psi]/|\nabla\psi|^2$ is the plasma surface displacement, $\xi_\psi = \vec{\xi} \cdot \nabla\psi$ is the radial displacement, $k_s(\theta) \equiv 2\vec{\kappa} \cdot [\mathbf{B} \times \nabla\psi]/|\nabla\psi|^2$ is the geodesic curvature and $\vec{\kappa} = (\mathbf{B}/B) \cdot \nabla(\mathbf{B}/B)$ and $\mathbf{B}$ are vectors of the magnetic curvature and magnetic field [7, 37]. Due to the fact that the zeroth order gap mentioned previously, known as the $\beta-$induced gap, results from the existence of sound waves in the plasma, it is dependent on the existence of finite compressibility. This is demonstrated by setting $\nabla \cdot \vec{\xi} = 0$ in equations 3.3.1 and 3.3.2, which amounts to eliminating the coupling between the Alfvén and sound waves. This simplifies the system to a single equation, closes the zeroth order gap and results in an overall down-shift of the frequency continuum [7]. Thus, as mentioned in section 3.1.3, finite compressibility becomes essential for the existence of Alfvén eigenmodes at frequencies much lower than that of the TAE.

3.3.2 Beta-induced Alfvén eigenmodes (BAEs) and beta-induced acoustic Alfvén eigenmodes (BAAEs) in ideal MHD

It is found that discrete Alfvén-type global modes exists within the β-induced gap [38]. As these modes exist within a gap that results from the coupling between the Alfvénic and sound waves, their polarisations are neither purely Alfvénic nor acoustic, but a mixture of both [38]. Purely Alfvénic waves will result in a perpendicular displacement of the plasma $\xi_\perp$, while acoustic waves are longitudinal and displace the plasma in the parallel direction $\xi_\parallel$. Thus, the nomenclature used to identify them, which will be employed in this work, is primarily based on their dominant polarisation i.e. whether $|\xi_\perp| > |\xi_\parallel|$ or vice versa [38].
Concerning the conceptual understanding of these modes, it is important to realise that acoustic wave propagation is not treated properly by ideal MHD, as they are found to be highly damped. Thus, the interaction between sound waves and Alfvén wave is found to come from the compressional response of the plasma to a propagating Alfvén wave, and not from the propagation of compressional

acoustic waves themselves [38]. Thus, an assumption known as the slow sound approximation (SSA) is made with $\gamma p/\omega^2\rho \ll 1$, which retains the compressional response of the Alfvénic waves but omits the sound wave propagation [7]. The upward shift in the frequency continuum which results in the β-induced gap is found to result from the associated compressional energy of the Alfvén wave [38].

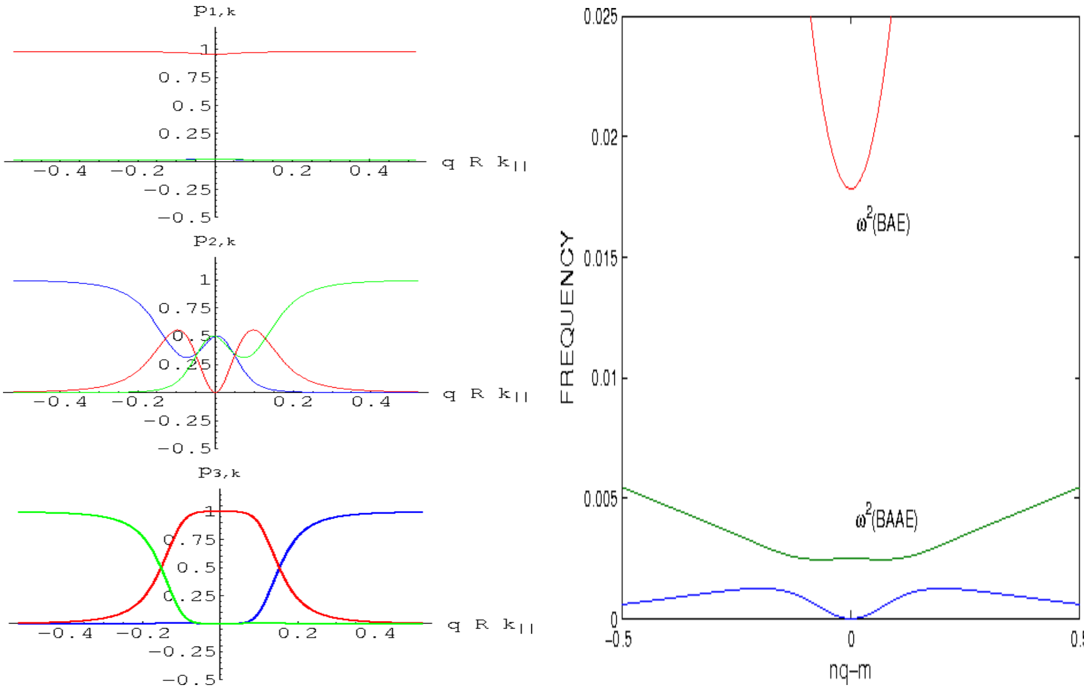

(a) (b)

Figure 3.6. (a) Polarisation (Alfvénic in red, acoustic in blue/green) and (b) low frequency coupling of modes showing the continuous spectrum of the three branches $\omega^2 = \omega^2(k_{\|j}qR_0)$ normalized to ω_{A0}^2, where j refers to the index number of the shear Alfvén and acoustic wave contributions. The higher frequency branch is purely Alfvénic and corresponds to the shear Alfvén continuum with accumulation point ω_{BAE}. The lower frequency branch has acoustic polarisation far from the coupling zone and Alfvénic polarisation in the coupling zone. The medium frequency branch has mostly acoustic polarisation far from the coupling zone while it has both Alfvénic and acoustic polarisations in the coupling zone [39–41].

Two distinct discrete modes of interest are found to exist within the β-induced gap. The first is known as the beta-induced Alfvén eigenmode (BAE) and possesses a polarisation dominated by the $\xi_\perp$ component, and thus is primarily Alfvénic, similar to the TAE. Within the ideal MHD framework, the second type of mode is known as the beta-induced acoustic Alfvén eigenmode (BAAE). It possesses a much larger acoustic component than the BAE, while still retaining a significant Alfvénic component to its polarisation [37,40]. The frequency spectrum branches for the above two types of modes can be recovered by again considering equations 3.3.1 and 3.3.2. Assuming nearly circular flux surfaces, a small Shafranov shift and approximating the geodesic curvature by $\kappa \approx 2(\epsilon/q)\sin\theta$, equations 3.3.1 and 3.3.2 can be written as [40,41]

$$\frac{\omega^2}{v_A^2}\xi_s + (b\cdot\nabla)^2\xi_s + \gamma\beta\epsilon\frac{q}{a^2}\sin\theta\nabla\cdot\vec{\xi_s} = 0 \tag{3.3.3}$$

$$\frac{\omega^2}{v_A^2}\nabla\cdot\vec{\xi_s} + \frac{\gamma\beta}{2}(b\cdot\nabla)^2\nabla\cdot\vec{\xi_s} + 2\frac{\epsilon}{q}\frac{\omega^2}{v_A^2}\sin\theta\xi_s = 0 \tag{3.3.4}$$

Employing Fourier decomposition in θ, and considering the j-th shear Alfvén contribution and $(j\pm1)$-th acoustic wave contributions, this procedure yields the vectorial equation $M\cdot\vec{\xi} = 0$ with M and $\vec{\xi}$ defined after equation 2.49 in [41]. This is an eigenvalue problem, with ω^2 as the eigenvalues and the corresponding $\vec{\xi}$ as eigenvectors [41]. The polarisations of the different modes are shown in figure 3.6 (a), with red representing the Alfvénic contribution and blue/green the acoustic poloidal side-band contributions. This is done purely to illustrate the form of solution obtained from equations 3.3.3 and 3.3.4, and is not intended to be compared with experiment. The reasons for this are discussed in the section that follows. It is clear from figure 3.6 (a) that the higher frequency mode (BAE) has almost purely Alfvénic polarisation while the medium frequency branch (BAAE) has mostly acoustic polarisation away from the coupling zone and mixed Alfvénic and acoustic polarisation in the coupling zone. Three continuous spectrum branches are recovered by setting the determinant of the matrix M equal to zero [39–41] and are shown in figure 3.6 (b). Thus, it is seen that ideal MHD indicates the existence of discrete low-frequency modes in the $\beta-$induced gap resulting from the coupling between Alfvén and acoustic waves.

3.4 Low-frequency Alfvén eigenmodes: Move to kinetic description

3.4.1 Phenomena neglected in ideal MHD description of Alfvén eigenmodes

It has been shown in sections 3.1-3.3 how the ideal MHD model is very useful for illustrating the basic features of low-frequency Alfvén eigenmodes. The primary features of interest recovered with the model include initial estimates of (i) the frequency continua resulting from the interaction between ideal MHD waves in an inhomogeneous plasma, (ii) the gaps that can appear in these continua and (iii) the structure and stability of the discrete eigenmodes that can exist within these gaps. However, the ideal MHD model is incomplete as it neglects a number of important physical phenomena. These phenomena are essential for accurately estimating the stability and evolution of low frequency eigenmodes such as BAEs and in particular modes with a high degree of coupling between acoustic and shear Alfvén waves.

Diamagnetic effects An important consideration neglected in ideal MHD is the role that plasma diamagnetic effects play in determining the behaviour of low-frequency modes such as BAEs. In the hydromagnetic limit where $\omega \gg \omega_{ti}$, where $\omega_{ti} = \sqrt{2T_i/m_i}/qR_0$ is the thermal ion transit frequency, the $\mathbf{E} \times \mathbf{B}$ drift is assumed to be dominant compared to drifts related to spatial gradients. However, for low-frequency modes where $\omega \approx \omega_{*p}$, with the ion diamagnetic frequency given by $\omega_{*pi} = (T_i/e_iB)k_\theta \nabla p_i/p_i$, where $k_\theta = -m/r$, this assumption is no longer valid and effects resulting from background gradients become important and must be considered [11, 42]. The contribution from plasma diamagnetism is proposed to occur through the coupling of BAEs with kinetic ballooning modes (KBMs), which have a similar polarisation to BAEs [42, 44, 45]. Both modes occur in the same frequency regime, with $\omega \approx \omega_{ti} \approx \omega_{*p}$ [42]. The presence of finite background temperature and density gradients can act as a source of free energy for the modes and can play an important role in determining the stability and behaviour of low-frequency Alfvén eigenmodes with $\omega \approx \omega_{*p}$.

Parallel dynamics and kinetic resonances Another major weakness of the ideal MHD model stems from its inability to treat parallel dynamics in a plasma. While the Lorentz force confines particles in the perpendicular direction no such confining mechanism exists in the parallel direction [46, 47]. The main symptom of this weakness is the absence of kinetic resonances between modes and particles with various characteristic orbit frequencies. As these kinetic resonances, which control the parallel dynamics, are not included in the ideal MHD model, there is no parallel acceleration [46, 47] and hence charge separation is not considered in the parallel direction [11]. This is manifested in the ideal MHD assumption that the parallel electric field perturbation is zero $\delta E_{\parallel} = 0$ [46, 47], an assumption which may not be strictly true in the presence of kinetic resonances.

The omission of kinetic resonances stems from the ideal MHD treatment of the plasma compressibility. As has been discussed in section 3.3.2, the slow sound approximation (SSA) is used in ideal MHD in order to recover the compressional effect of low-frequency Alfvén modes on the plasma [7]. However, this approximation still corresponds to $\omega \gg \omega_{ti}$, as is the case in the hydromagnetic limit [11], while the frequency range of the modes is in fact ordered as the thermal ion transit frequency $\omega_{ti} = \sqrt{2T_i/m_i}/qR_0$, with $\omega \approx \omega_{ti}$ [42]. The ideal MHD treatment of the ion compressibility precludes kinetic resonances between the modes and ions along the magnetic field lines, as can occur through Landau damping when the mode frequency is in the range $\omega \approx \omega_{ti}$, as well as resonances related to the characteristic orbits of trapped ions. The kinetic approach addresses this by considering the effects of both the adiabatic and non-adiabatic core ion compressibility contributions to the perturbed particle distribution function [42, 48]. This has important consequences as it has been demonstrated that such interactions with the background ions are essential to fully describe the modes dynamics and must be included in any model that purports to do so [42, 49–51]. Kinetic resonances with fast particles are also not correctly treated by ideal MHD [46, 47], however this is not considered in this work.

FLR effects Finite Larmor radius effects are neglected in the ideal MHD model. This is significant as ion FLR terms are found to be essential in correctly describing the coupling between the pure Alfvén and kinetic Alfvén waves [52]. As the kinetic approach deals with particle motion, FLR effects can be treated accurately within its framework.

Considering these significant weaknesses in the ideal MHD model, all of which are addressed by kinetic theory, it is clear that a kinetic description of these modes is necessary to explain the experimentally observed behaviour. A number of approaches aimed at achieving this have been developed over the last number of years including the modern gyrokinetic approach [46, 47, 60] and the kinetic ballooning mode representation [42]. The equations underlying one of these approaches [48] will be utilised in the analysis sections of this work and are presented in the sections that follow.

3.4.2 Gyrokinetic background theory

In order to take advantage of the scale lengths inherent to low-frequency Alfvén eigenmodes, a gyrokinetic description of the plasma is employed which can describe modes of arbitrary wavelength down to the gyro radius scale. This approach has the advantage of being able to describe how kinetic effects influence the modes, as well as retaining all background equilibrium effects and thus retaining all features of ideal MHD. In this section, a brief overview of the gyrokinetic approach is presented, without considering the detailed mathematics involved in deriving the gyrokinetic equation, quasi-neutrality equation and current equation. This is beyond the scope of this work and details of it can be found in [46, 47]. For the remainder of section 3.4 we primarily follow the descriptions presented in [41, 43, 46, 47, 52–54].

Orderings and coordinate system The gyrokinetic approach begins with the Vlasov equation, which describes how the particle distribution function F_a evolves in time

$$[\frac{\partial}{\partial t} + \mathbf{v} \cdot \nabla + \frac{e}{m}(\mathbf{E} + \frac{\mathbf{v} \times \mathbf{B}}{c}) \cdot \frac{\partial}{\partial \mathbf{v}}]F_a = 0 \tag{3.4.1}$$

where the electric field $\mathbf{E} = -\nabla\Phi - \partial_t \mathbf{A}/c$ is written in terms of the electric scalar and magnetic vector potentials. The Vlasov equation can be simplified by considering the spatial and temporal scales inherent to the system. Firstly, the particle velocity is divided into one component parallel to the magnetic field direction and another describing fast gyro motion about the field line

$$\mathbf{v} = v_{\|}\mathbf{b} + \mathbf{v}_{\perp} \tag{3.4.2}$$

$$\mathbf{v}_{\perp} = v_{\perp}[\mathbf{e}_1 \cos\xi + \mathbf{e}_2 \sin\xi] \tag{3.4.3}$$

where ξ is the phase angle of the gyromotion and $(\mathbf{e}_1, \mathbf{e}_2, \mathbf{b})$ are the basis vectors of the local orthogonal coordinate system defined by $\mathbf{e}_1 \cdot \mathbf{b} = 0$ and $\mathbf{e}_2 = \mathbf{b} \times \mathbf{e}_1$ [41, 43, 53]. Instead of using phase space coordinates $(\mathbf{x}, \mathbf{v})$, the particle motion is then described in terms of its guiding centre coordinates $(\mathbf{X}, \mathbf{V})$, where $\mathbf{V} = \mathbf{V}(E, \mu, \xi, \sigma)$, $E = v^2/2 + e\Phi/m$ is the particle's total energy per unit mass, $\mu = v_{\perp}^2/(2B)$ is the magnetic moment per unit mass, $\sigma = sgn[v_{\|}]$ gives the direction of the parallel velocity and the guiding centre position is given by [41]

$$\mathbf{X} = \mathbf{x} + \frac{\mathbf{v}_{\perp} \times \mathbf{b}}{\Omega_c} \tag{3.4.4}$$

where Ω_c is the particle cyclotron frequency. At this point, a number of scalings and expansions are introduced to simplify the Vlasov equation. Firstly, the distribution function F_a is assumed to consist of an equilibrium component F_{0s} and a small perturbed component f_a, so that $F_a = F_{a0} + f_a$. The assumption that F_{a0} is Maxwellian is also made with

$$F_{a0} = \frac{n_{a0}}{(2\pi T_a)^{3/2}} e^{-m_s v^2/2T_a} \tag{3.4.5}$$

where $a = i, e$ and n_a is the particle species density [41]. These assumptions allow the kinetic equation to be linearised and effects dependent on the plasma equilibrium quantities to be treated separately from those resulting from small perturbations. Next, the assumption is made that

$$\omega/\Omega_i \sim \rho_{\perp i}/L_0 \ll 1 \tag{3.4.6}$$

where Ω_i is the ion cyclotron frequency, $\rho_{\perp i}$ is the ion gyro radius and L_0 is the characteristic equilibrium scale length of the system [53]. This means that the mode frequency is considered to be much lower than the ion cyclotron frequency, which is a reasonable assumption as modes with frequencies close to Ω_i will be subject to ion cyclotron damping [53]. Equation 3.4.6 also implies that the ion gyroradius is taken to be much smaller than the characteristic scale length of the plasma. Finally, only modes with a flute-like structure are considered, such that

$$k_\parallel/k_\perp \ll 1 \tag{3.4.7}$$

The reasoning behind this stems from the fact that the effects of variations along the magnetic field lines, such as field line bending and the excitation of sound waves, are assumed to be stabilising [53]. If the mode structure varies little in the $k_\parallel$ direction, it cannot avail of these stabilising influences and thus is expected to be more prone to destabilisation.

Gyro averaging The Vlasov equation can be made more tractable via the separation of the fast gyroscopic motion of the particle from the motion of its gyro centre. This is achieved through the use of the gyro-average operator which is a space-averaging operator that allows the omission of details of the gyromotion, while retaining the slower guiding center motion [11]. This is found to be equivalent to multiplication by a zeroth order Bessel function J_0 in Fourier space, the first three terms of which are given by

$$J_0(k_\perp\rho_\perp) = 1 - \frac{1}{4}(k_\perp^2\rho_\perp^2) + \frac{1}{32}(k_\perp^4\rho_\perp^4)... \tag{3.4.8}$$

Thus, for modes with $k_\perp\rho_\perp \ll 1$ it follows that $J_0 \to 1$, indicating that the gyroradius is so small that it does not sample the perturbations. For modes with $k_\perp\rho_\perp \gg 1$ it follows that $J_0 \to 0$, indicating that while the particle experiences various perturbations over its orbit, the average effect of these cancels overall [11]. As the assumption that $k_\perp\rho_\perp \sim 1$ is made in this analysis, meaning that the ion gyroradius is comparable to the mode perpendicular wavelength, the inclusion of finite Larmor radius (FLR) effects is necessitated [53]. An illustration of the influence of $J_0(k_\perp \rho_\perp)$ at different scale lengths is given in figure 3.7.

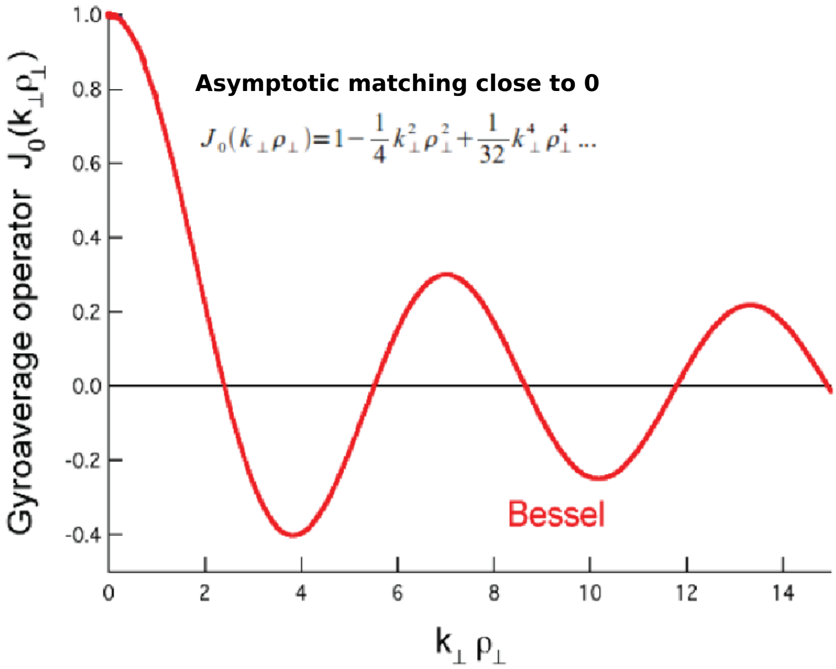

Figure 3.7. Variation of gyrophase operator with $k_\perp \rho_\perp$ [11]

We now introduce three perturbed scalar field variables $\delta B_\parallel, \delta\psi$ and $\delta\phi$ which represent the perturbed parallel magnetic field, perturbed scalar magnetic potential and perturbed scalar electric potential respectively. These will be used in the derivation of the kinetic equations. As was the case for the perturbed distribution function, the perturbed potentials and field quantities are small compared to the equilibrium quantities. The perturbed magnetic field and corresponding gauge can be written as

$$\delta \mathbf{B} = \nabla \times \delta \mathbf{A} \tag{3.4.9}$$

$$\nabla \cdot \delta \mathbf{A} = 0 \tag{3.4.10}$$

where $\delta\mathbf{A}$ can be decomposed into its parallel and perpendicular components $\delta\mathbf{A}_\parallel$ and $\delta\mathbf{A}_\perp$ respectively. In the context of this analysis it is found that only $\delta\mathbf{A}_\parallel$ plays a role, and it is thus assumed that $\delta\mathbf{A}_\perp = 0$ [46, 47]. This is equivalent to eliminating the effects of the compressional Alfvén wave, which is related to $\delta B_\parallel$. $\delta\psi$ can be written in terms of the parallel vector potential

$$\delta A_{\|} = -i(\frac{c}{\omega})\mathbf{b}\cdot\nabla\delta\psi \tag{3.4.11}$$

while the perturbed parallel electric field $\delta E_{\|}$ can be recovered from

$$\delta\mathbf{E} = -\nabla\delta\phi + (i\omega/c)\delta\mathbf{A} \tag{3.4.12}$$

$$\mathbf{b}\cdot\delta\mathbf{E} = \delta E_{\|} = -\mathbf{b}\cdot\nabla(\delta\phi - \delta\psi) \tag{3.4.13}$$

Thus, it is seen that the ideal MHD limit of $\delta E_{\|} = 0$ is recovered when $\delta\phi = \delta\psi$ [41].

3.4.3 Overview of kinetic theory of low-frequency AEs

System of gyrokinetic equations In order to investigate long wavelength electromagnetic perturbations in a tokamak plasma using a fully kinetic approach, a linear gyrokinetic system of equations has been derived [42, 46–48, 52]. In this section these equations and their properties are introduced, following the derivations given in [41, 42, 46, 47, 52]. We begin with the linear gyrokinetic equation (GKE), which is the form of the Vlasov equation obtained after applying the gyrokinetic approach [46, 47], and which can be written as

$$\frac{\partial f_a}{\partial t} + (U\mathbf{b} + \mathbf{v}_d)\cdot\nabla f_a = \frac{c\mathbf{b}}{eB}\cdot(\nabla F_{a0}\times\nabla H_1) + \frac{\partial F_{a0}}{\partial E}(U\mathbf{b} + \mathbf{v}_d)\cdot\nabla H_1 \tag{3.4.14}$$

where U is the parallel velocity and H_1 the perturbed Hamiltonian given by

$$H_1 = e(\phi - \frac{Uk_{\|}}{\omega}\psi) \tag{3.4.15}$$

It can be seen that the contributions from the electrostatic ϕ and electromagnetic ψ perturbations are introduced via H_1 [46, 47], where the δ before the perturbed field variables has been dropped for clarity. The expression for the drift velocity is defined as follows

$$\mathbf{v}_d = \frac{\mathbf{b}}{\Omega_c}\times(\upsilon_{\|}^2\kappa + \frac{\upsilon_{\perp}^2}{2}\frac{\nabla B}{B}) \tag{3.4.16}$$

where the magnetic field line curvature is defined as $\kappa = (\mathbf{b} \cdot \nabla)\mathbf{b}$ [46,47,52]. The gyrokinetic versions of the quasi-neutrality (QN) equation and parallel Ampere's law are used to provide closure to the system and are given by equations 3.4.17 and 3.4.18 respectively [46, 47, 54].

$$0 = \sum_a \frac{e_a}{\epsilon_0}[\int J_0 f_a d^2\mathbf{v} + \frac{e_a}{m_a}\nabla_\perp \frac{n_{a0}}{B^2}\nabla_\perp \phi + \frac{3e_a v_{th,a}^2 n_{a0}}{8m_a\Omega_a^4}\nabla_\perp^4 \phi] \tag{3.4.17}$$

$$[\nabla \times \nabla \times \mathbf{A}_\parallel]_\parallel = \frac{4\pi}{c}\sum_a e_a[\int J_0 U f_a d^2\mathbf{v} + \int \frac{e}{mc}\frac{\partial F_{a0}}{\partial U}U A_\parallel d^3\mathbf{v} + \frac{e_a^2 n_{a0} v_{th,a}^2}{2m_a c\Omega_a^2}\nabla_\perp^2 A_\parallel] \tag{3.4.18}$$

Equations 3.4.14, 3.4.17 and 3.4.18 form the complete system of linearised gyrokinetic equations. Further insight into the system is gained by considering the zeroth order moment of the GKE, known as the gyrokinetic moment (GKM) equation [54]. Utilising the QN equation and Ampere's law, and neglecting some higher order terms, the GKM equation can be written as [52]

$$\begin{aligned} -\omega^2\nabla_\perp \frac{1}{v_A^2}\nabla_\perp \phi + [\nabla(\nabla\psi)_\parallel \times \mathbf{b}] \cdot \nabla(\frac{\mu_0 j_{0\parallel}}{B}) + (\mathbf{B}\cdot\nabla)\frac{(\nabla \times \nabla \times (\nabla\psi)_\parallel)\cdot \mathbf{B}}{B^2} &= \\ -(i\omega)^2\mu_0 \sum_a e_a \int \frac{\mathbf{v}_{d,a}\cdot\nabla}{i\omega} J_0 f_a d^3\mathbf{v} & \end{aligned} \tag{3.4.19}$$

Treatment of non-adiabatic component of distribution function At this point we separate the perturbed particle distribution function f_a into its adiabatic component and its non-adiabatic kinetic compression component by the following expansion [41, 46, 47, 52]

$$f_a = h_a + H_1\frac{\partial F_{a0}}{\partial E} - [e\frac{\partial F_{a0}}{\partial E} - \frac{c\nabla F_{a0}}{i\omega B}\cdot(\mathbf{b}\times\nabla)]J_0\psi \tag{3.4.20}$$

On including this substitution in equation 3.4.14, the GKE can be written in terms of h_a, which is the non-adiabatic component of f_a

$$\frac{\partial h_a}{\partial t} + (U\mathbf{b} + \mathbf{v}_d)\cdot\nabla h_a = [\frac{c\mathbf{b}}{eB}\times\nabla F_{a0}\cdot\nabla - \frac{\partial F_{a0}}{\partial E}\frac{\partial}{\partial t}]J_0[\phi - (1 - \frac{\omega_d}{\omega}\psi)] \tag{3.4.21}$$

where $\omega_d = \frac{\mathbf{v}_d}{i} \cdot \nabla$ is the drift operator [52]. The components of this equation can be identified as follows: field line bending $U\mathbf{b} \cdot \nabla h_a = U(\partial/\partial l)h_a$, kinetic (non-MHD) non-adiabatic particle compression $i\omega_d h_a$, inertia $i\omega h_a$, fluid compression coupled to magnetic curvature $i(\omega_d/\omega)J_0\psi$ and perturbed parallel electric field $\phi - \psi$ [41]. These forces can roughly be associated with the generation of the ideal MHD waves: ψ for shear Alfvén waves and $\phi - \psi$ for slow magnetoacoustic waves, while $\delta B_\parallel \approx 0$ has been assumed, eliminating the compressional Alfvén wave [41]. We then consider the velocity space integrals in the QN equation and the GKM equation. The QN equation 3.4.17 then gives [52]

$$0 = \sum_a \frac{e_a}{\epsilon_0}\tilde{n}_a = \sum_a \frac{e_a}{\epsilon_0}[\int J_0 f_a d^3\mathbf{v}] = \sum_a e_a[\int J_0 h_a d^3\mathbf{v} + \frac{e_a n_{a0}}{T_a}\Gamma_{0a}[\phi - \psi + (1 + \eta_a G_0(\chi_a))\frac{\omega_{*a}}{\omega}\psi]] + \frac{e_a^2 n_i}{\epsilon_0 T_a}(\Gamma_0 - 1)\phi \quad (3.4.22)$$

and for the GKM equation 3.4.19 the velocity space integral is given by

$$\int e_a \frac{\mathbf{v}_d}{\omega} \cdot \nabla J_0 f_a d^3\mathbf{v} = \int e_a \frac{\mathbf{v}_d}{\omega} \cdot \nabla J_0 h_a d^3\mathbf{v} + [\frac{\mathbf{b}}{\omega B} \times (\mathbf{b} \cdot \nabla)\mathbf{b}] \cdot e_a n_{a0} e^{-\chi} I_0[\psi - \phi - (1 + \eta_a + \eta G_0)\frac{\omega_{*a}}{\omega}\phi] + [\frac{\mathbf{b}}{\omega B} \times (1 + G_0)\frac{\nabla B}{B}] \cdot e_a n_{a0} e^{-\chi} I_0[\psi - \phi - (1 + \eta_a + \frac{2\eta(G_1 - G_0)}{1 + G_0})\frac{\omega_{*a}}{\omega}\phi] \quad (3.4.23)$$

where

$$\omega_{*a} = [\frac{T_a\mathbf{b}}{ie_aB} \times \frac{\nabla n_a}{n_a} \cdot \nabla];\ \omega_{*e} = -\tau\omega_{*i};\ \tau = \frac{T_e}{T_i};\ \eta_a = \frac{\nabla T_a}{T_a} / \frac{\nabla n_a}{n_a} \quad (3.4.24)$$

$$\chi = \frac{\upsilon_{th}^2 k_\perp^2}{2\Omega^2};\ \upsilon_{th,a}^2 = \frac{2T_a}{m_a};\ \Omega_a = \frac{eB}{m_a};\ \Gamma_0 = e^{-\chi}I_0(\chi);\ G_0(\chi) = -\chi + \chi I_1(\chi)/I_0(\chi) \quad (3.4.25)$$

Recovery of GKM equation for ideal MHD Before progressing further with the derivation, it is useful to demonstrate how this fully kinetic approach recovers all features of ideal fluid theory. In the ideal MHD limit FLR effects are neglected ($\chi \propto k_\perp \rho_\perp \to 0$), meaning that the following terms go to zero [52, 54]

$$e^{-\chi} I_0 \to 0;\ G_0, G_1 \to 0 \tag{3.4.26}$$

Likewise, in the incompressible ideal MHD limit non-adiabatic effects are ignored, resulting in $h_a \to 0$. Applying these simplifications to the QN and GKM equations, the ideal MHD version of the shear Alfvén eigenmode equation is recovered, where the last term is the reduced MHD convective pressure term [52, 54]

$$-\omega^2 \nabla_\perp \frac{1}{v_A^2} \nabla_\perp \psi + [\nabla(\nabla\psi)_\parallel \times \mathbf{b}] \cdot \nabla(\frac{\mu_0 j_{0\parallel}}{B}) + (\mathbf{B}\cdot\nabla)\frac{(\nabla \times \nabla \times (\nabla\psi)_\parallel)\cdot \mathbf{B}}{B^2} + \\ \mu_0 P_0 \frac{\mathbf{b}}{B} \times [(\mathbf{b}\cdot\nabla)\mathbf{b} + \frac{\nabla B}{B}] \cdot \nabla[\frac{\nabla P}{B}(\mathbf{b}\times\nabla)\psi] = 0 \tag{3.4.27}$$

Treatment of propagator integrals The next step involves obtaining an explicit expression for h. The following ansatz is thus introduced for the non-adiabatic part of the perturbed distribution function:

$$h = \hat{h} e^{in\phi - i\omega t} \tag{3.4.28}$$

and using this the GKE can be written as

$$\hat{h} = ie \sum_m \int_{-\infty}^{t} dt' e^{i[n(\varphi' - \varphi) - m(\theta' - \theta) - \omega(t' - t)]} e^{-im\theta} \frac{\partial F_0}{\partial E}[\omega - \\ \omega_*] J_0[\phi_m(r') - (1 - \frac{\omega_d(r', \theta')}{\omega})\psi_m(r')] \tag{3.4.29}$$

This expression already exhibits many of the features recovered by the fully kinetic approach. The exponential term, known as the phase factor, takes into account the periodic particle orbits in the toroidal and poloidal directions, called bounce harmonics [52]. The inclusion of diamagnetic effects ω_*, parallel dynamics $\propto \phi - \psi$, particle drifts ω_d and finite Larmor radius (FLR) effects $\propto J_0$ are also evident. From the expression for the phase factor two propagator coefficients can be derived which contain the orbit integrals over unperturbed orbits [54]. These are given by equations 3.4.30 and 3.4.31 and contain all relevant information pertaining to the motion of the particles

$$a_{m,k,\sigma} = \frac{1}{\tau_t}\int_{-\tau_t/2}^{\tau_t/2} d\hat{t'}\, e^{i[S_m^0\theta' - (\sigma S_m^0 + k)\omega_t \hat{t'}]} \tag{3.4.30}$$

$$a_{k,m,\sigma}^G = \frac{1}{\tau_{b,t}}\int_{-\tau_{t,b}/2}^{\tau_{t,b}/2} d\hat{t'}\, e^{i[S_m^0\theta' - (\sigma S_m^0 + k)\omega_t \hat{t'} + W']} \frac{\mathbf{v}_d(\mathbf{r}', \theta') \cdot \nabla}{i\omega} \tag{3.4.31}$$

$a_{k,m,\sigma}^G$ contains the terms related to the drift motion of the particles, r^0 is the orbit average radial position of the particles and the following definitions are made [52]

$$\omega_D = n(\frac{\partial \varphi}{\partial t} - q(r^0)\frac{\partial \theta}{\partial t});\ \omega_D^0 = \frac{1}{\tau_{b,t}}\int dt \omega_D;\ b(r,\theta) = \frac{B_0}{B(r,\theta)} \tag{3.4.32}$$

$$S_m(r^0) = nq(r^0) - m;\ W' = \int_0^{t'} dt'' \Delta\omega_D;\ \Delta\omega_D = \omega_D - \omega_D^0 \tag{3.4.33}$$

Perturbed circulating particle density and integration over whole plasma volume By considering the velocity space integration term in the QN equation it is now possible to define the non-adiabatic density response for circulating particles $\tilde{n}_a$

$$\tilde{n}_a = (\int J_0 h d^3\mathbf{v})^{circ} = -\frac{\pi}{2} e_a v_{th}^3 \sum_m \int_0^{b_{min}(r^0)} \frac{d\Lambda}{b(r,\theta)\sqrt{1 - \frac{\Lambda}{b(r,\theta)}}} \int_0^\infty dY\sqrt{Y} \cdot$$
$$\sum_k \sum_\sigma \frac{\partial F_0}{\partial E} \frac{(\omega - \hat{\omega}_*) e^{-i[S_m^0\theta - (\sigma S_m^0 + k)\omega_t \hat{t}]}}{\omega - \omega_D^0 - (\sigma S_m^0 + k)\omega_t} \cdot J_0^2 [a_{k,m,\sigma}\phi_m(r^0) - (a_{k,m,\sigma} - a_{k,m,\sigma}^G)\psi_m(r^0)] \tag{3.4.34}$$

For obtaining the dispersion relation and for constructing the weak form, one has to integrate over the whole plasma volume [52]. Using the projection operator $e^{ip\theta}$ for integration in the poloidal direction, for the QN equation this is given by equation 3.4.35

$$(\int_{-\pi}^{\pi} \frac{d\theta}{2\pi} \mathcal{J}_\theta e^{ip\theta} \int J_0 h d^3\mathbf{v})^{circ} = -\frac{\pi}{2} e_a v_{th}^3 \sum_m \int_0^{b_{min}(r^0)} d\Lambda \int_0^\infty dY\sqrt{Y} \cdot \sum_k \sum_\sigma$$
$$\frac{\partial F_0}{\partial E} \frac{\omega - \hat{\omega}_*}{\omega - \omega_D^0 - (\sigma S_m^0 + k)\omega_t} K_{m,p,k,\sigma} \cdot J_0^2 [a_{k,m,\sigma}\phi_m(r^0) - (a_{k,m,\sigma} - a_{k,m,\sigma}^G)\psi_m(r^0)] \tag{3.4.35}$$

where

$$K_{m,p,k,\sigma} = \frac{1}{2\pi}\int_{-\pi}^{\pi}\frac{d\theta}{\sqrt{1-\frac{\Lambda}{b(r,\theta)}}}e^{i[S_p^0\theta-(\sigma S_m^0+k)\omega_t\hat{t}(\theta)]} \tag{3.4.36}$$

It is then necessary to take into account the contribution from the GKM equation which contains an explicit dependence on the drift velocity

$$(\int_{-\pi}^{\pi}\frac{d\theta}{2\pi}e^{ip\theta}\int e_a\frac{\mathbf{v}_d}{i\omega}\cdot\nabla J_0 h d^3\mathbf{v})^{circ} = -\frac{\pi}{2}e_a\upsilon_{th}^3\sum_m\int_0^{b_{min}(r^0)}d\Lambda\int_0^{\infty}dY\sqrt{Y}\cdot\sum_k\sum_\sigma$$
$$\frac{\partial F_0}{\partial E}\frac{\omega-\hat{\omega}_*}{\omega-\omega_D^0-(\sigma S_m^0+k)\omega_t}K_{m,p,k,\sigma}^G\cdot J_0^2[a_{k,m,\sigma}\phi_m(r^0)-(a_{k,m,\sigma}-a_{k,m,\sigma}^G)\psi_m(r^0)] \tag{3.4.37}$$

where

$$K_{m,p,k,\sigma}^G = \frac{1}{2\pi\omega}\int_{-\pi}^{\pi}\frac{d\theta}{\sqrt{1-\frac{\Lambda}{b(r,\theta)}}}e^{i[S_p^0\theta-(\sigma S_m^0+k)\omega_t\hat{t}(\theta)]}\frac{\mathbf{v}_d(\mathbf{r}',\theta')\cdot\nabla}{i\omega} \tag{3.4.38}$$

and where

$$\Lambda = \frac{\mu B_0}{E};\ Y = \frac{E}{T} \tag{3.4.39}$$

The terms responsible for Landau damping can now be seen clearly in equations 3.4.35 and 3.4.37. When the denominator $\omega - \omega_D^0 - (\sigma S_m^0 + k)\omega_t$ is close to zero the particle is resonant with the wave and energy exchange is possible [54]. A self-consistent non-perturbative linear gyrokinetic code called LIGKA (Linear Gyrokinetic Shear Alfvén Physics) has been developed in order to solve this system numerically [51]. LIGKA can treat modes of arbitrary wavelengths and takes into accounts all interesting features resulting from inhomogeneities in the background magnetic field, current, density and temperature profiles [46, 47, 54].

3.4.4 Low-frequency kinetic dispersion relation

While the linear gyrokinetic system of equations outlined previously can describe the global structure of the low-frequency Alfvén eigenmodes, it is also highly instructive to consider the local kinetic dispersion relation which can be derived from this system. The local eigenvalues can be recovered from this equation, allowing the determination of the low-frequency continuum with kinetic effects included. A numerical root-solver for this dispersion relation, as opposed to the LIGKA code, was used for analysis during this work as calculations were significantly faster and many more cases could be considered than would be possible by running LIGKA within the time-frame of the analysis. The derivation of this low-frequency kinetic dispersion relation is sketched below, following the approach given in [48, 52].

In order to recover the dispersion relation in low ($\omega < \omega_{ti}, \omega_{bi}$) and intermediate ($\omega_{ti}, \omega_{bi} < \omega < \omega_{te}, \omega_{be}$) frequency regimes, it is necessary to retain the coupling between the pure Alfvén, sound and drift waves [48, 52]. This coupling is due to curvature terms in this equation, with the drifts becoming more important for lower frequencies. In fact, it turns out that for the drift velocity $\mathbf{v}_{dr}$ it is the geodesic curvature component of $\mathbf{v}_{dr} \sim \sin\theta$ that is essential for recovering the BAE and geodesic acoustic mode (GAM) dispersion relations [48,52]. From this it follows that the poloidal side-bands of the density and the pressure perturbations have to be retained [48, 52].

Drift operator Acting on the perturbed potentials, the drift operator $\mathbf{v}_d \cdot \nabla/i$, introduced after equation 3.4.21, can be rewritten in the following more convenient form [52]

$$\mathbf{v}_d \cdot \nabla\phi/i = [\tilde{\omega}_d^r + \tilde{\omega}_d^n + S_m(\dot{\theta} - v_\parallel \mathbf{b} \cdot \nabla\theta)]\phi \tag{3.4.40}$$

Here, $\tilde{\omega}_d^r$ is the radial component of the drift operator, $\tilde{\omega}_d^n \approx \omega_{prec} + \frac{v_{th,i}^2}{\Omega_i}\frac{(-\cos\theta)}{R_0}\frac{-m}{r}$ is the poloidal drift and the precessional drift frequency is given by $\omega_{prec} = \langle n(\dot{\varphi} - q\dot{\theta})\rangle$. Upon applying the approximation $\mathbf{v}_d \cdot \nabla r = \frac{v_{th,i}^2}{\Omega_i}\mathbf{b} \times \kappa \cdot \nabla r \approx -\frac{v_{th,i}^2}{\Omega_i}\sin\theta/R_0$ and neglecting ω_{prec} due to its smallness, equation 3.4.40 can be rewritten as [52]

$$\mathbf{v}_d \cdot \nabla\phi/i = [-\omega_d^r \sin\theta/i\frac{\partial}{\partial r} + \omega_d^n \cos\theta]\phi \tag{3.4.41}$$

Note that the last term in equation 3.4.21 vanishes to lowest order in ϵ due to the application of the circulating particle approximation $\omega_t\hat{t} \approx \theta$ and $\omega_t \approx |v_\parallel/qR_0|$ [52]. We also define here the following quantity

$$\omega_d^{\pm} \equiv \frac{\upsilon_{th,i}^2}{\Omega_i}\frac{1}{R_0}(\frac{m}{r} \pm \frac{\partial}{\partial r}) = \omega_d^n \pm \omega_d^r \tag{3.4.42}$$

Simplification of propagator integrals The next step involves using these approximations in the integration of the propagator along the particle orbits, from which simplified expressions for equations 3.4.30, 3.4.31, 3.4.36 and 3.4.38 can be obtained. Continuing to follow [52], these are given by

$$a_{k,m,+1} = a_{k,m,-1} = \delta_k;\ a_{k,m,+1} = a_{-k,m,-1} \tag{3.4.43}$$

$$a^G_{k,m,+1} = \frac{1}{\tau_t \omega}\int_0^{\tau_t} dt[\omega_d^n \cos\theta - \frac{\omega_d^r}{i}\sin\theta]e^{ik\omega_t t} = \frac{\delta_{k,\pm 1}}{2\omega}\omega_d^{\pm} \tag{3.4.44}$$

$$a^G_{k,m,-1} = \frac{1}{\tau_t \omega}\int_0^{\tau_t} dt[\omega_d^n \cos(-\omega_t t) + \frac{\omega_d^r}{i}\sin(-\omega_t t)]e^{ik\omega_t t} = \frac{\delta_{k,\pm 1}}{2\omega}\omega_d^{\mp} \tag{3.4.45}$$

$$K_{m,p,k,+1} = \delta_{p,m-k} \tag{3.4.46}$$

$$K_{m,p,k,-1} = \delta_{p,m+k} \tag{3.4.47}$$

$$K^G_{m,p,k,+1} = \frac{1}{2\pi}\int_{-\pi}^{\pi} d\theta[\omega_d^n \cos\theta - \frac{\omega_d^r}{i}\sin\theta]e^{-i(-p+m-k)\theta} = \delta_{p,m-k\pm 1}\frac{\omega_d^{\mp}}{2\omega} \tag{3.4.48}$$

$$K^G_{m,p,k,-1} = \frac{1}{2\pi}\int_{-\pi}^{\pi} d\theta[\omega_d^n \cos\theta - \frac{\omega_d^r}{i}\sin\theta]e^{-i(-p+m+k)\theta} = \delta_{p,m+k\pm 1}\frac{\omega_d^{\mp}}{2\omega} \tag{3.4.49}$$

where m is the poloidal mode number, k counts the harmonics of the circulating motion, $\sigma = 1$ for co-passing and $\sigma = -1$ for counter passing particles and as mentioned previously ω_{prec} is small for background ions and is therefore neglected in the present treatment [48,52]. p counts the harmonics of the projection operator $e^{ip\theta}$ [48, 52].

Velocity space integration and recovery of kinetic dispersion relation Taking into account the $k \pm 1$ resonances and summing up over co- and counter-passing particles in the QN and GKM equations, four terms involving different combinations of $a_{k,m,\sigma}$, $a^G_{k,m,\sigma}$, $K_{m,p,k,\sigma}$ and $K^G_{m,p,k,\sigma}$ are obtained [52]. The final step involves integration over velocity space for the phase space integrals in the QN and GKM equations 3.4.35 and 3.4.37 respectively. Combining the results of these integrations, adding the adiabatic part (and polarisation term in the QN equation) and summing over the ions and electrons, the following expressions are obtained for the QN and GKM equations respectively [52]

$$\sum_{m'=m-1}^{m+1} \delta_{m',p} D^m(x_{m'})(\phi_{m'} - \psi_{m'}) = \tag{3.4.50}$$

$$\begin{pmatrix} P_{m-1} & \tau N^m(x_{m-1})\omega^+_{di}/\omega & 0 \\ \tau N^{m-1}(x_m)\omega^-_{di}/\omega & P_m & \tau N^{m+1}(x_m)\omega^+_{di}/\omega \\ 0 & \tau N^m(x_{m+1})\omega^-_{di}/\omega & P_{m+1} \end{pmatrix} \begin{pmatrix} \psi_{m-1} \\ \psi_m \\ \psi_{m+1} \end{pmatrix}$$

$$\frac{\tau|e|^2 n_e}{\omega^2 T_e}\delta_{m,p}[((\omega^n_d)^2 - (\omega^r_d)^2)H^m(x_{m-1}) + ((\omega^n_d)^2 - (\omega^r_d)^2)H^m(x_{m+1})]\psi_m + \frac{|e|^2 n_e}{\omega^2 T_e}\cdot \tag{3.4.51}$$

$$\begin{pmatrix} 0 & \tau N^m(x_m)\omega^+_{di} & 0 \\ \tau N^{m-1}(x_m)\omega^+_{di} & 0 & \tau N^{m+1}(x_m)\omega^-_{di} \\ 0 & \tau N^m(x_m)\omega^-_{di} & 0 \end{pmatrix} \begin{pmatrix} (\phi-\psi)_{m-1} \\ (\phi-\psi)_m \\ (\phi-\psi)_{m+1} \end{pmatrix}$$

where P is the polarisation terms and the terms $D(x_m), H(x_m)$ and $N(x_m)$ represent the sound wave, geodesic curvature and poloidal side-band coupling contributions respectively [52], with

$$D(x_m) = [1 + \tilde{D}(x_{e,m})] + \tau[1 + \tilde{D}(x_{i,m})] \tag{3.4.52}$$

$$H(x_m) = \tilde{H}(x_{i,m}) + \tau\tilde{H}(x_{e,m}) \tag{3.4.53}$$

$$N^m(x_m) = \tilde{N}^m(x_{i,m}) - \tilde{N}^m(x_{e,m}) \tag{3.4.54}$$

$$P_m = \tau(\Gamma_0 - 1)[1 - \frac{\omega_i^*}{\omega}(1 + \eta_i \frac{\Gamma_0 G_0}{\Gamma_0 - 1})] \tag{3.4.55}$$

and,

$$\tilde{D}^m(x) = (1 - \frac{\omega_{*p}^m}{\omega})xZ(x) - \frac{\omega_{*p}^m}{\omega}\eta(x^2 + xZ(x)(x^2 - \frac{1}{2})) \tag{3.4.56}$$

$$\tilde{H}^m(x) = \frac{1}{2}[(1 - \frac{\omega_{*p}^m}{\omega})\tilde{F}(x) - \eta\frac{\omega_{*p}^m}{\omega}\tilde{G}(x)] \tag{3.4.57}$$

$$\tilde{F}(x) = \frac{1}{2}(xZ(x)(\frac{1}{2} + x^2 + x^4) + \frac{3x^2}{2} + x^4) \tag{3.4.58}$$

$$\tilde{G}(x) = \frac{1}{2}(xZ(x)(\frac{3}{4} + x^2 + \frac{x^4}{2} + x^6) + 2x^2 + x^4 + x^6) \tag{3.4.59}$$

$$\tilde{N}^m(x) = \frac{1}{2}((1 - \frac{\omega_{*p}^m}{\omega})[x^2 + xZ(x)(x^2 + \frac{1}{2})] - \frac{\omega_{*p}^m}{\omega}\eta[(x^4 + \frac{x^2}{2}) + xZ(x)(\frac{1}{4} + x^4)]) \tag{3.4.60}$$

$Z(x)$ is the plasma dispersion function and ω_{*p} is the diamagnetic frequency for the respective species [48, 52]. The QN equation 3.4.50 can then be solved for $\phi - \psi$ and the result substituted into the GKM equation 3.4.51. The kinetic dispersion relation is obtained by considering only second order radial derivatives of the GKM equation and expanding up to second order in ω_d^r. The resulting kinetic dispersion relation is then given by the following equation [48, 52]

$$\begin{aligned}\omega^2(1 - \frac{\omega_{*p}}{\omega}) - \overline{k_\parallel}\frac{R_0^2}{\upsilon_{A0}^2} = 2\sqrt{\frac{2}{1+\kappa^2}}\frac{\upsilon_{thi}^2}{R_0^2\omega_{A0}^2}(-[H(x_{m-1}) + H(x_{m+1})]+ \\ \tau[\frac{N^m(x_{m-1})N^{m-1}(x_{m-1})}{D(x_{m-1})} + \frac{N^m(x_{m+1})N^{m+1}(x_{m+1})}{D(x_{m+1})}])\end{aligned} \tag{3.4.61}$$

where $x_m = \frac{\omega}{k_{\parallel m}\upsilon_{th}}$, $\upsilon_{thi}^2 = 2T_i/m_i$, $\omega_{ti} = \upsilon_{thi}/qR_0$, $\tau = T_e/T_i$, $\omega_{*p_s} = \omega_{*n_s} + \omega_{*T_s} = \frac{T_s}{eB}k_\theta(\frac{\nabla n_s}{n_s})(1+\eta)$ with $\eta = \frac{\nabla T_s}{T_s}/\frac{\nabla n_s}{n_s}$, s is the species index and $\overline{k_\parallel}$ is defined in equation 4.6.3. Equation 3.4.61 has been modified in order to take account of plasma elongation effects via the $\sqrt{\frac{2}{1+\kappa^2}}$ term pre-multiplying the RHS of the equation [55]. On the LHS of equation 3.4.61, the modified dispersion relation for shear Alfvén waves is evident. Equation 3.4.61 is similar to the kinetic ballooning mode dispersion relation first derived by [42] and will be solved numerically as part of the analysis conducted in chapters 5 and 6.

Chapter 4

Analysis procedure

4.1 Classification of modes

The primary goal of this work was the classification of low-frequency Alfvén eigenmode activity during different plasma parameter regimes. Using recently improved diagnostic capabilities at ASDEX Upgrade, a number of these experimentally observed modes - specifically beta-induced Alfvén eigenmodes (BAEs) [57], low-frequency modes of mixed acoustic and Alfvénic polarisation [37], and toroidicity-induced Alfvén eigenmodes (TAEs) [35] - were investigated [59]. These observations were then compared with results obtained by solving the kinetic dispersion relation 3.4.61, which describes the primary physical mechanisms governing much of the experimentally observed low-frequency Alfvén eigenmode behaviour, as well as with results obtained by solving the full set of gyrokinetic equations [42, 46–48, 60] using LIGKA [48]. After obtaining satisfactory agreement between experimental observations and theoretical predictions, sensitivity studies were carried out to investigate the response of different types of modes to potential tokamak plasma scenarios, including different background kinetic profile gradients. In the present section, the methodology employed in this analysis is outlined.

4.2 Experimental observations using Mirnov coil, soft x-ray (SXR) and electron cyclotron emission (ECE) diagnostics

The first step in the analysis procedure was the observation and identification of the different types of low-frequency modes to be investigated. A suite of diagnostics, which included Mirnov coil [15], soft x-ray (SXR) [16] and electron cyclotron emission (ECE) [17, 18] diagnostics, was available at ASDEX Upgrade in order to facilitate this. In the following sections, examples of observations made using these diagnostics, as well as considerations of the potential uses of these observations in enhancing the analysis procedure, are presented. The physical principles underlying the operation of the diagnostics have been presented in chapter 2 of this work.

4.2.1 Mirnov coils

The primary magnetic field diagnostic at ASDEX Upgrade consists of toroidally and poloidally arrayed Mirnov coils, which are used to measure poloidal and toroidal magnetic field perturbations at the plasma edge. From these measurements, the mode frequency and amplitude could be determined via the methods described in chapter 2. The positions of these coils in the poloidal and toroidal planes are shown in figure 2.8 (a) and (b) respectively [5, 15].

Two sets of so-called 'ballooning coils', which are marked in red in figure 2.8, measured the radial magnetic field perturbations and were primarily used during this analysis due to their proximity to the plasma. An example of these measurements is given in figure 4.1, which shows frequency spectrograms of TAE activity measured with toroidal ballooning coils B31-02, B31-13 and B31-14 respectively. These particular coils have a toroidal span of approximately 180 degrees. It can be seen that the mode activity measured via the Mirnov coils is very prominent in this case. This is due to the the fact that the magnetic coil measurements are based on the expression $d\tilde{B}_\theta/dt \approx f\tilde{B}_\theta$, where f is the mode frequency and $\tilde{B}_\theta$ is the size of the perturbation. Thus, even small Alfvénic perturbations can be observed due to their relatively high frequencies.

Marginal variations in the mode amplitude and a frequency separation between distinct toroidal eigenmodes measured by each coil are also evident. These variations are most likely a result of small differences in the distances of the coils from the plasma edge and variations in the structure of the mode itself. In this case, the B31-14 coil measured the highest amplitude and the highest degree of frequency separation between distinct toroidal eigenmodes. Comparing the phase of the Fast Fourier Transform (FFT) bandpass filtered signals of adjacent ballooning coils, the total phase offset could be determined in the toroidal and poloidal direction. From this determination, estimates of the toroidal and poloidal mode numbers n and m could be obtained [61].

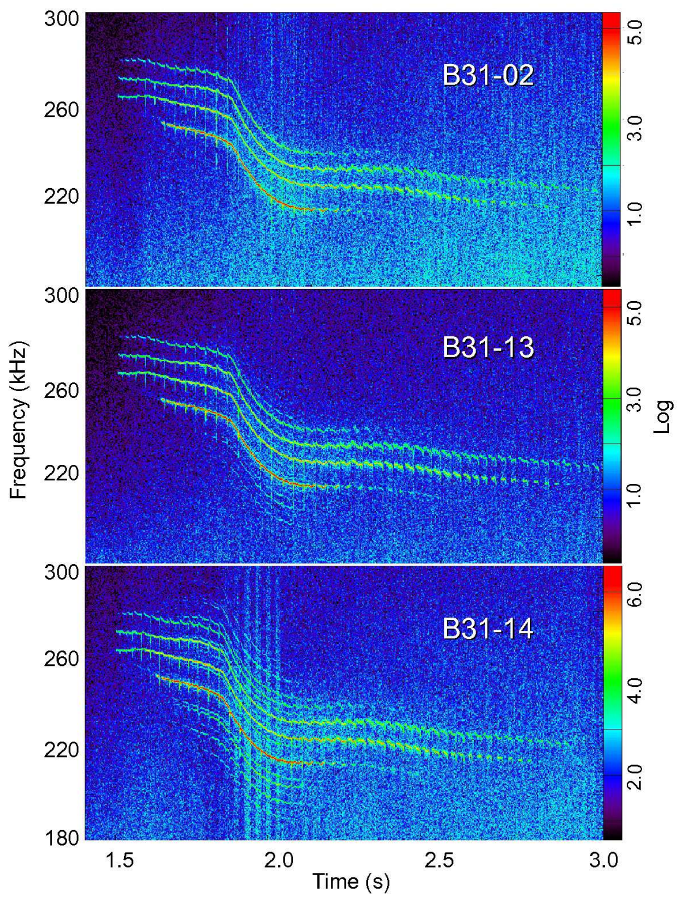

Figure 4.1. TAE activity measured using Mirnov coils B31-14, B31-13 and B31-02 from $t = 1.4 - 3.0$s for discharge 25546.

4.2.2 Soft x-ray

As has been described in section 2.3.2, the soft x-ray (SXR) diagnostic at ASDEX Upgrade provides 208 lines of sight of the plasma, 128 of which have a fast sampling rate of 2MHz [16]. From these, information on the frequency, amplitude and position of modes could be obtained. Figure 4.2 shows the frequencies and amplitudes of BAEs, measured using a number of core channels of the SXR I camera. Also shown is the approximate tangency radius of each channel. The tangency radius is determined by the unique flux surface with which the chord has a single intersection point. The maximum intensity observed by each line of sight is dependant on the shape of the mode eigenfunction [62]. The degree to which the observed amplitudes of these modes differ at each tangency radius provides an indication as to the approximate radial localisation of the BAEs. From theoretical predictions and numerical calculations the BAE eigenfunction is expected to be peaked close to the $q = 1$ surface [63].

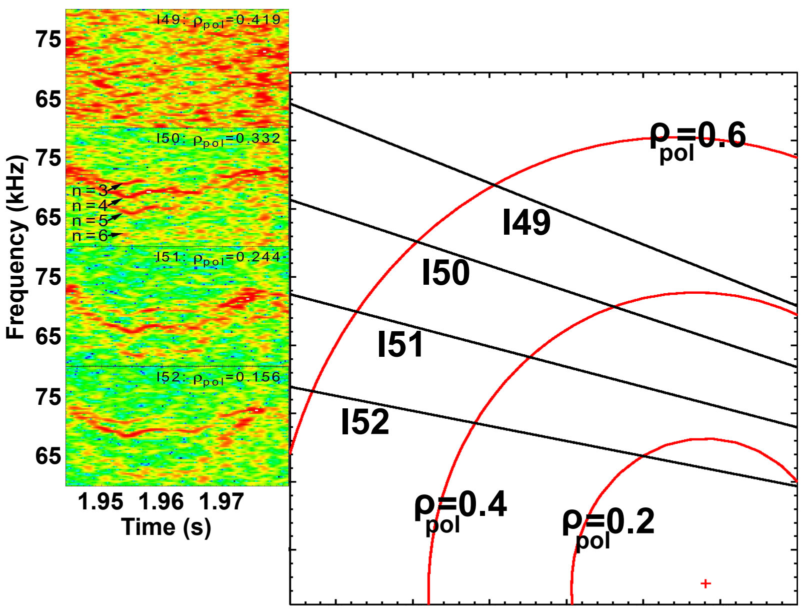

Figure 4.2. BAE amplitude measured by a number of core SXR channels of the I camera, showing their approximate tangency radii and flux surfaces at $\rho_{pol} = 0.2, 0.4$ and 0.6 at $t = 1.96$s during discharge 25546.

It is seen from figure 4.2 that core SXR signals $I50$ and $I51$, which surround the predicted radial location of the $q = 1$ surface, possess the largest amplitude.

With these observations, information on the mode position could be inferred. Figure 4.3 shows TAE activity during discharge 25546, measured with (a) Mirnov coil B31-14 and (b) soft x-ray channel $I50$, which has a tangency radius of $\rho_{pol} \approx 0.33$.

Figure 4.3 (b) also shows the toroidal mode numbers of the distinct eigenmodes exhibiting frequency separation, estimated using measurements from the toroidal ballooning coils. Not all of the frequency separations between distinct TAEs observed using the magnetics diagnostic are seen using soft x-ray. This may be a result of this particular SXR channel not intersecting the TAE eigenfunction for these mode numbers, and/or a result of the TAE peak being hidden by noise which can be large at higher frequencies [64].

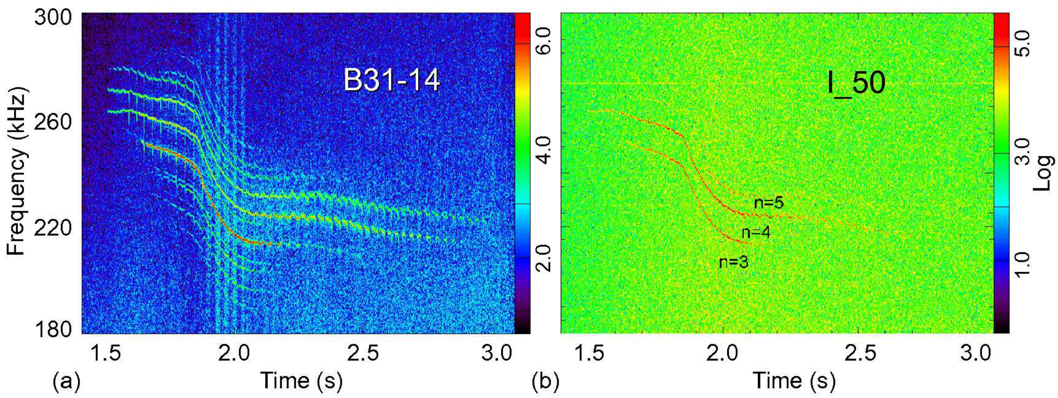

Figure 4.3. TAE activity during discharge 25546 measured using (a) Mirnov coil B31-14 and (b) soft x-ray channel $I50$ for toroidal mode numbers $n = 3 - 5$.

The number of global minima in the amplitude profile will then give the poloidal mode number m, assuming that the mode consists of only one poloidal mode number. If the mode consists of more than one poloidal mode number then the structure of the amplitude minima can be quite complicated, and the mode number difficult to establish [65]. The SXR intensity measured by individual channels during the sawtooth cycle also provided information on the approximate location of the sawtooth inversion radius and hence the $q = 1$ surface location. The method by which this was undertaken is described in more detail in section 4.4 of this chapter.

4.2.3 Electron cyclotron emission

Fast electron cyclotron emission (ECE) and 2D ECE imaging (ECEI) measurements at ASDEX Upgrade provided further information on the radial localisation, 2D structure and frequency of certain modes [17, 18]. Due to the availability of ECE data with a high sampling rate for many ASDEX Upgrade discharges, it was possible to calculate the frequency spectrogram of modes up to 500kHz in these cases. The high radial resolution of the ECE diagnostic means that information on the 1D radial localisation of the modes could be obtained based on observations of the amplitude measured using different channels. Figure 4.4 (a) shows time-traces of the electron temperature measured using the ECE diagnostic from $t = 2.6 - 3.7$s for discharge 28112, with sawtooth behaviour evident throughout this period. The locations of the core ECE channels on the low field side of the plasma are shown in figure 4.4 (b), with the channel colours corresponding to those in figure 4.4 (a).

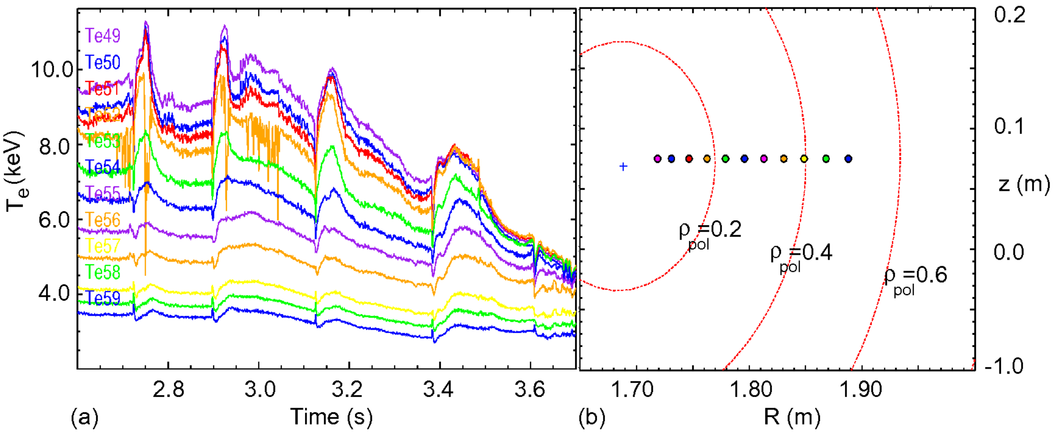

Figure 4.4. (a) Electron temperature time-traces measured using ECE from $t = 2.6 - 3.7$s and (b) positions of core ECE channels at $t = 3.4$s for discharge 28112.

Figure 4.5 shows measurements for several core fast ECE channels during the same period of discharge 28112 presented in figure 4.4 (a). Strong sawtooth precursor activity is observed in the periods leading up to the sawtooth crashes using the innermost core channels 49, 51, 53 and 55. Second and third harmonics of these precursors are also observed. For channel 57, which is further from the plasma centre than most of the other channels, the observed amplitudes are much lower, and for channel 59, which is the furthest out of the six channels, almost no activity is visible. This gives another verification of the approximate position of the sawtooth inversion radius, and hence the $q = 1$ surface, as one would not expect to observe precursor oscillations outside the $q = 1$ surface. A 2D ECE imaging system is also in operation at ASDEX upgrade, as has been discussed in section 2.3.4 [18]. From this, an estimation of the 2D structure of modes can be obtained if the electron temperature perturbation which they induce are large enough to be observed.

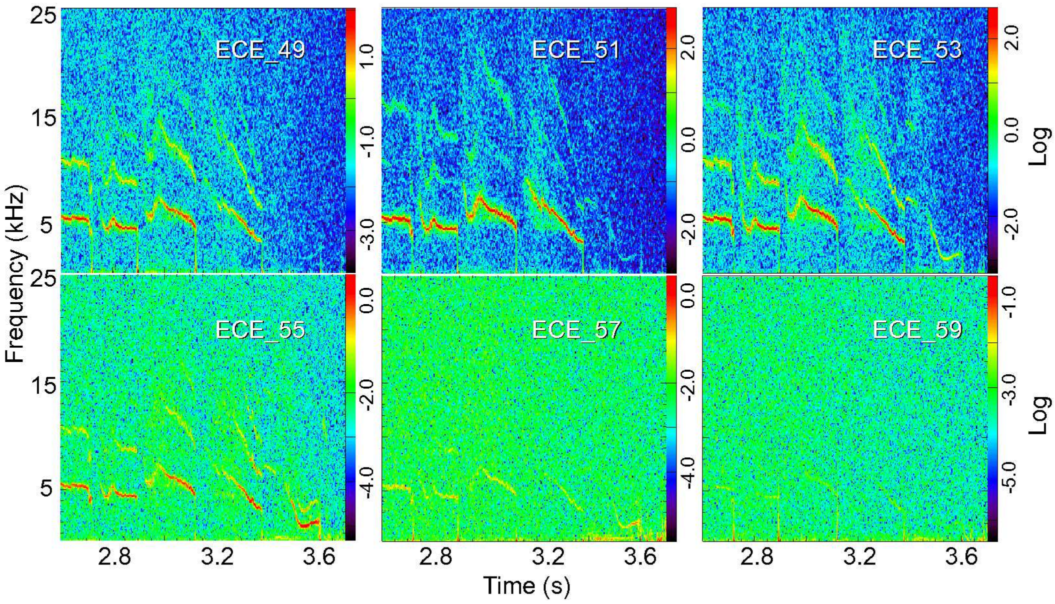

Figure 4.5. Frequency spectrograms for six core ECE channels from $t = 2.6 - 3.7$s for discharge 28112.

4.3 Coherence and radial displacement eigenfunction (RDE) analysis

4.3.1 Coherence analysis

It has been demonstrated that signal processing techniques can be applied successfully in determining various properties of plasma instabilities [66, 68]. For example, while the Mirnov coils alone cannot give any direct information regarding the radial localisation of a mode, when used in conjunction with SXR and/or ECE via a coherence analysis approach the approximate radial position of certain modes considered in this work can be estimated [68]. In this section, primarily following the approach given in [66, 68], an outline of the background theory and practical methods employed in determining the coherence between different signals is presented.

Signal processing background theory The sample cross-correlation function of two discrete random time signals $u_1(t)$ and $u_2(t)$ is defined as:

$$R_{12}(\tau) = \frac{1}{n-m}\sum_{q=1}^{n-m} u_1(t_q)u_2(t_q+\tau) \tag{4.3.1}$$

where $t_q = q\Delta t(q = 0, 1, ..., n)$, Δt is the sample interval of the data and the time delay is $\tau = r\Delta t(r = 0, 1, ..., m)$ with $m \ll n$ (not to be confused with the toroidal and poloidal mode numbers). The correlation between these time series gives a measure of their similarity. This can be used to obtain information about the radial position of an instability by comparing signals from different diagnostics. The value that quantifies this is called the cross-correlation coefficient or the normalised cross correlation function [66]. This is given by the following expression:

$$\rho_{12}(\tau) = \frac{R_{12}(\tau)}{\sqrt{R_{11}(0)R_{22}(0)}} \tag{4.3.2}$$

where $R_{11}(0)$ and $R_{22}(0)$ are the auto-correlations for the two signals at zero time-delay. Moving to the frequency domain, the coherence $\gamma(f)$ (which is a normalised cross power spectrum) can be obtained by taking the Fourier transform of $\rho_{12}(\tau)$. It is computed by taking the FFT of signals $u_1(t)$ and $u_2(t)$ and is defined as

$$\gamma(f) = \frac{\langle S_{12}(f)\rangle}{[\langle S_{11}(f)\rangle.\langle S_{22}(f)\rangle]^{1/2}} \tag{4.3.3}$$

where $S_{12}(f)$ is the cross power spectrum of $u_1(t)$ and $u_2(t)$, and $S_{11}(f)$ is the auto power spectrum of $u_1(t)$. $S_{12}(f)$ is computed via the co- and quad-spectra $C_{12}(f)$ and $Q_{12}(f)$, defined in [66]

$$S_{12}(f) = (C_{12}(f)^2 + Q_{12}(f)^2)^{1/2} \tag{4.3.4}$$

$S_{11}(f)$ is computed by

$$S_{11}(f) = (Re(U_1(f)))^2 + (Im(U_1(f)))^2 \tag{4.3.5}$$

where $Re(U(f))$ and $Im(U(f))$ are the real and imaginary transform coefficients [66]. The brackets $\langle\rangle$ represent ensemble averages as the coherence is a statistical parameter obtained by ensemble averaging the cross-power spectrum over many data sets [68]. If the number of degrees of freedom n_{DOF} is moderately large, e.g. $n_{DOF} > 30$, then the distribution approaches a Gaussian and for the FFT the percentage error is defined by the number of FFT averages M_{av}, with the minimum level of statistical significance in the coherence given by $\gamma_0 = 1/\sqrt{M_{av}}$ [67] [68] [69].

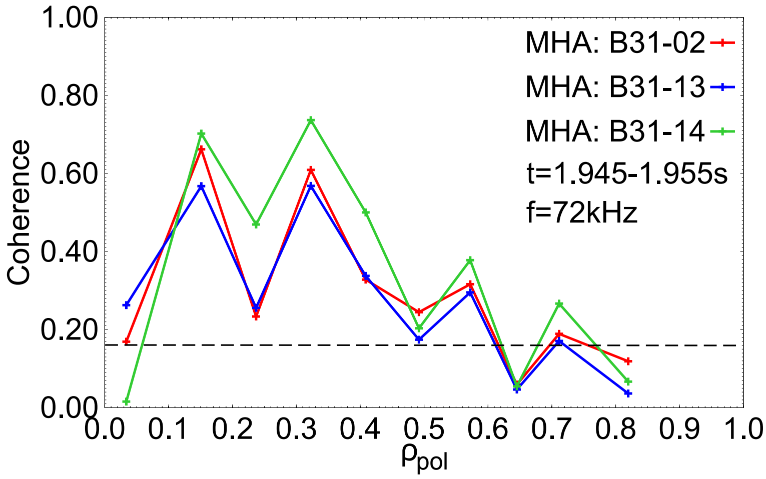

Figure 4.6. Calculated coherence between Mirnov coils B31-14, B31-13 and B31-02, and signals from SXR cameras I and J for $f \approx 72$kHz, at their respective tangency radii from $t = 1.945 - 1.955$s. The labelled magnetic coil signals are each combined with the soft x-ray channels specified above to generate a coherence plot.

Application to experimental measurements Figure 4.6 shows the coherence between Mirnov coil signal B31-14, B31-13 and B31-02 and various lines of sight of soft x-ray cameras I and J for discharge 25546. Due to the fact that the radial structure and position of the BAEs is not expected to vary much over short time-scales, a time window of 10ms and a FFT data length of 1024 points and 50% window overlap was used [68]. It is observed that the highest coherence occurs in the region $\rho_{pol} \approx 0.1 - 0.5$, peaking at $\rho_{pol} \approx 0.3$ as expected from previous considerations of the BAE radial localisation. The horizontal dashed black line represents the minimum significance threshold, results under which can be considered as noise [70]. It is also seen that the coherence between the soft x-ray channels and the Mirnov coil signal exhibits a pattern of minima and maxima in the core region. Following the explanation given in [72], this is due to the line-integrated nature of the soft x-ray measurements. A helical mode with a single poloidal mode number m has a soft x-ray fluctuation profile with m minima and $m + 1$ maxima [72].

4.3.2 Radial displacement eigenfunction (RDE) analysis

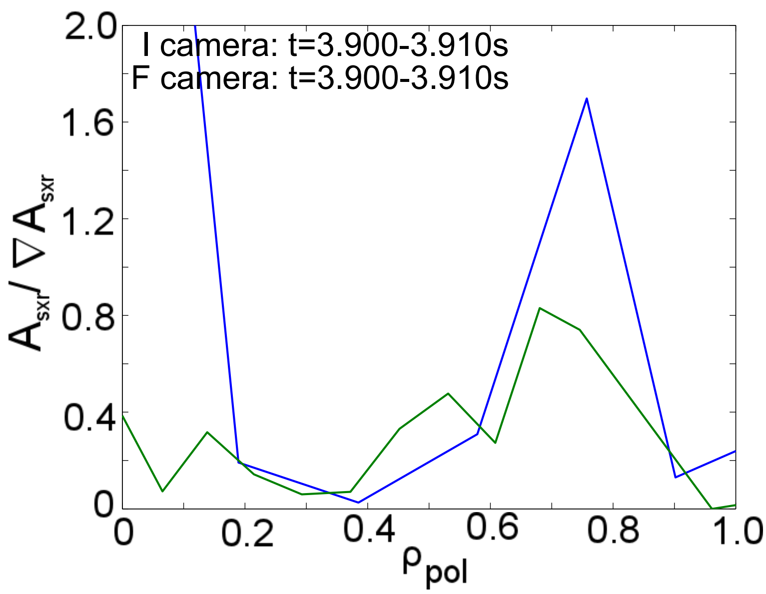

Figure 4.7. Mode radial displacement eigenfunction calculated for discharge 28112 from $t = 3.900 - 3.910$s at $f \approx 185$kHz for I and F cameras of the SXR diagnostic. Off-scale data at $\rho_{pol} \approx 0.1$ is a result of a vanishing gradient.

The 128 "fast" channels of the soft x-ray diagnostic at ASDEX Upgrade, with sampling frequencies of 2MHz, allow the study of the low to medium frequency Alfvén eigenmodes dealt with in this work, which are normally observed to have frequencies under 250kHz. These lines of sight provide moderately high radial resolution, and using them the soft x-ray fluctuation amplitude of the above modes can be recovered [16]. Upon calculating the gradient of the mean SXR fluctuation amplitude profile A_{sxr} with respect to ρ_{pol}, a measure for the plasma radial displacement at the tangency radius of each SXR line of sight is obtained [62]. This in turn provides a radial displacement eigenfunction (RDE), for the particular mode in question [64]. The radial displacement ξ_r at a given radial position is given approximately by the expression

$$\xi_r(\bar{\rho}_{pol}) \approx -\tilde{A}_{sxr}/\nabla_{\bar{\rho}} A_{sxr} \tag{4.3.6}$$

where $A_{sxr}(\bar{\rho}_{pol})$ is the mean soft x-ray brightness profile. This equation is an approximation of the expression $\xi_r(\bar{\rho}_{pol}) \approx -\tilde{T}/\nabla_{\bar{\rho}} T_0$, which is itself derived from the linear MHD approximation. The differences between the two expressions come from the effects of line integration and impurity radiation. An example of a radial displacement eigenfunction, calculated for discharge 28112 from $t = 3.90 - 3.91$s at $f \approx 185$kHz is shown in figure 4.7.

4.4 Determination of safety factor profile information via experimental observations

4.4.1 $q = 1$ radius from sawtooth inversion radius

As described in section 4.1, low-frequency Alfvén eigenmodes such as Alfvén cascades (ACs) [71], toroidicity-induced Alfvén eigenmodes (TAEs) and beta-induced Alfvén eigenmodes (BAEs) [63] are observed to exist close to low-order rational surfaces. Of particular interest for the study of BAEs is the $q = 1$ surface as in most cases it is observed to exist in the inner core region where the temperature profile gradients can be relatively large. This overlap of mode radial localisation with large background kinetic profile gradients can have important consequences for the mode frequency evolution and stability [59, 63], which will be examined in chapters 5-7. It should be noted that since B_T and I_p are anti-parallel in ASDEX Upgrade, $q < 0$. Thus, throughout the thesis, whenever the value of the safety factor is referenced, it is the magnitude that is being referred to.

The majority of the mode activity considered in this work took place during periods of sawtooth activity. The sawtooth instability, the physics of which is described in chapter 2, is characterised by a large drop or "crash" in the core temperature at the end of a sawtooth period. When this process repeats itself over a given time range, the process is known as the sawtooth cycle. The sawtooth cycle is dependent on the existence of a $(1, 1)$ kink mode in the plasma. The

(1, 1) mode has been shown to survive the sawtooth crash process, indicating the continuous presence in the plasma of a $q = 1$ surface [25]. It has also been demonstrated that the position of the $q = 1$ surface does not change appreciably over the course of successive sawtooth periods [25]. Thus, as the radial location of the BAE peak has been found to occur close to the $q = 1$ surface [63], it was important that a reliable estimate for the radial location of the $q = 1$ surface be obtained. The two methods by which this was achieved are described in the section that follows.

Intersection of T_e profiles before and after sawtooth crash The first method involved electron temperature profile measurements using the ECE and Thomson scattering diagnostics. For successive sawtooth periods there exists a radial location where the difference in electron temperature measured immediately prior to and following the sawtooth crash is approximately zero. This is known as the sawtooth inversion radius [74]. From theoretical considerations, the $q = 1$ surface is expected to exist close to the sawtooth inversion radius for many cases of practical interest [73].

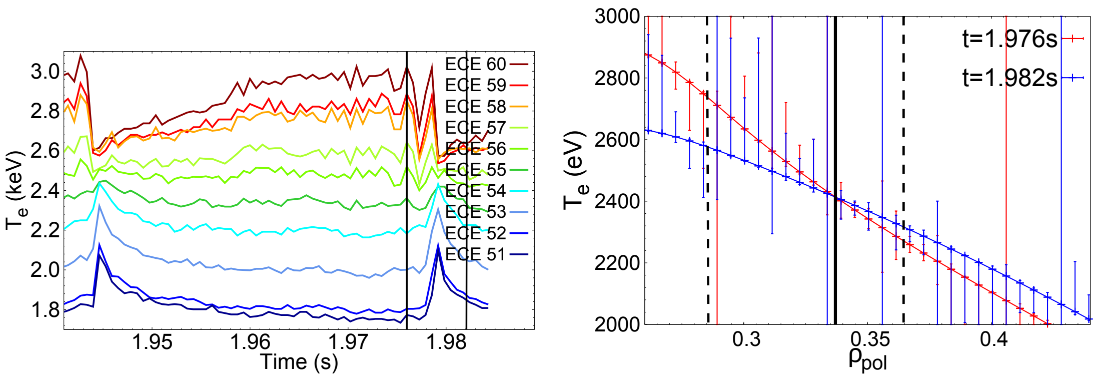

(a) (b)

Figure 4.8. (a) Time-traces of core ECE channels during sawtooth cycle $t = 1.945 - 1.979$s measured using channels of the ECE radiometer diagnostic covering the radial range $0.244 \leq \rho_{pol} \leq 0.438$. Vertical black lines indicate times used to calculate sawtooth inversion radius. (b) Electron temperature profiles from integrated data analysis (IDA) before ($t = 1.976$s) and after ($t = 1.982$s) the sawtooth crash at $t \approx 1.980$s. Solid vertical black line indicates estimate for sawtooth inversion radius. Dashed vertical lines indicate estimated error bars in sawtooth inversion radius.

However, its exact location is dependant on the safety factor and temperature profiles before the crash, as well as on the model used to explain the sawtooth process. Upon assuming parabolic q and T_e profiles as well as the Kadomtsev model [26], the $q = 1$ surface is found to coincide with the sawtooth inversion radius [73]. This will not be the case for an extremely flat core safety factor profile with rapid variation outside the $q = 1$ surface [73]. Without detailed numerical simulations, the assumption that the $q = 1$ radius and sawtooth inversion radius coincide is the most accurate that can be achieved, and is adequate for this analysis. Proceeding under the assumptions outlined above, an estimate for the $q = 1$ radius at a given time-point is obtained by determining the approximate sawtooth inversion radius close to this time-point. The radial point of intersection of these profiles is taken to be the $q = 1$ surface radial location.

Realistic T_e profiles are obtained from integrated data analysis (IDA), as described in section 2.3.8 [23]. As the $q = 1$ surface position has been shown not to change appreciably over the course of a sawtooth period [25], this radial location was assumed to remain constant for the analysis of each sawtooth period.

An example of this procedure is demonstrated in figure 4.8 (a), which shows time-traces of core ($\rho_{pol} \approx 0.24 - 0.37$) ECE channels during a sawtooth period from $t = 1.945 - 1.979$s, as well as partial periods of the preceding and subsequent periods. The electron temperature measured by ECE channel 56, which is at $\rho_{pol} \approx 0.32$, appears to exhibit the least variation over the period before and after the sawtooth crash at $t \approx 1.980$s, suggesting that the sawtooth inversion radius is located in this region. The intersection of two electron temperature profiles from IDA, before and after the crash, are shown in figure 4.8 (b). The radial location where they intersect is taken as the sawtooth inversion radius, and hence the $q = 1$ surface radial location, and also occurs at $\rho_{pol} \approx 0.335$. An estimate for the error in the $q = 1$ surface radial location was obtained by inspecting results for a fitted q-profile at $t = 2.066$s during discharge 25546, obtained using CLISTE, which included confidence bands for the q-profile and has similar parameters.

Changes in measured SXR intensity The soft X-ray diagnostic can be used as another tool in determining the sawtooth inversion radius. While the radial resolution of SXR is not as high as that of the ECE diagnostic, a number of the SXR channels provide a high temporal resolution of 2MHz, which is important for observing the rapid sawtooth crash event. As the measured SXR intensity depends on the temperature, an estimate for the sawtooth inversion radius is obtained by finding the outermost line of sight with a decreasing signal in time for the SXR intensity and the innermost with an increasing signal close to the time of the sawtooth crash [61]. From this, the $q = 1$ radius can be inferred to occur in the region between the tangency radii of these two channels. This method has the advantage that information from two extremes of a flux surface is available, leading to a more accurate estimate for the flux surface diameter at the sawtooth inversion radius. The method also provides bounds on the maximum and minimum possible values for the inversion radius. An example of signals from lines of sight (LOS) of the I camera of the SXR diagnostic is shown in figure 4.9. As the signal from LOS I51 drops sharply at $t \approx 2.15$s, while that of $I50$ increases, it can be inferred that the sawtooth inversion radius occurs in the region between the tangency radii of these two LOS. The same is true of LOS $I57$ and $I58$.

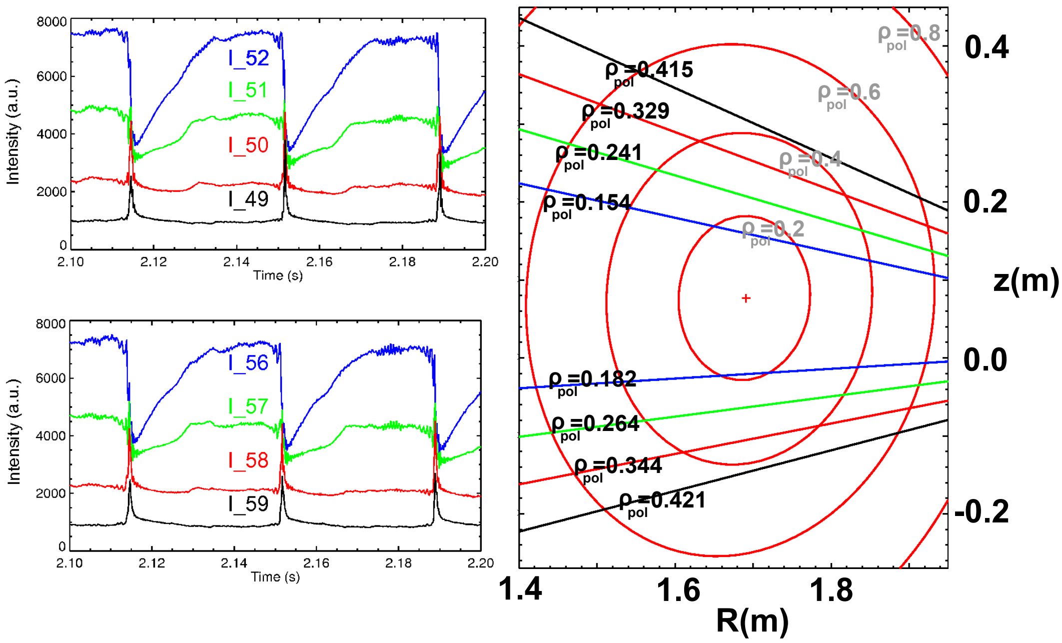

Figure 4.9. Intensity of core SXR signals at successive sawtooth crashes during discharge 25546 and corresponding lines of sight plotted along with flux surfaces at $\rho_{pol} = 0.2, 0.4, 0.6$ and 0.8.

4.4.2 CLISTE equilibrium reconstructions

Implementation

The theory underlying tokamak plasma equilibria has been outlined in section 2.1.3. In this section, a method for reconstructing the constrained equilibria is presented. Analytical solutions to the GSE can be obtained in a limited number of cases where j_ϕ is restricted to be a linear function of psi [79]. In practice, non-linear solutions with spline-parameterised $p(\psi)$ and $FF'(\psi)$ source profiles are numerically calculated. The CLISTE code, which is an acronym for the CompLete Interpretive Suite for Tokamak Equilibria, has been developed for this purpose [78]. CLISTE finds a numerical solution to the GSE for a given set of poloidal field coil currents and limiter structures by varying the free parameters in the parametrisation of the $p(\psi)$ and $FF'(\psi)$ source profiles which define the toroidal current density j_ϕ [78, 79], as seen in equation 2.1.39. This is done in order to gain the best possible fit in the least squares sense to a set of experimental measurements [79]. The experimental data utilised as input is described in the next section.

Input data and assumptions

CLISTE uses various experimental measurements as input data for the least-squares fitting procedure. Primary among these are measurements of the poloidal and radial magnetic field inside the vacuum vessel from an array of coils which are arranged outside the plasma, as well as the currents in the various poloidal field coils [15]. Background temperature and density profile data for the ions and electrons can also be used to constrain the equilibria, as well as fast particle pressure profile data if an estimate of it is available. These are obtained via a range of diagnostics including ECE [17], core and edge Thomson scattering [20], lithium ion beam analysis [21], interferometry [19], charge exchange recombination spectroscopy (CXRS) [24], as well as from IDA analysis [23]. It should be noted that the interferometric measurements in figure 4.10 are actually consistent with the fits, and are lower in magnitude than the overall fit due to the line integrated nature of the measurements. Information about the location of rational flux surfaces, used to constrain the q-profile and obtained from theoretical and experimental considerations, allow improved reconstructions of the toroidal current density profile. The methods by which this data is obtained are detailed in section 4.5.

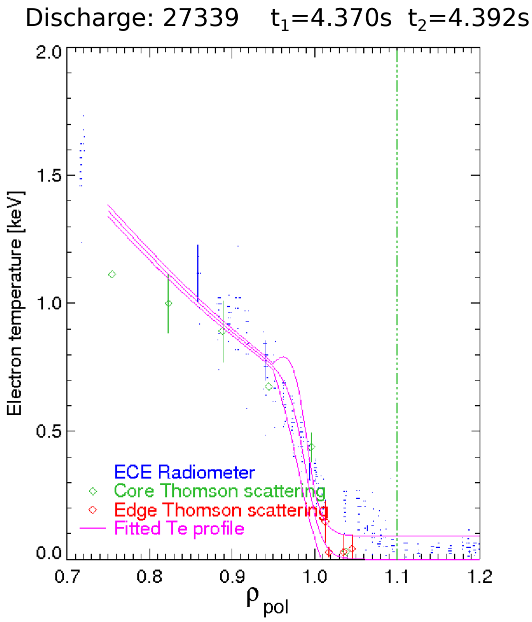

(a)

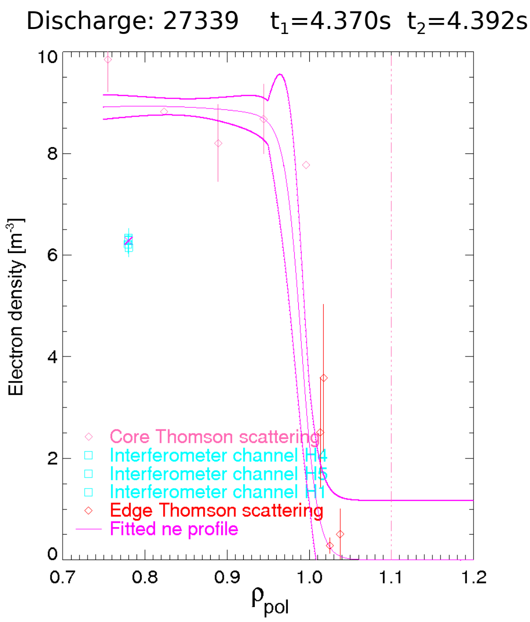

(b)

Figure 4.10. Fits to electron (a) temperature and (b) density measurements from $t = 4.370 - 4.392$s for $\rho_{pol} = 0.75 - 1.05$ for discharge 27339 used as CLISTE input.

4.4.3 Sample results for constrained CLISTE equilibria

In order to illustrate the steps involved in the above process, input data and results from an equilibrium reconstruction of ASDEX Upgrade discharge 27339 are presented in this section. Discharge 27339 is predominantly a H-mode or high energy confinement discharge, with a toroidal magnetic field of $B_t = -2.490$T and a plasma current of $I_p = 1.200$MA. All three primary available methods of external heating were applied during the course of this discharge, with 4.079MW ICRH power, 0.664MW ECRH power and 12.100MW NBI power employed at the time-point of interest.

In order to constrain the reconstruction of the total plasma pressure, measurements of the background kinetic profiles from core and edge Thomson scattering, ECE radiometer and interferometry diagnostics were included. An estimate of

Z_{eff} was also required in order to determine the ion density profile. The fits to these measurements were only utilised in the region around the plasma edge, from $\rho_{pol} = 0.75 - 1.05$. This was due to the fact that the fraction of the pressure contributed by fast particles in the core would be expected to be relatively large due to the significant amount of NBI and ICRH heating employed. Thus, the kinetic profiles are only reflective of the actual total pressure outside the plasma core region in this case, as the fast particle pressure at the edge is assumed to be negligible [80]. A consequence of this is that CLISTE equilibrium reconstructions can be used as an indicator of the plasma fast particle pressure as they include the total calculated plasma pressure which will vary from the core kinetic pressure in the presence of a large fast particle population [80]. No ion temperature data was available in this case so the assumption that $T_i = T_e$ was made. The fits to the electron temperature and density are shown in figure 4.10.

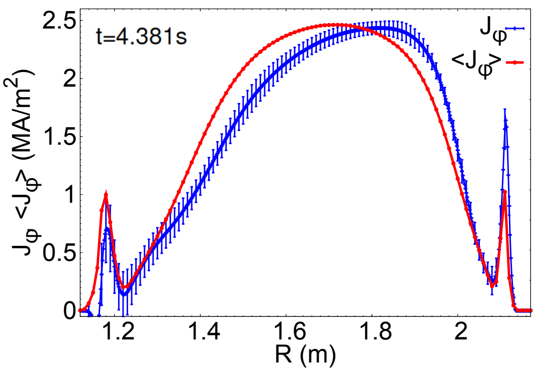

(a)

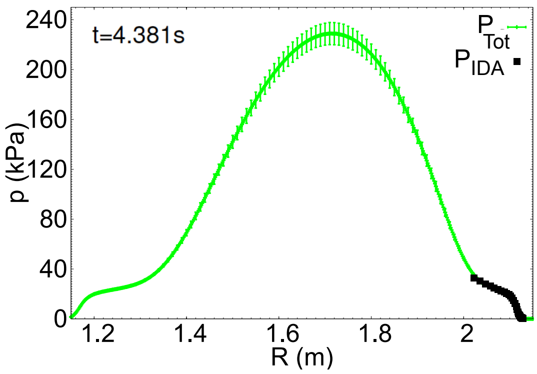

(b)

Figure 4.11. Magnetic midplane profiles for (a) reconstructed current density profiles (blue: local; red: flux surface averaged) and (b) reconstructed equilibrium pressure for discharge 27339 at $t = 4.381$s.

A clear steepening of the electron temperature and density profiles is visible in the region from $\rho_{pol} \approx 0.95 - 1.00$. This is known as the pedestal region and is indicative of the H-mode phase of a discharge, when the plasma energy and particle confinement is high. Following the methods described in section 4.4.1, the $q = 1$ surface is found to occur at $d_{mid} \approx 0.349$m, where d_{mid} is the magnetic mid-plane diameter of the flux surface at which the $q = 1$ surface is located. This information was then used to constrain the equilibrium reconstructions. Figure 4.11 shows the (a) reconstructed local and flux surface averaged toroidal current density and (b) reconstructed total pressure profile P_{Tot} and input edge pressure profile from IDA measurements for discharge 27339 at $t = 4.381$s, where the local toroidal current density J_Φ is plotted in blue and the flux surface averaged current density $\langle J_\Phi \rangle$ is plotted in red. The pedestals present in figures 4.10 (a) and (b) is clearly reproduced in figure 4.11 (b). The result of these high pressure gradients at the edge is the presence of large bootstrap current peaks.

This is due to the fact that the magnitude of the bootstrap current is directly proportional to the pressure gradient [77]. The rmse fit error for magnetic flux difference measurements $\langle dF \rangle$ and magnetic probe B_θ measurements $\langle dB \rangle$ are found to be 2.0mT and 1.7mT respectively. The corresponding errors, expressed as a percentage of the rms value of all the converted flux differences, are 1.9% and 0.6% respectively, indicating relatively low errors in the fits. As these constrained CLISTE equilibria take into account much more available experimental information than a magnetics only reconstruction, they provide a much more representative result for the flux surface geometry.

4.5 Results calculated using constrained CLISTE equilibria

4.5.1 RSAEs and BAEs

In this section, results for Alfvén eigenmode activity published in [81], calculated using modelled q-profiles from CLISTE, are discussed. The dark blue profile in figure 4.12 (a) shows a modelled q-profile obtained from an equilibrium reconstructed using CLISTE for ASDEX Upgrade discharge 25506 at $t \approx 0.45$s, while the other profiles are scaled versions of the initial q-profile, modelling its potential evolution in time. Figure 4.12 (b) shows the corresponding evolution of the continuum extrema for a reversed shear Alfvén eigenmode (RSAE) and beta-induced Alfvén eigenmode (BAE), calculated using LIGKA [48,81]. A minimum in the continuum located at $\rho_{pol} \approx 0.3$ initially moves downwards before a local maximum is formed with the appearance of a $q = 2$ surface in the plasma. This maximum then moves upwards as the local minimum in the safety factor profiles shifts downwards, causing the upward sweeping in frequency observed experimentally [81].

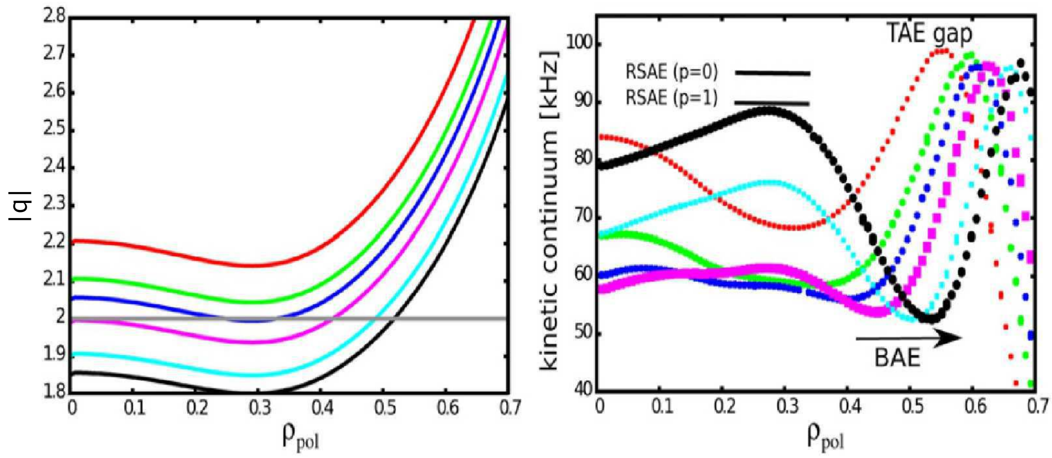

(a) (b)

Figure 4.12. (a) Expected safety factor evolution during discharge 25506 calculated using CLISTE. Note that only the magnitude of q is plotted. (b) RSAE and BAE continuum extrema evolution with safety factor profile beginning at $t \approx 0.45$s [81].

The formation of the $q = 2$ surface also results in a frequency continuum accumulation point forming at $\rho_{pol} \approx 0.4$, below which the BAEs sit. This accumulation point is observed to shift outwards with the outward radial movement of the $q = 2$ surface.

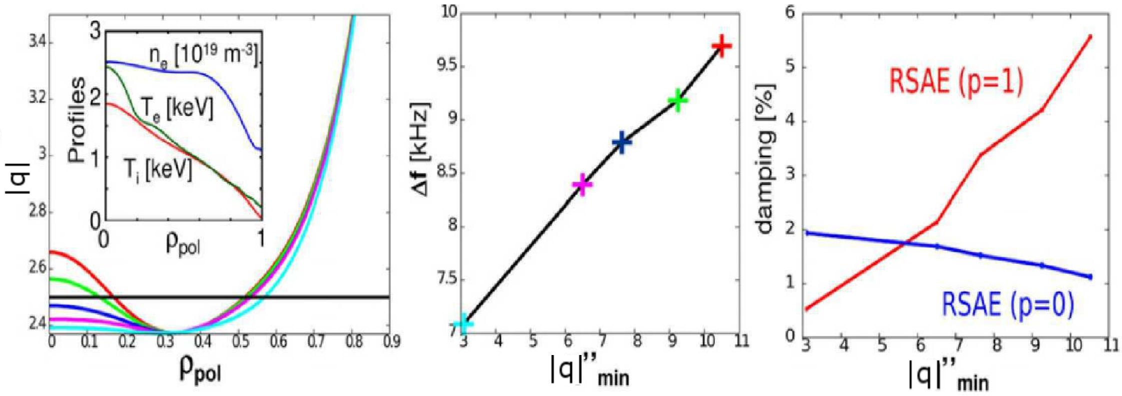

(a) (b) (c)

Figure 4.13. (a) Modelled safety factor profiles and background temperature/density profiles for discharge 25506. Note that only the magnitude of q is plotted. (b) Difference between lowest and first harmonics of RSAE with the second radial derivative of the q-profile at R_{qmin} (c) Damping rates for the lowest ($p = 0$) and first ($p = 1$) harmonic of an RSAE with the second radial derivative of the q-profile at R_{qmin} [81].

Whereas in figure 4.12 the shape of the q-profile was fixed and only q_0 was scaled, figure 4.13 shows the effects of the variation in the second radial derivative of the q-profile at the radial location of the minimum in the q-profile R_{qmin} on the frequencies of the 1st and 2nd harmonics of the RSAE as well as their damping rates. For the experimentally observed $\Delta f \approx 8$kHz, the damping rates of the two harmonics are approximately equal [81].

4.6 Numerical root-solver for low-frequency kinetic dispersion relation

4.6.1 Nyquist root-solver algorithm

The next step in the analysis procedure was to solve the kinetic dispersion relation 3.4.61 numerically using experimental data as input, and to compare the results with the experimentally observed mode behaviour. The kinetic dispersion relation describes a complicated physical system and its solutions are complex eigenfrequencies. The determination of these eigenfrequencies involves finding the roots of an analytic function. The description of how this is done follows those given in [82, 83]. After a numerical discretisation, the spectral problem of a system can be cast in the following general form [82, 83]

$$M(\omega)\vec{x} = 0 \tag{4.6.1}$$

where $\vec{x}$ is an eigenvector. Except for cases with simple dispersion relations, the matrix $M(\omega)$ is an intricate function of the eigenfrequency ω, which may take complex values in the presence of damping and/or destabilising mechanisms. Therefore, the spectral problem can usually not be reduced to the standard form $A\vec{x} = \lambda(\omega)B\vec{x}$, and the corresponding well-known methods of solution cannot be applied [82,83] . Nonetheless, one can always establish the characteristic equation for the eigenvalue problem

$$D(\omega) = detM(\omega) = 0 \tag{4.6.2}$$

Determining the eigenfrequencies thus reduces to solving for the zeros of the function $D(\omega)$ [82,83]. This is achieved using a FORTRAN 90 code, which solves for the roots of a complex polynomial equation, in this case the kinetic dispersion relation 3.4.61 [59]. All input data was read directly from ASDEX Upgrade shot-files, within which all relevant data describing the plasma is stored, as described in the next section.

4.6.2 Input data and assumptions

In order to solve the kinetic dispersion relation numerically, a number of background plasma profiles and parameters were required as input data. These included the background ion and electron temperature and density profiles (T_e, T_i, n_e and n_i), their gradients with respect to the magnetic mid-plane radius (∇T_e, ∇T_i, ∇n_e and ∇n_i), the toroidal magnetic field profile B_t, the safety factor profile q, as well as the plasma elongation κ, plasma major and minor radii (R_0 and a), and the toroidal and poloidal mode numbers n and m respectively. The kinetic temperature and density profiles were obtained through a combination of data from the IDA diagnostic and estimates of the dominant plasma impurity and its relative concentration and through the availability of Z_{eff} profiles for certain time-points [84]. The parameters concerning the plasma geometry were obtained from ASDEX Upgrade equilibrium reconstructions, and the mode numbers were obtained from Mirnov coil and in certain cases SXR measurements. Equilibrium reconstructions, constrained using kinetic and q-profile information, as described in the previous sections of this chapter, were generated using the CLISTE code [78] [12] in order to obtain more realistic safety factor profiles.

4.6.3 Numerical investigation of shear Alfvén wave dispersion relation in zero and finite toroidicity cases

We begin with the simplest case of a shear Alfvén wave, whose dispersion relation is given by $\omega(r) = k_{\parallel}(r)v_A(r)$. In a uniform plasma, the shear Alfvén wave is completely stable, with $Im(\omega) = 0$. However, when more complicated geometries are considered, this wave can couple with the magnetoacoustic wave, and the eigenfrequency can possess a non-zero imaginary component, which can lead to instability. The frequency continuum for a shear Alfvén wave in cylindrical geometry with dispersion relation $\omega(r) = k_{\|}(r)\upsilon_A(r)$ and with $k_{\|}(r) = (n - m/q(r))/R_0$ in the region of interest close to the $q = 1$ surface is given in figure 4.14 with the safety factor profile over-plotted. It is seen that at the position of the $q = 1$ surface the continuum frequency reduces to zero for modes with equal toroidal and poloidal mode numbers ($n = m$). This is due to the radial dependence of $k_{\|}$ on the safety factor profile.

The continuum frequency then proceeds to increase monotonically towards the plasma edge as $\omega(r) \propto k_{\|}(r) \propto 1/\sqrt{n_i}(r)$, both of which increase rapidly in this region. As a result, the continuum is completely closed in this low-frequency regime and any instabilities with frequencies coincident with it are rapidly dispersed due to phase mixing [29], as has been discussed in chapter 3. If we now introduce toroidal geometry, a modification to the dispersion relation is necessary due to poloidal mode number coupling resulting from the presence of finite plasma toroidicity. The term which describes this coupling is

$$\overline{k_{\|}} = \frac{k_{\|m}^2\upsilon_A^2 + k_{\|m+1}^2\upsilon_A^2 \pm \sqrt{(k_{\|m}^2\upsilon_A^2 - k_{\|m+1}^2\upsilon_A^2)^2 + 4\epsilon^2x^2k_{\|m}^2\upsilon_A^2k_{\|m+1}^2\upsilon_A^2}}{2(1-\epsilon^2x^2)} \tag{4.6.3}$$

Thus, the shear Alfvén dispersion relation, without kinetic effects, becomes

$$\omega^2 - \frac{k_{\|m}^2\upsilon_A^2 + k_{\|m+1}^2\upsilon_A^2 \pm \sqrt{(k_{\|m}^2\upsilon_A^2 - k_{\|m+1}^2\upsilon_A^2)^2 + 4\epsilon^2x^2k_{\|m}^2\upsilon_A^2k_{\|m+1}^2\upsilon_A^2}}{2(1-\epsilon^2x^2)}\frac{R_0^2}{\upsilon_{A0}^2} = 0 \tag{4.6.4}$$

where $x = r/a$. Figure 4.15 (a) shows the coupled continua for a single toroidal mode number and differing poloidal mode numbers, calculated using the kinetic dispersion relation numerical rootsolver. The continua characterised by different poloidal mode numbers no longer intersect in the coupled case. Instead, gaps open up in the continuum, centred approximately on the former crossing points of the continua. The size of these gaps is proportional to the inverse aspect ratio $\epsilon = r/R_0$ [36]. From theory, it is known that the dispersion curves of counter-propagating shear Alfvén waves, with poloidal mode number m and $m+1$ respectively, cross at the radius where the parallel wave-numbers have the same absolute value but opposite signs, or where $|k_{\|m}| = -|k_{\|m+1}|$ [35]. The safety factor at this location is given by $q(r) = \frac{m+1/2}{n}$. This can be seen in figure 4.15

(a) by comparing the location of the mode coupling with the corresponding value of the q-profile at these locations. For $n = 4$ and $m = n+1, n+2, ...$, the coupling is seen to occur at increasing rational q-surfaces $q = 9/8, 11/8...$ etc. Due to the fact that the continuum is no longer completely closed, it is possible for toroidicity induced Alfvén eigenmodes with discrete frequencies to be excited within the gaps resulting from the poloidal mode number coupling [35].

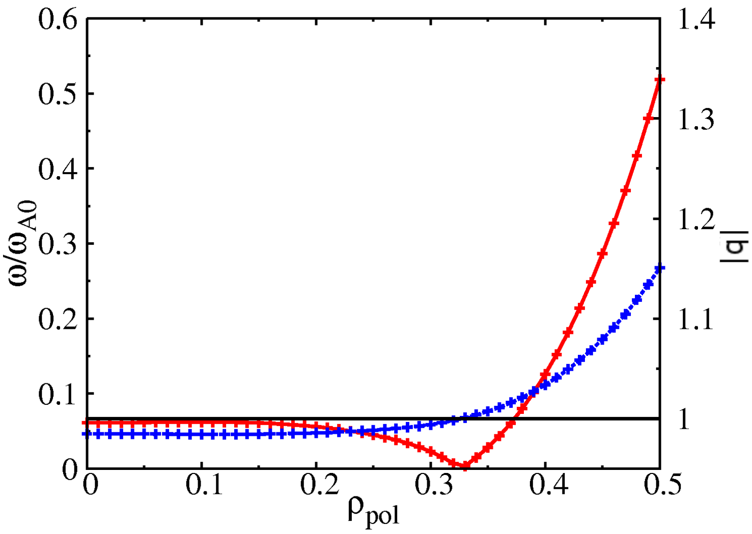

Figure 4.14. Sample shear Alfven wave frequency continuum (red) and overlaid magnitude of q-profile (blue).

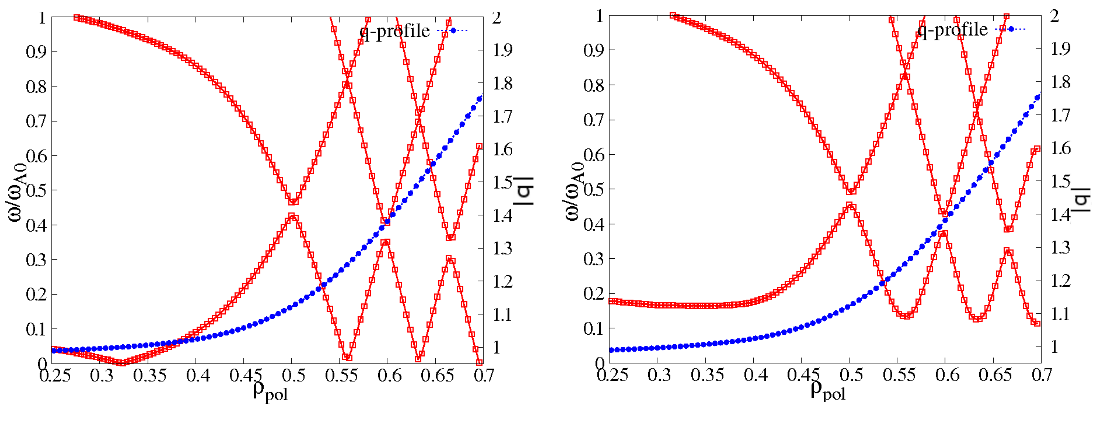

(a)

(b)

Figure 4.15. (a) Illustrative shear Alfvén continuum with toroidal coupling effects included (b) Illustrative Alfvén continuum with geodesic curvature and finite compressibility effects included, showing resultant beta-induced gap. The q-profile is overplotted for both (a) and (b).

4.6.4 Low-frequency kinetic dispersion relation

In order to investigate low-frequency Alfvén eigenmode activity in various plasma parameter regimes, a kinetic dispersion relation, which has been re-derived for the gyrokinetic model [42, 46–48, 60] underpinning the eigenvalue code LIGKA [48], was solved numerically. This is derived from the system of quasineutrality, gyrokinetic and gyrokinetic moment (GKM) equations, the details of which can be found in [48] and [42]. A discussion of the underlying physics has been given in the chapter 3 of this work and the equation is stated again here for convenience

$$\omega^2(1-\frac{\omega_{*p}}{\omega}) - \overline{k_\|}\frac{R_0^2}{\upsilon_{A0}^2} = 2\sqrt{\frac{2}{1+\kappa^2}}\frac{\upsilon_{thi}^2}{R_0^2\omega_{A0}^2}(-[H(x_{m-1})+H(x_{m+1})]+ \\ \tau[\frac{N^m(x_{m-1})N^{m-1}(x_{m-1})}{D(x_{m-1})}+\frac{N^m(x_{m+1})N^{m+1}(x_{m+1})}{D(x_{m+1})}]) \quad (4.6.5)$$

The term 'kinetic dispersion relation' is used in this work to distinguish it from the purely MHD dispersion relation, as presented in [37]. However, it has been demonstrated that the MHD limit can also be recovered analytically from the system of equations mentioned above [42, 46–48]. The inadequacies of the MHD model, which necessitate the move to a kinetic description, have also already been enumerated in chapter 3.

Specific kinetic effects appear in this analysis as, due to the inclusion of finite core ion compressibility, wave-particle resonances can now occur for modes with $\omega \approx \omega_{ti} \approx \omega_{*p}$ [42, 48]. ω_{ti} is the ion transit frequency, defined after equation 3.4.61. Diamagnetic effects become important when appreciable temperature and/or density gradients are present [42, 48, 59]. The kinetic dispersion relation is comprised of polynomials in $x_{m\pm1} = \omega/\omega_{ti}$ and $Z(x_{m\pm1})$, where $x_{m\pm1}$ is a measure of the degree of resonance between the modes and passing particles, and where $Z(x_{m\pm1})$ is the plasma dispersion function. Thus, specific kinetic effects enter into the kinetic dispersion relation and alter the value of the calculated continuum frequency and drive/damping, as well as allowing one to maintain the vanishing highest derivative terms in the system as in the ideal MHD case. In this work, when the term 'continuum' is used, it will refer to the continuum calculated using this kinetic dispersion relation as derived via the kinetic analyses in [48]

and [42].
If we begin with the cold plasma case where $\beta = 0$ then finite compressibility will not contribute to the dispersion relation. In this case, the continuum will have the same form as that presented for the purely shear Alfvén case in figure 4.14 . However, if we now assume a finite but low plasma β, a low-frequency gap is opened below the continuum. This gap cannot form without the coupling of the shear Alfvén wave to the sound wave. Thus, the inclusion of finite ion compressibility in the model, which allows the existence of the sound wave, is vital not just for the dynamics of the modes, but is a necessary condition for the existence of the low frequency gap to begin with.
Figure 4.15 (b) shows the effect of the form of the kinetic dispersion relation on the continuum. A lower gap is opened beneath the continuum, with an extremum in the continuum, known as the BAE continuum accumulation point, forming close to the $q = 1$ surface. Discrete modes can now be excited beneath this extremum. The fact that the continuum accumulation point is located close to the $q = 1$ surface is important for stability as here $k_{\|} \approx 0$. This condition corresponds to minimal line-bending which, if present, will act as a stabilising mechanism. Thus, the absence of line-bending facilitates the existence of potentially unstable modes.
The dependence of the continuum accumulation point frequency on the radial coordinate, in this case the normalised poloidal radius ρ_{pol}, can be understood by considering how the inclusion of finite-β effects alter the continuous spectrum, where β is determined primarily by the thermal velocity υ_{thi}. The kinetic dispersion relation contains different powers of ω_{*p} which are proportional to the toroidal mode number n and have a radial dependence from $T(\rho_{pol})$,$\partial T(\rho_{pol})/\partial \rho_{pol}$, $n(\rho_{pol})$, $\partial n(\rho_{pol})/\partial \rho_{pol}$ and $B(\rho_{pol})$. If we take the derivative of this equation with respect to the radial coordinate ρ_{pol}, $\partial \omega / \partial \rho_{pol} = 0$ will be no longer occur simply where $k_{\|} = 0$ as a result of these additional terms, and the BAE continuum accumulation point will be shifted radially by an amount dependant on the mode toroidal mode numbers.
The dependence of these modes on the toroidal mode number will be discussed further throughout the thesis. Specifically, it will be seen that there is a splitting

of distinct toroidal mode numbers by kinetic effects. This is different to that caused by toroidal rotation or non-linear frequency splitting due to strong energetic particle drive of one and the same toroidal mode. In the cases of the BAEs and acoustic Alfvén eigenmodes investigated in this work the resultant distinct eigenmodes will be referred to as distinct toroidal eigenmodes. This will be in reference to modes with different toroidal mode numbers separated by a finite frequency.

In this chapter, the experimental observations and numerical methods used in the analysis conducted in this work have been discussed. In the chapters that follow these observations and methods are applied to the investigation of low-frequency Alfvén eigenmodes under different experimental conditions at the ASDEX Upgrade tokamak.

Chapter 5

Investigation of beta-induced Alfvén eigenmodes (BAEs) and low-frequency acoustic Alfvén eigenmodes during ICRH phase of selected discharges

5.1 Overview of low-frequency Alfvén eigenmodes at ASDEX Upgrade

Low-frequency mode activity has been observed repeatedly in the frequency range between that of the kink instability and toroidicity-induced Alfvén eigenmode (TAE), which are typically observed at ASDEX Upgrade at $f \leq 10$kHz and $f \geq 150$kHz [64] respectively. These observations have been made during ICRH [48], ECRH and NBI [81] heated discharges. While the qualitative and quantitative behaviour of this low-frequency mode activity differs somewhat depending on the heating scheme employed, there is strong evidence that each of these modes is characterised by the possession of varying degrees of Alfvénic and acoustic polarisation [48]. In the present chapter, two different mode types are investigated. The first is the beta-induced Alfvén eigenmode (BAE), which is normally observed in the frequency range from $f \approx 50 - 90$kHz at ASDEX Upgrade [48, 59]. The second type of mode is observed in the beta-induced acoustic Alfvén eigenmode (BAAE) frequency regime, from $f \approx 10-45$kHz, and possesses a much higher degree of acoustic polarisation than the BAE, while still retaining a significant Alfvénic component [63]. An example of these modes, measured using a core directed line of sight of the soft x-ray diagnostic during successive sawtooth periods of discharge 25546, is shown in figure 5.1, where $nfft$ is the FFT window length and $nstp$ is the number of points.

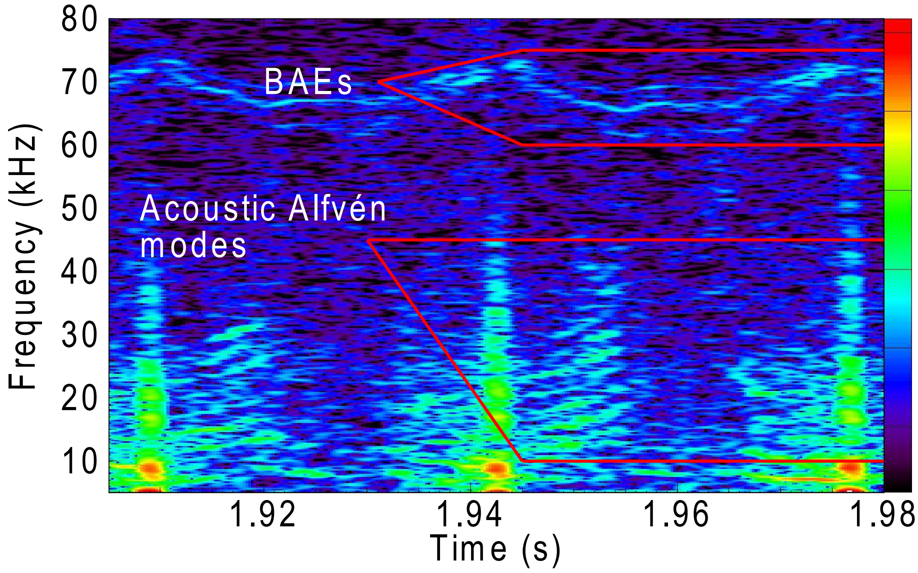

Figure 5.1. Low-frequency mode activity during two successive sawtooth cycles from $t \approx 1.91 - 1.98$s for discharge 25546, measured using core soft x-ray channel I51, with $nfft = 8192$ and $nstp = 512$, with a tangency radius of $\rho_{pol} \approx 0.244$.

As has been discussed in chapter 3, both of these types of modes occur in the low-frequency β-induced gap that develops beneath the Alfvén continuum as a result of geodesic curvature and finite ion compressibility effects [48, 57]. Unlike TAEs, where the gap is formed by the crossing of the dispersion curves of counter-propagating waves with adjacent poloidal harmonics, BAEs possess frequencies which lie beneath an extremum in the Alfvén frequency continuum, known as the continuum accumulation point. This forms close to integer q-surfaces where $k_{\|} \approx 0$, meaning that the stabilising effect of field line bending is minimised [46, 47]. In the case of the modes dealt with in this section, it is the $q = 1$ surface that is observed to be the rational surface of greatest importance. The lower frequency acoustic Alfvén eigenmodes are observed to occur close to

an extremum in a second frequency branch, obtained by solving the kinetic dispersion relation, that is also localised close to the $q = 1$ surface [59].
In section 5.2, observations of the main experimental parameters and low-frequency modes from three primarily ICRH heated ASDEX Upgrade discharges - 25544, 25546 and 25549 - are presented. Observations of BAEs and low-frequency acoustic Alfvén eigenmodes made using the soft x-ray and Mirnov coil diagnostics during selected sawtooth periods, and their observed dependencies on the evolution of the background temperature and density profiles are then presented in section 5.3. In section 5.4, a numerical analysis of the frequency evolution and damping/growth rate of both types of mode is conducted using a numerical rootsolver for the kinetic dispersion relation presented in chapter 3 and a fully numerical approach using the LIGKA code. A comparison between these numerical results and the experimentally observed mode frequencies is also presented in this section.

5.2 Overview of experimental observations during ICRH phase of discharges 25544, 25546 and 25549

5.2.1 Overview of primary experimental parameters

An analysis of ASDEX Upgrade discharges 25544, 25546 and 25549, all of which exhibit varying degrees of low-frequency Alfvén eigenmode activity, is commenced in this section.

Discharge	I_p (MA)	B_t (T)	n_e (m^{-3})	P_{ICRH} (MW)
25544	0.800	-2.490	7.37×10^{19}	4.330
25546	0.800	-2.488	6.41×10^{19}	4.395
25549	0.800	-2.490	6.35×10^{19}	4.377

Table 5.1. Main parameters of discharges 25544, 25546 and 25549

The same time-period, from $t = 1.700 - 2.500$s, is considered for all three discharges. During this period, these discharges all remain in the low-confinement or L-mode regime and attain moderate peak electron densities. While discharges 25544, 25546 and 25549 each experience periods of ECRH and NBI heating, only periods during which ICRH alone is utilised are investigated in this chapter. ICRH was present from $t = 1.068 - 4.296$s, $t = 1.076 - 4.296$s and $t = 1.070 - 4.696$s during discharges 25544, 25546 and 25549 respectively. The effects of ECRH on low-frequency mode behaviour are treated in chapter 6. Table 5.1 shows the main parameters of the discharges in question. The plasma current I_p, on-axis toroidal magnetic field strength B_t, peak electron density and ICRH power are similar in each case.

5.2.2 Observed core electron temperature and density evolution during ICRH phase

Discharges 25544, 25546 and 25549 each exhibit sawtooth activity of moderate intensity during the time periods considered, with sawtooth periods typically lasting from approximately $30 - 40$ms.

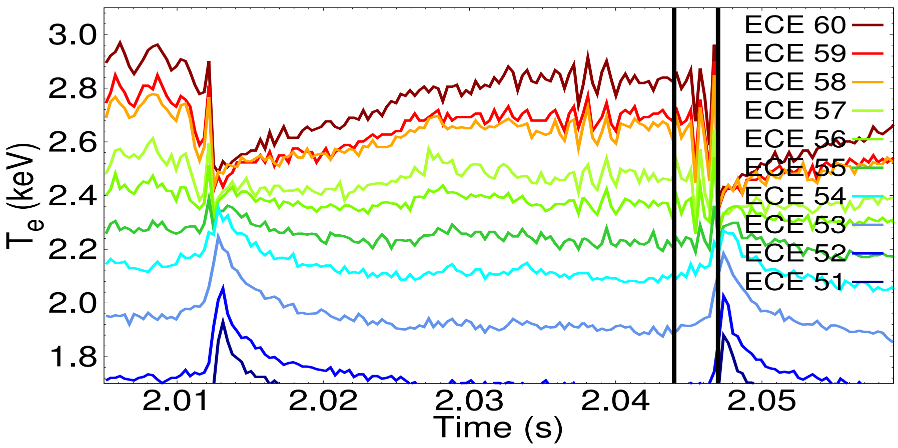

Figure 5.2. Evolution of core electron temperature, measured using channels of the ECE radiometer diagnostic covering the radial range $0.237 \leq \rho_{pol} \leq 0.383$, during a sawtooth period lasting from $t \approx 2.013 - 2.048$s for discharge 25546.

The character of a typical sawtooth period observed during discharge 25546 is illustrated in figure 5.2. In the case of the above discharges, the typical maximum drop in the electron temperature during a sawtooth crash, comprising the final few milliseconds of a sawtooth period and measured by the innermost ECE channel, varies from $\sim 0.3 - 0.4$keV. For the purposes of this analysis, the event referred to as the sawtooth crash comprises that period beginning with the appearance of sawtooth precursor oscillations and ending with a commencement in core electron temperature recovery, demonstrated by the region enclosed by the two vertical black lines in figure 5.2 to occur at $t \approx 2.044$s and $t \approx 2.047$s respectively.

Discharges 25546 and 25549 exhibit similar electron density and temperature evolution during the period considered from $t = 1.700 - 2.500$s. In the case of the electron density, this consists of a gradual increase in the core and edge values, as measured using the core H-1 and edge H-5 channels of the interferometry diagnostic. During discharge 25546 the core density increases from $n_e \approx 3.1 - 4.8 \times 10^{19}\text{m}^{-3}$, while in the case of discharge 25549 the increase is from $n_e \approx 2.9 - 4.3 \times 10^{19}\text{m}^{-3}$, as demonstrated in figure 5.3 and figures 5.4 (b) and (c) respectively. In figure 5.4, the electron temperature considered is that measured just prior to the commencement of sawtooth precursor activity, and is indicated by a dashed black line.

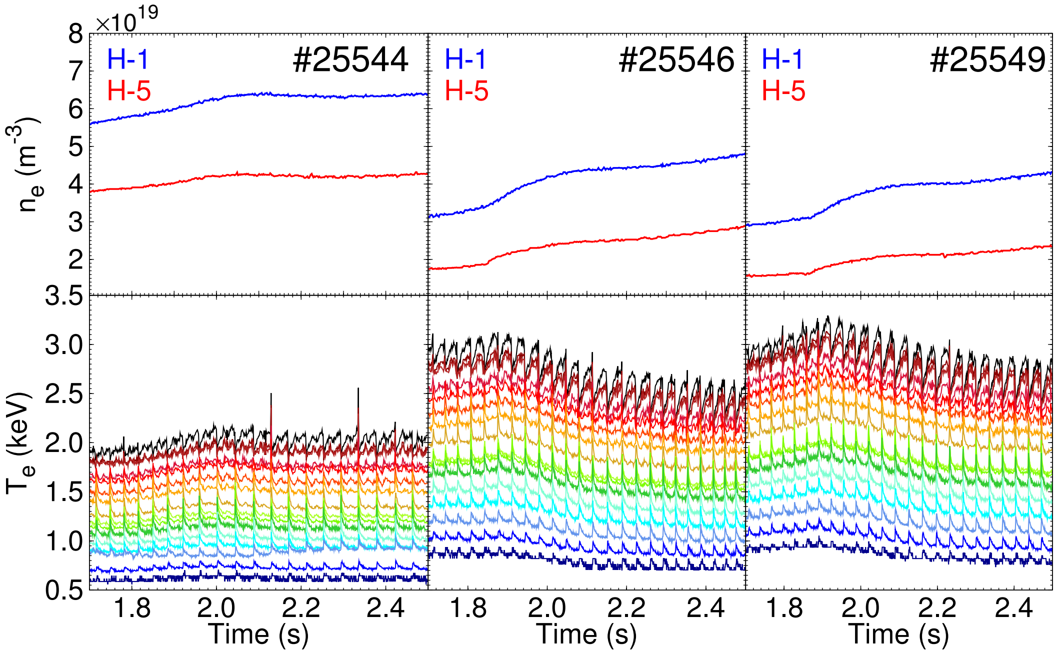

Figure 5.3. Time-traces of core and edge electron density, measured using interferometry, from $t = 1.700 - 2.500$s for discharges 25544, 25546 and 25549

Beginning at $t \approx 1.9$s during discharges 25546 and 25549, the maximum core electron temperature observed during a sawtooth period commences falling, as seen in figure 5.3. Prior to this point, this maximum core electron temperature exhibits a moderate increase. During discharge 25546 the local peak electron temperature is approximately 3.08keV at $t \approx 1.905$s, which is close to the time when the overall maximum core electron temperature observed during the time period from $t = 1.700 - 2.500$s is observed, as shown in figures 5.4 (b), while the equivalent measurement at $t = 2.494$s is approximately 2.58keV. Discharge 25549 exhibits a similar decrease in the overall core electron temperature after the early peak level at $t \approx 1.9$s, as seen in figure 5.3 and figure 5.4 (c).

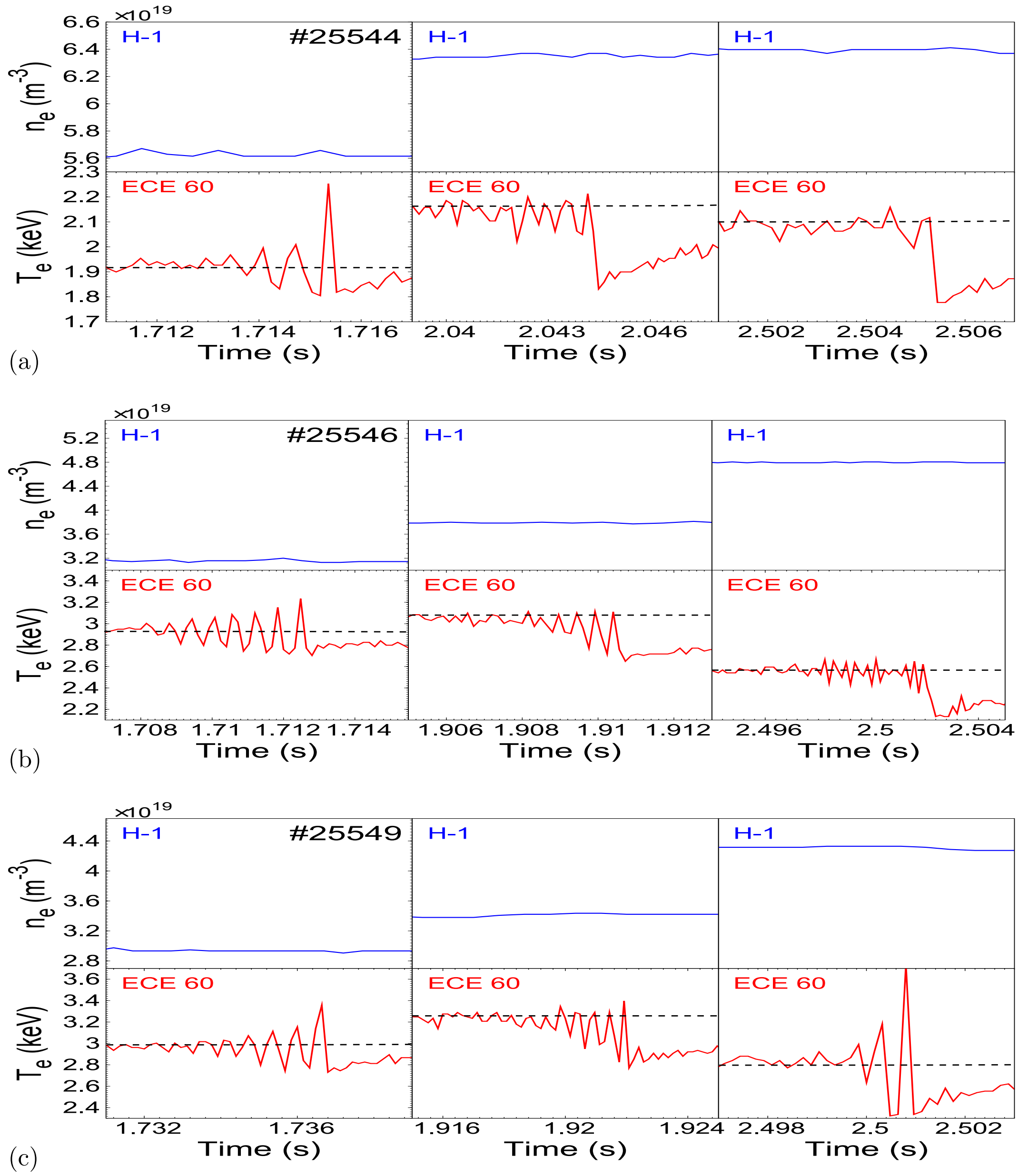

Figure 5.4. Time-traces of core electron temperature and density, measured using the ECE and interferomtery diagnostics, for selected time-slices during discharges (a) 25544, (b) 25546 and (c) 25549 respectively.

Discharge 25544 demonstrates a smaller change in the core electron density, increasing from $n_e \approx 5.6 - 6.4 \times 10^{19}\text{m}^{-3}$ during the period $t = 1.700 - 2.500$s, with the majority of this increase occurring at the beginning of this period from $t = 1.700 - 2.100$s, as seen in figure 5.3. Likewise, the maximum core electron temperature observed during the each sawtooth period of discharge 25544 does not vary greatly during the overall period from $t = 1.700 - 2.500$s. From figures 5.4 (a), it is seen that the innermost electron temperature measurement at $t \approx 2.038$s is approximately 2.16keV, via ECE, while that at $t = 2.501$s is approximately 2.10keV. The effects that these differences in the background density and temperature profile behaviour have on the mode evolution will be investigated experimentally and numerically in sections 5.3 and 5.4 respectively.

5.2.3 Overview of low-frequency mode observations during ICRH phase

As has been introduced in section 5.1, low-frequency mode activity in the frequency range from $10 - 90$kHz, consisting of BAEs and acoustic Alfvén eigenmodes, have been observed using the Mirnov coil and soft x-ray diagnostics during certain ASDEX Upgrade discharges. In this section, examples of these observations are presented for discharge 25546 and the overall trend in mode frequency during the time-slice from $t = 1.700 - 2.500$s is considered.

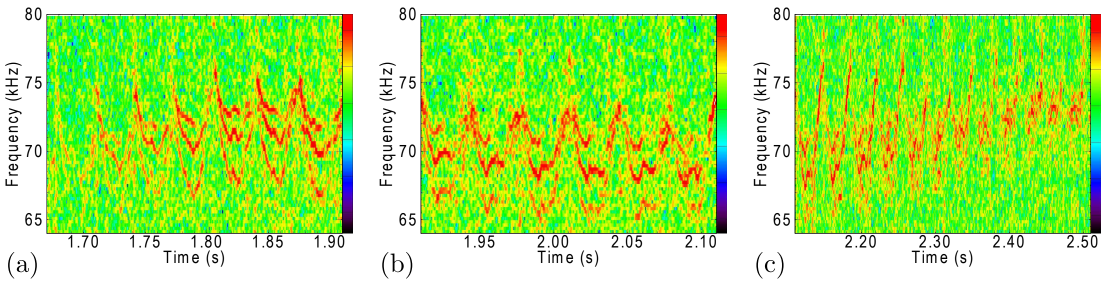

Figure 5.5. Spectrograms of BAE frequency evolution during discharge 25546 spanning the period from $t = 1.67{-}2.51$s, measured using line of sight $I50$ of the soft x-ray diagnostic, with $nfft = 8192$ and $nstp = 512$, with a tangency radius of $\rho_{pol} \approx 0.32$.

For discharge 25546, BAE activity in the frequency range $f \approx 65 - 80$kHz is first observed at $t \approx 1.65$s, as demonstrated in figure 5.5. These observations were made using line of sight I50 of the soft x-ray diagnostic, with a tangency radius of $\rho_{pol} \approx 0.32$. It is seen that the BAE activity is initially only faintly observed, increasing in amplitude as the discharge progresses. During discharge 25546, the BAE activity ends abruptly with the introduction of NBI heating at $t \approx 3.00$s. While the low-frequency mode activity returns subsequently at $t \approx 3.20$s, during the joint ICRH/ECRH phase, it is of a different character to that during the earlier exclusively ICRH phase, and is not observed as clearly using the Mirnov coil or soft x-ray diagnostics. The impact that the introduction of ECRH has on the low-frequency modes is treated in chapter 6. The character of the low-frequency mode activity also changes for discharge 25549 with the introduction of ECRH at $t \approx 2.50$s.

Taking the observed frequency of the central distinct toroidal eigenmode at the approximate median time-point of each sawtooth period as a reference frequency f_{ref} in figure 5.5, it is evident that this exhibits noticeable shifts throughout the period from $t = 1.700 - 2.500$s. From $t \approx 1.700 - 1.860$s, f_{ref} increases by $\sim$ 3kHz, before falling to its initial frequency of $f \approx 68$kHz by $t \approx 2.130$s. f_{ref} is then observed to increase steadily, increasing in frequency by $\sim$ 5kHz by the end of the time period considered at $t = 2.500$s. It is seen by comparing figures 5.3 and figure 5.5 that the reversal in direction of the time evolution of f_{ref} at $t \approx 1.9$s occurs at approximately the same time as that of the core electron temperature. Likewise, the change in direction of the frequency evolution at $t \approx 2.130$s appears to coincide approximately with a reduction in the rate of change of the electron temperature and density profiles, which decrease and increase respectively during the remaining period of the discharge. The effects that the background profiles have on the mode frequency evolution will be considered in detail in sections 5.3 and 5.4.

5.2.4 Observed low-frequency mode evolution during a selected sawtooth period

In this section, observations of low-frequency mode activity during a sawtooth period from $t \approx 1.945 - 1.980$s of discharge 25546 will be presented and an estimate for the radial location of the modes will be obtained using multiple lines of sight of the soft x-ray diagnostic.

BAEs BAE activity is observed during discharge 25546 using the Mirnov coil diagnostic and various lines of sight of the soft x-ray diagnostic. Figure 5.6 shows BAE activity, measured using three different ballooning coils of the Mirnov coil diagnostic during a sawtooth period from $t \approx 1.945 - 1.980$s. Using the method described in section 4.2, the BAE is found to have a toroidal mode number of $n = 3$.

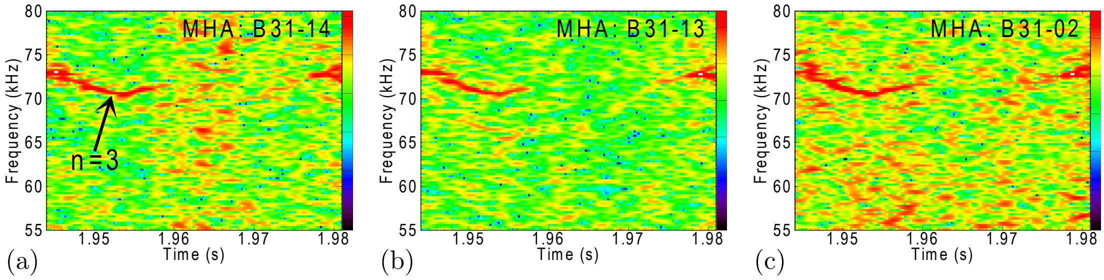

Figure 5.6. Spectrograms of $n = 3$ BAE, measured using Mirnov coils (a) B31-14 (b) B31-13 and (c) B31-02 during the sawtooth period from $t = 1.944 - 1.981$s of discharge 25546, with $nfft = 8192$ and $nstp = 512$.

By combining observations from multiples lines of sight of a given soft x-ray camera, an initial estimate of the mode radial localisation can also be made. Figure 5.7 shows observations of BAE activity, made using lines of sight I52-I49 of SXR camera G, during the sawtooth period from $t \approx 1.945 - 1.980$s for discharge 25546. In figure 5.7, the modes are most clearly observed for lines of sight I52, I51 and I50, which have tangency radii of $\rho_{pol} \approx 0.156, 0.244$ and 0.332 respectively. The mode amplitude measured using soft x-ray lines of sight I49, with a tangency radius of $\rho_{pol} \approx 0.419$, is significantly lower than that measured using the inner channels. This suggests that the modes are localised inside the region $\rho_{pol} \approx 0.419$. However, it should be noted that the SXR intensity at the tangency radii will depend on the structure of the eigenfunction, and without a definitive determination of this it is not possible to obtain the exact position of the modes [64].

Observations of BAE behaviour Considering the frequency evolution of the observed BAE activity in figure 5.7, a clear frequency separation between distinct toroidal eigenmodes is observed throughout the sawtooth period, suggesting modes with a range of toroidal mode numbers. Limiting the analysis to the four most prominent distinct toroidal eigenmodes, these are found, using Mirnov coil and soft x-ray measurements, to range from $n = 3 - 6$, in order of decreasing frequency. Considering the $n = 4$ case, it is observed to begin with an initial frequency of $f \approx 72$kHz at $t \approx 1.944$s. A maximum dip in frequency of approximately 5kHz is observed, and it exhibits a local minimum frequency of approximately 68kHz at $t = 1.954$s. The frequency of the $n = 4$ BAE then increases by approximately 1kHz over the next 4ms before essentially plateauing from $t = 1.958 - 1.965$s. Finally, the mode begins a reasonably steady increase in frequency before again reaching $f \approx 73$kHz at $t = 1.977$s. This behaviour, and its relation to the background profile evolution will be considered further in section 5.3.3 and numerically in section 5.4.

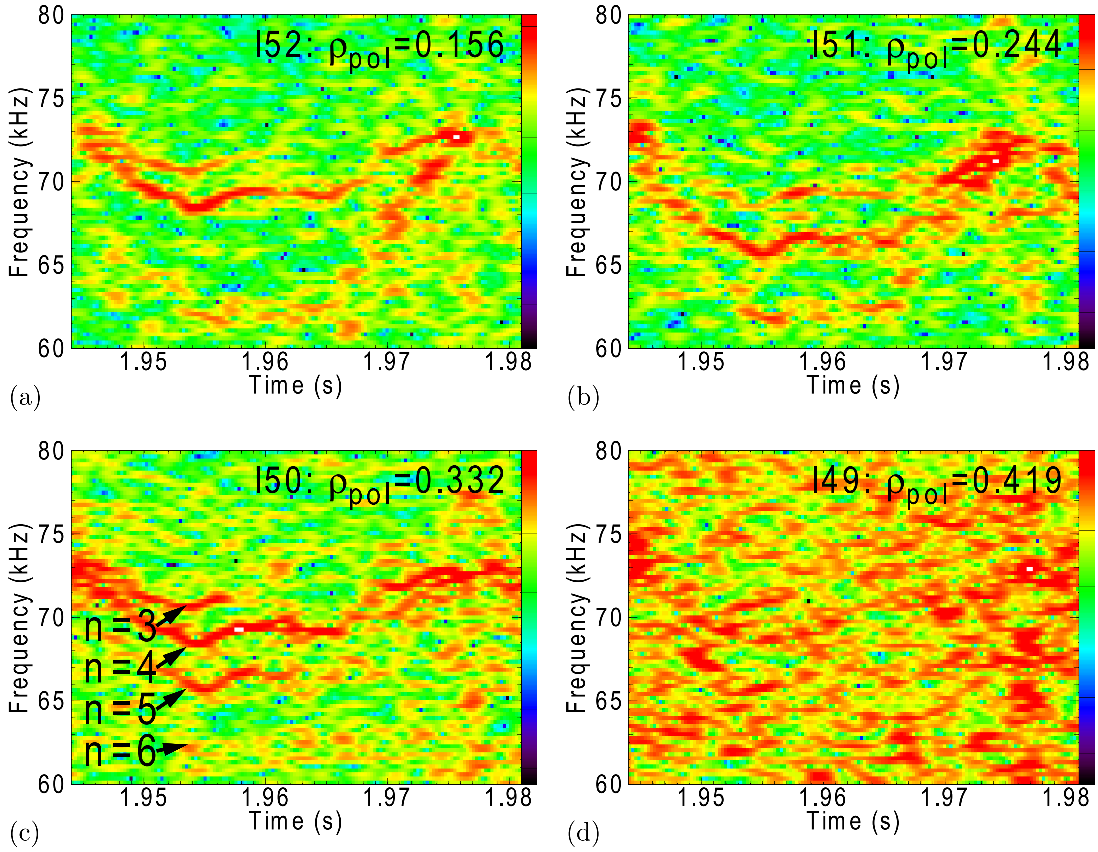

Figure 5.7. BAEs with toroidal mode numbers $n = 3 - 6$, measured using lines of sight $I52 - I49$ of the soft x-ray diagnostic, with $nfft = 8192$ and $nstp = 512$, during the period from $t = 1.945 - 1.980$s of discharge 25546.

Acoustic Alfvén eigenmodes Low-frequency acoustic Alfvén eigenmodes are also observed during the time period considered from $t \approx 1.945 - 1.980$s. These modes are observed in the frequency range from $f \approx 10 - 45$kHz, as seen in figure 5.8. As with the BAEs, information about the radial localisation of the acoustic Alfvén modes can be obtained by considering observations from different soft x-ray lines of sight. Figure 5.8 shows observations from soft x-ray lines of sight I52-I49. From these it is clear that the most clearly observed mode activity occurs for channels I52-I50, again indicating that the modes are likely to be core localised in the region inside $\rho_{pol} \approx 0.419$.

Observations of acoustic Alfvén eigenmode behaviour

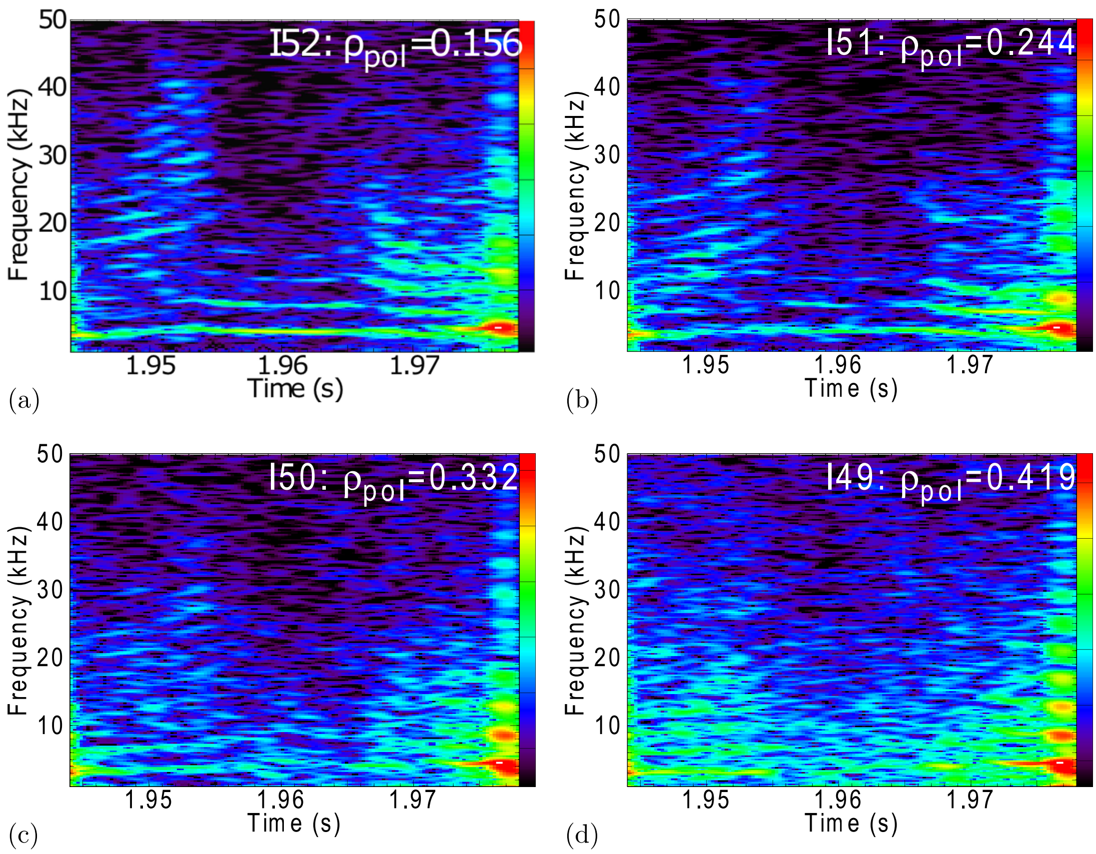

Figure 5.8. Spectrograms of acoustic Alfvén eigenmode frequency evolution, measured using lines of sight $I52-I49$ of the soft x-ray diagnostic, with $nfft = 8192$ and $nstp = 512$, during the period from $t \approx 1.945 - 1.980$s of discharge 25546.

As is the case for the BAEs, a frequency separation between distinct toroidal eigenmodes is observed for the acoustic Alfvén modes using channel I52, as seen in figure 5.8 (a). However, in this case no definitive mode number identification is possible. The acoustic Alfvén eigenmodes differ from the BAEs in two main respects. Firstly, while they are clearly observed in the initial and final $\sim$ 10ms of the sawtooth period, they are almost completely absent in the central portion of the period. Secondly, the evolution of their frequencies appears to run counter to that of the BAEs, increasing in the initial stage of the sawtooth period and decreasing in the later stage. These features of the acoustic Alfvén modes will be considered further experimentally in section 5.3.4 and numerically in section 5.4

Observed background electron and ion density and temperature profiles during selected sawtooth period

It has been mentioned in chapter 4 how the electron density and in particular the temperature can experience large variations during the course of a sawtooth period. In this section, the behaviour of the electron and ion density and temperature profiles during the sawtooth period from $t \approx 1.945 - 1.980$s will be considered. The background profiles for the electron population are obtained using the IDA diagnostic [23].

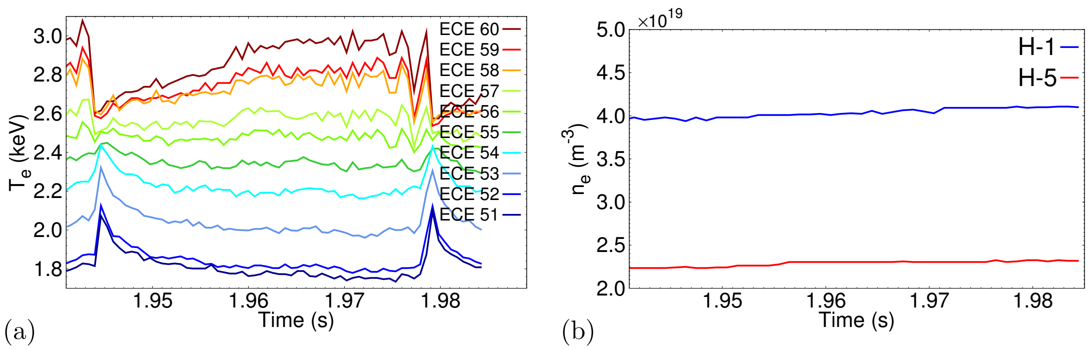

Figure 5.9. Electron (a) temperature and (b) density evolution over the course of a sawtooth period from $t \approx 1.945 - 1.980$s for discharge 25546 measured using channels of the ECE radiometer diagnostic covering the radial range $0.244 \leq \rho_{pol} \leq 0.438$ and interferometry respectively.

Ion density profiles were used when available by utilising estimates for the primary plasma impurity Z and the Z_{eff} radial profile, which was available for certain time-points at ASDEX Upgrade using the IDZ diagnostic [84]. No ion temperature data was available for the discharges considered in this section. Figure 5.9 shows the electron temperature and density evolution over the course of the sawtooth period from $t \approx 1.945 - 1.980$s for discharge 25546, as measured by core ECE channels and core and edge interferometry channels respectively.

As can be seen from figure 5.9 (b), the overall core electron density does not vary much over the course of the sawtooth period, increasing from $n_e \approx 4.0 \times 10^{19}\text{m}^{-3}$ at $t = 1.945$s to $n_e \approx 4.1 \times 10^{19}\text{m}^{-3}$ at $t = 1.980$s. Thus, when making a fit to the electron density, it was deemed reasonable to average the data over an entire sawtooth period. From figure 5.9 (a), the electron temperature measured by the six innermost ECE channels is observed to increase steadily from $t = 1.945 - 1.956$s, before jumping sharply from $t = 1.956 - 1.960$s and saturating somewhat from $t = 1.960$s until the end of the sawtooth period, when sawtooth precursor oscillations become pronounced from $t \approx 1.976 - 1.979$s.

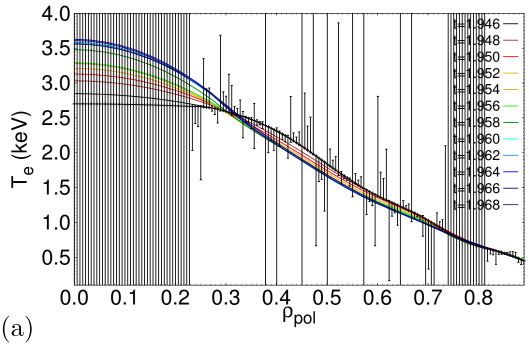

(a)

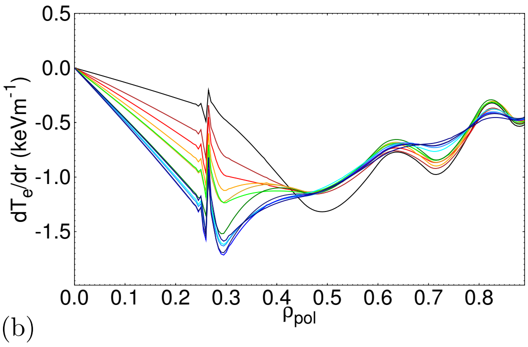

(b)

Figure 5.10. Fitted electron temperature (a) profiles and (b) gradients, from IDA diagnostic, for discharge 25546 from $t = 1.946 - 1.968$s.

Figure 5.10 (a) shows the evolution of the electron temperature profile, obtained using the IDA diagnostic, for the time period $t = 1.946 - 1.968$s for discharge 25546 with the corresponding profile gradients with respect to the outboard mid-plane radius shown in figure 5.10 (b). The profiles are averaged over three IDA measurements spanning 2ms. The profiles inside $\rho_{pol} \approx 0.25$ are obtained using a least square fit to the data. The gradient in the region from $\rho_{pol} \approx 0.30 - 0.43$ is observed to increase steadily during the early phase of the sawtooth period from $t = 1.946 - 1.964$s, before saturating and eventually decreasing again. The significance of this behaviour for the mode frequency evolution will be considered in detail in section 5.3. Figure 5.11 (a) shows the evolution of the electron density profile, obtained from IDA, during the same time-slice considered above, with the corresponding gradient evolution shown in figure 5.11 (c). The ion density profiles and their corresponding gradients are presented in figures 5.11 (b) and (d) respectively. While the profiles vary somewhat quantitatively over the course of each sawtooth period, the qualitative change is small in the region inside $\rho_{pol} \approx 0.419$ where the BAEs are expected to be localised. This is reflected by relatively small variations in the radial gradient compared to those observed in the temperature gradient.

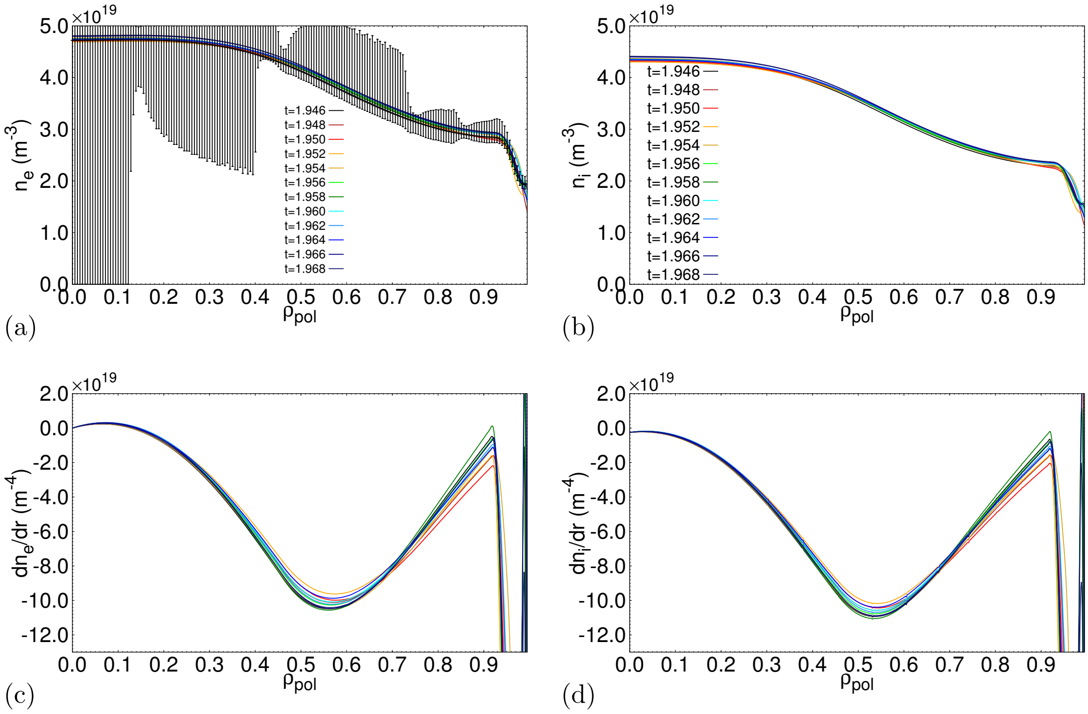

Figure 5.11. Electron and ion density profiles and gradients, from IDA and IDZ, for discharge 25546 from $t = 1.946 - 1.968$s.

This observation, in conjunction with the fact that Z_{eff} data is available with quite a low time resolution, suggests that variations in the ion density profile should not play a large role in interpreting the small scale behaviour of the modes.

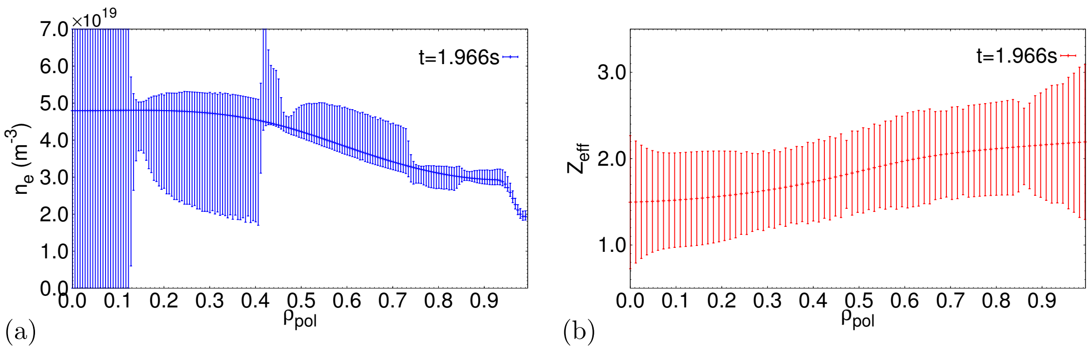

Figure 5.12. Electron density and Z_{eff} profiles, from IDA and IDZ respectively, for discharge 25546 at $t = 1.966$s.

This stems from the fact that the large uncertainties in the Z_{eff} profile, and hence in the n_i profile, as well as uncertainties in the core n_e value, will make the effect of the variation in the ion density on the mode behaviour difficult to quantify. Examples of these profiles are presented in figure 5.12. It can be seen in figure 5.12 (a) that sudden changes in the error bars of the IDA electron density profile occur in certain places. The ρ_{pol} values of these changes correspond to the tangency radii of the DCN interferometer channel lines of sight.

5.3 Investigation of low-frequency mode behaviour dependence on plasma background profiles close to $q = 1$ surface

For the purpose of this analysis, the low-frequency mode activity observed during four different sawtooth periods of discharge 25546 from $t = 1.65 - 2.50$s is considered. Period I consists of the mode activity during the first clearly observed sawtooth period in the ICRH only regime. Periods II and III represent periods of BAE and acoustic Alfvén eigenmode activity during typical sawtooth periods, occurring during the period from $t \approx 1.94 - 2.08$s. Period IV treats a slight variation in the behaviour of the low-frequency modes that occurs towards the end of a sawtooth period.

5.3.1 Determination of rational surface location from sawtooth inversion radius

It has been demonstrated that low-frequency Alfvén eigenmodes are predominantly radially localised close to low-order rational surfaces. The position of these rational surfaces in relation to gradients in the background plasma profiles plays an important part in determining the mode dynamics [48, 59]. Thus, a knowledge of the rational surface location is necessary for an accurate treatment of the modes. For this analysis, an investigation of the rational surface evolution over the course of the discharge was conducted, based on estimates of the electron temperature inversion radius during the sawtooth cycle, in order to facilitate the study of the mode evolution over the course of the discharges considered.

As has been described in section 4.4.1, the estimate for the radial position of the $q = 1$ surface is based on the point of intersection between the electron temperature profiles just prior to and following the sawtooth crash. This location, where the electron temperature is observed to remain approximately constant over the course of the sawtooth crash, is known as the sawtooth inversion radius. The time-point before the sawtooth crash was taken immediately prior to the observed commencement of sawtooth precursor activity in order to obtain a more representative estimate of the temperature at this stage of the sawtooth period, while the time-point after the crash was, when possible, taken at the next available time-point provided by IDA, usually approximately 1ms after the crash.

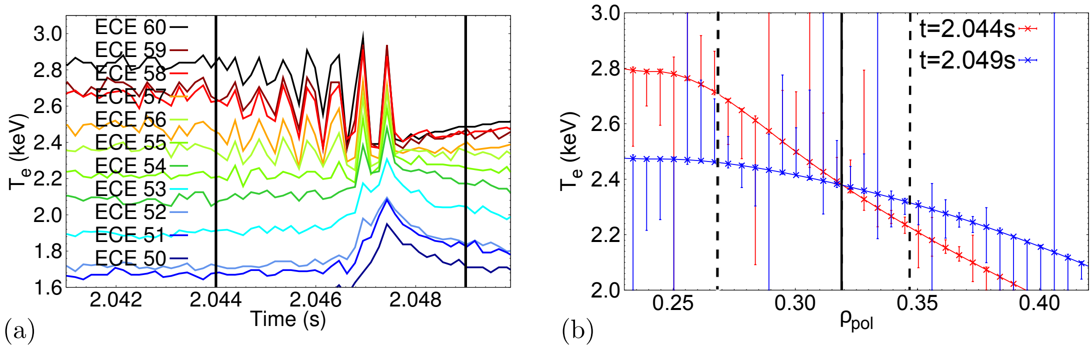

Figure 5.13. (a) Time traces of core ECE channels close to a sawtooth crash at $t \approx 2.048$s during discharge 25546 measured using channels of the ECE radiometer diagnostic covering the radial range $0.241 \leq \rho_{pol} \leq 0.460$. (b) Intersection between T_e profiles, from IDA, measured at $t \approx 2.044$s and $t \approx 2.049$s, indicated by solid vertical black line. Dashed vertical black lines indicate estimated error in $q = 1$ surface location.

An example of the time-points where this data was taken from is given in figure 5.13, with an estimate of $\rho_{pol} \approx 0.315$ obtained for the sawtooth inversion radius. The data was not averaged over multiple time-points due to the rapid variations in the temperature before and after the sawtooth crash. This investigation consisted of estimates for the approximate rational surface radial locations as well as the time-points at which these values were determined. In the majority of cases, the location of the rational surface was assumed to remain constant over the course of an individual sawtooth period. This assumption is based on observations made in [16]. In addition to providing q-profile constraints for the equilibrium reconstruction, this data also afforded a cursory comparison between the evolution of the experimentally observed mode behaviour and rational surface position. The evolution of the estimated $q = 1$ surface location over the time periods considered during discharges 25544, 25546 and 25549 is presented in figure 5.14. In the interest of clarity, whenever the term "$q = 1$ radial location" is used in this section, it will refer to the estimate obtained from the approximate sawtooth inversion radius. An estimate for the error in the $q = 1$ surface radial location was obtained by inspecting results for a fitted q-profile at $t = 2.066$s during discharge 25546, obtained using CLISTE, which included confidence bands for the q-profile and has similar parameters. For the period during discharge 25546 from $t = 1.60 - 1.90$s the $q = 1$ radial location can be seen to initially vary somewhat from $\rho_{pol} \approx 0.28 - 0.35$, as demonstrated in figure 5.14 (b). However, from $t \approx 1.90 - 2.90$s the location settles somewhat to values restricted to the range $\rho_{pol} \approx 0.29 - 0.34$.

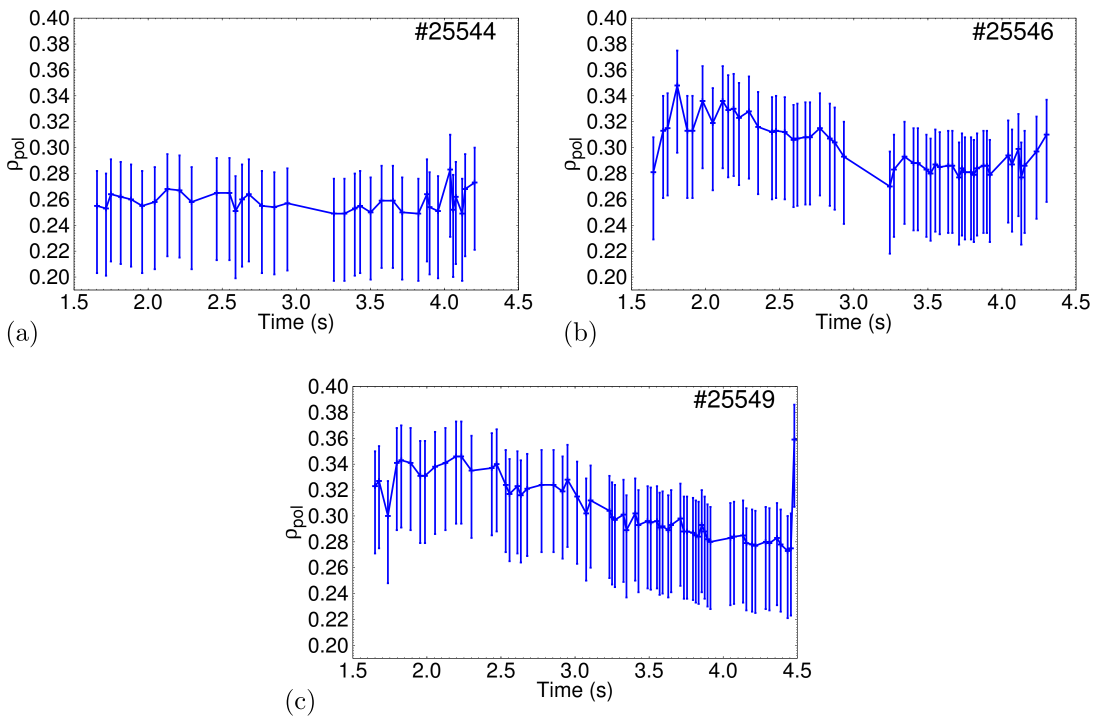

Figure 5.14. Time-traces of $q = 1$ surface location, estimated from sawtooth inversion radius, for discharges (a) 25544, (b) 25546 and (c) 25549 respectively.

This behaviour is also observed during discharge 25549 from $t = 1.60 - 2.50$s, with the $q = 1$ radial position remaining within the bounds of $\rho_{pol} \approx 0.32 - 0.35$, with the exception of that at $t = 1.737$s, which drops to $\rho_{pol} \approx 0.30$. Thus, the position of the $q = 1$ surface appears to remain quite constant over the course of the ICRH heating phases of discharges 25546 and 25549. For discharge 25544, the $q = 1$ surface location also appears to remain relatively constant, but possesses values substantially closer to the core, ranging from $\rho_{pol} \approx 0.25 - 0.27$ for $t \approx 1.6 - 4.0$s. These estimates for the $q = 1$ surface location were utilised as input constraints for CLISTE equilibrium reconstructions [78]. It can be seen from figure 5.14 (b) and (c) that the introduction of ECRH appears to have the effect of moving the $q = 1$ radial surface further inward. This will impact the background gradient that the eigenmodes experience.

5.3.2 Estimate of BAE radial localisation via coherence analysis

The theory underpinning the determination of the coherence between two experimental signals has been outlined in chapter 4. In this section, results for the coherence between Mirnov coil and soft x-ray signals during sawtooth periods I-VI of discharge 25546 are presented. In each case, a 10ms time window was considered, with 1024 Fast Fourier points used.

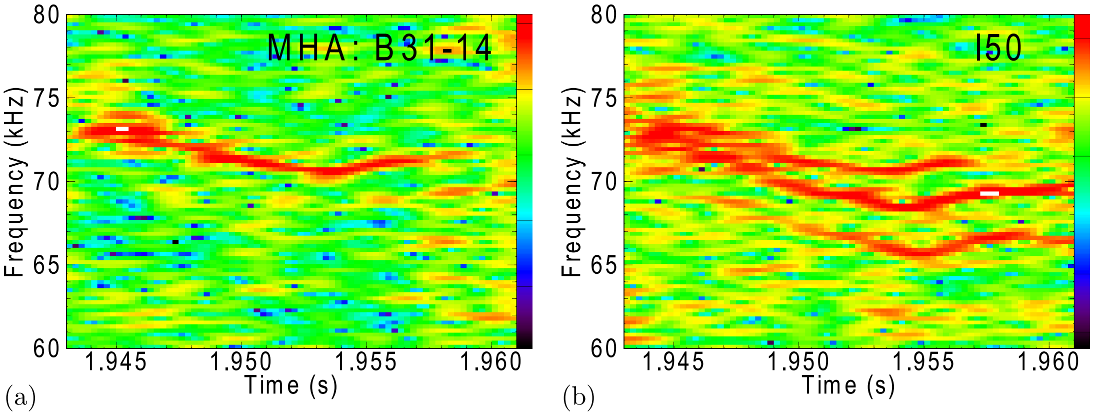

Figure 5.15. Spectrograms of BAE activity from $t = 1.943 - 1.960$s during discharge 25546, measured using (a) Mirnov coil B31-14 and (b) soft x-ray channel I50, with $nfft = 8192$ and $nstp = 512$.

The coherence levels between the signals from ballooning coil B31-14 and several soft x-ray lines of sight from the I and J cameras were determined, the results of which are shown in figure 5.16. The horizontal dashed line in each coherence plot represents the noise level, below which results are not reliable. Figure 5.15 shows example spectrograms for a BAE measured using Mirnov coil B31-14 and soft x-ray line of sight $I50$, from a time slice from $t = 1.945 - 1.955$s during discharges 25546, with the corresponding coherence plot shown in figure 5.16 (b). From figure 5.16, which shows results for various time-slices during discharge 25546, it can be seen that the highest level of coherence occurs for more core localised soft x-ray channels, such as $I52$ and $I50$.

As discussed in chapter 4, the coherence between the soft x-ray channels and the Mirnov coil signal exhibits a pattern of minima and maxima in the core region. Following the explanation given in [72], this is due to the line-integrated nature of the soft x-ray measurements. A helical mode with a single poloidal mode number m has a soft x-ray fluctuation profile with m minima and $m + 1$ maxima [72]. In spite of this feature, it can be inferred that the BAEs are localised in the region inside $\rho_{pol} \approx 0.5$, outside of which the level of coherence drops rapidly below the background noise level in most cases.

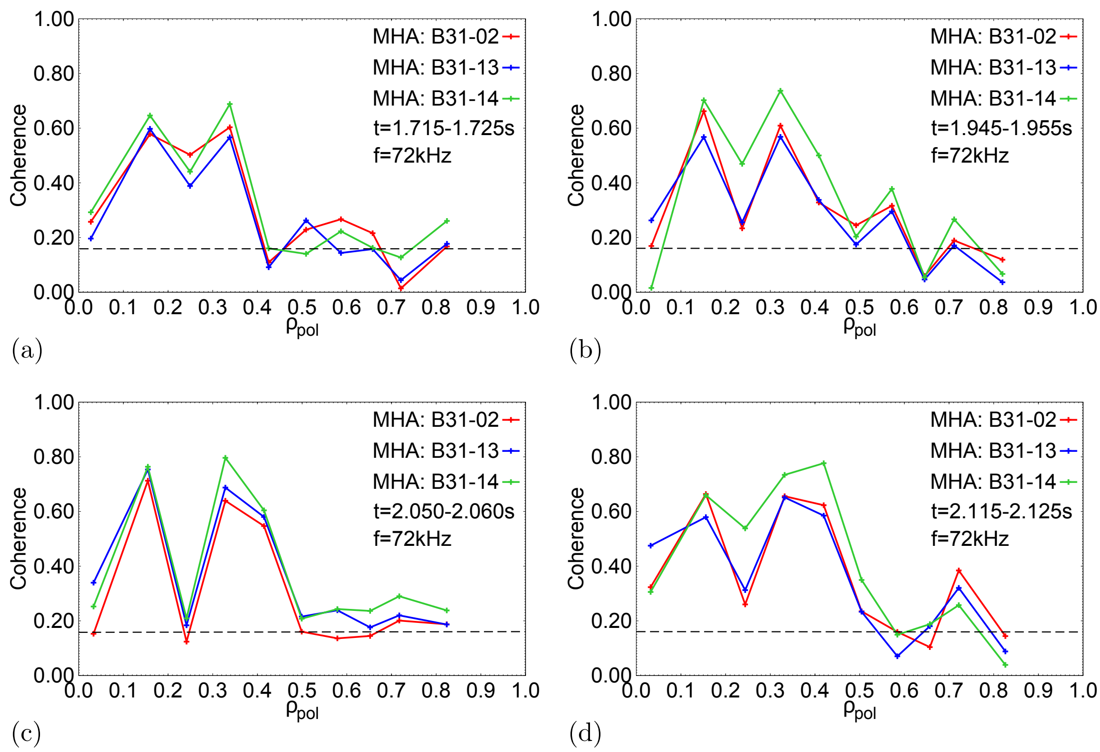

Figure 5.16. Coherence between Mirnov coils B31-14, B31-13, B31-02 and soft x-ray channels J53, I52-45 and I43 with lines of sight increasing radially, for the time periods specified in panels (a)-(d) during discharge 25546. The labelled magnetic coil signals are each combined with the soft x-ray channels specified above to generate a coherence plot.

It also appears that the highest level of coherence, normally observed using line of sight $I50$, which has a tangency radius of $\rho_{pol} \approx 0.33$, occurs close to the estimated $q = 1$ surface radial location, as expected from theory [48].

5.3.3 Comparison of BAE frequency evolution with background profile values at $q = 1$ surface during selected sawtooth periods

In this section, observations of BAE and acoustic Alfvén eigenmode frequency evolution, made using core channels of the soft x-ray diagnostic during periods I-IV, will be considered.

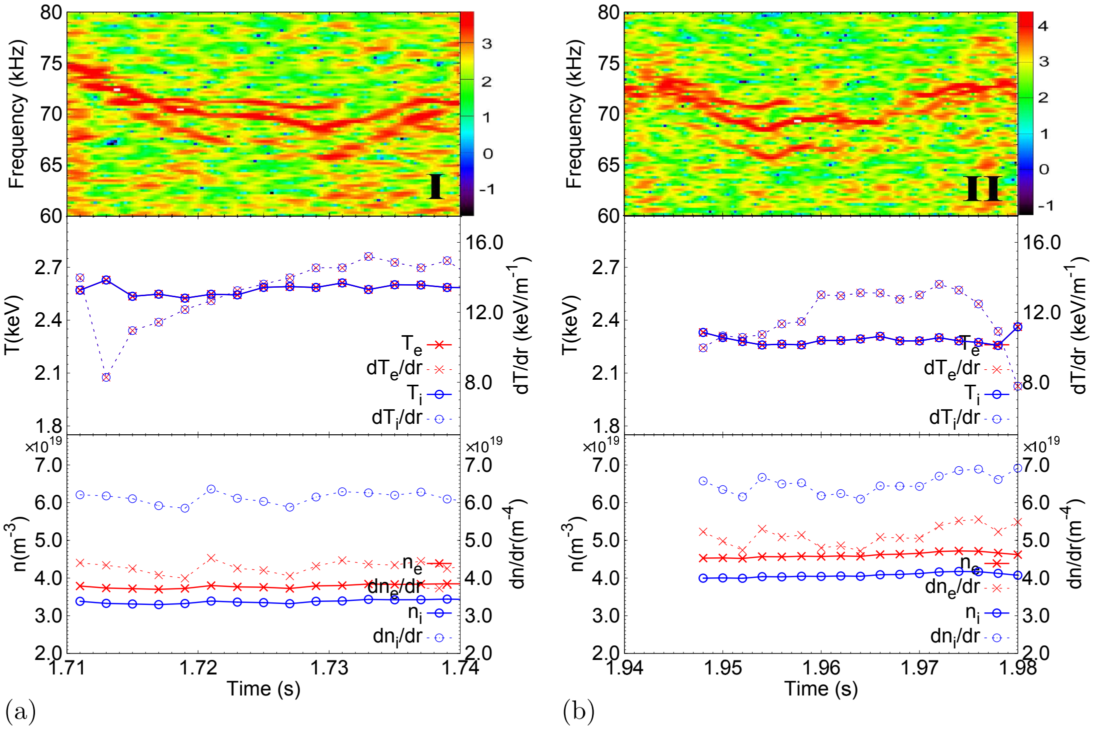

Figure 5.17. BAE frequency evolution from (a) $t = 1.710 - 1.740$s and (b) $t = 1.940 - 1.980$s during discharge 25546, measured using line of sight $I50$ of the soft x-ray diagnostic, with $nfft = 8192$ and $nstp = 512$, with a tangency radius of $\rho_{pol} \approx 0.32$ and the corresponding evolution in the background profiles at the $q = 1$ surface. Note that $T_i = T_e$ is assumed in this case.

The frequency behaviour of these modes will then be compared with that of the background temperature and density profiles at the $q = 1$ surface, as well as their gradients, during the corresponding time periods. As introduced in section 5.2.4, the BAE activity during these sawtooth periods is characterised by a prominent frequency separation between distinct toroidal eigenmodes, with the highest mode numbers experiencing the greatest frequency down-shift. As can be seen in figures 5.17 and 5.18, each mode is observed to drop markedly in frequency during the first $\sim 10 - 15$ms of the sawtooth period, before either reducing their rate of frequency decrease, plateauing in frequency, or rising slightly in frequency, depending on the individual case. The final $\sim 10 - 15$ms of these sawtooth periods is characterised by a swift recovery in the mode frequencies to values approaching those possessed at the beginning of the sawtooth periods.

In the case of discharge 25546, period I exhibits a clearly defined frequency separation between distinct toroidal eigenmodes with the most prominent eigenmode, the $n = 4$, having an initial frequency of approximately 74kHz, before dropping by approximately 6kHz by $t = 1.730$s, as seen in figure 5.17 (a). The $n = 4$ frequency is then observed to increase steadily from $f \approx 68$kHz to $f \approx 72$kHz from $t = 1.730 - 1.738$s.

While the $n = 4$ eigenmode in figure 5.17 (a) exhibits a monotonic decrease in frequency during its initial phase, the rate of decrease changes as the period progresses. From $t \approx 1.710 - 1.718$s, the decrease is approximately constant. However, from $t \approx 1.718 - 1.725$s, the rate of decrease falls substantially, before approximately resuming its previous rate of decrease from $t \approx 1.725 - 1.730$s. Periods II-IV exhibit similar initial frequency decreases, occurring from $t \approx 1.945 - 1.955$, $t \approx 2.048 - 2.053$s and $t \approx 2.117 - 2.124$s during periods II, II and IV respectively. However, these differ from period I in that they each then demonstrate a slight recovery in the mode frequency, before plateauing somewhat in frequency for the ~ 10ms after reaching this local frequency maximum. This frequency recovery is observed to begin at $t \approx 1.955$s, 2.058s and 2.125s for periods II, III and IV respectively. The final phase of frequency recovery occurs from $t \approx 1.730 - 1.738$s, $t \approx 1.966 - 1.978$s, $t \approx 2.068 - 2.078$s and $t \approx 2.134 - 2.150$s for periods I, II, III, and IV respectively, with the rates of increase differing somewhat in each case.

Having considered the observed BAE frequency behaviour, it is instructive to compare its evolution with that of the background temperature and density profiles at the estimated $q = 1$ surface location. It has been described in earlier sections of this work how the BAEs are found to be localised close to the $q = 1$ surface. Thus, the values of the background profiles close to this location are expected have an important impact on the BAE dynamics. While the ion and electron density can play an important part in determining the mode damping/growth rate and overall frequency, it can be seen from figures 5.17 and 5.18 that n_i and n_e do not vary much close to the $q = 1$ surface over the course of an individual sawtooth period. Thus, they are unlikely to play a role in the small scale mode frequency behaviour of interest in this section and their influence is not considered here. The first profile considered is the background electron temperature gradient. From figure 5.17 it can be seen immediately that the initial frequency decreases observed in periods I and II are accompanied by substantial increases in the electron temperature gradient in each case. For period I, during the frequency decrease from $t \approx 1.713 - 1.718$s, dT_e/dr increases from $\sim$ 8.0keVm^{-1} to $\sim$ 12.0keVm^{-1}. For period II, the frequency decrease from $t \approx 1.948 - 1.955$ is accompanied by an increase in dT_e/dr from $\sim$ 10.0keVm^{-1} to $\sim$ 11.0keVm^{-1}. Similar increases are observed during periods III and IV, as can be seen in figure 5.18 (a) and (b) respectively.

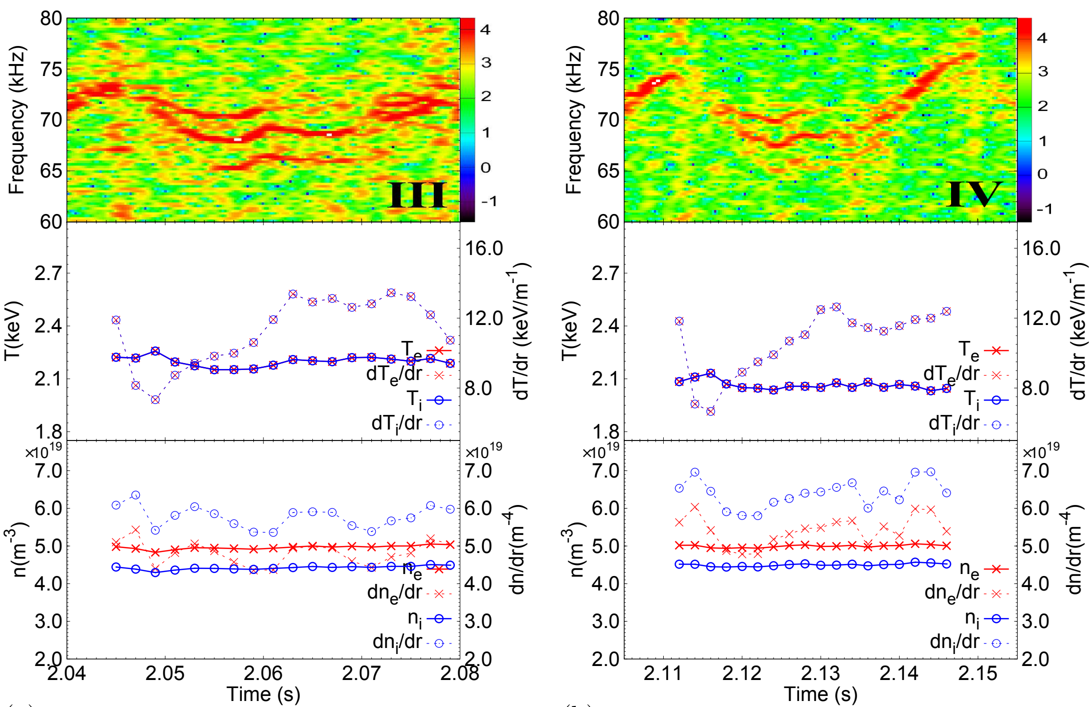

(a) (b)

Figure 5.18. BAE frequency evolution from (a) $t = 2.040 - 2.080$s and (b) $t = 2.105 - 2.155$s during discharge 25546, measured using line of sight $I50$ of the soft x-ray diagnostic, with $nfft = 8192$ and $nstp = 512$, with a tangency radius of $\rho_{pol} \approx 0.32$ and the corresponding evolution in the background profiles at the $q = 1$ surface. Note that $T_i = T_e$ is assumed in this case.

While the periods during which the gradients are observed to continue to increase persist somewhat beyond those of the frequency decreases in figures 5.17 and 5.18, the gradient evolution in time very clearly levels off for a moderately long phase shortly following the appearance of the frequency plateauing. This electron temperature gradient saturation is observed to begin at $t \approx 1.960$s, 2.063s and 2.131s for periods II, III and IV respectively. This similarity in the evolution of the BAE frequency and the background temperature gradient suggests a possible relationship between the two, and hence a relationship between the mode frequency and the diamagnetic frequency, which is proportional to the temperature and density gradients. This relationship will be investigated in detail in section 5.4.3.

Although the electron temperature gradient is not observed to saturate during the central phase of period I, neither does the mode frequency plateau in the same manner as observed in periods II-IV. Rather it decreases throughout the first $\sim$ 20ms of period I. In fact, the detailed behaviour of the most clearly observed eigenmodes is observed to respond to that of the electron temperature gradient. As seen in figure 5.17 (a), from $t = 1.713 - 1.719$s, the rise in dT_e/dr is quite high, and is accompanied by a period of relatively rapid frequency decrease. From $t = 1.719 - 1.730$s, dT_e/dr continues to increase, with the frequency continuing to decrease, albeit not quite as rapidly. While the electron temperature gradient does begin to decrease overall in the final $\sim$ 7ms of the sawtooth periods in question, the decrease is not as extended in time as the initial increase and does not fully account for the corresponding increase in mode frequency observed to occur. This is also the case for periods II-IV.

The evolution of the electron temperature itself at the $q = 1$ surface is also of interest. During all four periods, it is observed to initially decrease overall in value, before reaching a local minimum and then increasing in value for a brief period. This behaviour can be seen most clearly in figures 5.17 (b) and 5.18 (a). In the former case, T_e decreases from $t = 1.948 - 1.954$s, when it attains a minimum value. It then increases slightly until $t = 1.966$s before plateauing somewhat in the middle phase of the sawtooth period until $t \approx 1.972$s. This is reminiscent of the behaviour of the BAE frequency itself, which decreases, reaching a minimum at $t \approx 1.955$s, before increasing slightly and plateauing. Likewise, in the latter example, T_e decreases initially before reaching a minimum at $t \approx 2.057$s. This is followed by a local peaking in temperature at $t \approx 2.063$s, a plateauing and a gradual decrease thereafter. Again, this is similar to the observed frequency evolution, which decreases initially, before reaching a minimum close to 2.057s, a local maximum at $t \approx 2.060$s and plateauing somewhat thereafter until $t \approx 2.070$s. However, as with its gradient, a relationship between the electron temperature and the BAE frequency is not obvious in the final stage of the sawtooth periods.

As discussed previously, an accurate estimate for the electron and ion density in the core region is difficult to obtain. Thus, it is not reliable to infer conclusions about the observed mode frequency behaviour from the density gradient close to the $q = 1$ surface. As with other uncertain quantities introduced previously in this section, the potential impact of the density gradient on the mode evolution will be considered numerically in section 5.4.

5.3.4 Comparison of low-frequency acoustic Alfvén eigenmode frequency evolution with background profile values at $q = 1$ surface during selected sawtooth periods

The observed frequency behaviour of low-frequency acoustic Alfvén eigenmodes has been discussed in section 5.2.4, with the most interesting features being the clear frequency separation between distinct toroidal eigenmodes, the almost complete absence of strong mode activity during the central phase of a sawtooth period and a mode frequency that evolves in a manner opposite to that of the BAE. We begin by considering the initial phase of sawtooth periods II-IV. As can be seen in figure 5.19 (a), the various observed distinct toroidal eigenmodes exhibit moderate increases in frequency of up to approximately 5kHz over the period from $t \approx 1.945 - 1.955$s. This frequency behaviour is also observed in figure 5.19 (b), with a frequency increase of up to 5kHz observed during the period $t \approx 2.048 - 2.057$s. Conversely, in the latter phase of each sawtooth periods, the distinct toroidal eigenmodes are observed to decrease in frequency.

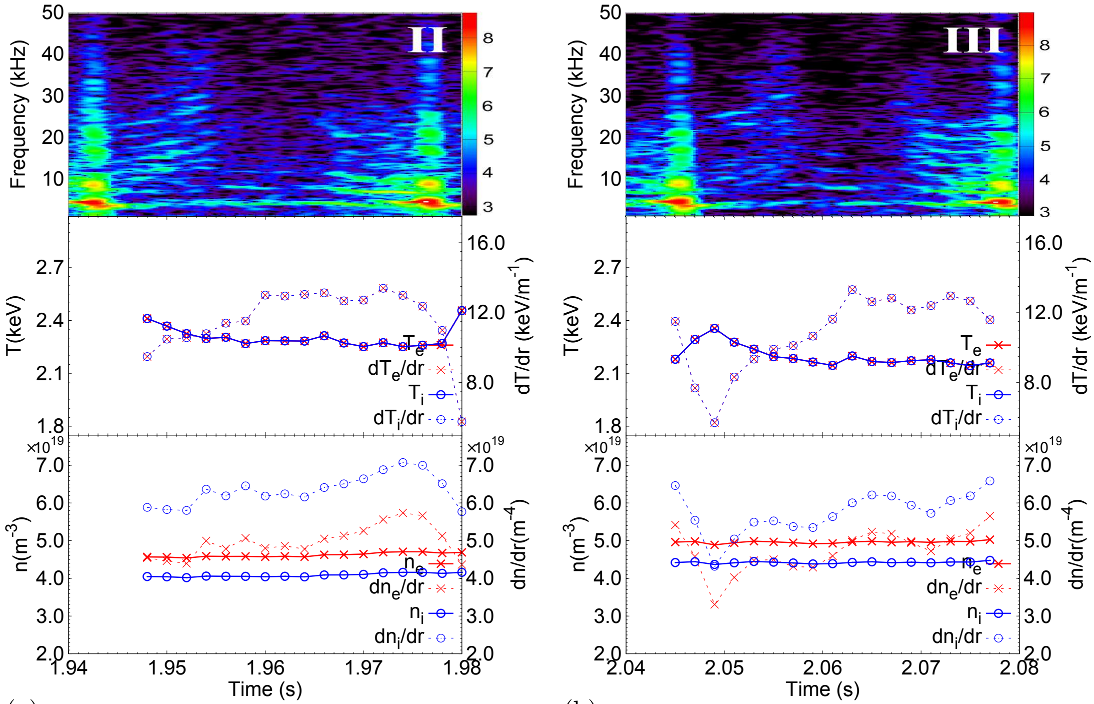

(a) (b)

Figure 5.19. Acoustic Alfvén eigenmode frequency evolution from (a) $t = 1.940 - 1.980$s and (b) $2.040 - 2.080$s during discharge 25546, measured using line of sight $I5I$ of the soft x-ray diagnostic, with $nfft = 8192$ and $nstp = 512$, with a tangency radius of $\rho_{pol} \approx 0.24$ and the corresponding evolution in the background profiles at the $q = 1$ surface. Note that $T_i = T_e$ is assumed in this case.

A clear observation of this behaviour is found in figure A.1, from $t \approx 2.134 - 2.147$s. For example, the eigenmode starting at $f \approx 15$kHz which appears at $t \approx 2.134$s in figure A.1 reduces approximately linearly to $f \approx 10$kHz. However, for periods II-IV, there is a distinct reduction in the observed mode activity during the central phase of the sawtooth periods, particularly for the higher frequency eigenmodes. For example, in figure A.1 mode activity essentially ceases above $f \approx 8$kHz at $t \approx 2.126$s and only recommences at $t \approx 2.134$s.

While for the BAEs, the mode frequency decreased with an increasing electron temperature gradient, the opposite is the case for the low-frequency Alfvén acoustic modes, which increase with dT_e/dr in the early phase of each sawtooth period. However, as with the BAEs, the acoustic Alfvén eigenmode behaviour late in the sawtooth periods cannot be fully accounted for by the electron temperature gradient behaviour. As has been seen, the electron temperature gradient does appear to decrease in the final $\sim$ 5ms of the sawtooth periods, but this does not account for the decrease in acoustic Alfvén eigenmode frequency which begins up to a further $\sim$ 5ms before this in the example given in figures 5.19 and A.1. Potential relationships between the background profiles and the acoustic Alfvén eigenmode frequency evolution will be considered in section 5.4.

5.3.5 Conclusions based on experimental observations

It is possible to draw some initial conclusions about the nature of the observed BAE and acoustic Alfén eigenmodes based on the experimental observations presented it sections 5.1-5.3. Firstly, it can be said with a high degree of certainty that these modes are both core localised. That is, they appear to exist in the region inside $\rho_{pol} \approx 0.5$. This is based on observations of the modes, made using the soft x-ray diagnostic, as presented in figures 5.7 and 5.8. These clearly indicate that the modes possess higher amplitudes in the core region, with this amplitude decaying as one observes regions further towards the plasma edge. This assertion is re-enforced by a coherence analysis of the BAEs, which indicates that the highest coherence between the Mirnov coil and soft x-ray signals occurs in the core region where $\rho_{pol} < 0.5$, as demonstrated by figure 5.16, with the level of coherence falling rapidly outside this region.

The low-frequency mode localisation also appears to be intimately tied to the position of low-order rational surfaces. In the case of the BAEs and acoustic Alfvén modes considered here, it is the $q = 1$ surface that is important. While this has already been established through theoretical analysis of the modes, it is important to study how this relationship operates experimentally. Evidence of this assertion is presented in figure 5.14, which shows clearly that the location of the $q = 1$ surface occurs in approximately the same region as that of the modes. Its position also remains quite constant during the period considered in this analysis from $t = 1.70 - 2.50$s, hovering between $\rho_{pol} \approx 0.31 - 0.35$ for discharge 25546.

Finally, strong links have been drawn between the low-frequency mode behaviour and the properties of the background temperature and density profiles in the region where these modes are proposed to be localised. It has been demonstrated in figure 5.10 that during the sawtooth periods considered, the electron temperature experiences its highest gradients in the region $\rho_{pol} \approx 0.30$. This again coincides with the region where the low-frequency modes are proposed to exist. Furthermore, in sections 5.3.3 and 5.3.4, evidence has been presented as to how the mode frequency evolution appears to be influenced by the electron temperature profile and its gradient close to the $q = 1$ surface.

All of the assertions made in this section will be tested in section 5.4 via a numerical analysis using the kinetic dispersion relation 3.4.61 and the LIGKA code, as well as through comparing these results with experimental observations of the low-frequency mode activity.

5.4 Numerical investigation of low-frequency mode continua during discharge 25546

5.4.1 Overview of numerical analysis procedure

In this section, an analysis of the BAE and acoustic Alfvén eigenmodes investigated in sections 5.1-5.3 will be conducted numerically. Results for tokamak plasma equilibria reconstructed using the CLISTE code, for use in the subsequent numerical analysis of the low-frequency modes, are presented in section 5.4.2. From these equilibrium reconstructions, realistic q-profiles are also obtained for use in the local Alfvén continuum analysis. Section 5.4.3 presents numerical results for the evolution of the BAE continuum accumulation point and continuum damping/growth rate over the course of several periods of discharges 25546. These results are obtained by solving the kinetic dispersion relation, given by equation 3.4.61, using a numerical rootsolver, the theory underpinning which is outlined in section 4.6. This is followed in section 5.4.4 by an equivalent analysis for acoustic Alfvén eigenmodes. In these two sections, the experimental observations of BAE and acoustic Alfvén eigenmodes from sections 5.1-5.3 are compared with numerical results from the complex root-solver, and with results obtained from LIGKA, as introduced in section 3.4.3.

5.4.2 CLISTE equilibrium reconstructions

Input data for CLISTE equilibrium reconstructions The theory underpinning, the implementation of, and the input and output data utilised for the CLISTE equilibrium reconstruction code have been presented in section 4.4.2.

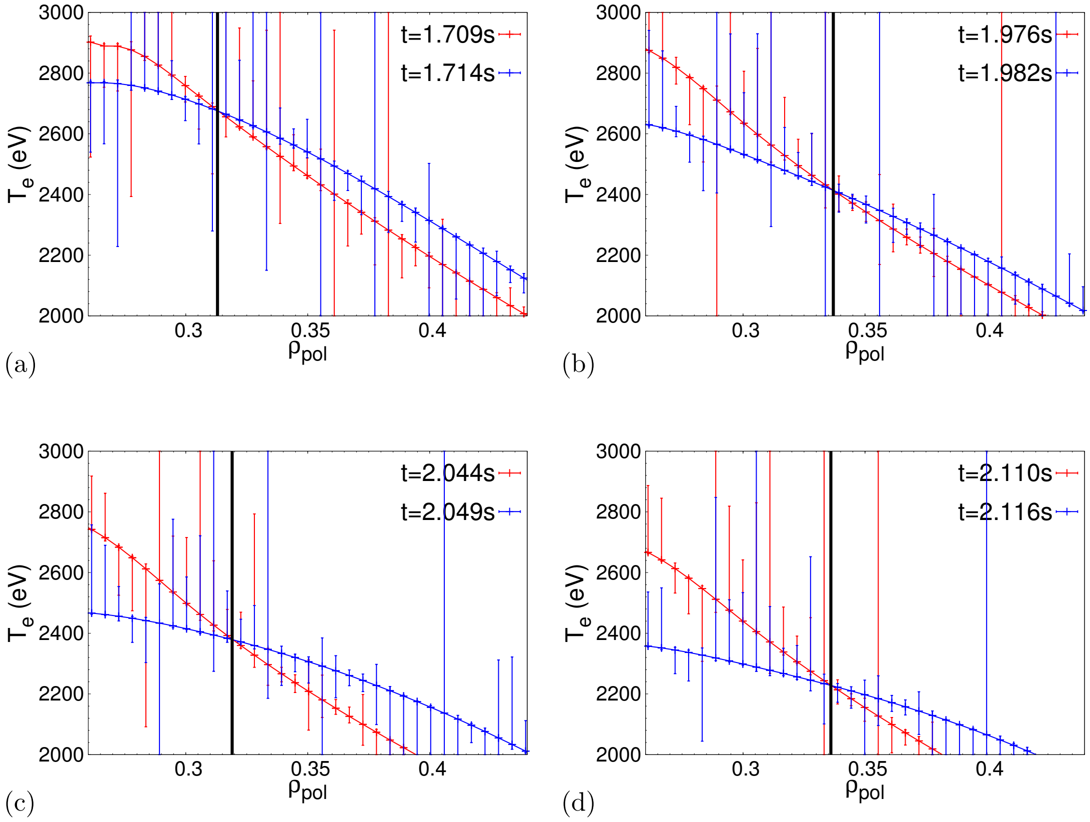

Figure 5.20. Intersection between electron temperature profiles before and after sawtooth crashes at $t \approx 1.709$s, $t \approx 1.979$s, $t \approx 2.048$s and $t \approx 2.115$s. In each case, the estimate for the sawtooth inversion radius, and hence the $q = 1$ surface location, is indicated by a vertical black line.

In this section, details of the input data used in the numerical analysis of discharge 25546 are presented. As has been introduced in section 5.3, four different time periods are considered in the analysis of discharge 25546 during the ICRH only phase. These are $t = 1.711 - 1.745$s, $t = 1.946 - 1.984$s, $t = 2.045 - 2.018$s and $t = 2.110 - 2.154$s and consist of the first sawtooth period exhibiting typical low-frequency mode activity during discharge 25546, two periods exhibiting typical BAE and acoustic Alfvén eigenmode behaviour and one period exhibiting a variation in the BAE behaviour at the end of the sawtooth cycle respectively.

In order to reconstruct a realistic equilibrium for each of these periods, it was necessary to select appropriate time points that best reflected the state of the plasma during the sawtooth periods, where the most reliable experimental data was available. The times selected for the equilibrium reconstructions, designated $t_{eq1} - t_{eq4}$ for the four periods respectively, were $t_{eq1} = 1.716$s, $t_{eq2} = 1.966$s, $t_{eq3} = 2.066$s and $t_{eq4} = 2.120$s. These time-points were chosen due to the availability of Z_{eff} radial profile data at or close to each one . For each of the equilibrium reconstructions, an estimate for the $q = 1$ surface radial location was obtained, using the methods presented in section 5.3.1.

As the location of the $q = 1$ surface was assumed to remain constant throughout each sawtooth period [16], the estimate for it closest in time to the relevant t_{eq} was used for each equilibrium reconstruction. From figure 5.20 it can be seen that for $t_{eq1} - t_{eq4}$, the sawtooth inversion radii, and hence under our previous assumption the $q = 1$ surface locations, occur at $\rho_{pol} \approx 0.313$, $\rho_{pol} \approx 0.336$, $\rho_{pol} \approx 0.319$ and $\rho_{pol} \approx 0.336$ respectively. These estimates were then converted to flux surface mid-plane diameter measurements and used as q-profile constraints for the CLISTE equilibrium reconstructions. It was then necessary to input the electron and ion temperature and density profiles to act as further constraints on the equilibrium reconstruction. The electron temperature and density profiles were obtained from the IDA diagnostic [23]. As no ion temperature data was available for discharge 25546, the assumption that $T_i = T_e$ was made. The estimate for the ion density profile was based on the dominant impurity Z_{imp}, assumed to be carbon or $Z_{imp} = 6$ in this case, and Z_{eff} radial profiles, obtained from the IDZ diagnostic [84].

Examples of output of CLISTE equilibrium reconstruction Utilising the CLISTE code, in combination with the input data described in section 4.6.2, reconstructions of the plasma equilibrium at $t_{eq1} - t_{eq4}$ were obtained. In each case, 27 points on the background temperature and density profiles were used as input, these points being equally spaced in the core region and grouped closely together towards the plasma edge in the region starting approximately where $R \approx 2.08$m. This spacing pattern was implemented to aid the fitting process towards the plasma edge. Two important outputs of the equilibrium reconstruction procedure included radial estimates of the local toroidal current density $J_\Phi(R)$, flux surface averaged toroidal current density $\langle J_\Phi(R)\rangle$ and the total plasma pressure $P_{Tot}(R)$ profiles, as well as $\pm 1\sigma$ confidence bands for $J_\Phi(R)$ and $P_{Tot}(R)$.

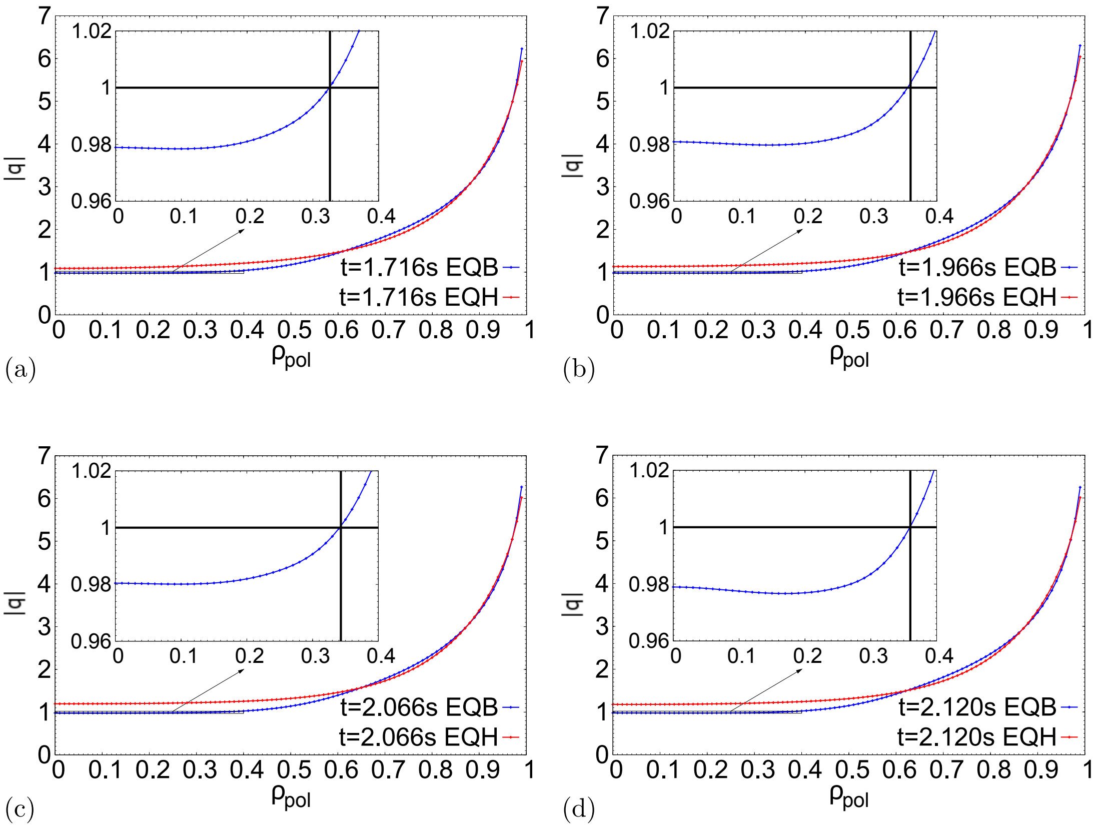

Figure 5.21. Comparison between safety factor profiles recovered using magnetic and coil current data only (EQH) and with the addition of background kinetic profile and a rational surface constraint (EQB) for discharge 25546. Note that only the magnitude of the safety factor profiles is plotted.

Examples of these profiles for $t_{eq1} - t_{eq4}$ are shown in figures A.3 and 5.22 respectively. Upon comparing these profiles with the example from discharge 27339 given in figure 4.11 of section 4.4.3, the qualitative differences in the profile behaviour are immediately apparent. While the figure 4.11 (a) exhibits pronounced peaks in the local and flux surface averaged edge toroidal current density, these peaks are essentially absent in figure A.3. Similarly, figure 4.11 (b) possesses a distinct pedestal in the pressure in the edge region which is not observed in figure 5.22 (b). This pedestal is a characteristic of H-mode or high confinement regime discharges like 27339, where the steep pedestal leads to a high bootstrap current in the edge region, explaining the strong peaks in the edge toroidal current density.

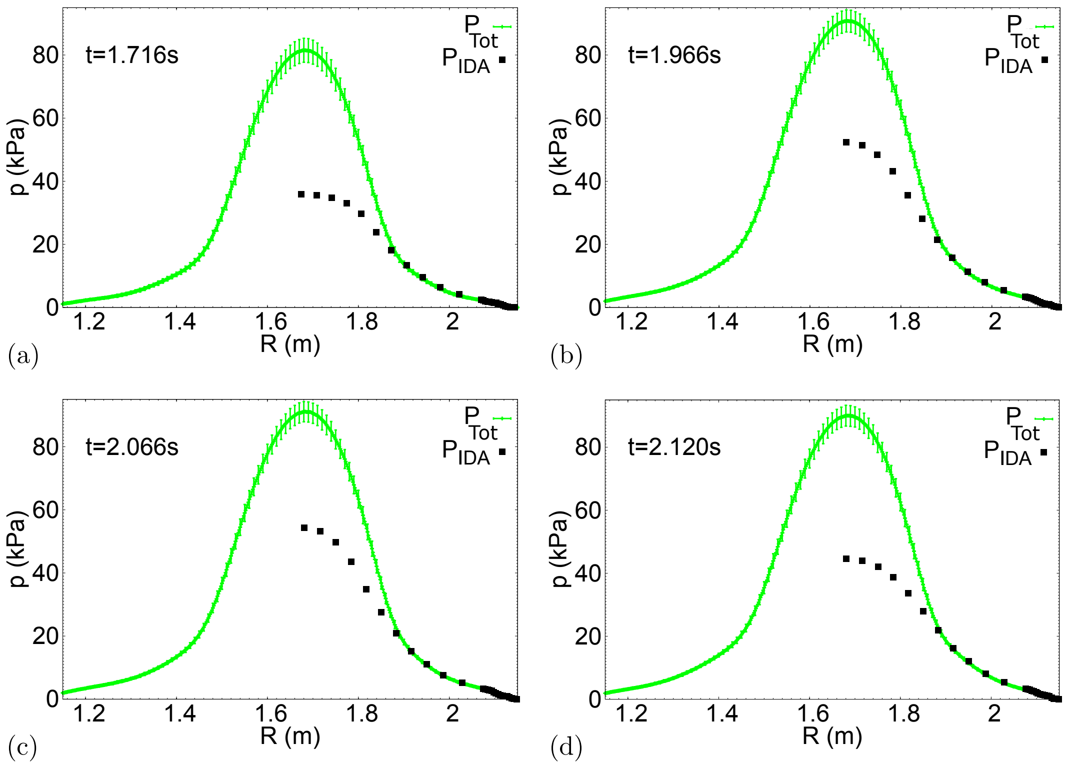

Figure 5.22. Output total plasma pressure P_{Tot} and background plasma pressure P_{IDA} profiles for CLISTE equilibrium reconstructions during discharge 25546.

Unlike discharge 27339, discharges 25546 is an L-mode or low confinement regime discharge, and does not possess the same edge pressure pedestal and hence has no pronounced peak in the edge toroidal current density. Figure 5.22 also show the pressure calculated from the input background ion and electron temperature and density kinetic profiles alone, as obtained from IDA and IDZ, where IDZ is a diagnostic for determining $Z_{effective}$. While these conform closely to the pressure profile calculated by CLISTE in the edge region and outer core, they begin to diverge as one moves towards the plasma centre. This disparity in the input and calculated pressure can be accounted for by the contribution to the total pressure from fast particles, which is expected to be significant in the core region. The user specified weighting of the input kinetic background profile channels decays quickly to zero inboard of the pedestal. This is done as it is expected that the kinetic pressure data becomes an increasingly inadequate representation of the total pressure the further one moves from the pedestal, the force balance being determined by $J \times B = \nabla P_{Tot}$.

Certain codes such as FAFNER and TRANSP provide estimates of the fast particle pressure and can be included as input for CLISTE if such results are available. In this case, the solution can be constrained by pressure data across the full radial range. The effects of fast particles are not treated in this work owing to the local nature of the analysis. As the energetic particles possess very large orbits, they will contribute only globally to the mode dynamics. However, it is important to acknowledge the importance that they can potentially play. Figure 5.22 highlights the difference between the total pressure P_{Tot} and the background pressure P_{IDA}, which can be used as an estimate for the fast particle contribution to the total pressure.

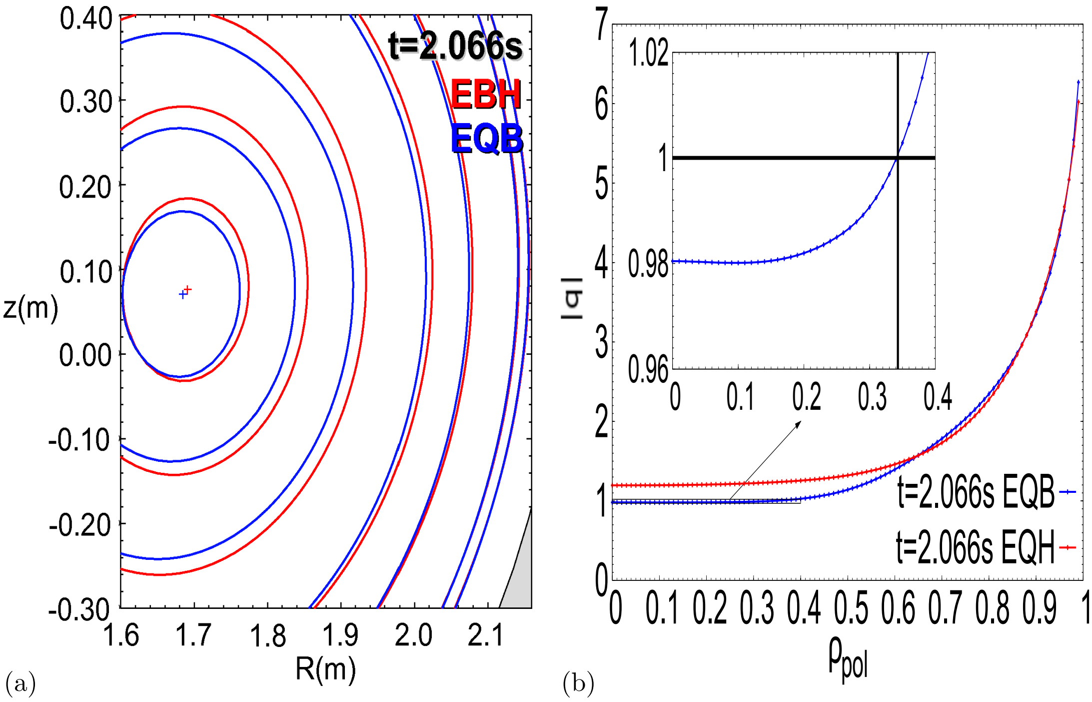

Figure 5.23. Comparison between (a) equilibrium reconstructions and (b) safety factor profiles recovered using magnetic and coil current data only (EQH) and with the addition of background kinetic profiles and a rational surface constraint (EQB) for discharge 25546.

The standard equilibrium mapping procedure for ASDEX Upgrade discharges primarily utilises flux surfaces obtained from equilibrium reconstructions that use magnetic field measurements and external coil currents alone as input data. The impact that the inclusion of background kinetic profile data and a rational surface constraint can have on the equilibrium reconstruction procedure is demonstrated by comparing examples of these more accurate reconstructions, with the background kinetic profiles included, (EQB) with the magnetics and external coil current only reconstructions (EQH), as presented in figure 5.23 (a).

As has been highlighted in section 5.4.2, the inclusion of kinetic profile data and rational surface constraints can improve the accuracy of an equilibrium reconstruction. It follows from this that the calculated q-profile will be more representative if this improved input data is included. Figures 5.21 and 5.23 (b) compare the q-profiles obtained from magnetic data and coil current only equilibrium reconstructions with those obtained from equilibrium reconstructions utilising background kinetic profiles and rational surface data. It can be seen that in figure 5.23 (b) that no $q = 1$ surface is present in the plasma in the EQH cases, while a core localised $q = 1$ surface is present in the more accurate EQB case.
As the modes of interest in this work are core localised and dependent on the existence of low-order rational surfaces, this difference in the qualitative behaviour of the q-profiles for the two equilibria has important consequences for the study of the Alfvénic modes considered in sections 5.4.3 and 5.4.4, as well as those considered in chapters 6 and 7.

5.4.3 Numerical recovery of BAE continuum accumulation point and continuum damping/growth rate

Recovery of low-frequency Alfvén eigenmode dynamics through numerical solution of kinetic dispersion relation The physics underpinning the kinetic dispersion relation 3.4.61 has been discussed extensively in chapter 3 and it has been demonstrated in section 4.6 how it can be solved numerically to recover the frequency continua and continuum damping/growth rates for different types of low-frequency Alfvén eigenmode. In this section, the properties of the numerically calculated BAE continuum will be analysed by utilising realistic q-profiles obtained from CLISTE equilibrium reconstructions, as demonstrated in section 5.4.2, electron and ion density and temperature profiles from the IDA and IDZ diagnostics, as well as various other experimental profiles and parameters obtained from ASDEX Upgrade diagnostics as input data, as discussed in section 4.6.2.

Radial properties of numerically calculated BAE continuum It is instructive to consider the radial properties of the numerically calculated BAE continua for a range of toroidal mode numbers. Figure 5.24 (a) shows the BAE frequency continua for toroidal mode numbers $n = 3 - 6$, close to the estimated $q = 1$ surface at $t = 2.058$s during discharge 25546, obtained by solving the kinetic dispersion relation 3.4.61 and from LIGKA calculations. The BAE continuum accumulation point (CAP) frequency is plotted in terms on the mode frequency ω, normalised to the on-axis Alfvén frequency ω_{A0}, and will be designated as ω_{BAE} for the rest of this analysis. It should be noted that the value for n_i used in this normalisation does not include the impurity contribution. This is found to have a minimal impact on the value, in addition to the fact that the on-axis ion density has large errors associated with it. It should be noted that the equilibrium used in the calculations for this figure differs slightly from that utilised in the root-solver analysis of the same time-point later in this section. This resulted from a reassessment of the estimate for the $q = 1$ surface position used in the subsequent analysis. However, the qualitative results remain essentially unchanged.

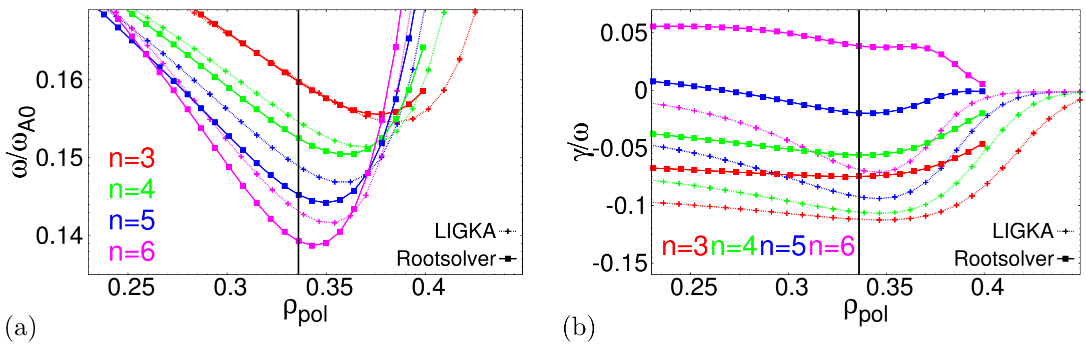

Figure 5.24. (a) BAE frequency continua and (b) continuum damping/growth rates, obtained by solving the kinetic dispersion relation 3.4.61 and from LIGKA, close to the estimated $q = 1$ surface location for toroidal mode numbers $n = 3 - 6$ at $t = 2.058$s during discharge 25546. The radial location of the $q = 1$ surface is indicated by the vertical black lines.

It is immediately evident from figure 5.24 (a) that the continua for the different toroidal mode numbers are separated in frequency in a manner similar to that observed experimentally in section 5.2.4, continua with higher toroidal mode numbers associated with them having lower frequencies close to the $q = 1$ surface than those with lower toroidal mode numbers. It can also be seen that the CAP in the case of each distinct toroidal eigenmode is localised close to the $q = 1$ surface, which lies at $\rho_{pol} \approx 0.341$ in this case and is indicated by a black vertical line, and that higher mode number eigenmodes are more core localised. For example, the CAP of the $n = 6$ eigenmode is the most core localised, while that of the $n = 3$ eigenmode is located further outwards radially. The BAE continuum damping/growth rate calculated from equation 3.4.61 and LIGKA are presented in figure 5.24 (b). Continua with higher toroidal mode numbers associated with them are found to experience higher growth rates and reduced damping rates than those with lower toroidal mode numbers. This is to be expected due to the destabilising effect of ω_{*p}, which is proportional to the toroidal mode number n. This will be discussed in detail later in this section.

From figures 5.24 (a) and (b) it is clear that differences exist between the continua and damping/growth rates calculated by the numerical root-solver for the kinetic dispersion relation and by LIGKA. These stem from the fact that the physics included is not identical for the two approaches. For example, the elongation is treated locally in the kinetic dispersion relation, which will result in a slightly different shift in the CAP frequency. In addition, finite $E_{\|}$ effects and higher bounce resonances are not taken into account in the kinetic dispersion relation, which would explain the differences observed in the continuum damping/growth rates. However, the qualitative behaviour is similar enough that insights can be gained by analysing the low-frequency Alfvén eigenmodes through solving the kinetic dispersion relation using the numerical root-solver.

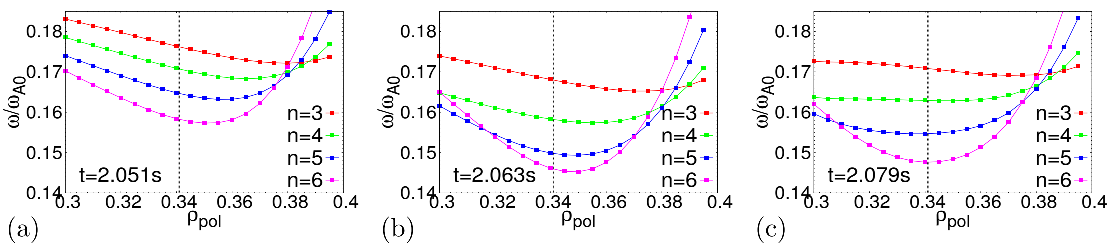

Figure 5.25. Radial profiles for numerically calculated BAE frequency continua at a series of time-points from $t = 2.051 - 2.079$s during period III of discharge 25546. The radial location of the $q = 1$ surface is indicated by the vertical black lines.

Figure 5.25 presents a series of snapshots of the BAE frequency continua close to the $q = 1$ surface at the beginning, middle and end of sawtooth period III from $t = 2.051 - 2.079$s during discharge 25546. The $q = 1$ surface location is indicated by a vertical grey line. During the initial phase of the sawtooth period, as seen in figures 5.25 (a) and (b), the BAE CAPs are subject to a moderate decrease in frequency from their initial values. Their rate of frequency change slows substantially during the central phase, before recovering somewhat by the final time-point shown , as seen in figures 5.25 (b) and (c). A gradual inward shift in the radial position of the CAPs is observed.

Equivalent snapshots in time of the continuum damping/growth rate, plotted as a fraction of the real continuum frequency γ/ω, are shown in figure 5.26. Again, it can be seen that the continua with higher toroidal mode numbers associated with them experience higher growth rates than the lower ones, with this behaviour persisting throughout the entire period. The evolution of the BAE frequency and damping/growth rate at the radial position of the CAP, $\rho_{pol}(CAP)$, will be investigated in detail in the sections that follow.

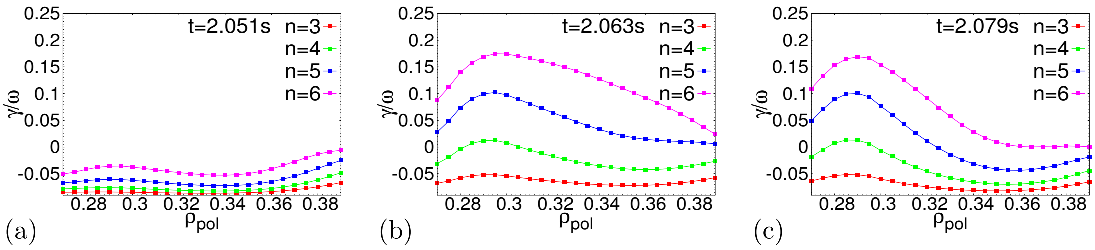

Figure 5.26. Radial profiles for numerically calculated BAE continua damping/growth rates at a series of time-points from $t = 2.051 - 2.079$s during period III of discharge 25546.

BAE continuum accumulation point evolution during sawtooth periods I-IV In this section, the evolution of the numerically calculated BAE continuum frequency accumulation point during sawtooth periods I-IV of discharge 25546 is investigated. It has been demonstrated that gradients in the background temperature and density profiles can have a significant influence on low-frequency Alfvén eigenmode dynamics, causing sizeable downward shifts in the BAE frequency, upwards shifts in the acoustic Alfvén eigenmode frequency and destabilising the BAEs [48, 59].

Thus, this investigation will focus on the effects of changes in the background temperature and density gradients, which enter into the kinetic dispersion relation through the presence of terms proportional to the diamagnetic frequency ω_{*p}. A single q-profile, obtained from a CLISTE equilibrium reconstruction at an appropriate time-point during the particular sawtooth period being considered, was used for calculations at all time-points during that period. The kinetic dispersion relation was then solved numerically at 2ms intervals, allowing the evolution of the continuum accumulation point with background profile gradients over time to be investigated.

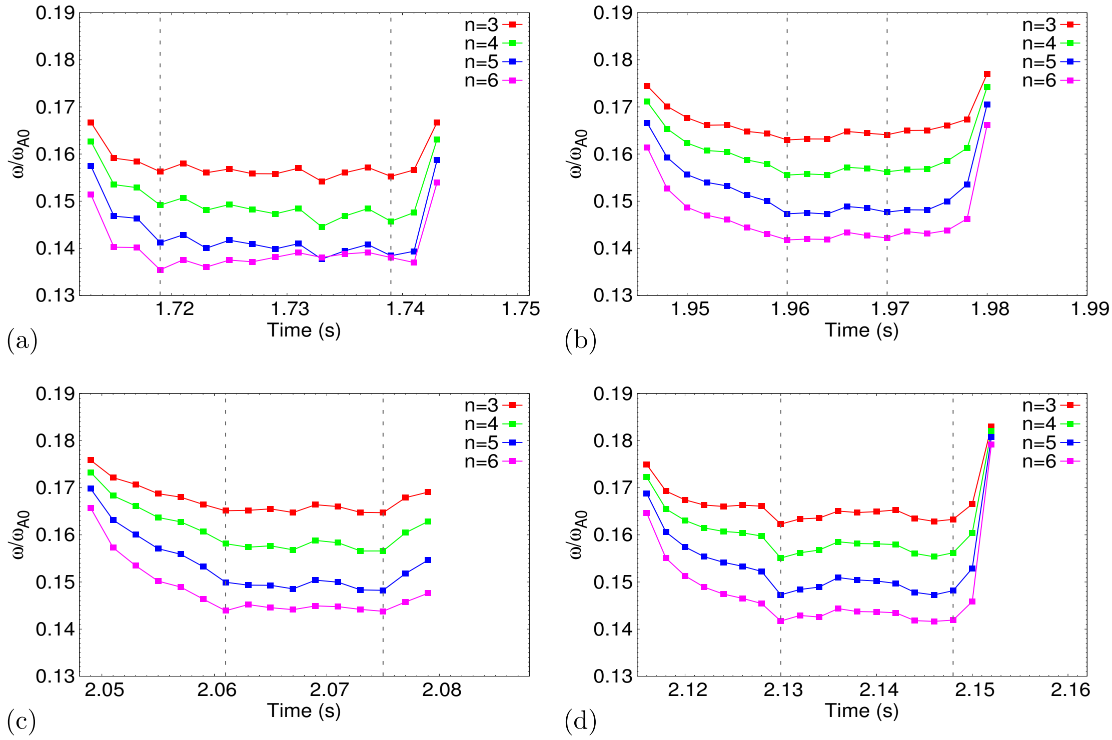

Figure 5.27. Evolution of numerically calculated BAE continuum accumulation point frequency for toroidal mode numbers $n = 3 - 6$ during sawtooth periods I-IV of discharge 25546.

Un-averaged IDA data, which has a resolution in time of approximately 1ms, was utilised in each case. The time-points available for the IDA data did not typically arise in exact 1ms increments. Thus, the IDA data nearest to the millisecond being considered was used in each case. Figure 5.27 shows the evolution of the numerically calculated BAE CAP frequency for $n = 3 - 6$ during sawtooth periods I-IV of discharge 25546. It is evident that the frequency separation between distinct toroidal eigenmodes observed experimentally in section 5.2.4 is well reproduced numerically, with BAEs of higher toroidal mode number calculated almost ubiquitously to have frequencies lower than those of lower toroidal mode numbers. The evolution of the BAE CAP frequency also broadly follows that observed experimentally.

The mode frequency during each period typically begins at its highest observed value for the period, before experiencing a marked drop in frequency over the first $\sim 10-15$ms of each sawtooth period. This gradual decrease in frequency is evident in figure 5.27 from $t = 1.713 - 1.719$s, $t = 1.946 - 1.960$s, $t = 2.049 - 2.061$s and $t = 2.116 - 2.130$s during periods I-IV respectively. This is followed by a phase during which the BAE frequency remains quite stationary for $\sim$ 10ms, calculated during periods I-IV to last from $t = 1.719 - 1.739$s, $t = 1.960 - 1.970$s, $t = 2.061 - 2.075$s and $t = 2.130 - 2.148$s respectively. Finally, in the last $\sim 5 - 10$ms of each period, from $t = 1.739 - 1.743$s, $t = 1.970 - 1.980$s $t = 2.075 - 2.079$s and $t = 2.148 - 2.152$s during periods I-IV respectively, the mode frequency begins a short recovery, approaching its initial value. These three distinct phases of frequency increase, approximate stationarity and decrease are separated in figure 5.27 and in all further figures presenting the time-evolution of BAEs by dashed vertical grey lines, and will from now on be referred to as $|t_1|$, $|t_2|$ and $|t_3|$ for whichever sawtooth period is being considered.

	$\lvert t_1\rvert$ (s)	$\lvert t_2\rvert$ (s)	$\lvert t_3\rvert$ (s)
Period I	$1.713 - 1.719$	$1.719 - 1.739$	$1.739 - 1.743$
Period II	$1.946 - 1.960$	$1.960 - 1.970$	$1.970 - 1.980$
Period III	$2.049 - 2.061$	$2.061 - 2.075$	$2.075 - 2.079$
Period IV	$2.116 - 2.130$	$2.130 - 2.148$	$2.148 - 2.152$

Table 5.2. Phases of BAE CAP frequency increase, approximate stationarity and decrease during periods I-IV of discharge 25546.

Table 5.2 presents the times encompassed by each phase during periods I-IV. The imaginary component of the numerically calculated solution to the kinetic dispersion relation 3.4.61 was also calculated. This represents the local growth or damping rate of the Alfvén continuum and is plotted for sawtooth periods I-IV in figure 5.28 in terms of the real frequency as γ/ω. From figure 5.28 it can be seen that BAEs with higher toroidal mode numbers associated with them experience a higher growth rate at their CAP then those with lower toroidal mode numbers, with the $n = 6$ continuum at $\rho_{pol}(CAP)$ experiencing the highest growth rates and the $n = 3$ continuum at $\rho_{pol}(CAP)$ experiencing the lowest, as has been noted in section 5.4.3.

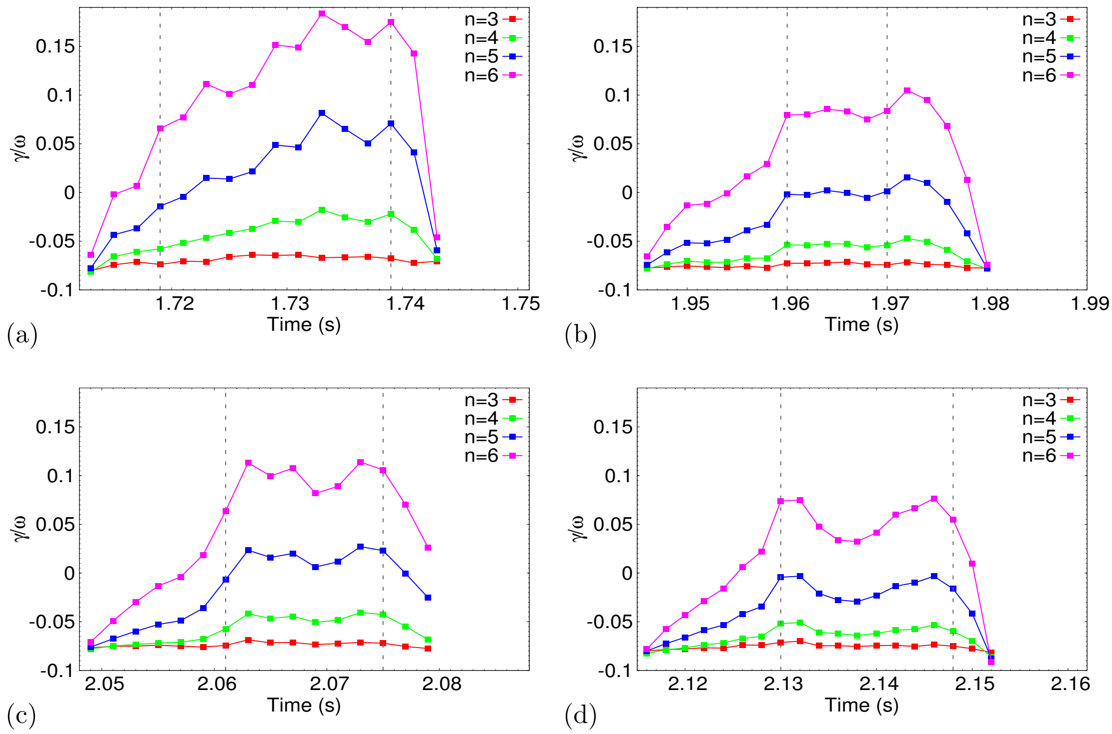

Figure 5.28. Evolution of numerically calculated BAE damping/growth rate at $\rho_{pol}(CAP)$ for toroidal mode numbers $n = 3 - 6$ during sawtooth periods I-IV of discharge 25546.

The BAEs are relatively damped to begin with during periods I-IV, their growth rates increasing during $|t_1|$ at a rate dependent on their toroidal mode numbers. Similarly to the CAP frequency, the damping/growth rates appear to plateau during $|t_2|$ of each period with the growth rates falling off again during $|t_3|$. The $n = 3$ and $n = 4$ modes remain completely damped during the periods considered, with the $n = 5$ mode hovering close to marginal stability during $|t_2|$ and the $n = 6$ mode having a high growth rate for much of periods I-IV. It should be noted that the phases $|t_1| - |t_3|$ do not match up exactly with the times when the qualitative behaviour of the damping/growth rate changes, though are close enough that they are still used to distinguish between these changes in this section. It is instructive to consider how the evolution of various plasma background profiles influence the numerically calculated BAE CAP frequency evolution. Over the course of the following sections, the evolution of the BAE CAP and damping/growth rate will be compared with that of the electron and ion temperature and density profile values at $\rho_{pol}(CAP)$, as well as with the diamagnetic frequency. The change in radial position of the BAE CAP over the course of the sawtooth periods will also be investigated.

BAE CAP evolution with background profile gradients and diamagnetic frequency The analysis begins by considering the relationship between ω_{BAE} and the corresponding temperature gradient at $\rho_{pol}(CAP)$.

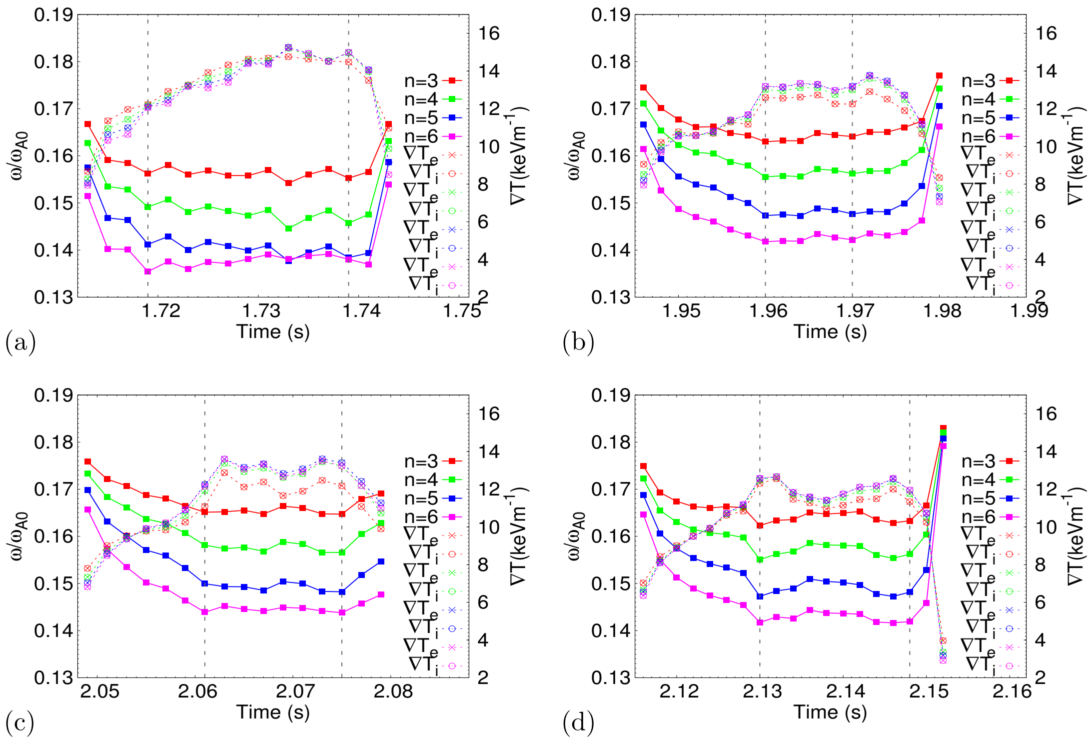

Figure 5.29. Evolution of numerically calculated BAE CAP frequency for $n = 3-6$ with the electron and ion temperature gradients at $\rho_{pol}(CAP)$ during sawtooth periods I-IV of discharge 25546.

Figure 5.29 shows the evolution of ω_{BAE} with $\nabla T(\rho_{pol}(CAP))$ for toroidal mode numbers $n = 3-6$ during periods I-IV of discharge 25546. It should be noted that due to the absence of ion temperature data during discharge 25546, the ion temperature was assumed to be equal to the electron temperature for this analysis. Thus, when the term temperature is used here, it refers to both the electron and ion temperatures. An investigation of the effect of employing different electron and ion temperature profiles, where $T_i \neq T_e$, is conducted in section 6.3. It is immediately evident that a strong relationship exists between ω_{BAE} and $\nabla T(\rho_{pol}(CAP))$. This can be seen be considering the BAE frequency evolution during $|t_1|$ of periods II-IV in particular. Significant decreases in frequency of $\Delta\omega_{BAE} \approx 0.019, 0.022$ and 0.023 occur during these phases respectively in the

$n = 6$ case. The corresponding evolution of $\nabla T(\rho_{pol}(CAP))$ during this phase is observed to match the changes in ω_{BAE} closely, with an increasing gradient clearly leading to a larger downward shift in ω_{BAE} in each case.
The overall behaviour of ω_{BAE} continues to follow that of $\nabla T(\rho_{pol}(CAP))$ throughout periods I-IV. The correlation between these two quantities has been determined for the time periods considered, and is presented in table 5.3. These were calculated using the expression $corr = \frac{\sum_t[(\omega - <\omega>)(\nabla T - <\nabla T>)]}{\sigma(\omega)\sigma(\nabla T)}$, where σ denotes the standard deviation. It can be seen that there is a strong negative correlation between the two quantities.

t(s)	$corr(n=3)$	$corr(n=4)$	$corr(n=5)$	$corr(n=6)$
$1.713 - 1.743$	-0.8578	-0.9363	-0.9320	-0.7713
$1.946 - 1.980$	-0.9108	-0.9527	-0.9669	-0.9403
$2.049 - 2.079$	-0.9217	-0.9682	-0.9782	-0.9449
$2.116 - 2.152$	-0.9665	-0.9846	-0.9892	-0.9829

Table 5.3. Correlation between ω_{BAE} and $\nabla T(\rho_{pol}(CAP))$ during periods I-IV of discharge 25546, where $corr$ represents $corr(\omega_{BAE}, \nabla T)$.

As has been noted earlier in this chapter, once the initial decrease in frequency has ceased it is found that ω_{BAE} plateaus somewhat during $|t_2|$ of each period. This plateauing is accompanied by a corresponding saturation of the observed temperature gradient and is observed most clearly during $|t_2|$ of periods II and III respectively, as seen in figures 5.29 (b) and (c). This is again in agreement with the BAE frequency plateauing observed experimentally in section 5.2.4. Finally, in all four periods, the frequency increases which occur during $|t_3|$ are accompanied by simultaneous decreases in $\nabla T(\rho_{pol}(CAP))$. Thus, while this relationship deviates slightly in places, for example from $t = 2.071 - 2.075$s during period III, $\nabla T(\rho_{pol}(CAP))$ is observed to be a parameter with a substantial influence over the evolution of ω_{BAE}. Figure 5.30 shows the evolution of the continuum damping/growth rate γ/ω at $\rho_{pol}(CAP)$ for $n = 3 - 6$, as well as the corresponding temperature gradient $\nabla T(\rho_{pol}(CAP))$ during periods I-IV. As in the case of the ω_{BAE} evolution, a direct relationship is apparent between the continuum damping/growth rate and the background temperature gradient at

$\rho_{pol}(CAP)$.

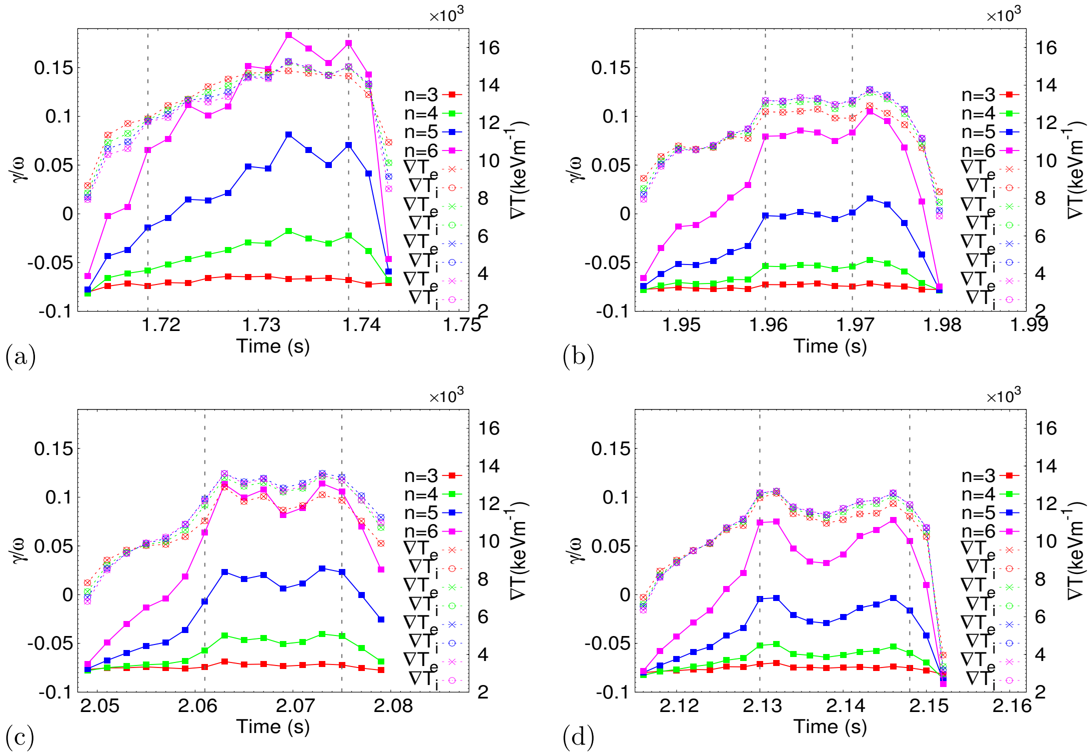

Figure 5.30. Evolution of numerically calculated BAE damping/growth rate for $n = 3-6$ with the electron and ion temperature gradients at $\rho_{pol}(CAP)$ during sawtooth periods I-IV of discharge 25546.

During each of the periods, the growth rates of the $n = 4, 5$ and 6 modes are seen to increase significantly during $|t_1|$, with the rate of increase approximately proportional to the toroidal mode number. This increase in growth rate coincides with that of $\nabla T(\rho_{pol}(CAP))$. After this initial monotonic increase in growth rate, the evolution begins to steady somewhat during $|t_2|$, with smaller dips and rises in the growth rate observed. Again, this behaviour is mirrored by the temperature gradient which saturates somewhat during this period. In addition to this overall relationship between the continuum damping/growth rate and the temperature gradient, smaller changes in the temperature gradient during $|t_2|$ are mirrored by the continuum damping/growth rate. For example, between $t = 1.966$s and $t = 1.970$s a slight dip in the temperature gradient is observed during period II, contrary to the prevailing increase in temperature gradient. This dip is also seen in the $n = 4, 5$ and 6 continuum growth rates. A similar dip is observed between $t = 2.067$s and $t = 2.073$s during period III for the $n = 5$ and $n = 6$ continua. Finally, a significant dip in the temperature gradient from $t = 2.132 - 2.146$s is accompanied by a corresponding dip in the growth rate observed for the $n = 4, 5$ and 6 BAE CAPs.

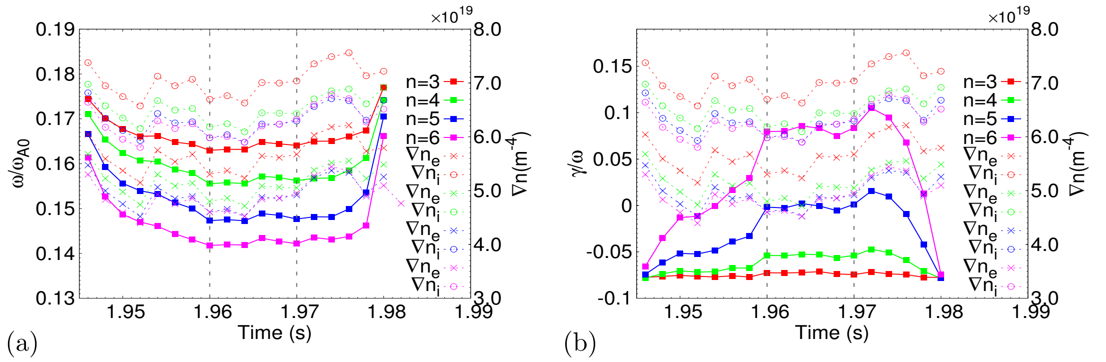

(a) (b)

Figure 5.31. Evolution of numerically calculated BAE frequency and damping/growth rate with the background ion and at electron density gradients at $\rho_{pol}(CAP)$ during sawtooth period II of discharge 25546.

These observations reinforce the assertion that the continuum damping/growth rate is strongly related to the temperature gradient at $\rho_{pol}(CAP)$. During the final $\sim 5 - 10$ms of $|t_3|$, the continuum growth rate begins to decrease, returning approximately to the same damping rates observed at the beginning of each period. As has been noted previously, the temperature gradient also decreases during this period. The electron and ion density profile gradients at $\rho_{pol}(CAP)$ exhibit a relatively large degree of variation over the course of the sawtooth periods considered. An example demonstrating the relationship between ω_{BAE}, γ/ω and $\nabla n_{i,e}$ at $\rho_{pol}(CAP)$ is presented in figure 5.31, with further examples given in appendix B.2, along with examples from discharge 25549 in appendix B.1. It will be discussed later in this section that the density contribution to the diamagnetic frequency, ω_{*n}, through which the density gradient influences the mode dynamics, is much smaller than the temperature contribution ω_{*T}, and hence does not play as significant a role in determining the overall evolution of the BAE frequency. It must also be reiterated that uncertainties in the core electron density and Z_{eff} profiles limit the inferences that can be made regarding the influence of the ion density gradient on the BAE evolution. It was observed above that the BAE frequency evolution follows that of $\nabla T(\rho_{pol}(CAP))$ closely, with an increase in the temperature gradient generally leading to a downward shift in the frequency and vice versa. As such, it is vital to consider the influence that the diamagnetic frequency, which is directly proportional to $\nabla T/T$, $\nabla n/n$ and the toroidal mode number n, has on the BAE CAP frequency evolution.

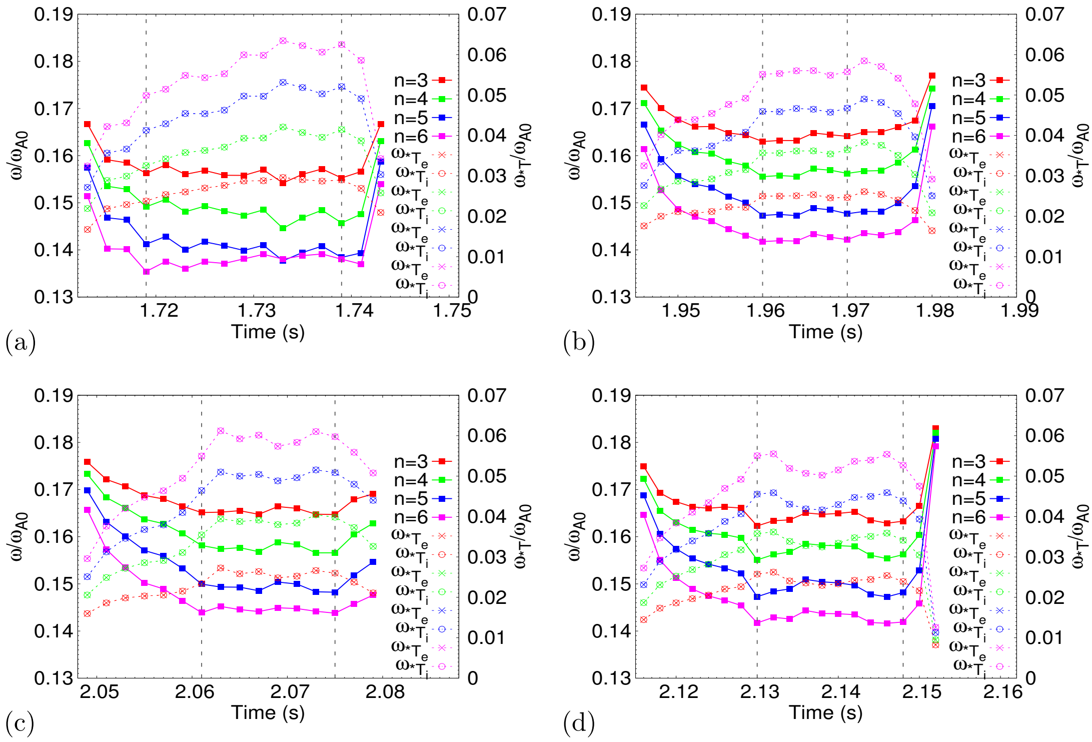

Figure 5.32. Evolution of numerically calculated BAE CAP frequency for toroidal mode numbers $n = 3 - 6$ with the temperature component of the electron and ion diamagnetic frequencies at $\rho_{pol}(CAP)$ during sawtooth periods I-IV of discharge 25546.

The diamagnetic frequency features prominently in the kinetic dispersion relation 3.4.61, and is thus an essential parameter to consider when investigating the BAE frequency evolution as it is the mechanism through which the background temperature and density profile gradients affect the mode frequency evolution and stability. Figure 5.32 shows the evolution of the BAE frequency with the electron and ion temperature components of the diamagnetic frequency $\omega_{*T_{i,e}}$ at $\rho_{pol}(CAP)$, normalised to the on-axis Alfvén frequency ω_{A0}. It can be seen that the relationship between ω_{*T} and ω_{BAE} is very similar to that between the temperature gradient and mode frequency, with an initial increase in ω_{*T} resulting in a decrease in the mode frequency during $|t_1|$. This is followed by a steadying in the change in ω_{*T} during $|t_2|$, accompanied by a plateauing of ω_{BAE}.
Finally, ω_{*T} is observed to fall during $|t_3|$ of each sawtooth period, with a simultaneous increase in frequency observed. This similarity in the evolution of ω_{*T} and $\nabla T(\rho_{pol}(CAP))$ is to be expected given that ω_{*T} is determined primarily by the

influence of $\nabla T(\rho_{pol}(CAP))$. The value of ω_{*T} is scaled by its dependence on various other parameters, as seen in equation $\omega_{*p} = \omega_{*n_s} + \omega_{*T_s} = \frac{T_s}{eB} k_\theta (\frac{\nabla n_s}{n_s})(1+\eta)$, where $\eta = \frac{\nabla T_s}{T_s} / \frac{\nabla n_s}{n_s}$ whose terms have been defined previously, following the definition of equation 3.4.61. A particular factor that determines the level of influence that ω_{*T} exerts on the mode dynamics is the toroidal mode number n. As can be seen from the above expression for the diamagnetic frequency, $\omega_{*T} \propto n$. Thus, continua with larger toroidal mode numbers will be affected to a greater degree by ω_{*T}. This is clear from figure 5.32, where ω_{*T} for $n = 6$ is observed to be at least double that of the $n = 3$ case. Figure 5.33 shows the evolution of ω_{BAE} with the density contribution to the overall diamagnetic frequency ω_{*n}. While ω_{*n} does appear play a role in the BAE frequency down-shift, it is observed to be much smaller than that of ω_{*T}.

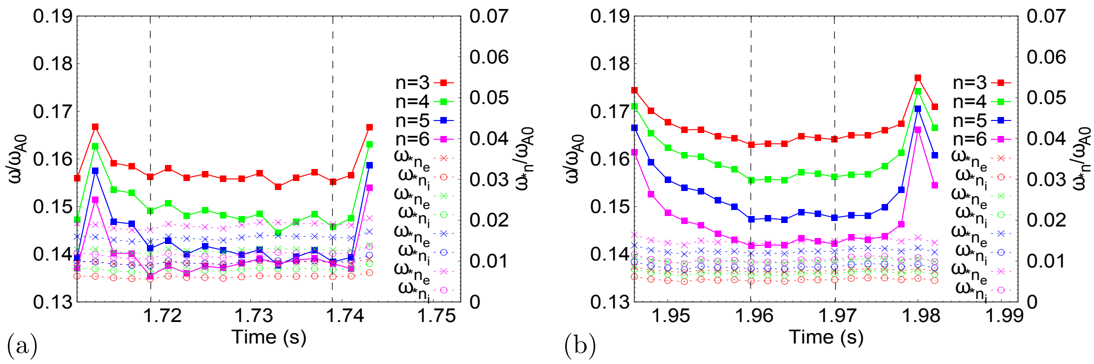

Figure 5.33. Evolution of numerically calculated BAE CAP frequency for toroidal mode number $n = 3 - 6$ with the density components of the electron and ion diamagnetic frequencies at $\rho_{pol}(CAP)$ during sawtooth periods I and II of discharge 25546.

This can be seen by comparing figures 5.32 and 5.33. During the four periods considered in this analysis ω_{*T} peaks at a value of approximately 0.07 at $t = 1.972$s during period II. At the same time-point, the density contribution to the diamagnetic frequency is found to be $\omega_{*n} \approx 0.015$, slightly over 20% that of ω_{*T}. In addition, ω_{*n} does not exhibit the same degree of variation over the course of each sawtooth period, suggesting that while it contributes modestly to the overall frequency down-shift, it does not influence greatly the short time-scale variation in the BAE behaviour over the course of an individual sawtooth period. It has been shown in the previous section that the evolution of the BAE damping/growth rate is related to the background temperature gradient.

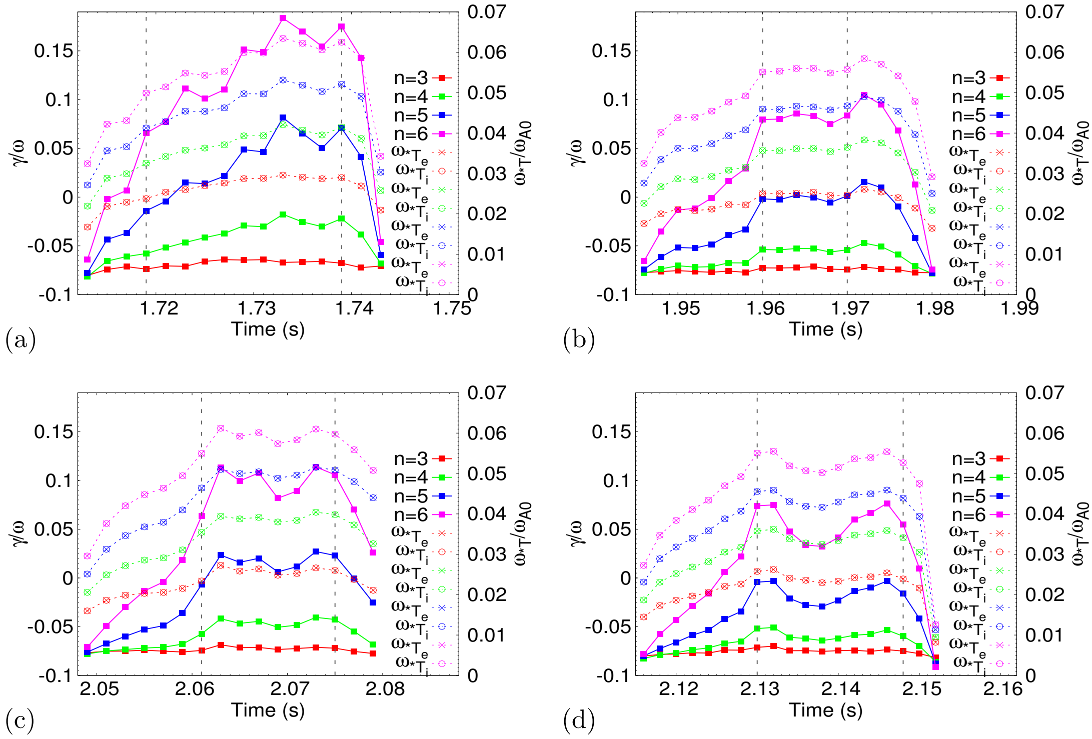

Figure 5.34. Evolution of numerically calculated BAE damping/growth rate at $\rho_{pol}(CAP)$ for toroidal mode numbers $n = 3 - 6$ with the temperature components of the electron and ion diamagnetic frequencies at $\rho_{pol}(CAP)$ during sawtooth periods I-IV of discharge 25546.

Thus, it is reasonable to infer that the BAE damping/growth rate is likely to be affected by ω_{*T}, as was the case for the BAE CAP frequency. Figure 5.34 shows the nature of this relationship for periods I-IV. As was the case for $\nabla T(\rho_{pol}(CAP))$, the mode continuum growth rate is observed to increase with ω_{*T}, with the rate of increase proportional to the toroidal mode number n. Likewise, any short time-scale changes in the BAE continuum growth rate evolution are mirrored by the diamagnetic frequency, as it was by the temperature gradient during the equivalent time-periods. As was observed when considering the effect of the density component of the diamagnetic frequency on the BAE CAP evolution, ω_{*n} is not observed to change greatly over the course of each period and assumes a value much lower than that of ω_{*T}. Thus, it is observed to contribute to a lesser degree to the BAE CAP growth rate, as seen in appendix B.2.

BAE CAP evolution with background temperature and density profiles

Figure 5.35 shows the evolution of ω_{BAE} with the electron and ion temperatures at $\rho_{pol}(CAP)$ for toroidal mode numbers $n = 3-6$ during sawtooth periods I and II of discharge 25546. In section 5.4.3, it has been demonstrated that numerically calculated BAE continua with lower toroidal mode numbers will exhibit a BAE CAP situated further outwards radially than those with a higher toroidal mode number.

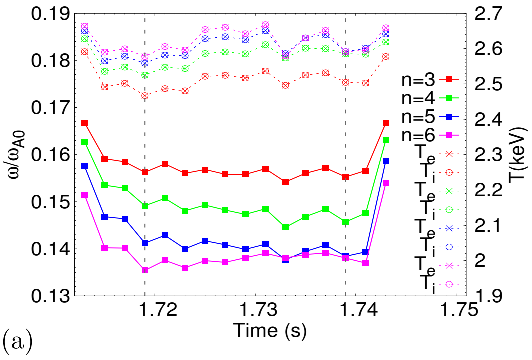

(a)

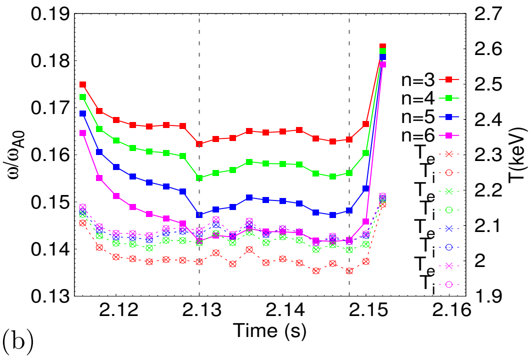

(b)

Figure 5.35. Evolution of numerically calculated BAE CAP frequency for toroidal mode numbers $n = 3-6$ with the electron and ion temperatures at $\rho_{pol}(CAP)$ during sawtooth periods I and IV of discharge 25546.

Thus, the $n = 3$ CAP is typically found to be the furthest from the magnetic axis. This is highlighted by the observation that the temperature at the $n = 3$ BAE CAP is appreciably lower than that at the CAP for the larger toroidal mode numbers. This is expected, based on the fact that the temperature decreases the further towards the plasma edge that one observes. ω_{BAE} decreases along with the temperature during $|t_1|$ of each period. However, the agreement in the direction of their evolution is not always observed during phases $|t_2|$ and $|t_3|$ of each period. For example, from $1.972-1.978$s of period II, the frequency clearly increases while the temperature decreases.

Likewise, during phase $|t_2|$ of periods II and III, the evolution of the ω_{BAE} is not always consistent with that of the temperature, with an increase in ω_{BAE} sometimes accompanied by an increase in the temperature, but not in other cases. However, this behaviour is not always observed, as an inspection of period I reveals. In this case, the behaviour of ω_{BAE} and the corresponding temperature is observed to agree quite well, with decreases in temperature generally accompanied by decreases in frequency and vice versa, as seen in figure 5.35 (a). This suggests that while the temperature may not be the dominant parameter in determining the ω_{BAE} evolution, it can influence it appreciably under certain conditions.

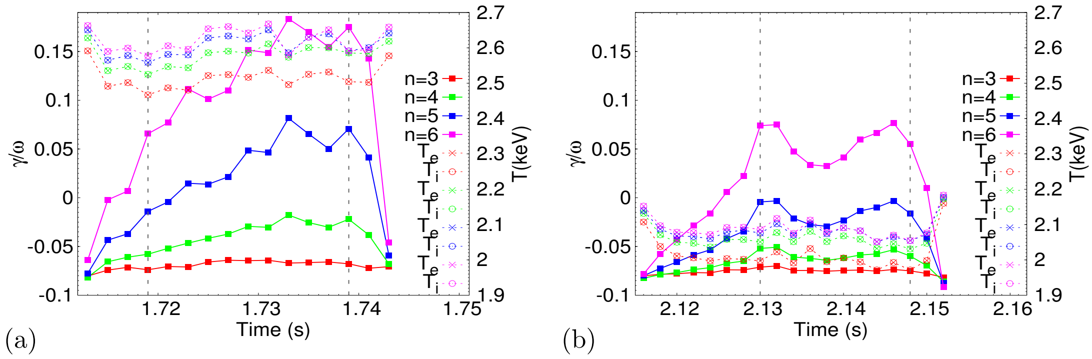

Figure 5.36. Evolution of numerically calculated BAE damping/growth rate at $\rho_{pol}(CAP)$ for toroidal mode numbers $n = 3 - 6$ with the electron and ion temperatures at $\rho_{pol}(CAP)$ during sawtooth periods I and IV of discharge 25546.

The temperature at $\rho_{pol}(CAP)$ is also observed to decrease substantially over the course of periods I-IV, with a peak value of $T \approx 2.65$keV during period I and $T \approx 2.15$keV during period IV. This could account for the decreasing influence of the temperature on the BAE CAP evolution over the four periods considered. It has been discussed earlier in this section how the mode frequency decreases as along with the temperature at the beginning of each period. Thus, a method by which the temperature profile can influence the mode evolution is evident. Any decrease in the temperature would have the effect of increasing ω_{*T} through its $1/T$ dependence.

Considering figure 5.36, an inconclusive relationship appears to exist between the BAE damping/growth rate and the temperature at $\rho_{pol}(CAP)$. Period I exhibits the highest growth rates, along with the highest temperature at the CAP, while period IV exhibits the lowest growth rates, along with the lowest temperature at the CAP. This relationship is not as obvious for periods II and III which exhibit similar damping/growth rates, with period II typically having the higher temperature at $\rho_{pol}(CAP)$. Thus, it is not possible to formulate a definitive relationship between the temperature and the BAE continuum damping/growth rate. The influence that τ, representing the ratio between the electron and ion temperatures $\tau = T_e/T_i$, has on the damping/growth rate is predicted to play a more important than the individual temperatures of the species [59], and this assertion is investigated in section 6.3.

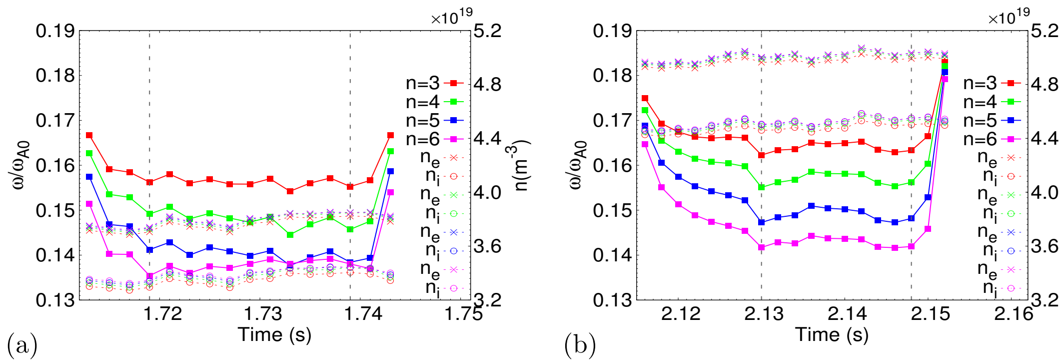

Figure 5.37. Evolution of numerically calculated BAE CAP frequency for toroidal mode number $n = 3-6$ with the electron and ion densities at $\rho_{pol}(CAP)$ during sawtooth periods I and IV of discharge 25546.

In contrast to the evolution of the temperature at $\rho_{pol}(CAP)$, that of the electron and ion densities appear to be somewhat more quiescent, with fewer sharp changes and less variation observed between the individual distinct toroidal eigenmodes. Considering figure 5.37, a potential cause for the difference in the level of agreement between temperature and BAE frequency behaviour for the periods I-IV can be postulated. From figure 5.37 (a), the ion density at the BAE CAP location can be seen to lie between approximately $n_i \approx 3.3 - 3.5 \times 10^{19}\text{m}^{-3}$ during period I. However, the ion density is observed to be substantially higher by period IV, with a value of approximately $n_i \approx 4.5 \times 10^{19}\text{m}^{-3}$. This difference in the ion density could explain the variation in behaviour between the different periods described above, with the temperature contribution to the mode behaviour seemingly increasing during instances of lower density and waning somewhat as the density increases. This hypothesis is tested further in section 6.3.
Figure 5.38 shows the evolution of numerically calculated BAE damping/growth rate for toroidal mode numbers $n = 3 - 6$ with the electron and ion densities at $\rho_{pol}(CAP)$ during sawtooth periods I and IV during discharge 25546. The increase in the density between periods I and IV discussed previously contributes to explaining the observed decrease in the overall continuum growth rates, as the BAEs are expected to experience more damping as the density increases. Further examples of the BAE behaviour described in this section are presented in appendix B for discharge 25549.

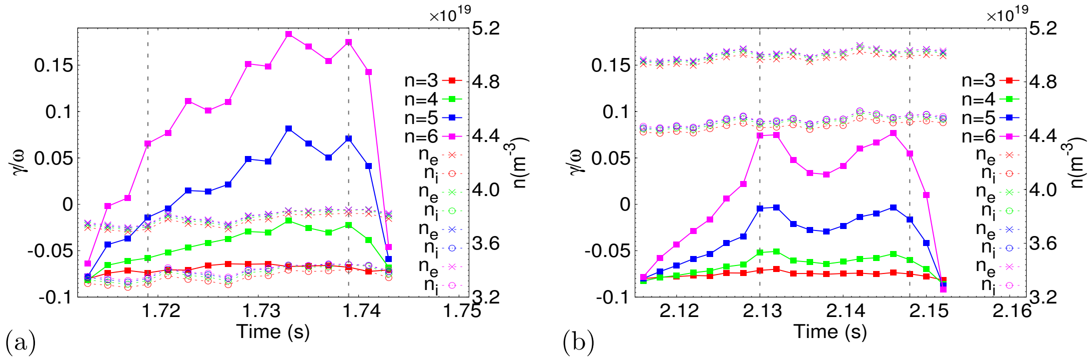

Figure 5.38. Evolution of numerically calculated BAE damping/growth rate at $\rho_{pol}(CAP)$ for toroidal mode numbers $n = 3 - 6$ with the electron and ion densities at $\rho_{pol}(CAP)$ during sawtooth periods I and IV of discharge 25546.

Evolution of radial location of BAE CAP Some interesting insights into the evolution of the BAE CAP for the various distinct toroidal eigenmodes are obtained if one considers the change in the radial location of the CAP in time during each sawtooth period, as presented in figure 5.39. During each period, $\rho_{pol}(CAP)$ for the various distinct toroidal eigenmodes is typically observed to move gradually inwards. For example, in figure 5.39 (a), the $n = 3$ and $n = 4$ CAPs at $t = 1.946$s are at $\rho_{pol} \approx 0.389$ and $\rho_{pol} \approx 0.379$ respectively before moving inwards to $\rho_{pol} \approx 0.380$ and $\rho_{pol} \approx 0.362$ respectively by $t = 1.974$s.
However, $\rho_{pol}(CAP)$ for the $n = 5$ and $n = 6$ eigenmodes appears to behave slightly differently, moving inward for the first ~ 10ms of the period before levelling off for most of the remainder of the period and being much closer to one another than for the other mode numbers. In fact, during period II, crossings occur where the radial ordering of the CAP for the $n = 5$ and $n = 6$ eigenmodes are inverted. This occurs at $t \approx 1.970$s, with some further reversals observed subsequently. This difference in the behaviour of the CAP for the various distinct toroidal eigenmodes could account for the greater proximity of the numerically calculated frequencies for the $n = 5$ and $n = 6$ modes, with the boost to the diamagnetic frequency provided by the higher $n = 6$ mode number offset somewhat by the stagnation in the contribution of the temperature gradients, caused by the radial position of the BAE CAP not decreasing sufficiently, unlike the $n = 3, 4$ and $n = 5$ eigenmodes.

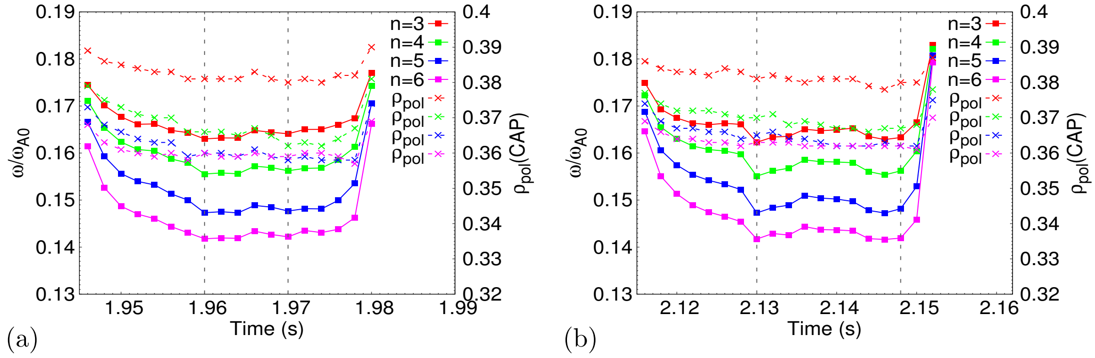

Figure 5.39. Evolution of numerically calculated BAE CAP frequency for toroidal mode numbers $n = 3-6$ and the corresponding $\rho_{pol}(CAP)$ evolution for sawtooth periods II and IV during discharge 25546.

Agreement between experimental observations of BAEs and numerical results In section 5.4.3 the evolution of the BAE CAP frequency during discharge 25546, obtained by solving the kinetic dispersion relation 3.4.61 numerically using a complex root-solver, was investigated.

In this section, these numerical results are compared qualitatively and quantitatively with experimental observations of BAEs from section 5.3. In order to facilitate this, results for the numerically calculated BAE continua at a certain time-point were obtained using the LIGKA code. This differed from the root-solver approach in that it was achieved through a full numerical solution of the system of gyrokinetic moment, quasi-neutrality and gyrokinetic equations. Separate LIGKA calculations for the continua were carried out for the case where the influence of trapped particles and particles with finite $v_\perp$ was included and that where it was omitted. This provided an estimate for the approximate downward shift in frequency brought about by the inclusion of the effects of trapped particle and particles with finite $v_\perp$, which could then be utilised when comparing the numerical results obtained by solving the kinetic dispersion relation at multiple time-points with the experimental results. The LIGKA results for the circulating particle case and the case with the effects of trapped particles and particles with finite $v_\perp$ included are presented in figure 5.40. It can be seen that their inclusion results in an additional down-shift ranging from approximately $17-25\%$ depending on the toroidal mode number, with the greatest down-shift observed for the $n = 6$ case.

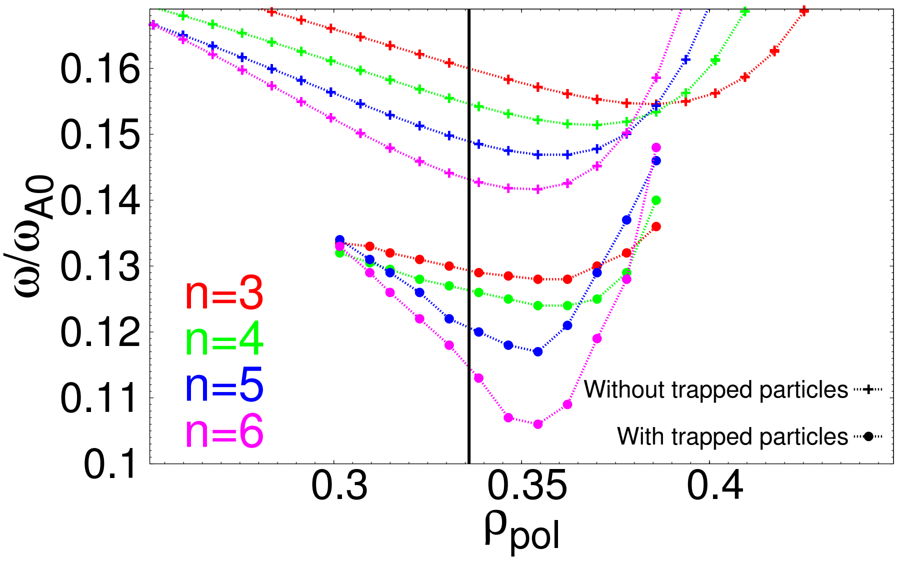

Figure 5.40. LIGKA results for the circulating particle case and the case with trapped particles and particles with finite $v_\perp$ included, for $t = 2.058s$ during discharge 25546.

While no estimates of the toroidal rotation were available for discharges 25544, 25546 and 25549, discharges with similar characteristics and for which toroidal rotation profiles were available - discharges 26621 and 26622 - were utilised instead. A comparison between certain parameters of discharges 25546, 26621 and 26622 are presented in figure 5.41.

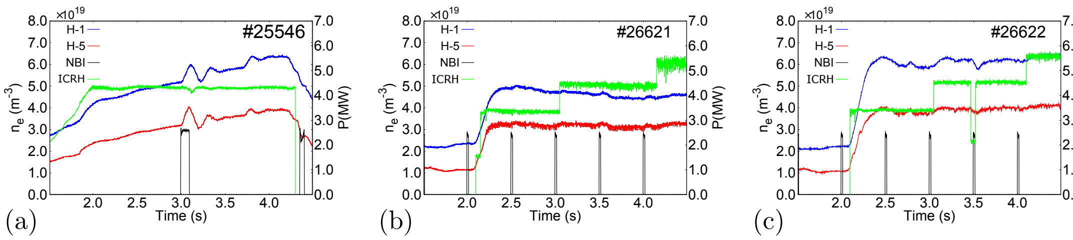

Figure 5.41. Comparison of main plasma parameters for discharges 25546, 26621 and 26622, where H1 and H5 refer to core and edge density measurements respectively.

All are medium density discharges and the input ICRH power, which will be the parameter with the greatest impact upon the toroidal rotation, is similar in each case, ranging from $P_{ICRH} \approx 4.3 - 4.5$MW. Discharge 25546 has an on-axis magnetic field strength of $B_t \approx -2.488$T and a plasma current of $I_p \approx 0.800$MA, while those of discharges 26621 and 26622 differ somewhat, with $B_t \approx -2.738$T, $I_p \approx 0.600$MA and $B_t \approx -2.290$T, $I_p \approx 0.600$MA respectively. Figures 5.42 and 5.43 compare the experimentally observed BAE frequency evolution during sawtooth periods I-IV of discharge 25546, obtained from core localised lines of sight of the soft x-ray diagnostic, with numerically calculated results for the equivalent time periods. In order to compare the numerical results with the experimental, it was necessary to take into account the Doppler shift in the mode frequency caused by the toroidal rotation of the plasma.

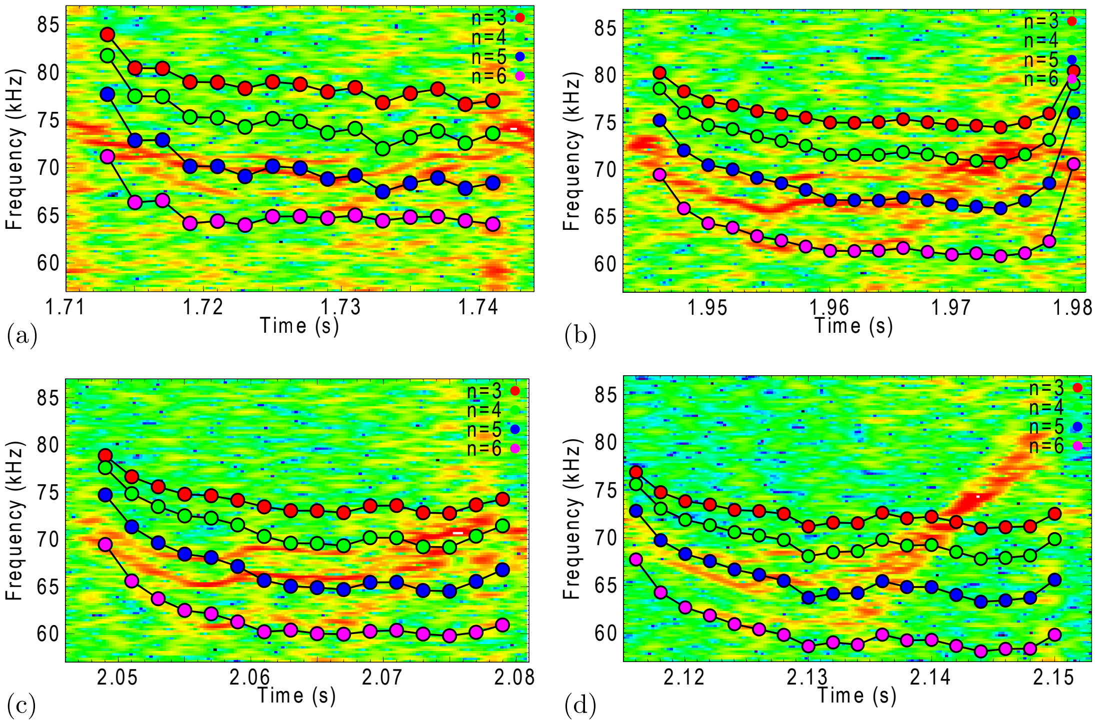

Figure 5.42. Comparison between numerically calculated BAE CAP frequencies for toroidal mode numbers $n = 3 - 6$ with mode frequencies observed experimentally using channel I51 ($nfft = 8192$ and $nstp = 512$) and I50 ($nfft = 8192$ and $nstp = 512$) of the soft x-ray diagnostic, with a tangency radius of $\rho_{pol} \approx 0.332$, during periods I-IV of discharge 25546. An estimate for the toroidal rotation is obtained from discharge 26621.

.

This results in an upward correction of nf_{rot} to the mode frequency. However, the toroidal rotation velocity measured during discharges 26621 and 26622 differ somewhat, with values at the CAP of $f_{rot} \approx 0.7$kHz and $f_{rot} \approx 1.4$kHz respectively. As it is not clear which discharge provides the more representative estimate of the toroidal rotation velocity for use in the numerical analysis, results obtained using both are presented and compared in figures 5.42 and 5.43 respectively.

Figure 5.42 is considered first, with results during period I compared with experimental observations from soft x-ray channel I50 and those from periods II-IV compared with observations from channel I51. This difference in the choice of channels was to provide the clearest observations of the mode activity in each case with the $n = 3-5$ eigenmodes clearest for I50 and the $n = 4-6$ eigenmodes clearest for I51, in decreasing frequency order.

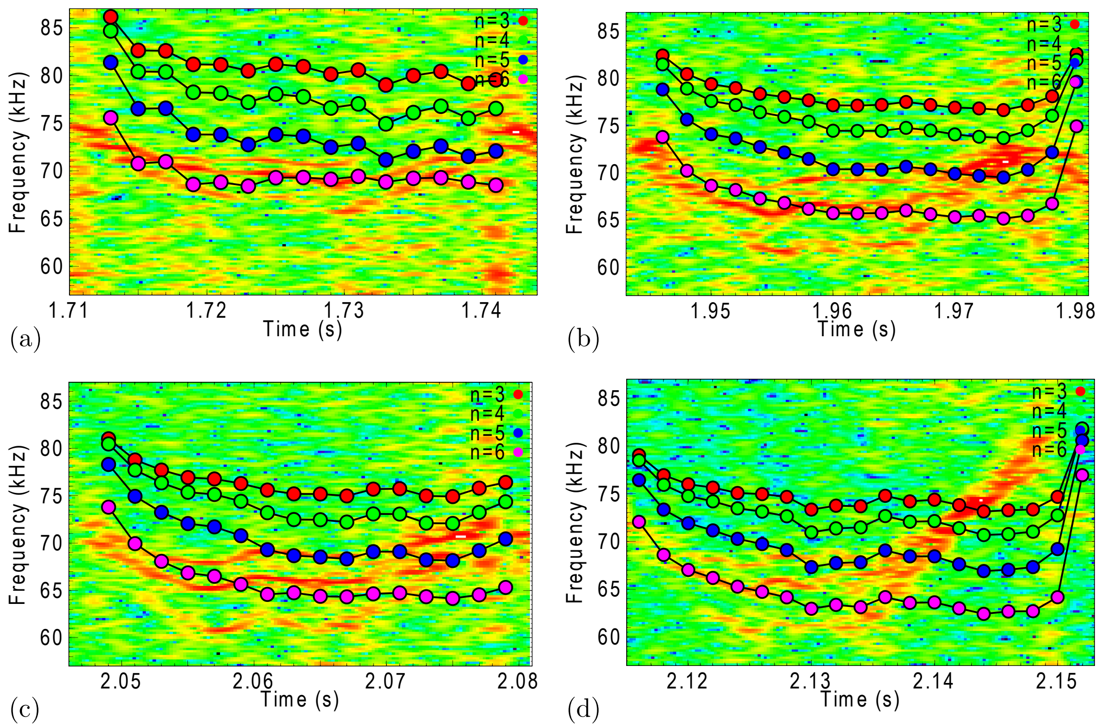

Figure 5.43. Comparison between numerically calculated BAE CAP frequencies for toroidal mode numbers $n = 3-6$ with mode frequencies observed experimentally using channels I51 ($nfft = 8192$ and $nstp = 512$) and I50 ($nfft = 8192$ and $nstp = 512$) of the soft x-ray diagnostic, with a tangency radius of $\rho_{pol} \approx 0.332$, during periods I-IV of discharge 25546. An estimate for the toroidal rotation is obtained from discharge 26622.

The numerically calculated modes $n = 3-6$ are represented by the red, green, blue and magenta data points respectively. The similarities in the frequency separation between distinct toroidal eigenmodes and temporal behaviour that exist between the experimentally observed BAEs and numerically calculated BAE CAPs have been introduced in section 5.4.3 and are presented again in figure 5.42. Again, the frequency separation between distinct toroidal eigenmodes is reproduced in each case, though it can be seen that the difference in spacing between the successive numerically calculated eigenmodes is larger than that observed experimentally. This is attributable to the low toroidal rotation velocity observed during discharge 26621, which is used in this comparison.

However, the relative spacing in the frequencies of the distinct toroidal eigenmodes is well reproduced, with the spacing increasing for higher mode numbers.

The evolution of the BAEs during the first $\sim$ 10ms of each period is also reproduced quite well numerically, with good agreement with the slope of the experimental BAE frequency evolution in time. The numerically calculated modes of higher toroidal mode number are observed to decrease in frequency more rapidly in time, as is observed experimentally. The quantitative agreement of the results is also quite good, with each numerically calculated eigenmode being within $\sim 1-5$kHz in the cases of the higher toroidal mode number eigenmodes, though diverging somewhat for the lower toroidal mode number eigenmodes.

The plateauing of the BAE frequency evolution during the central phase of periods I-IV is also reproduced, and while the experimentally observed frequency plateauing precedes the numerical by a number of milliseconds in each case, the overlap between the two over the course of each period is significant. As has been discussed in previous sections, the recovery of the mode frequency towards the end of each period is not as well reproduced, with an increase in the numerically calculated frequency only occurring in the final $\sim$ 5ms in most cases. Potential causes for this discrepancy are investigated in section 6.3. Figure 5.43 provides equivalent results, but using the estimate for the toroidal rotation obtained from discharge 26622, which is approximately twice that of discharges 26621. This results in a smaller frequency spacing between the distinct toroidal eigenmodes, closer to that observed experimentally. However, it also shifts the overall frequencies upwards, dis-improving the quantitative agreement between the numerical and experimental results.

While the results presented in figures 5.42 and 5.43 demonstrate that the experimentally observed BAE frequency evolution is well reproduced numerically over much of the sawtooth period, they also highlight the sensitivity of the results to parameters such as the toroidal rotation velocity and the frequency down-shift due to the inclusion of the effects of trapped particles and particles with finite $v_\perp$. Judging from these results, it seems likely that the true value for the toroidal rotation velocity lies somewhere between the estimates used above.

5.4.4 Numerical recovery of acoustic Alfvén eigenmode continuum accumulation point and damping/growth rate

Radial properties of numerically calculated acoustic Alfvén eigenmode continuum Experimental observations of acoustic Alfvén eigenmodes have been presented in section 5.2.4. In the following sections, results for the numerically calculated acoustic Alfvén eigenmode continuum accumulation point frequency evolution and its damping/growth rate during selected periods of discharge 25546 are presented.

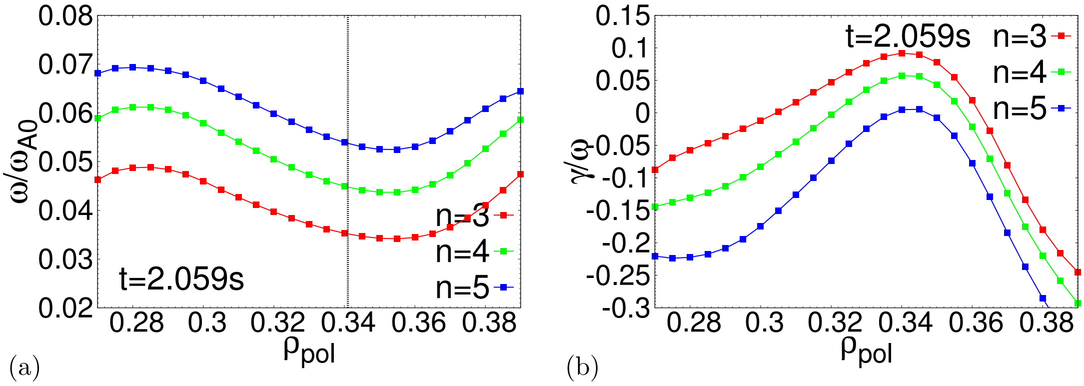

Figure 5.44. (a) Acoustic Alfvén eigenmode frequency continua and (b) their damping/growth rates from the solution to kinetic dispersion relation 3.4.61, close to the estimated $q = 1$ surface location for toroidal mode numbers $n = 3 - 5$ at $t = 2.059$s during discharge 25546

As was the case for the BAE analysis, the kinetic dispersion relation 3.4.61 was solved numerically for multiple time-points using the input data described in section 5.4.3. However in this case, the search region of the complex root-solver was lower in frequency than for the BAEs in order to facilitate the recovery of the lower frequency acoustic Alfvén eigenmode continuum. It is instructive to consider the radial properties of the numerically calculated acoustic Alfvén frequency continua and its corresponding damping/growth rate for different toroidal mode numbers. Figures 5.44 (a) and (b) show the acoustic Alfvén eigenmode frequency continua and their respective damping/growth rates for toroidal mode numbers $n = 3 - 5$, close to the estimated $q = 1$ surface location at $t = 2.059$s during discharge 25546. Firstly, the calculated frequencies of the acoustic Alfvén eigenmode CAPs are much lower than those of the BAEs though the continua are found to exhibit frequency separation between distinct toroidal eigenmodes, similar to that of BAEs. Likewise, the acoustic Alfvén continua appear to possess continuum accumulation points located beneath the continua.

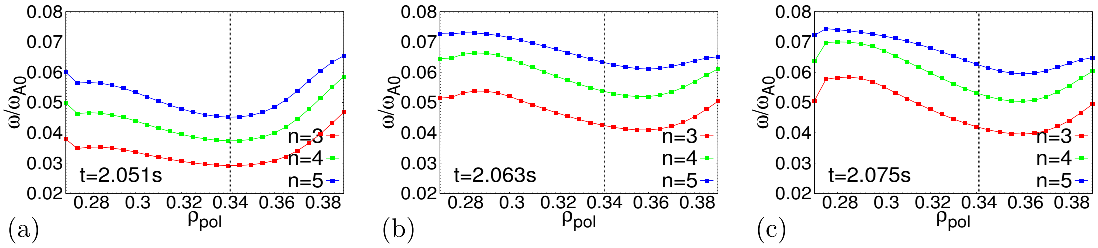

Figure 5.45. Radial profiles for numerically calculated real acoustic Alfvén continua for toroidal mode numbers $n = 3 - 5$ for time-points from $t = 2.051 - 2.075$s during period III of discharge 25546.

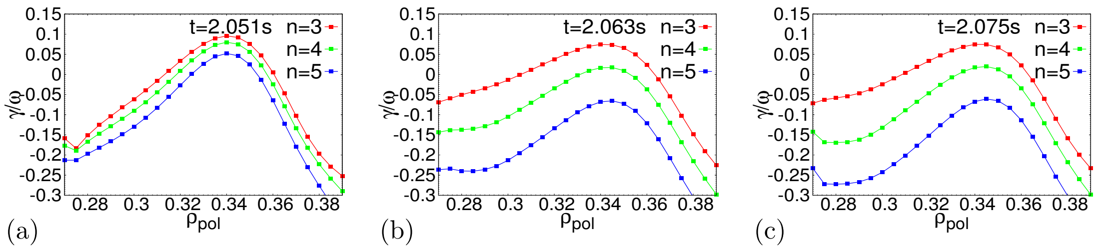

Figure 5.46. Radial profiles for numerically calculated acoustic Alfvén continua damping/growth rates for toroidal mode numbers $n = 3{-}5$ for time-points from $t = 2.051{-}2.075$s during period III of discharge 25546.

As was the case for BAEs, the continuum accumulation point of the acoustic Alfvén eigenmode appears to be localised close to the $q = 1$ surface, but with a much smaller spread in the CAP radial location for the different toroidal mode numbers, as can be seen in figure 5.44. However, unlike BAEs, the continua with higher toroidal mode numbers associated with them possess higher frequencies than those with lower mode numbers.

A series of snapshots of the time evolution of the acoustic Alfvén frequency continua and their damping/growth rates during period III of discharge 25546 are presented in figures 5.45 and 5.46 respectively. The radial position of the CAP, $\rho_{pol}(CAP)$, remains primarily in the region from $\rho_{pol} \approx 0.34 - 0.36$, with the difference in $\rho_{pol}(CAP)$ for the various toroidal mode numbers being minimal. This was otherwise in the case of the BAEs, with a significant difference existing between the radial position of the CAPs for different toroidal mode numbers, as seen in figures 5.39.

Acoustic Alfvén eigenmode continuum accumulation point evolution during sawtooth periods I-IV The evolution of the acoustic Alfvén continuum during sawtooth periods II-IV is investigated in greater detail during the sections that follow.

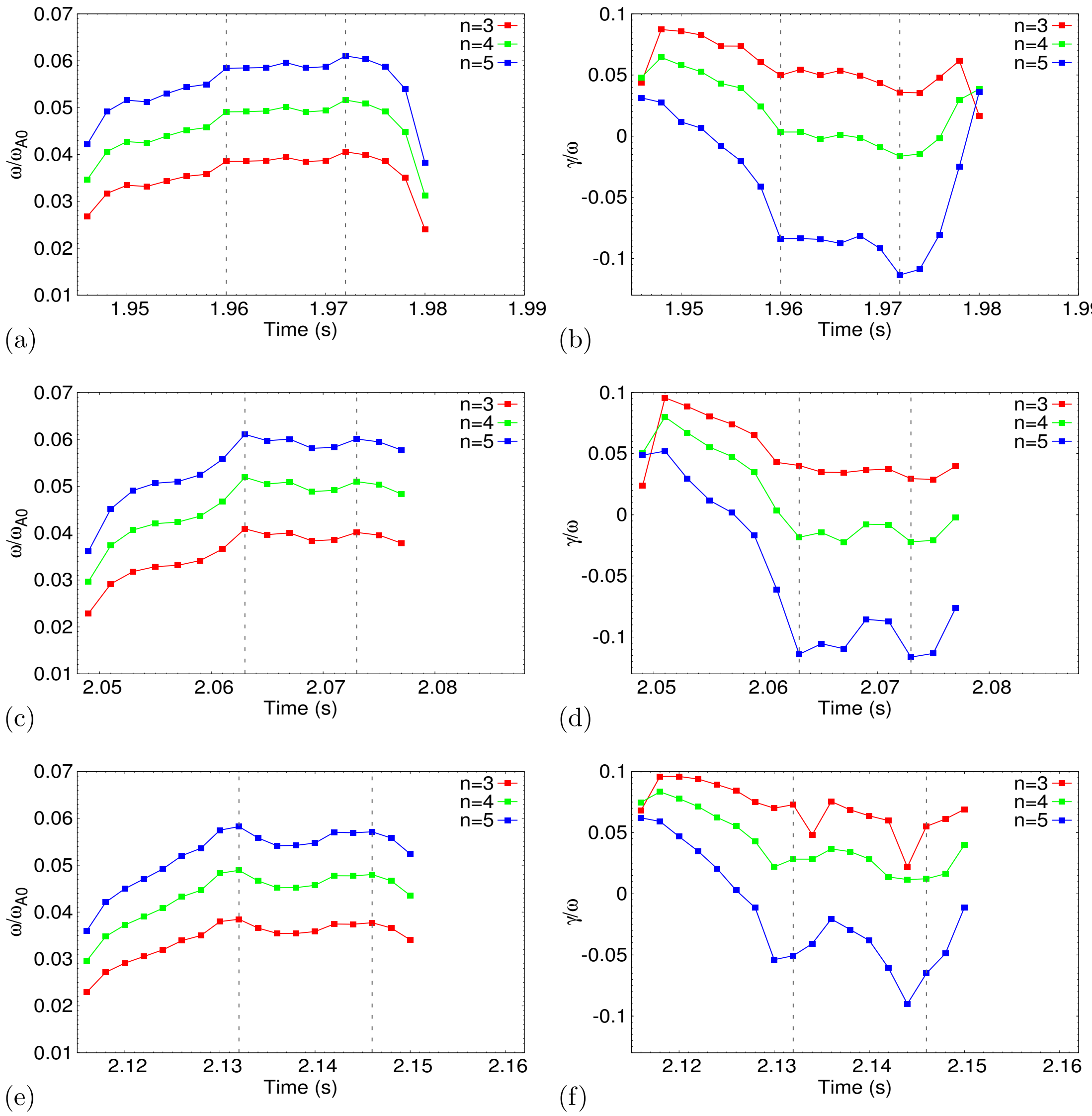

Figure 5.47. Evolution of numerically calculated acoustic Alfvén eigenmode continuum accumulation point frequency and its continuum damping/growth rate at $\rho_{pol}(CAP)$ for toroidal mode numbers $n = 3 - 5$ during sawtooth periods II-IV of discharge 25546.

As has been noted previously in this section, the ordering of the acoustic Alfvén eigenmode CAP frequency is inverted compared to that of BAEs, the continua with the lowest toroidal mode number associated with them having the

lower frequencies. This is evident in figure 5.47, which shows the numerically calculated acoustic Alfvén continuum accumulation point evolution for $n = 3-5$ during periods II-IV of discharge 25546. As has already observed experimentally in section 6.1.2, one of the ways in which these modes differ from BAEs is that they increase in frequency during the initial phase of a sawtooth period and decrease during the final phase. This behaviour is reproduced in figure 5.47, where the acoustic Alfvén eigenmode CAP frequency increases during the first $\sim 10-15$ms of each period. This increase is clearly visible from $t = 1.946-1.960$s, $t = 2.049-2.063$s and $t = 2.116-2.132$s of periods II-IV respectively. A frequency decrease is observed to occur, if not as rapidly as the initial frequency increase, over the final $t \leq 8$ms of each period, from $t = 1.972 - 1.980$s, $t = 2.073 - 2.077$s and $t = 2.146 - 2.150$s during periods II-IV respectively. Experimentally, the modes are not clearly observed during the central phase of each period, surrounded by the aforementioned periods of frequency increase and decrease.
From the numerical calculations, the frequency is observed to remain quite steady during this period. These three successive phases of frequency increase, approximate stationarity and decrease are indicated in figure 5.47 by dashed vertical grey lines separating them, and as was the case for the BAEs, will be referred to as $|t_1|$, $|t_2|$ and $|t_3|$ for whichever sawtooth period is being considered.

	$\|t_1\|$ (s)	$\|t_2\|$ (s)	$\|t_3\|$ (s)
Period II	1.946 – 1.960	1.960 – 1.972	1.972 – 1.980
Period III	2.049 – 2.063	2.063 – 2.073	2.073 – 2.077
Period IV	2.116 – 2.132	2.132 – 2.146	2.146 – 2.150

Table 5.4. Phases of acoustic Alfvén CAP frequency increase, approximate stationarity and decrease during periods II-IV of discharge 25546.

Table 5.4 presents the times encompassed by each phase for reference purposes. The imaginary component of the numerically calculated solution to the kinetic dispersion relation 3.4.61 for the acoustic Alfvén modes was also calculated. This represents the local growth rate or damping of the acoustic Alfvén continuum and is plotted as a fractions of the real frequency γ/ω for sawtooth periods II-IV in figure 5.47. The growth rate of the acoustic Alfvén modes decreases rapidly

initially during $|t_1|$, with the $n = 5$ mode moving from stable to unstable after $\sim$ 7ms, 10ms and 12ms during periods II-IV respectively.
The $n = 4$ mode experiences some damping after $\sim$ 10ms during periods II and III, but remains un-damped during period IV. The $n = 3$ mode remains un-damped during the periods in question. The period of maximum damping, which occurs during $|t_2|$ of each period, is followed by a reduction in the damping rate during $|t_3|$. As has been mentioned, the modes are not clearly observed experimentally during the central phase of each period, coinciding approximately with $|t_2|$. This would be in line with the numerical calculations suggesting high damping rates during this period and will be investigated further later in this section.

Acoustic Alfvén eigenmode CAP evolution with background profile gradients and diamagnetic frequency It has been demonstrated in section 5.4.3 how the background temperature profile and hence the diamagnetic frequency plays a dominant role in determining the BAE frequency evolution and stability.

t(s)	$corr(n = 3)$	$corr(n = 4)$	$corr(n = 5)$
$1.946 - 1.980$	0.9940	0.9943	0.9946
$2.049 - 2.077$	0.9970	0.9967	0.9953
$2.116 - 2.150$	0.9942	0.9975	0.9967

Table 5.5. Correlation between the acoustic Alfvén mode frequency ω and $\nabla T(\rho_{pol}(CAP))$ during select periods of discharge 25546, where $corr$ represents $corr(\omega, \nabla T)$

As such, the analysis of the acoustic Alfvén eigenmode evolution begins by investigating if the same is true of these lower frequency modes. Figure 5.48 shows the evolution of the acoustic Alfvén continuum CAP with the background temperature gradient. As has been introduced in the previous section, each period can be separated broadly into three successive phases of frequency behaviour; increase, approximate stationarity and decrease, indicated by $|t_1| - |t_3|$ respectively. It is immediately evident that a strong relationship exists between the two quantities. In each of the periods II-IV, the rise in frequency of the CAP during $|t_1|$ is accompanied by corresponding increases in the background temperature gradient. Likewise, the decrease in frequency during $|t_3|$ of each period is accompanied by an equivalent decrease in the background temperature gradient. The correlation between these two quantities has been determined for the time periods considered, and is presented in table 5.5. It can be seen that there is a strong positive correlation between the two quantities.

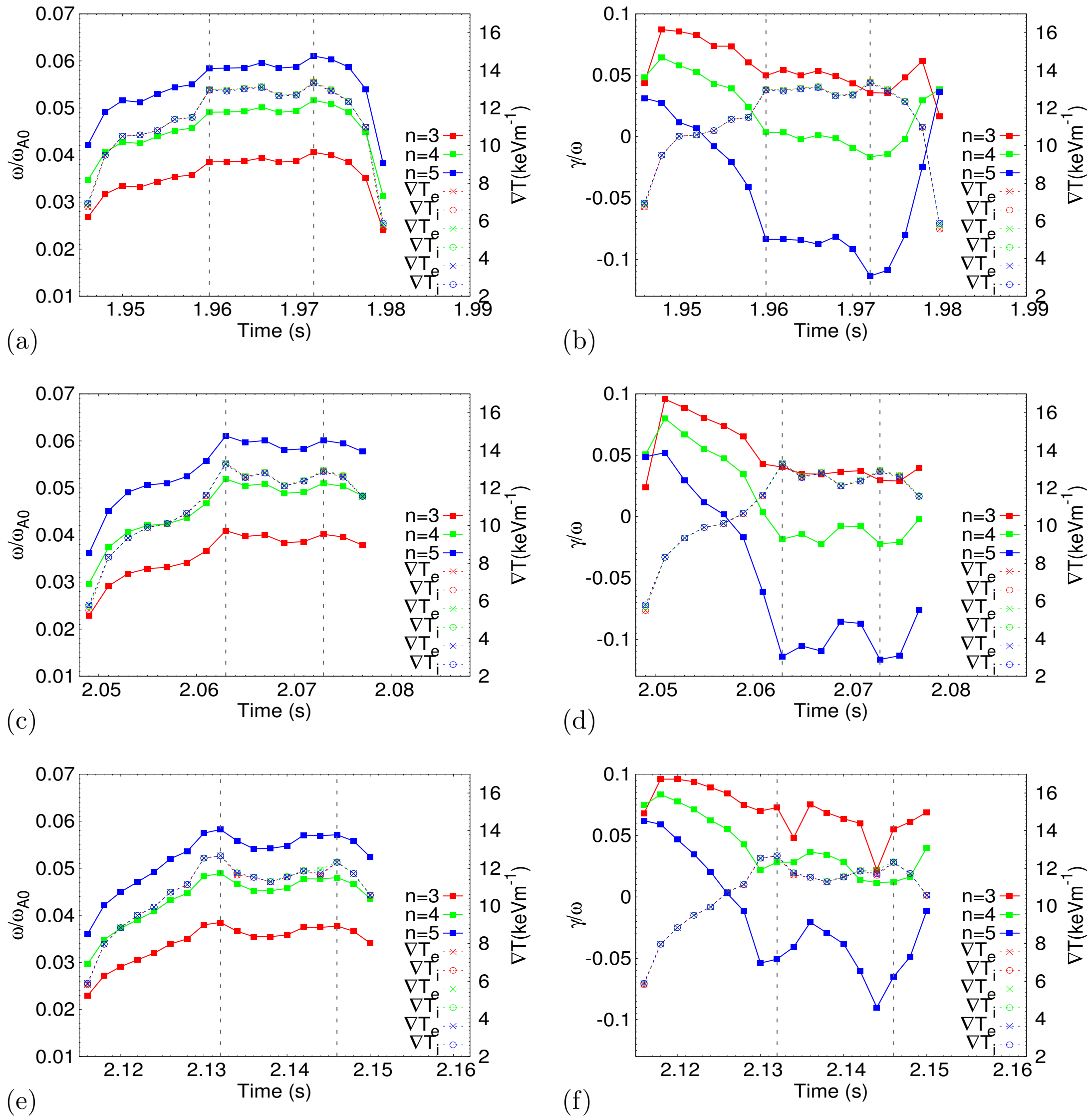

Figure 5.48. Evolution of numerically calculated acoustic Alfvén CAP (a)/(c)/(e) frequency and (b)/(d)/(f) damping/growth rate for $n = 3 - 5$ with the electron and ion temperature gradients at $\rho_{pol}(CAP)$ for sawtooth periods II-IV during discharge 25546.

During $|t_2|$ of each period, when the frequency is observed to remain quite stationary, the temperature gradient is also observed not to vary greatly. Short time-scale changes in the mode frequency during each period are also mirrored by changes in the background gradient, such as those from $t = 2.061 - 2.065$s and $t = 2.128 - 2.134$s during periods III and IV respectively. Figure 5.48 also shows the evolution of the acoustic Alfvén continuum damping/growth rate at $\rho_{pol}(CAP)$ for $n = 3 - 5$ with the electron and ion temperature gradients at the same location. While the growth rate is relatively high at the beginning of each period, this begins to decrease as the background temperature gradient increases during $|t_1|$. As the temperature gradient plateaus during $|t_2|$ of periods II-IV, the rate of change of the damping/growth rate also decreases substantially, steadying greatly excepting some smaller local deviations.

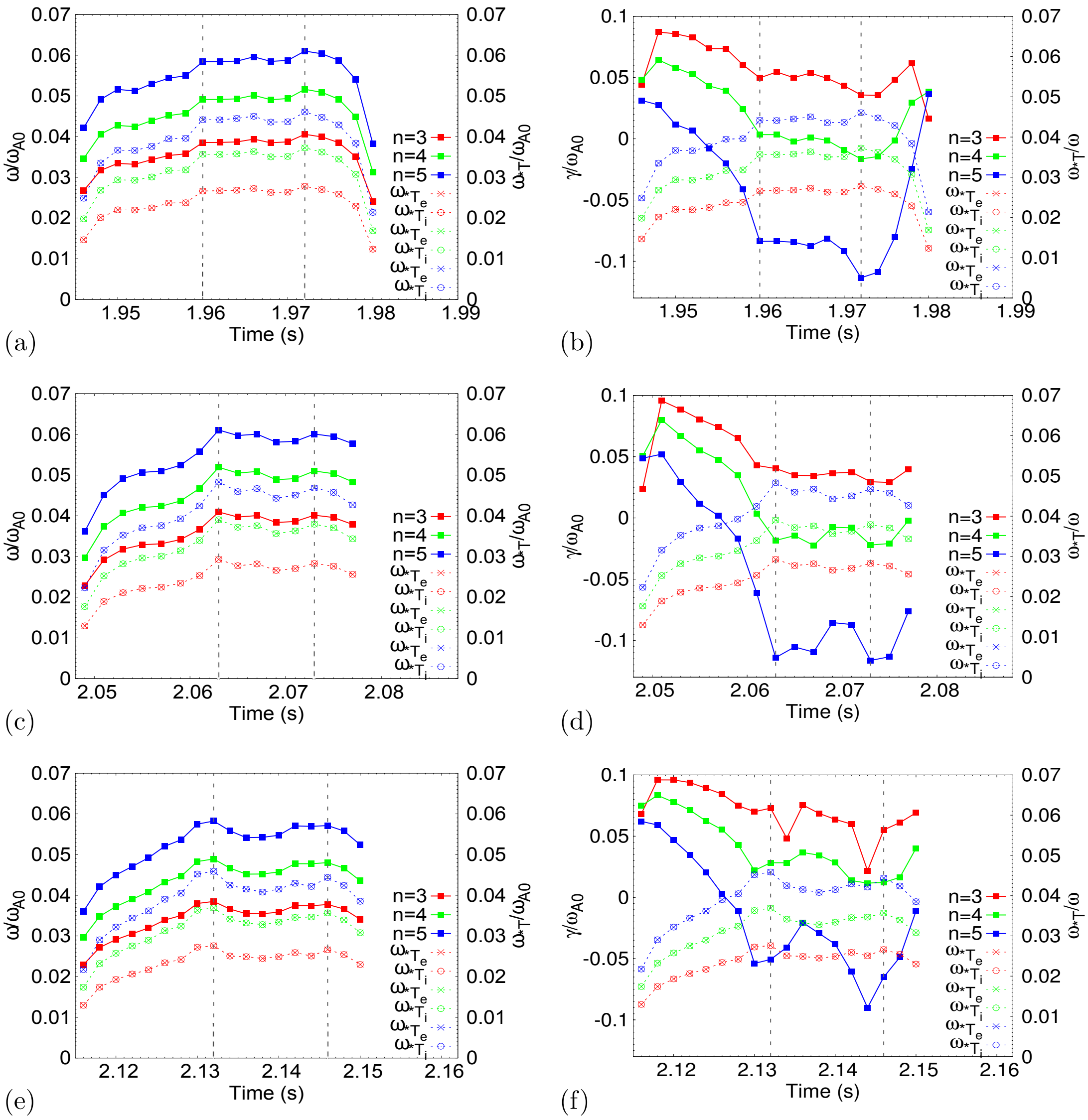

Figure 5.49. Evolution of numerically calculated acoustic Alfvén eigenmode frequency and damping/growth rate for $n = 3 - 5$ with ω_{*T} at $\rho_{pol}(CAP)$ for sawtooth periods I-IV during discharge 25546.

Finally, the decrease in the temperature gradient during $|t_3|$ is observed to be accompanied by a simultaneous decrease in the damping rate. These observations all indicate that the temperature gradient is an important factor in determining the continuum damping/growth rate. Figure 5.49 shows the evolution of the acoustic Alfvén CAP frequency for $n = 3 - 5$ with the electron and ion temperature components of the diamagnetic frequency at $\rho_{pol}(CAP)$. As was the case for the temperature gradient, a very strong relationship appears to exist between the two quantities with the acoustic Alfvén CAP frequency following the evolution of ω_{*T} closely in time. The nature of the relationship between the diamagnetic frequency and the temperature profile and its gradient has been discussed in section 5.4.3, with the dominant contributions of $\nabla T(\rho_{pol}(CAP))$ and the toroidal mode number n to it being highlighted.

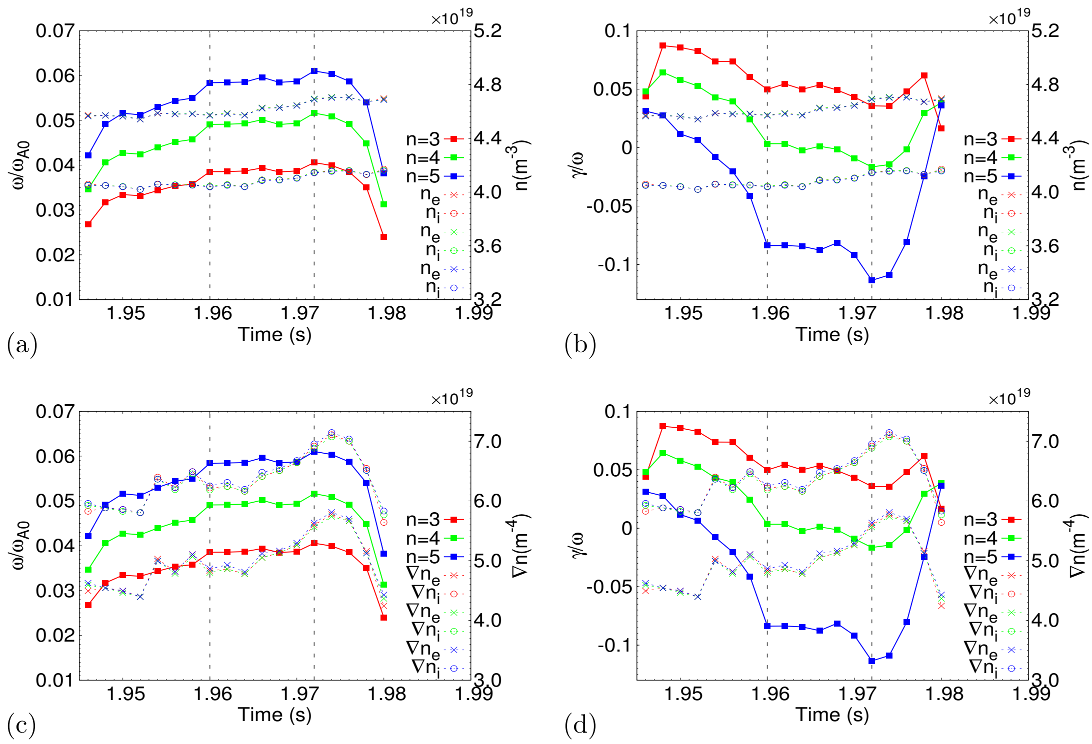

Figure 5.50. Evolution of numerically calculated acoustic Alfvén (a)/(c) CAP frequency and (b)/(d) damping/growth rate for $n = 3 - 5$ with the electron and ion densities and their gradients at $\rho_{pol}(CAP)$ for sawtooth period II during discharge 25546.

The primacy of the diamagnetic frequency in determining the acoustic Alfvén CAP frequency evolution becomes evident when one considers that this is the mechanism through which the background gradients enter into the kinetic dispersion relation. Thus, the increase in ω_{*T} during $|t_1|$ is accompanied by an increase in the mode frequency, the decrease in ω_{*T} during $|t_3|$ by an decrease in the mode frequency and the plateauing of ω_{*T} during $|t_2|$ by approximate stationarity in the mode frequency. The direct relationship between the acoustic Alfvén mode frequency and the diamagnetic frequency is to be expected given the fact that the diamagnetic frequency is of the same order as the mode frequency.

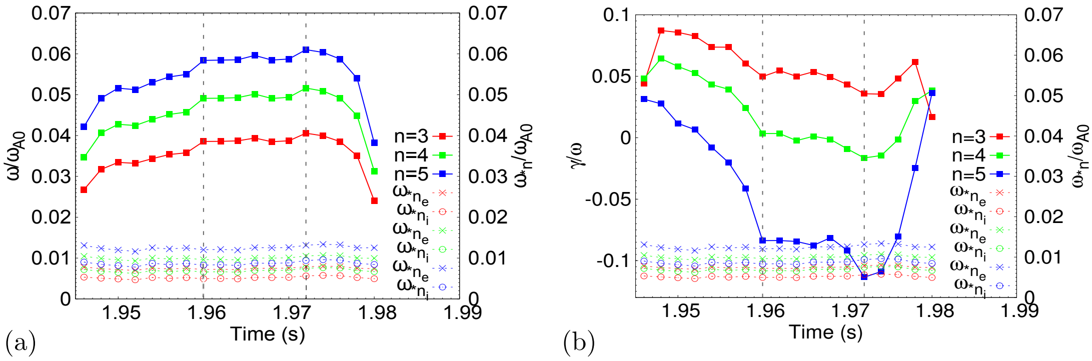

Figure 5.51. Evolution of numerically calculated acoustic Alfvén eigenmode frequency for $n = 3 - 5$ with ω_{*n} at $\rho_{pol}(CAP)$ for sawtooth period II during discharge 25546.

Similarly, the continuum damping/growth rate at the CAP appears to follow ω_{*T} closely, as seen in figure 5.49, with small scale changes in the value of the damping/growth rate being reflected by those of ω_{*T}. Conversely to the case of the BAEs, an increase in ω_{*T} is found to lead to a reduced growth rate. As noted during the BAE analysis, the density does not vary greatly over the course of the periods analysed. It has been demonstrated in section 5.2.4 that due to the large uncertainties in the core electron density and Z_{eff}, it cannot be ascertained for certain whether the density plays an appreciable role in determining the small scale behaviour of the modes. An example of the evolution of the acoustic Alfvén CAP frequency and the continuum damping/growth rate with the background ion and electron densities and their gradients can be seen in figure 5.50.

As has been discussed previously, the density contribution to the diamagnetic frequency is substantially smaller than that of the temperature. Thus, while it appears to play a role in the overall frequency of the acoustic Alfvén modes, it does not seem to influence the small scale behaviour in the same way that the temperature contribution does. Observations of this from period II for both the frequency and damping/growth rate are shown in figure 5.51, with results from the other periods available in appendix B.

Acoustic Alfvén eigenmode CAP evolution with background temperature and density profiles Figure 5.52 shows the evolution of the acoustic Alfvén eigenmode CAP frequency in time with that of the background temperature at $\rho_{pol}(CAP)$. It can be seen that the temperature at the CAP differs little for the different toroidal mode numbers, unlike for the BAEs. This is due to the fact that the radial position of the acoustic Alfvén eigenmode CAP is found not to vary much for different toroidal mode numbers, as has been noted in section 5.4.4. Considering figure 5.52, indicators of a relationship between the temperature and the acoustic Alfvén modes are evident.

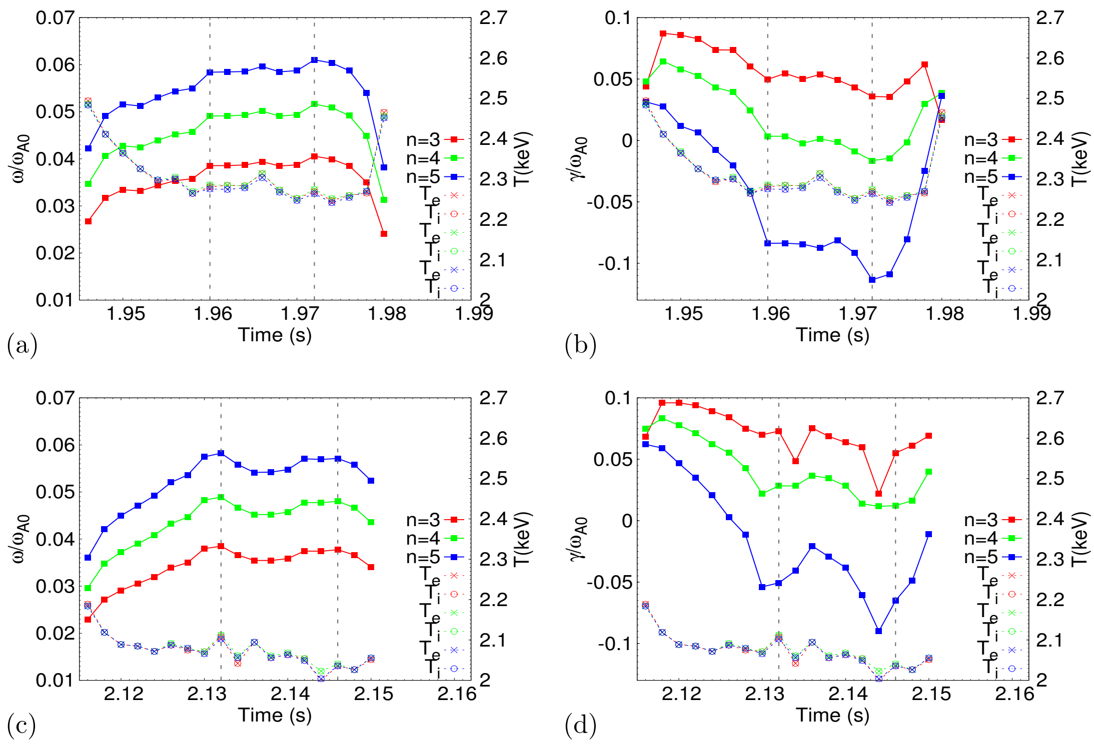

Figure 5.52. Evolution of numerically calculated acoustic Alfvén eigenmode CAP frequency and damping/growth rate for $n = 3 - 5$ with the electron and ion temperatures at $\rho_{pol}(CAP)$ for sawtooth periods II and IV during discharge 25546.

During $|t_1|$ of periods II-IV there are relatively large overall drop in the temperature at $\rho_{pol}(CAP)$, which is accompanied by rise in the mode frequency. Similarly, the temperature saturates during $|t_2|$ of each of the periods, with the frequency also plateauing, as observed in the case of the BAEs. Finally, the rise in temperature during $|t_3|$ is in general accompanied by a drop in the frequency. However, the relationship between temperature and frequency does not hold in all cases, with significant deviations occurring at times such as during $|t_2|$ of period

II. The relationship between the mode frequency and temperature observed in figure 5.52 is understood more clearly when one considers that $\omega_{*T} \propto 1/T$. Thus, any decrease in the temperature will increase ω_{*T} and vice versa.

Figure 5.52 also shows the evolution of the acoustic Alfvén damping/growth rate at $\rho_{pol}(CAP)$ with the background temperature at the same location. Due to the acoustic component of the acoustic Alfvén eigenmode polarisation, they would be expected to experience a greater level of damping at higher temperatures. Period II, which has an average temperature of approximately 2.3keV during $|t_2|$, does appear to experience a higher damping rates and a lower growth rate than period IV, which has a temperature that varies from $T \approx 2.0 - 2.1$keV during the equivalent period.

Evolution of radial location of acoustic Alfvén eigenmode CAP Figure 5.53 shows the evolution of the acoustic Alfvén frequency for $n = 3-5$ at the CAP radial locations, with the corresponding CAP radial location for sawtooth periods II-IV during discharge 25546. It can be seen that $\rho_{pol}(CAP)$ moves outwards as each period progresses, with values ranging from $\rho_{pol}(CAP) \approx 0.340 - 0.375$ during periods II and IV. Similar observations from period II are presented in appendix B.

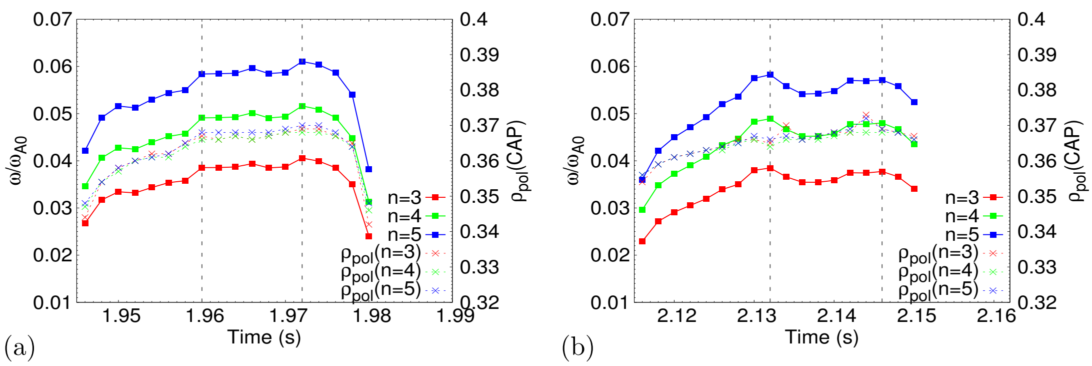

Figure 5.53. Evolution of numerically calculated acoustic Alfvén eigenmode frequency and damping/growth rate for $n = 3-5$ at the CAP radial locations, with the corresponding CAP radial loaation for sawtooth periods II and IV during discharge 25546.

Agreement between experimental observations of acoustic Alfvén eigenmodes and numerical results from rootsolver Figure 5.54 compares the evolution in time of the numerically calculated acoustic Alfvén CAP frequency with experimental observations during the equivalent periods from the core localised $I51$ channel of the soft x-ray diagnostic, with a tangency radius of $\rho_{pol} \approx 0.244$.

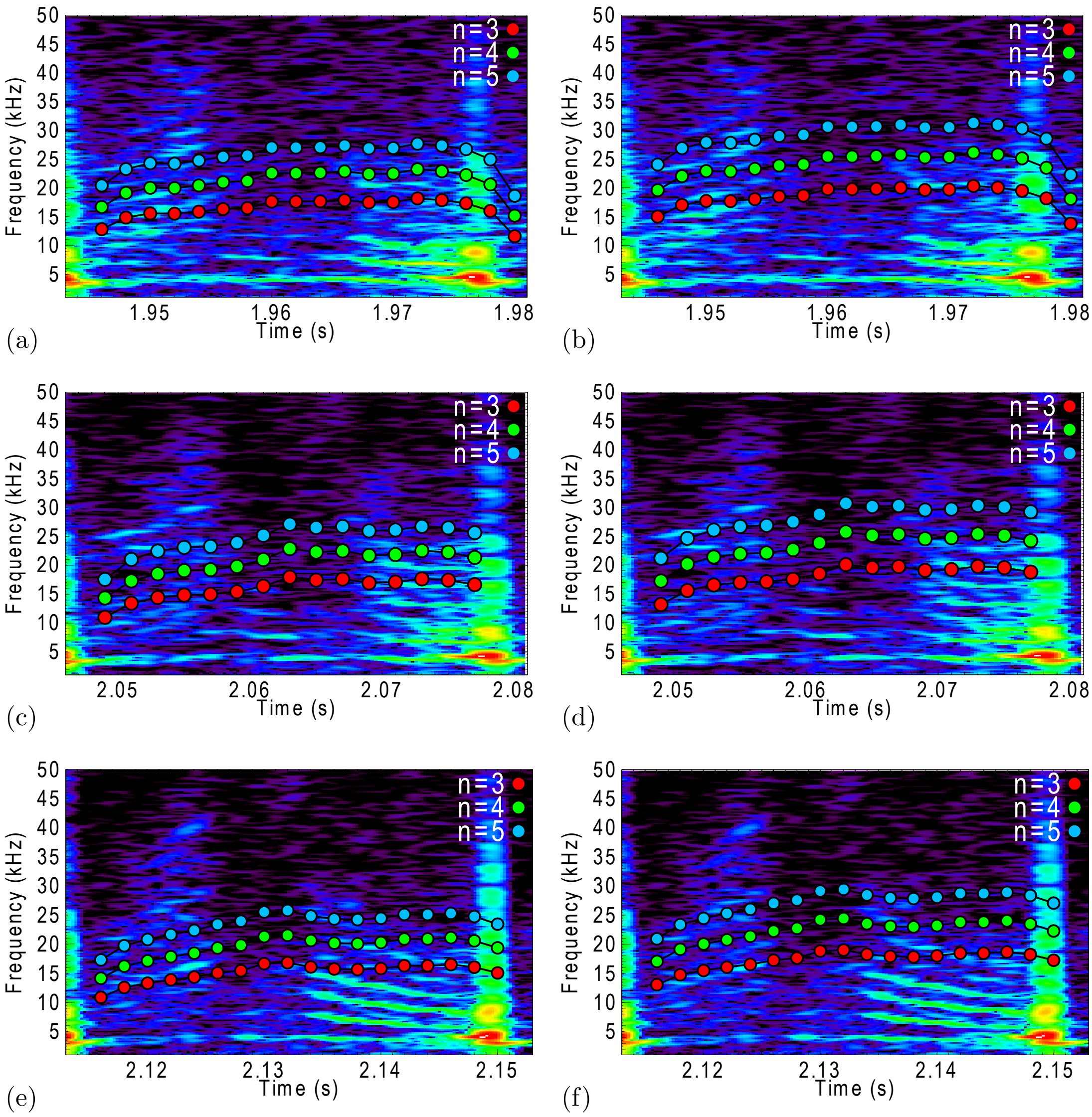

Figure 5.54. Comparison between numerically calculated acoustic Alfvén CAP frequencies for toroidal mode numbers $n = 3 - 5$ with mode frequencies observed experimentally using channel I51, with $nfft = 8192$ and $nstp = 512$, of the soft x-ray diagnostic, with a tangency radius of $\rho_{pol} \approx 0.244$, during periods II-IV of discharge 25546. Plots (a), (c) and (e) use an estimate for toroidal rotation from discharge 26621 while plots (b), (d) and (f) use an estimate from discharge 26622.

These numerical results are subject to an upward Doppler shift in frequency of nf_{rot}, as was the case for the BAEs. Thus, two sets of results are presented, using estimates for the toroidal rotation from discharges 26621 and 26622 for the reasons discussed in section 5.4.3. However, no estimate for the acoustic Alfvén eigenmode frequency with the effects of trapped particles and particles with finite $v_\perp$ taken into account was available from LIGKA in this case. This stems from the difficulty in locating the modes numerically, owing to their very low frequencies. Thus, as the acoustic Alfvén eigenmodes are expected to be even more susceptible to trapped particle effects than BAEs, due to their lower frequencies resulting in interactions with the bounce and drift orbit frequencies, the estimate for the maximum frequency down-shift obtained from the $n = 6$ case during the BAE analysis was applied here as a lower threshold for the estimated frequency down-shift due to the influence of trapped particle and particles with finite $v_\perp$. This lack of information regarding the frequency down-shift, added to the fact that no reliable estimates for the toroidal mode numbers of the acoustic Alfvén eigenmodes were available, meant that it was not possible to definitively compare the numerical and experimental results. Thus, this analysis serves more as a qualitative comparison between them than as a quantitative one.

Upon applying the previously discussed assumptions, it can be seen from figure 5.54 that the numerically calculated acoustic Alfvén mode frequencies occur within the same frequency regime as the experimentally observed modes, from $f = 10 - 45$kHz. During $|t_1|$, they increase in frequency at a rate similar to the experimentally observed modes, with the modes of higher toroidal mode number experiencing a higher rate of increase. The frequency separation between distinct toroidal eigenmodes is also well reproduced numerically. As discussed previously, and as can be seen from figure 5.54, mode activity is essentially absent above $f \approx 10$kHz during the central phase $|t_2|$ of each period. During the final phase of the three periods, the experimentally observed mode frequency decreases until the end of the sawtooth period. The numerically calculated modes are found to decrease slightly in frequency during this period, but not to the same extent as the experimentally observed modes. Despite this, the qualitative shift in the direction of the numerically calculated mode frequency evolution, from essentially stationary to decreasing, is observed to begin at approximately the same time-point that the modes become visible again in the experimental observations. This lack of agreement during $|t_3|$, as was the case for the BAEs, suggest the presence of additional physics towards the end of the sawtooth cycle that is not included in this analysis. This is considered further in section 6.3.

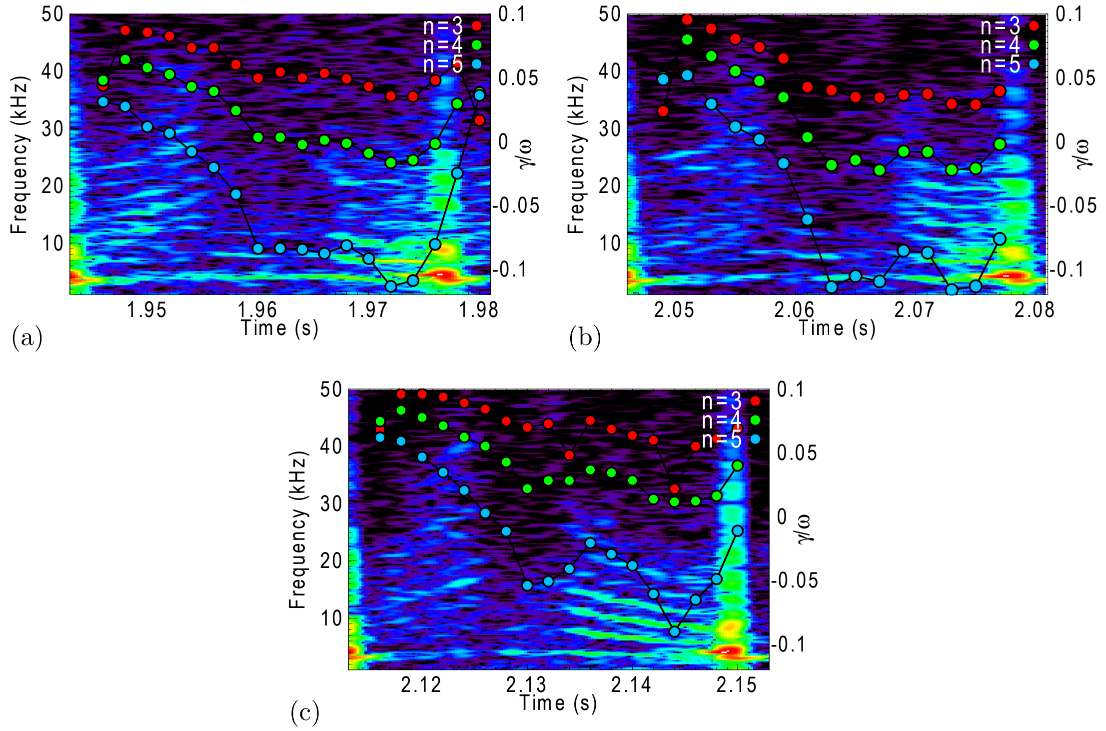

Figure 5.55. Comparison between numerically calculated acoustic Alfvén CAP damping/growth rates for toroidal mode numbers $n = 3 - 5$ with mode frequencies observed experimentally using channel I51, with $nfft = 8192$ and $nstp = 512$, of the soft x-ray diagnostic, with a tangency radius of $\rho_{pol} \approx 0.244$, during periods II-IV of discharge 25546.

Figure 5.55 shows again the experimentally observed mode evolution during periods II-IV, but this time with the numerically calculated continuum damping/growth rates over-plotted. It is seen that the highest growth rates occur during $|t_1|$, coinciding with a phase of experimentally observed acoustic Alfvén eigenmode activity. The growth rate at $\rho_{pol}(CAP)$ is calculated to be larger for modes with lower toroidal mode numbers. If one assumes that the experimentally observed acoustic Alfvén modes increase in frequency with increasing toroidal mode number, as is found from the numerical results, then these calculations are in broad agreement with the experimental observations, the modes with lower toroidal mode numbers being observed to have larger amplitudes, while decreasing in amplitude as one considers the modes with higher toroidal mode number and frequency. The calculated damping rate increases as the periods enter $|t_2|$, and this is accompanied by a corresponding decrease in the experimentally observed mode activity. During $|t_3|$, renewed prominent acoustic Alfvén eigenmode is observed. However, the numerically calculated growth rate is not observed to increase appreciable and remains steady in most cases, with increased damping in the $n = 5$ case.

5.5 Conclusion

The analysis conducted in this chapter focussed on the effect of background plasma profiles on BAEs and acoustic Alfvén eigenmodes. The character of the safety factor was also investigated, in particular the existence and radial location of the $q = 1$ surface. As expected, during the appearance of the sawtooth instability, a $q = 1$ rational surface in the core region of the plasma was recovered. This rational surface was typically found to occur in the same region as high background temperature gradients.

The evolution of the BAEs and acoustic Alfvén eigenmodes during the sawtooth cycle was investigated both experimentally and numerically in this chapter. It was found that both types of mode occur close to the $q = 1$ surface location and that their frequency evolution and damping/growth rates are determined mainly by the diamagnetic frequency, primarily through its dependence on the thermal profile gradients. These observations have important implications for the form of q-profile that will be chosen for future reactors, as they indicate that BAEs could be driven unstable if the $q = 1$ surface occurs too close to regions of high background gradient.

The acoustic Alfvén eigenmodes were observed during periods of ICRH only to be present during the early and latter phases of a sawtooth period. However, they were found to be absent during the central phase. It was determined numerically that the continuum damping rate for these modes increases during the central phase of the sawtooth period, in conjunction with the background temperature gradient increasing. This is in agreement with the observed mode behaviour, higher damping rates resulting in reduced mode activity during this period. The opposite is the case in the early and latter phases of the sawtooth period, with the observed mode activity being accompanied by increased mode drive.

Chapter 6

Low-frequency Alfvén eigenmode behaviour during ICRH/ECRH phase of selected discharges with parameter scans of potential plasma parameter regimes

Chapter 5 investigated the influence of background temperature and density profiles on BAEs and acoustic Alfvén eigenmodes during the ICRH phase of ASDEX Upgrade discharges 25544, 25546 and 25549. It was demonstrated that the background electron and ion temperature gradients in particular play an important role in determining the dynamics of these modes via terms in the kinetic dispersion relation 3.4.61 proportional to the diamagnetic frequency. In this chapter, the previous analysis will be extended to a period of discharge 25546 when both ICRH and ECRH are employed. As alluded to in chapter 5, the nature of the BAE and acoustic Alfvén eigenmode behaviour changes with the introduction of ECRH. The effect that this has on the temperature profile, and thus on the mode dynamics, will be investigated experimentally and numerically in sections 6.1 and 6.2 respectively, in a manner similar to the analysis carried out in chapter 5. Section 6.3 consists of a series of parameter sensitivity scans for BAEs and acoustic Alfvén eigenmodes. These aim at explaining certain discrepancies that were observed to arise between the experimental observations and the numerical results during chapter 5. This was undertaken by testing the effects of various model background profiles on the mode dynamics as well as by utilising experimental data obtained from similar discharges that was unavailable for discharge 25546.

6.1 Observations of low-frequency mode behaviour and plasma profile evolution during ICRH/ECRH phase of discharges 25544, 25546 and 25549

6.1.1 Observed evolution of electron temperature and density profiles

Observations of evolution of main plasma parameters The analysis conducted in chapter 5 dealt with the period of discharge 25546 from $t = 1.70 - 2.50$s, when ICRH was the only source of external heating. Figure 6.1 shows time-traces of the input ICRH, ECRH and NBI powers from $t = 1.70 - 5.00$s, as well as the core and edge electron densities measured by interferometry.

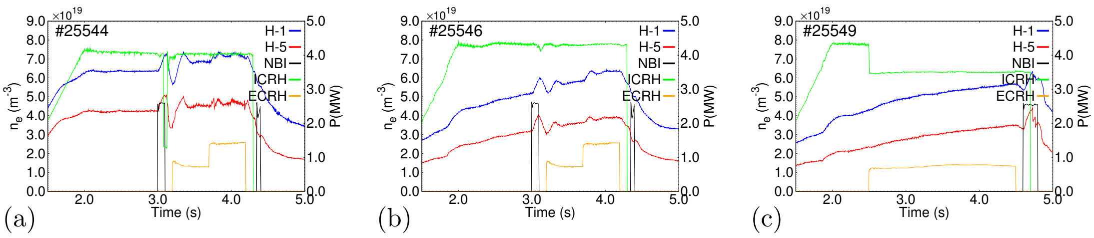

Figure 6.1. Time-traces of core and edge electron densities as well as ICRH, ECRH and NBI input powers during discharges 25544, 25546 and 25549.

In this section, the focus will be on the period of discharge 25546 from $t = 3.00 - 4.30$s, during which time ECRH is introduced to augment the total heating power. Approximately 0.9MW of ECRH power is introduced at $t \approx 3.2$s, and this is increased to approximately 1.5MW at $t \approx 3.7$s. This period was accompanied by a steady increase in the core and edge densities from $n_e \approx 5.35 - 6.36 \times 10^{19}\text{m}^{-3}$

and $n_e \approx 3.06 - 3.90 \times 10^{19}\text{m}^{-3}$ respectively. Small, temporary increases in the electron density accompany the increases in ECRH power at $t \approx 3.2$s and $t \approx 3.7$s, as is seen in figure 6.2. The ICRH power was kept at approximately the same level of $P_{ICRH} \approx 4.3$MW as during the analysis in chapter 5. The introduction of ECRH at $t \approx 3.2$s has an immediate effect on the electron temperature, with the core value jumping appreciably, this increase in temperature being compounded by the introduction of further ECRH power at $t \approx 3.7$s. This can be seen in figure 6.2, which presents time-traces of the electron density and temperature from $t \approx 1.7 - 5.0$s, as measured by interferometry and ECE diagnostics respectively. For discharges 25546 and 25549 it also marked the end of the prevailing downward trend in electron temperature that had persisted since $t \approx 2.0$s.

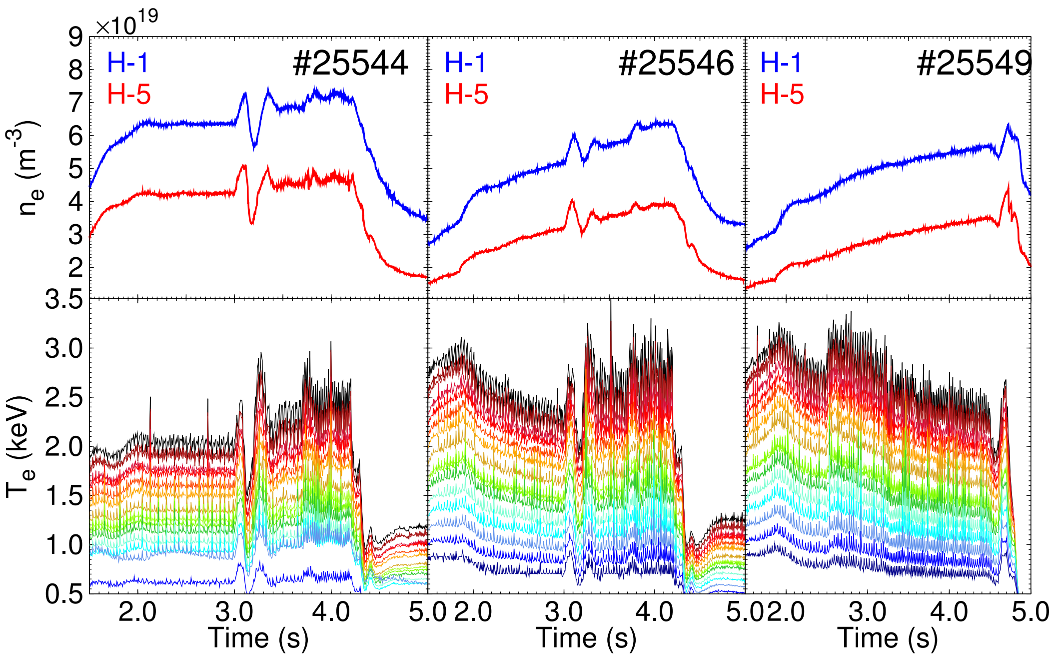

Figure 6.2. Time-traces of electron density and temperature from interferometry and ECE respectively during ECRH/ICRH phase of discharges 25544, 25546 and 25549.

Electron temperature evolution during individual sawtooth periods

For the purposes of this analysis, two different sawtooth periods during the ECRH phase of discharge 25546 were selected. These will be referred to as periods I and II during this chapter, and are distinct from the periods I and II considered in chapter 5. Period I lasts from $t \approx 3.303-3.342$s and occurs during the phase from $t \approx 3.20 - 3.70$s when ECRH power is first introduced while period II lasts from

$t \approx 3.873 - 3.898$s and occurs during the subsequent phase from $t \approx 3.70 - 4.20$s when the ECRH power is increased.

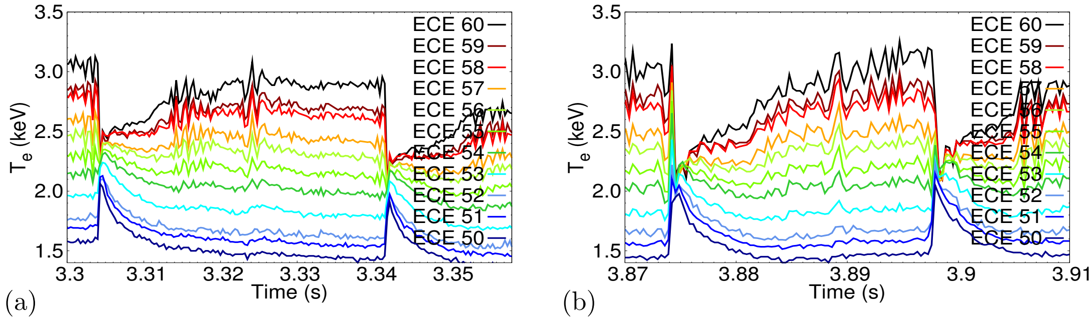

Figure 6.3. Time-traces of T_e during periods I and II of the ECRH/ICRH phase of discharge 25546, measured using channels of the ECE radiometer diagnostic covering the radial ranges $0.197 \leq \rho_{pol} \leq 0.403$ and $0.191 \leq \rho_{pol} \leq 0.399$ respectively.

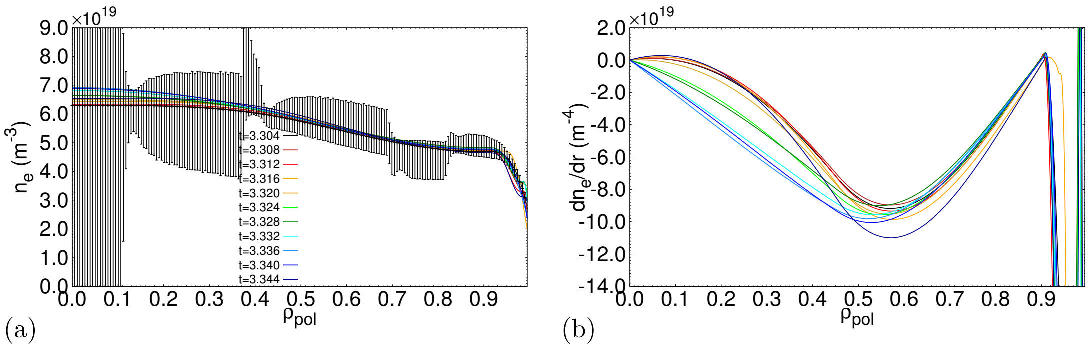

Figure 6.4. Electron density profile and gradient evolution during period I of the ECRH/ICRH phase of discharge 25546.

Figure 6.3 shows time-traces of the core electron temperature, measured using the ECE diagnostic, during these two periods. It should be noted that typically the electron temperature data was only available from $\rho_{pol} \approx 0.18$ outwards during these periods. As expected, the peak core electron temperature is higher during period II on account of the higher ECRH power. The electron temperature also continues to increase until the end of the period, while during period I it saturates after $t \approx 3.326$s. During periods I and II the evolution of the temperature channels stays steady until the sawtooth crash, not exhibiting the same convergence in temperature seen in the ~ 5ms leading up to the sawtooth crash in figure 5.2. This convergence signifies a flattening in the electron temperature profile in the vicinity of the radial location of these channels and appears to be absent during periods I and II.

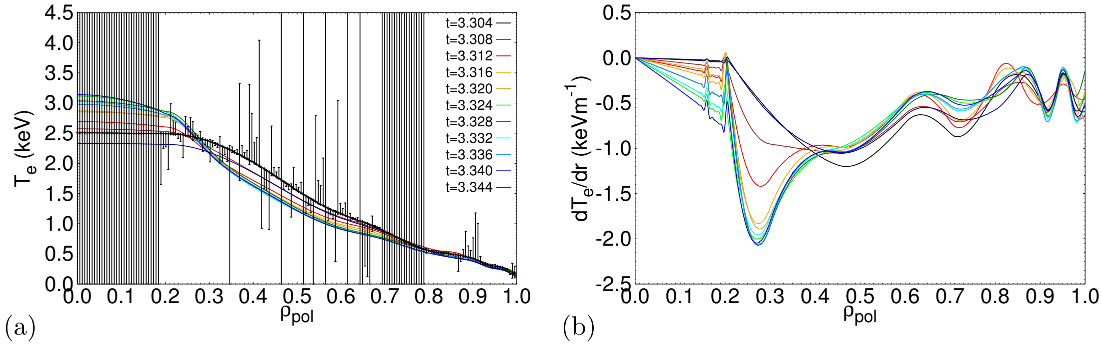

Figure 6.5. Electron temperature profile evolution during period I of ECRH/ICRH phase, as well as the corresponding gradients during discharge 25546.

Figure 6.5 demonstrates the evolution of the electron temperature profile during period I, as well as the gradients with respect to the mid-plane radius, obtained from IDA. The saturation in the electron temperature gradient towards the end of period I is evident in this figure, with the gradients increasing rapidly in the early phase of the period, before remaining quite steady for the remainder of the period.

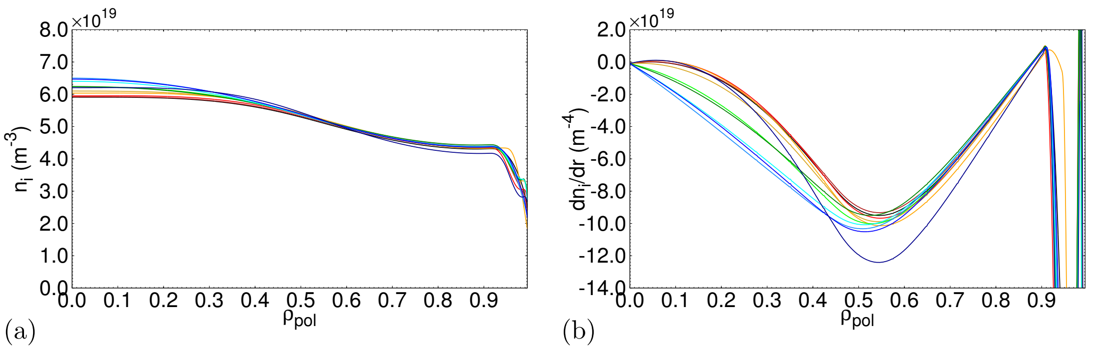

Figure 6.6. Ion density profile and gradient evolution during period I of ECRH/ICRH phase of discharge 25546.

Figures 6.4 and 6.6 show the evolution of the electron and ion density profiles and their respective gradients during period I. This period appears to exhibit significantly more variation in the core profiles and gradients than was the case during the ICRH only phase. This can be seen by comparing these observations with those from figure 5.11. The core ion density appears to increase appreciably during the later phase of the sawtooth period. As has been mentioned before, the core density has large uncertainties associated with it and thus any consideration of its effects are subject to significant caveats. Nonetheless, it is instructive to investigate whether these experimental observations of the density evolution agree with observations of the mode frequency evolution, as will be considered in sections 6.1.2 and 6.2.

6.1.2 Observed low-frequency mode evolution

BAEs In section 5.2, observations of the BAE frequency evolution during certain sawtooth periods from $t = 1.70 - 2.50$s were considered. It was observed that the BAEs possessed a clear frequency separation between distinct toroidal eigenmodes in most cases, with each distinct toroidal eigenmode exhibiting a drop in frequency over the course of a sawtooth period before returning to approximately its original value. The overall variation in the typical BAE frequency was also observed to have a range of approximately 5kHz from $t = 1.70 - 2.50$s, as observed in figure 5.5.

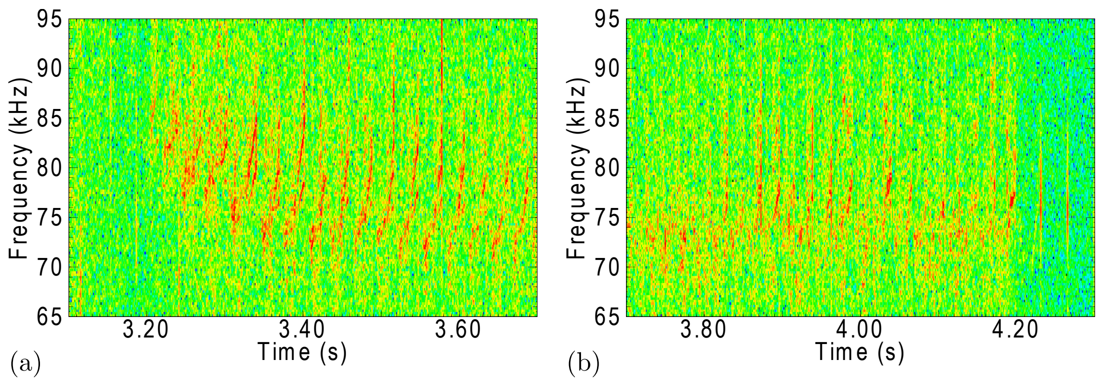

Figure 6.7. Observations of BAE frequency evolution from $t \approx 3.10 - 4.50$s during ECRH/ICRH phase of discharge 25546, made using channel I50 of the soft x-ray diagnostic, with $nfft = 8192$ and $nstp = 512$.

In the case of the modes observed upon the introduction of ECRH, this behaviour changes quite extensively. Firstly, the range of frequencies over which the BAEs are observed is much larger. As seen in figure 6.7, at $t \approx 3.23$s, when the BAE activity resumes, the most prominent mode activity observed has a frequency of ~ 82kHz. By $t \approx 3.77$s when the minimum BAE frequency is observed, this has dropped to ~ 70kHz. The observations of BAEs during individual sawtooth periods are much less distinct than in the ICRH only case, lacking the clear frequency separation between distinct toroidal eigenmodes observed during the

ICRH only periods during their initial phase.

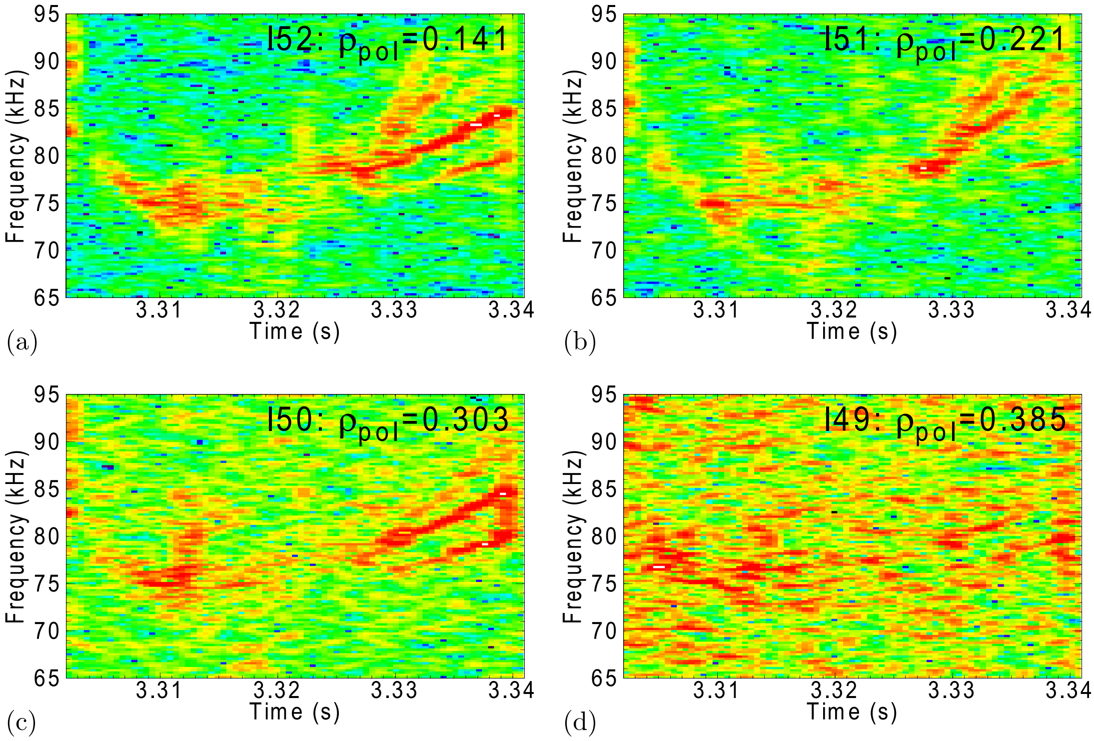

Figure 6.8. BAE activity during period I of discharge 25546, observed using channels I52-I49 of the soft x-ray diagnostic, with $nfft = 8192$ and $nstp = 512$.

An examples of the evolution of BAEs during period I, made using core channels of the soft x-ray diagnostic, is presented in figure 6.8. During the later phase of certain ECRH/ICRH sawtooth periods, such as period I, distinct toroidal eigenmodes with an almost linear increase in frequency are observed. These modes are clearly observed using channels I52-I50, which have tangency radii of $\rho_{pol} \approx 0.141, 0.221$ and 0.303, while the signal appears to be dominated by noise for channel I49, which has a tangency radius of $\rho_{pol} \approx 0.385$. This suggests that the modes are core localised, as was the case for the BAEs in chapter 5.

Acoustic Alfvén eigenmodes Observations of acoustic Alfvén eigenmodes have been investigated in sections 5.3.4, 6.1.2 and 5.4.4. It was observed that a prominent feature of these modes was the fact that they were primarily observed during the initial and latter phases of the sawtooth periods, with a distinct lack of activity during the central phase.

Figure 6.9 shows acoustic Alfvén eigenmode activity, measured using core soft x-ray lines of sight, during sawtooth period I of the ECRH/ICRH phase. It can be seen that the behaviour of the modes differs from that observed during the ICRH only phase, with the mode activity being primarily confined to the central region of each period, and the initial and latter regions exhibiting very little mode activity. The maximum mode frequency observed is also much less than in the case of the periods during the ICRH only phase, with frequencies typically less than $f \approx 20$kHz. As in the case of the BAEs, the clearest observations during both periods come from soft x-ray channels I52-I50, suggesting that the modes are localised in the region $\rho_{pol} < 0.385$.

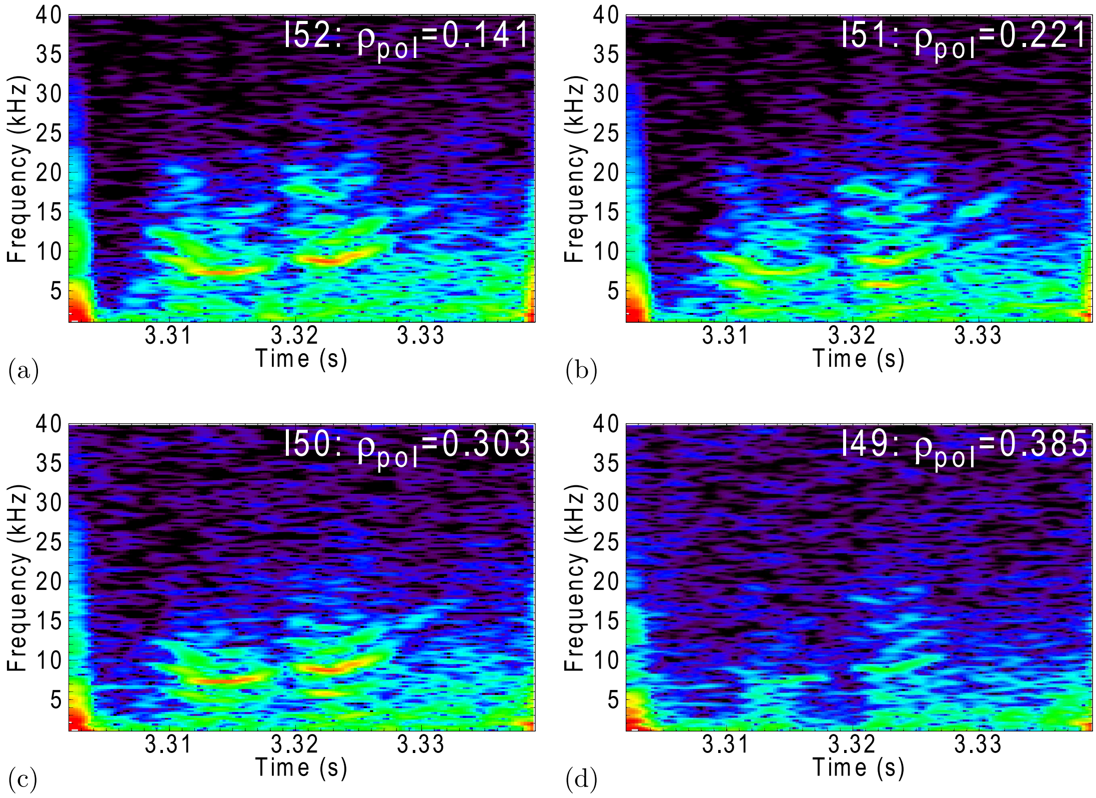

Figure 6.9. Acoustic Alfvén eigenmode activity during period I of discharge 25546, observed using channels I52-I49 of the soft x-ray diagnostic, with $nfft = 8192$ and $nstp = 512$.

6.1.3 BAE and acoustic Alfvén eigenmode frequency evolution with background profile values at q=1 surface

During the ICRH only phase of discharge 25546, the $q = 1$ surface was estimated to be radially localised in the region $\rho_{pol} \approx 0.31 - 0.35$, as has been discussed in section 5.3.1. An estimate for the error in the $q = 1$ surface radial location was obtained by inspecting results for a fitted q-profile at $t = 2.066$s during discharge 25546, obtained using CLISTE, which included confidence bands for the q-profile and has similar parameters.

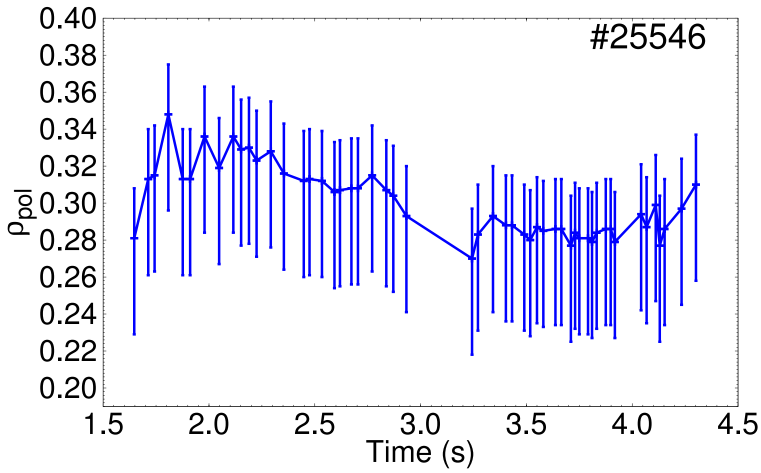

Figure 6.10. Time-trace of $q = 1$ surface location, estimated from sawtooth inversion radius, for discharge 25546.

The short period of NBI heating introduced at $t \approx 2.994$s and the introduction of ECRH at $t \approx 3.193$s result in the estimated $q = 1$ surface radial location being shifted further inwards.

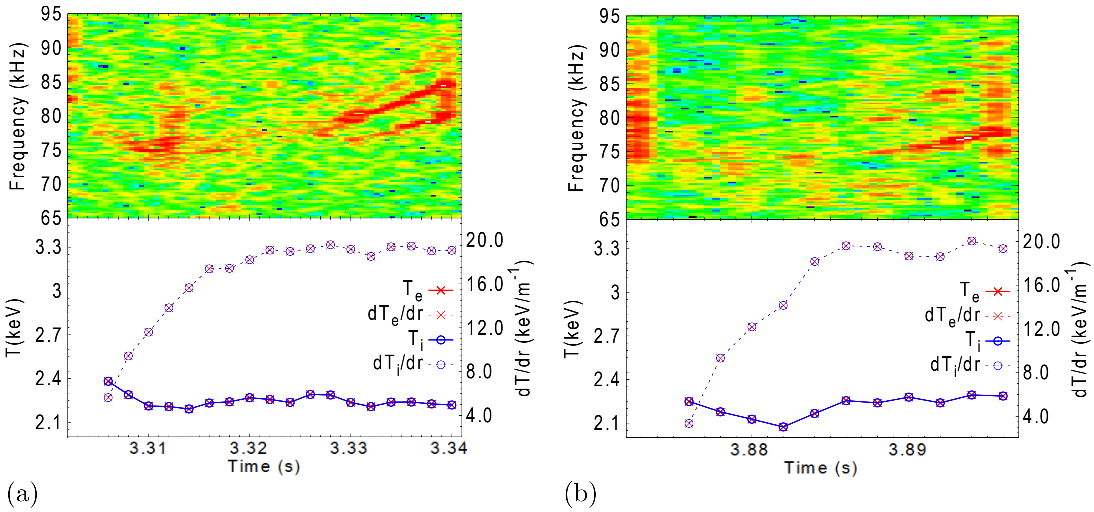

Figure 6.11. BAE frequency evolution from (a) $t = 3.302 - 2.341$s and (b) $t = 3.872 - 3.897$s during discharge 25546, measured using line of sight $I50$ of the soft x-ray diagnostic, with $nfft = 8192$ and $nstp = 512$, with a tangency radius of $\rho_{pol} \approx 0.303$ and the corresponding evolution in the background profiles at the $q = 1$ surface.

From $t \approx 3.3 - 4.0$s, it is estimated to be localised in the region $\rho_{pol} \approx 0.27 - 0.30$, as can be seen in figure 6.10. It has been discussed in chapter 5 how the positions of the $q = 1$ surface and regions of high background profile gradients relative to one another can have a significant impact on the low-frequency mode dynamics. Thus, the inward shift in the $q = 1$ surface could account to some degree for the differences in mode behaviour observed between the ICRH only phase and that when ECRH is also present. This will be investigated numerically in the sections that follow. Figure 6.11 presents observations of BAE activity during periods I and II from soft x-ray channel I50, as well as the evolution of the background temperature and density profiles and their gradients at the $q = 1$ surface location.

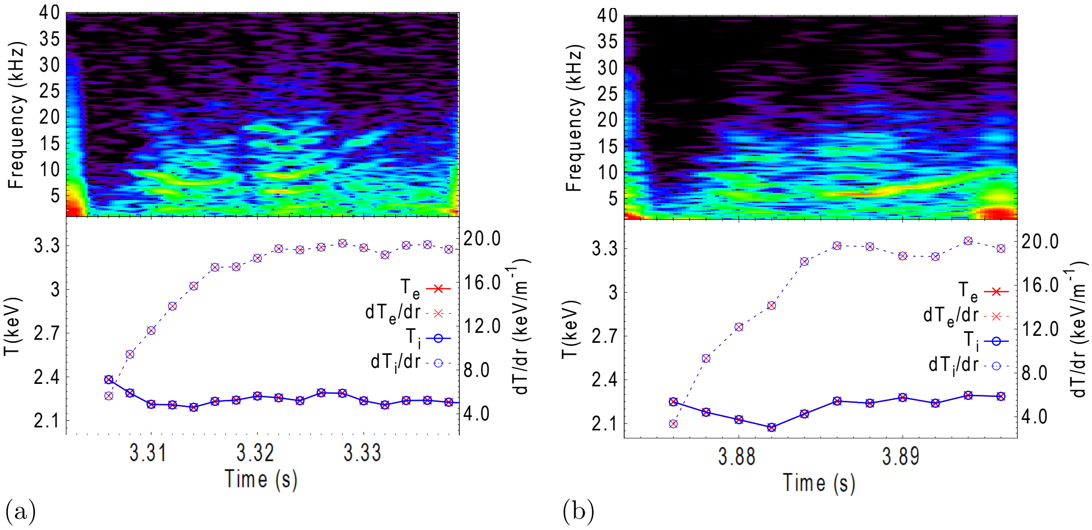

Figure 6.12. BAE frequency evolution from (a) $t = 3.302 - 3.339$s and (b) $t = 3.873 - 3.897$s during discharge 25546, measured using line of sight $I51$ of the soft x-ray diagnostic, with $nfft = 8192$ and $nstp = 512$, with a tangency radius of $\rho_{pol} \approx 0.303$ and the corresponding evolution in the background profiles at the $q = 1$ surface.

The saturation in the electron temperature discussed earlier in this chapter is observed at the $q = 1$ surface location during period I, shown in figure 6.11 (a), with the electron temperature gradient reaching a maximum of $\nabla T_e \approx 20\text{keVm}^{-1}$ at $t \approx 3.328$s and remaining close to this value for the remainder of the period. The electron temperature also does not vary greatly over the course of period I. Period II exhibits similar frequency and background profile behaviour to period I. Weak mode activity is observed from $t \approx 3.875 - 3.887$s, with moderate frequency separation between distinct toroidal eigenmodes observed from $t \approx 3.887 - 3.895$s. As during period I, the electron temperature gradient saturates from $t \approx 3.886$s onwards. As can be seen in figure 6.12, during periods I and II acoustic Alfvén eigenmode activity is observed from $t \approx 3.308 - 3.333$s and $t \approx 3.878 - 3.893$s respectively for the lowest frequency distinct toroidal eigenmodes, but not for the initial and final ~ 5ms of each sawtooth period. As the observed electron temperature gradient evolution differs during these initial and final phases it is not immediately clear what mechanism is responsible for this behaviour. This is investigated numerically later in this chapter.

6.2 Numerical investigation of low-frequency mode continua during ICRH/ECRH phase of discharge 25546

6.2.1 Numerical recovery of BAE continuum accumulation point and damping/growth rate

BAE continuum accumulation point evolution during sawtooth period I The evolution of the BAE continuum during sawtooth periods I and II of the ECRH/ICRH phase from discharge 25546 is investigated in this section, again by solving the kinetic dispersion relation 3.4.61 numerically and following the methods described in section 5.4.3.

Figure 6.13 shows the evolution of numerically calculated (a) BAE continuum accumulation point frequency and (b) continuum damping/growth rate at $\rho_{pol}(CAP)$ for toroidal mode numbers $n = 3 - 6$ during sawtooth period II of ECRH phase of discharge 25546. It can be seen that these results differ in certain aspects from those calculated for BAEs during the ICRH only case in section 5.4.3. The initial frequency of the various distinct toroidal eigenmodes is relatively high, ranging from $\omega_{BAE} \approx 0.187 - 0.201$, and dropping by $\Delta\omega_{BAE} \approx 0.028$ by $t = 3.882$s in the $n = 6$ case. This drop is much larger than that calculated for the BAEs in the previous chapter.

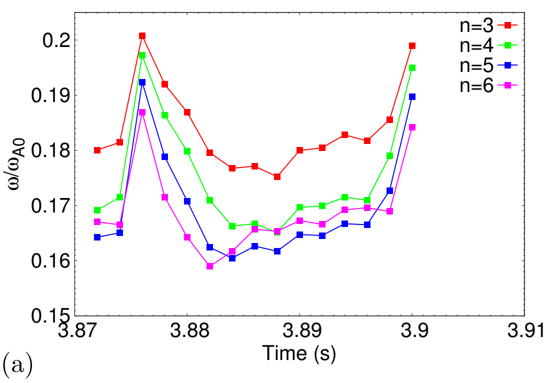

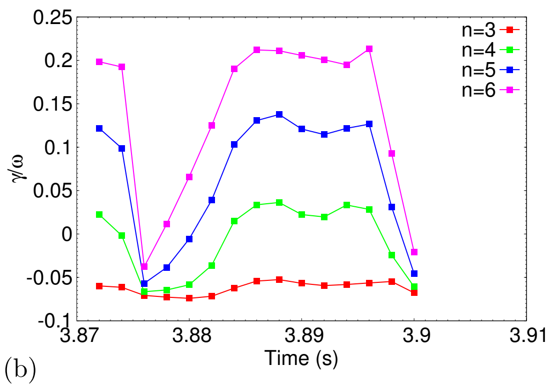

Figure 6.13. Evolution of numerically calculated (a) BAE continuum accumulation point frequency and (b) continuum damping/growth rate at $\rho_{pol}(CAP)$ for toroidal mode numbers $n = 3 - 6$ during sawtooth period II of ECRH phase of discharge 25546.

For the $n = 3 - 5$ modes a short period of frequency plateauing, similar to that observed during the ICRH only analysis, is observed from $t = 3.884 - 3.888$s. Following this, an increase in ω_{BAE} commences for all distinct toroidal eigenmodes and lasts until the end of the period. This increase starts slightly earlier, at $t = 3.882$s, for the $n = 6$ eigenmode.

The distinct toroidal eigenmodes are also much more closely spaced in frequency than in the ICRH only case, with the exception of the $n = 3$ eigenmode, with a difference of less than $\Delta\omega_{BAE} \approx 0.005$ typically existing from $t \approx 3.884 - 3.896$s. This is in broad agreement with the experimental results presented in section 6.1.2, which, though not very clearly observed, appear to lack the relatively wide frequency separations between distinct toroidal eigenmodes observed in the ICRH only case. Figure 6.13 (b) shows the damping/growth rate during the same period. As in the ICRH only case, the continuum growth rate increases rapidly during the initial phase of the period at a rate proportional to the toroidal mode number n, and saturates from $t \approx 3.886 - 3.896$s. It then decreases rapidly during the final $\sim$ 4ms of the period.

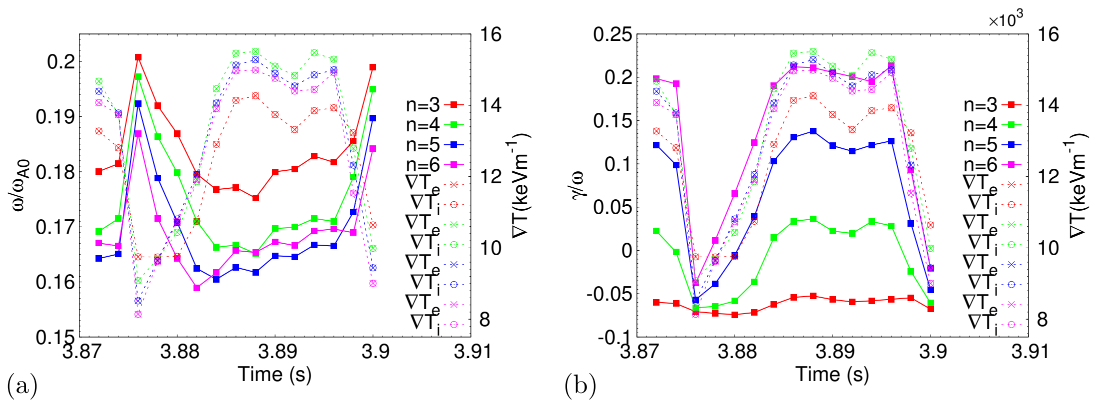

Figure 6.14. Evolution of numerically calculated (a) BAE CAP frequency and (b) continuum damping/growth rate at $\rho_{pol}(CAP)$ for $n = 3 - 6$ with the electron and ion temperature gradients at $\rho_{pol}(CAP)$ during sawtooth period II of ECRH phase of discharge 25546.

$\nabla T(\rho_{pol}(CAP))$ is also observed to increase rapidly during the initial phase of period I, from $t = 3.876 - 3.886$s, which corresponds to the period of rapid frequency decrease and growth rate increase observed previously. This can be seen in figure 6.14 (a) and (b) respectively. Likewise, the frequency increase and decrease in growth rate from $t = 3.896 - 3.900$s is accompanied by a decrease in the temperature gradient.

However, the intervening period does not behave exactly as observed during the ICRH only phase. While the temperature gradient essentially saturates during the central phase, excepting a dip centred at $t = 3.892$s, the BAE frequency increases steadily during this phase, as has been observed above already. The growth rate appears to act as it did during the ICRH only phase, following the evolution of $\nabla T(\rho_{pol}(CAP))$ closely. Figure 6.15 shows the evolution of ω_{BAE} with the temperature component of the diamagnetic frequency ω_{*T}.

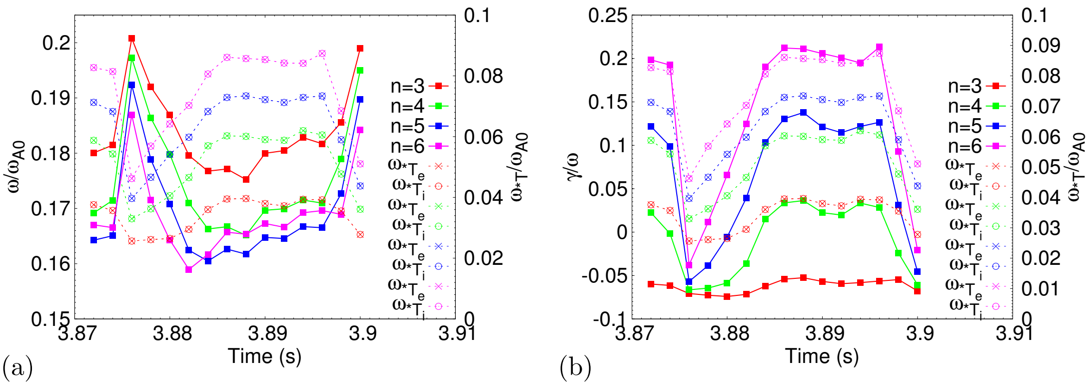

(a) (b)

Figure 6.15. Evolution of numerically calculated (a) BAE CAP frequency and (b) continuum damping/growth rate at $\rho_{pol}(CAP)$ for $n = 3-6$ with the temperature component of the electron and ion diamagnetic frequencies at $\rho_{pol}(CAP)$ during sawtooth period II of ECRH phase of discharge 25546.

It has been discussed previously how the diamagnetic frequency is determined primarily by the background temperature gradient, as is clear from comparing the two quantities in figures 6.14 and 6.15. It was also demonstrated that the BAE frequency evolution exhibited a strong dependence on ω_{*T}. While this relationship is evident during the initial and final phase of period I, it is not as clear during the central phase when ω_{*T} plateaus and ω_{BAE} increases continuously. Figure 6.16 shows the evolution of ω_{BAE} and the damping/growth rate at $\rho_{pol}(CAP)$ with the background temperature. It can be seen that the evolution of ω_{BAE} appears to follow that of the temperature. During the initial frequency drop, a corresponding drop in temperature is observed. Likewise, while the temperature gradient and diamagnetic frequency saturate during the central phase of this period, the temperature begins to increase overall at $t = 3.882$s, just prior to the commencement in the BAE frequency increase that lasts until the end of the period. The evolution of the radial position of the BAE frequency accumulation point $\rho_{pol}(CAP)$ is presented in figure 6.17. $\rho_{pol}(CAP)$ appears to vary quite extensively during the course of period II. For example, it exhibits a range from $\rho_{pol} \approx 0.360 - 0.327$ in the $n = 4$ case. This is substantially larger than the variation typically observed during the ICRH only cases.

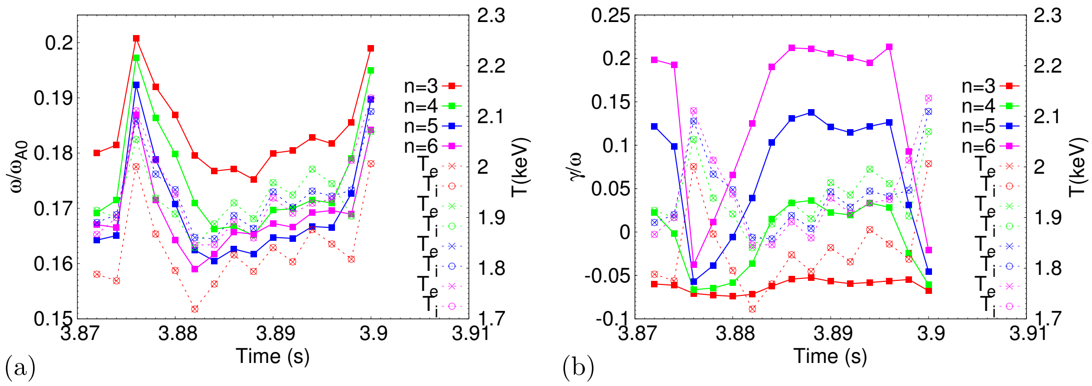

Figure 6.16. Evolution of numerically calculated (a) BAE CAP frequency and (b) continuum damping/growth rate at $\rho_{pol}(CAP)$ for $n = 3 - 6$ with the electron and ion temperatures at $\rho_{pol}(CAP)$ during sawtooth period II of ECRH phase of discharge 25546.

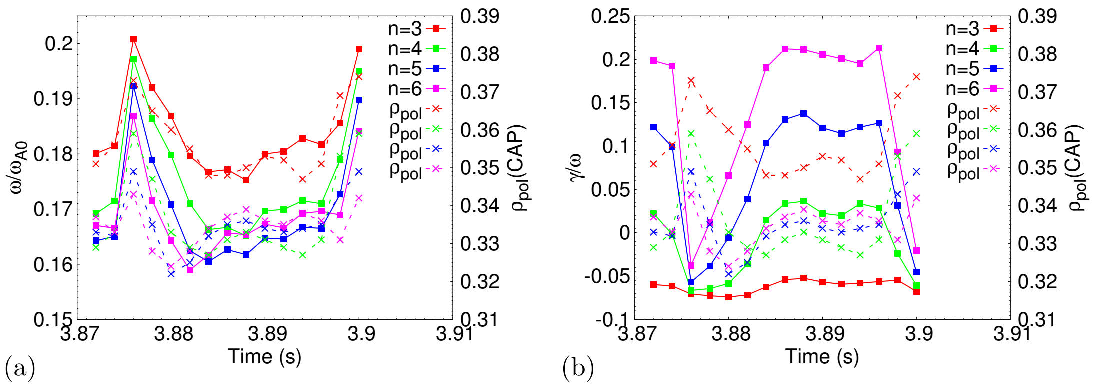

Figure 6.17. Evolution of numerically calculated (a) BAE CAP frequency and (b) continuum damping/growth rate at $\rho_{pol}(CAP)$ for $n = 3 - 6$ and the corresponding $\rho_{pol}(CAP)$ evolution for sawtooth period II during the ECRH phase of discharge 25546.

Agreement between experimental observations of BAEs and numerical results from rootsolver Figure 6.18 compares the numerically calculated BAE CAP and experimentally observed BAE activity during period II of the ECRH/ICRH phase of discharge 25546. While there is broad qualitative agreement during the initial $\sim$ 10ms, this breaks down during the latter $\sim$ 10ms. This lends further weight to the argument that an additional physical mechanism is at work during the end phase of a sawtooth period.

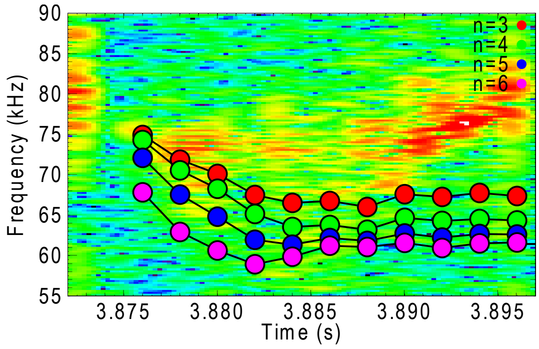

Figure 6.18. Comparison between numerically calculated BAE CAP evolution and experimental observations using channel I52 of the soft x-ray diagnostic, with $nfft = 8192$ and $nstp = 512$, during period II of ECRH/ICRH phase of discharge 25546.

6.2.2 Numerical recovery of acoustic Alfvén eigenmode continuum accumulation point and damping/growth rate

Acoustic Alfven continuum accumulation point evolution during sawtooth period I Figure 6.19 presents the evolution of the numerically calculated acoustic Alfvén continuum accumulation point during period I of the ECRH/ICRH phase of discharge 25546. The behaviour is found to be broadly similar to that during the ICRH phase, with an initial increase in frequency followed by a plateauing during the central phase.

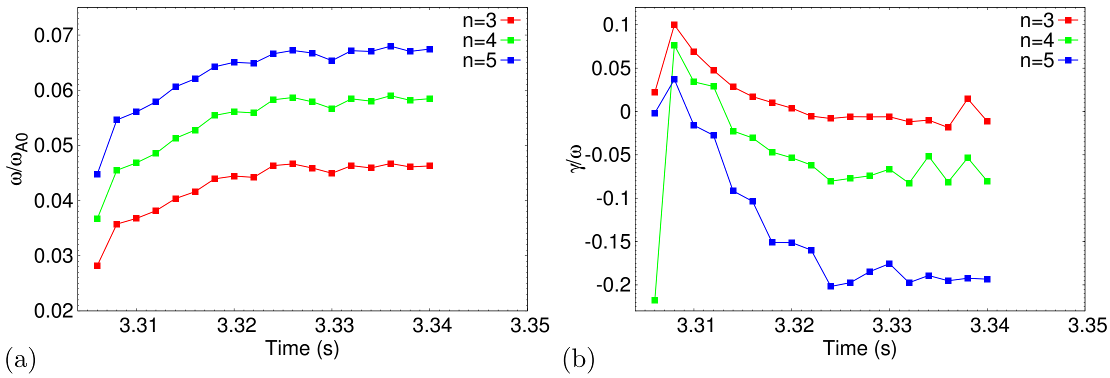

Figure 6.19. Evolution of numerically calculated (a) acoustic Alfvén eigenmode continuum accumulation point frequency and (b) continuum damping/growth rate at $\rho_{pol}(CAP)$ for $n = 3 - 6$ during sawtooth period I of ECRH phase of discharge 25546.

However, instead of the frequency decreasing towards the end of period I, it remains steady. Likewise, the damping/growth rate initially evolves in a similar manner to that during the ICRH phase, with an initial increase in the damping rate followed by a phase when the damping rate changes. However, in the ECRH/ICRH case, this steadying of the damping rate continues until the end of period I.

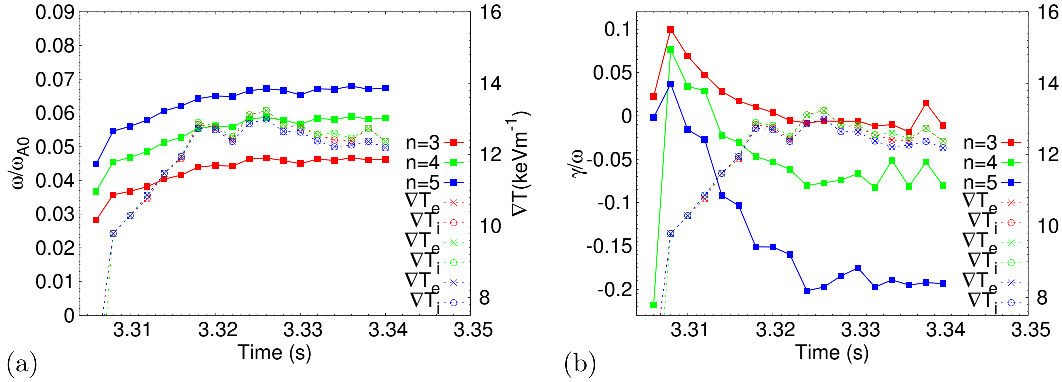

Figure 6.20. Evolution of numerically calculated (a) acoustic Alfvén eigenmode CAP frequency and (b) continuum damping/growth rate for $n = 3-6$ with the electron and ion temperature gradients at $\rho_{pol}(CAP)$ during sawtooth period I of ECRH phase of discharge 25546.

The maximum damping rate during the central phase of period I is found to be substantially higher than during the ICRH only case. This can be seen by comparing the damping during period I of the ECRH/ICRH phase with that during period III of the ICRH only phase.

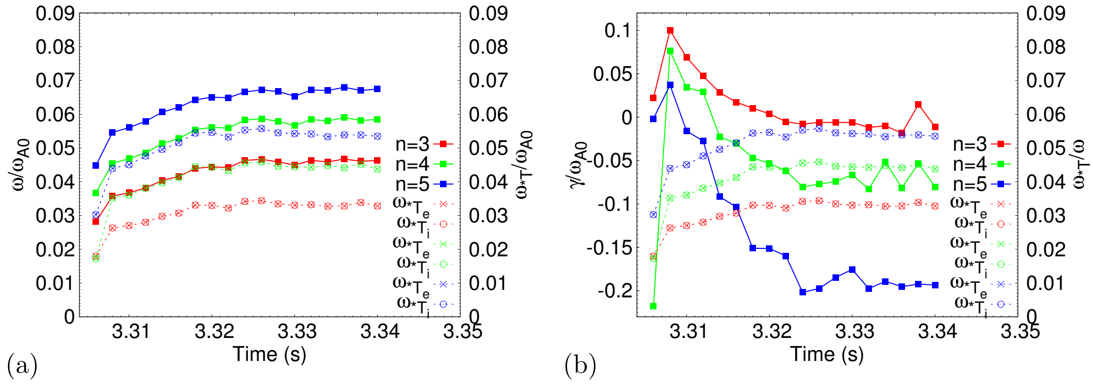

Figure 6.21. Evolution of numerically calculated (a) acoustic Alfvén eigenmode CAP frequency and (b) continuum damping/growth rate for $n = 3-6$ with the temperature component of the electron and ion diamagnetic frequencies at $\rho_{pol}(CAP)$ during sawtooth period I of ECRH phase of discharge 25546.

This is in broad agreement with the experimental observations for the acoustic Alfvén eigenmodes presented in section 6.1, which show that the modes are absent during the initial and late phases of periods I and II, with some moderate activity observed during the central periods. However, it is not immediately clear what mechanism is responsible for this change in the mode observations during the central period and further investigation is necessary to determine this.

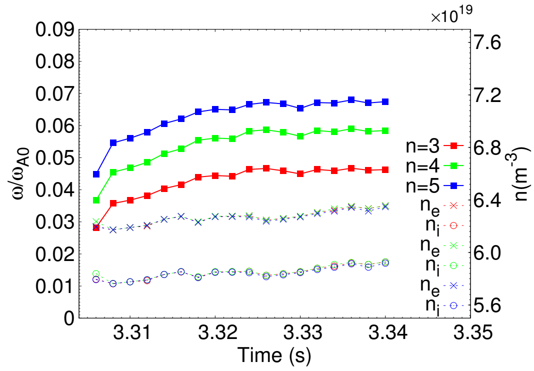

Figure 6.22. Evolution of numerically calculated acoustic Alfvén eigenmode CAP frequency with the background ion and electron densities at $\rho_{pol}(CAP)$ for sawtooth period I during the ECRH phase of discharge 25546.

This assertion is backed up by observations of the electron temperature evolution presented in figure 6.3 which show indications of sawtooth precursor activity at two instances during period I prior to the sawtooth crash and coincide broadly with the periods of observed acoustic Alfvén eigenmode activity.

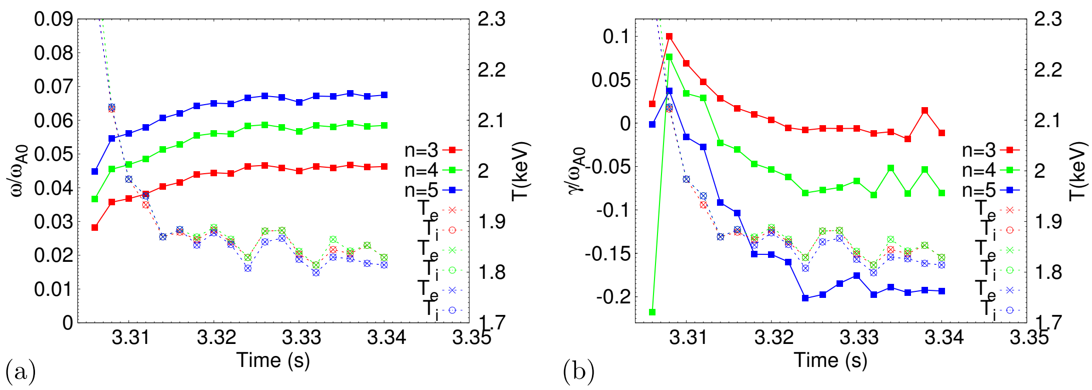

Figure 6.23. Evolution of numerically calculated (a) acoustic Alfvén eigenmode CAP frequency and (b) continuum damping/growth rate for $n = 3 - 6$ with the electron and ion temperatures at $\rho_{pol}(CAP)$ for sawtooth period I during the ECRH phase of discharge 25546.

Figure 6.20 shows the evolution of the acoustic Alfvén eigenmode frequency with the background temperature gradient. ∇T is not quite as high as in the case of the BAEs. This is due to the fact that $\rho_{pol}(CAP)$ for the acoustic Alfvén eigenmodes is located somewhat further outwards radially than in the case of the BAEs, as can be seen by comparing figures 6.24 and 6.17.

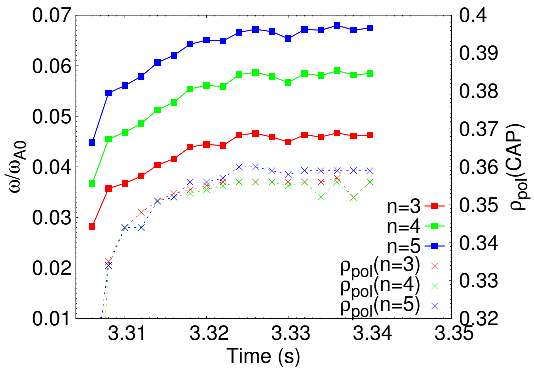

Figure 6.24. Evolution of numerically calculated acoustic Alfvén eigenmode CAP frequency for $n = 3 - 6$ and the corresponding $\rho_{pol}(CAP)$ evolution for sawtooth period I during the ECRH phase of discharge 25546.

It has been demonstrated in section 5.4.4 that an increase in the background temperature gradient ∇T results in an increase in the damping rate of the acoustic Alfvén eigenmodes. However, due to the fact that ∇T is very similar to that observed during the ICRH only phase, it suggests that some other factor is contributing to the higher damping rates observed during period I of the ECRH/ICRH phase. One possibility is that the higher density observed during period I, as presented in figure 6.22, contributes to the higher damping through ion Landau damping.

6.3 Parameter sensitivity scans for low-frequency Alfvén eigenmodes

The evolution of the numerically calculated BAE and acoustic Alfvén eigenmode continuum accumulation point frequencies with experimentally observed background profiles has been investigated in chapter 5 and in section 6.2 of this chapter. The experimentally observed mode behaviour was then compared with numerical results based on a theoretical model for low-frequency Alfvén eigenmodes.

It was demonstrated that the main parameters influencing the BAE and acoustic Alfvén eigenmode frequencies are the background profile gradients, in particular that of the background temperature profile. As such, it was desirable to extend the scope of this analysis by considering potential experimental conditions not observed during the discharges investigated. This was achieved by undertaking sensitivity scans involving various plasma parameters and observing the effects that altering these parameters had on the evolution of the numerically calculated mode frequencies and continuum damping/growth rates. Specifically, these scans were conducted for the background temperature and density gradients ∇T and the ratio between the electron and ion temperature profiles $\tau = T_e/T_i$. These parameters were chosen as they were deemed to be the factors most likely to impact the mode frequencies.

6.3.1 Parameter sensitivity scans

∇T scan The equilibrium reconstruction at $t = 2.066$s during period III of the ICRH only phase was taken as a reference equilibrium, and the q-profile obtained from it used in the subsequent calculations.

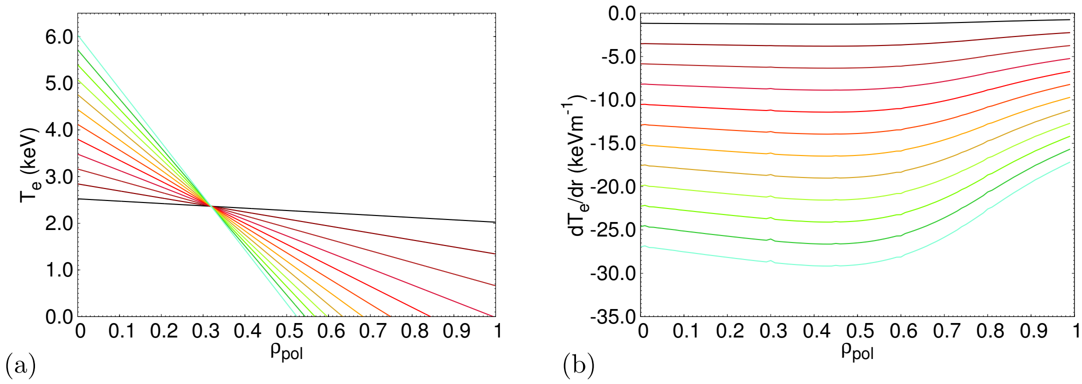

Figure 6.25. (a) Model linear temperature profiles and (b) corresponding gradients for determining impact of ∇T on the mode frequency and damping/growth rate.

During each scan, all other parameters were kept constant at the experimental values measured at $t = 2.066$s. Figures 6.25 (a) and (b) show the model temperature profiles and their corresponding gradients respectively. Linear model temperature profiles in the region surrounding the $q = 1$ surface were utilised, with the experimentally observed radial position of the sawtooth inversion radius

kept constant as well as its temperature at this position. The slope of the line, and hence the gradient of the temperature profile, was varied, allowing the impact of changes in the value of ∇T to be observed clearly. The evolution of the BAE CAP frequency ω_{BAE} with ∇T is presented in figure 6.26 (a) for toroidal mode numbers $n = 3 - 6$, with the BAE CAP frequency plotted versus the increase in the temperature component of the diamagnetic frequency ω_{*T} in figure 6.26 (b). The approximate experimentally observed temperature gradient at the $q = 1$ surface at $t = 2.066$s is approximately 13keV.
During the previous numerical analysis of the experimentally observed modes, the BAE frequency was found to decrease with increasing ω_{*T}. This is found to be true up to a certain point for the ∇T and ω_{*T} scans. ω_{BAE} decreases with increasing ∇T until the gradient reaches a value of $\nabla T \approx 15.1\text{keVm}^{-1}$ for the $n = 6$ case. After this point, ω_{BAE} begins to increase for the $n = 6$ mode. Similar reversals in the direction of the frequency evolution are observed to occur in the $n = 4$ and $n = 5$ cases at $\nabla T \approx 24\text{keVm}^{-1}$ and $\nabla T \approx 17.6\text{keVm}^{-1}$ respectively, while the $n = 3$ CAP does not reverse its frequency evolution within the range of ∇T values considered.

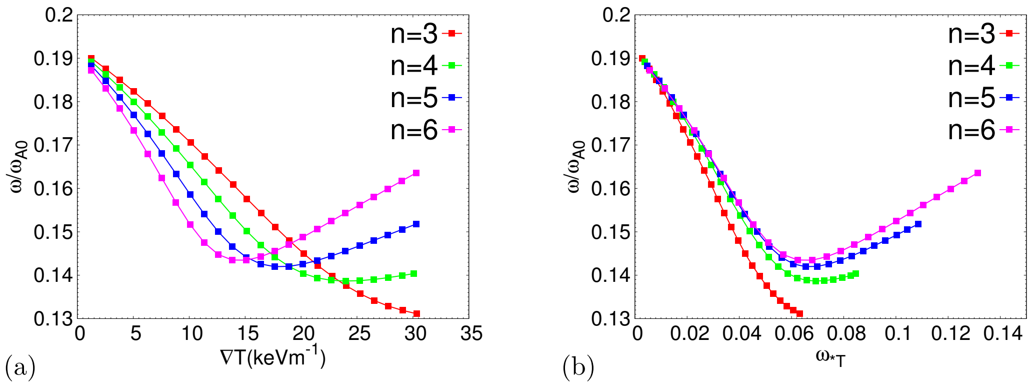

Figure 6.26. BAE CAP frequency evolution with increasing (a) background temperature gradient and (b) diamagnetic frequency.

On first inspection, these reversals in the frequency evolution would appear to offer a possible explanation for the decrease in frequency that occurs for the experimentally observed BAEs during the later phase of the sawtooth period. However, this is found to be unrealistic if one considers the numerical results obtained in section 5.4.3 in conjunction with the experimentally observed electron temperature gradients.

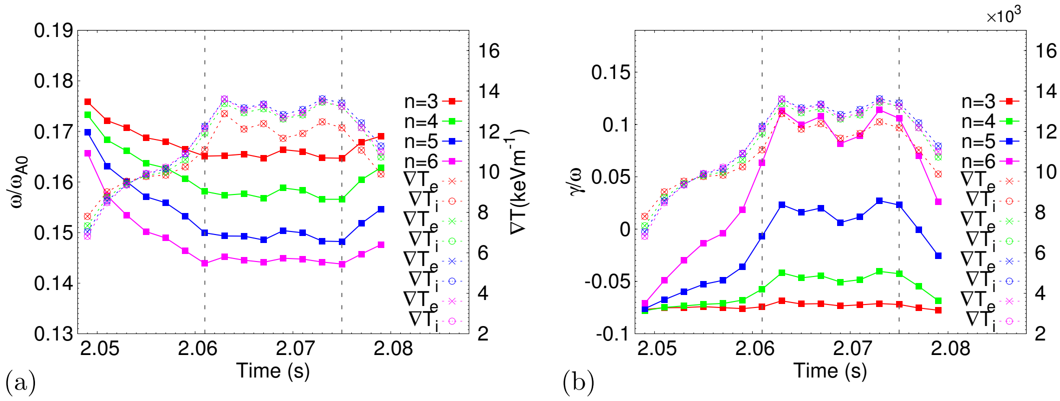

Figure 6.27. Evolution of BAE (a) CAP frequency and (b) continuum damping/drive during periods III of discharge 25546.

During the analysis of period III, which contains the time-point $t = 2.066$s under consideration, ω_{BAE} for $n = 6$ at the beginning of the period was calculated to be $\omega_{BAE} \approx 0.166$. If one extrapolates the data in figure 6.26 (a) to the point where this frequency is again achieved through an increase in the gradient, ∇T would be well in excess of 30keVm^{-1}. This is more than double the experimentally observed temperature gradient at $\rho_{pol}(CAP)$
Considering figure 6.26 (b), which shows the evolution of ω_{BAE} with ω_{*T}, the reversal in the direction of the evolution of ω_{BAE} is found to occur between $\omega_{*T} \approx 0.06 - 0.07$ for the $n = 4 - 6$ modes. This represents a frequency close to half that of ω_{BAE} in each case, suggesting that the reversal in frequency is due to a coupling between the BAE and kinetic ballooning mode (KBM) branches of the frequency spectrum, the KBM branch being strongly dependent on ω_{*T}.
Figure 6.28 (a) presents the change in the BAE damping/growth rate with ∇T. It can be seen that the modes remain heavily damped and with little increase in γ/ω_{A0} for $\nabla T < 5$keVm^{-1}. After this point, the behaviour begins to change, with the damping rate decreasing rapidly at a rate proportional to the toroidal mode number n. It can be seen that the modes become un-damped at $\nabla T \approx 20$keVm^{-1}, 15.5keVm^{-1}, 12.5keVm^{-1} and 10.5 keVm^{-1} for the $n = 3-6$ modes respectively. The growth rates increase for a period, before levelling off for $\nabla T \approx 29$keVm^{-1}, except in the $n = 3$ case where the growth rate continues to increase steadily in the range considered. Equivalent sensitivity scans to those conducted for the

BAEs were conducted for the acoustic Alfvén eigenmodes. As was observed in sections 5.4.4 and 5.4.4, the acoustic Alfvén eigenmode frequency is found to increase with increasing ∇T and ω_{*T}. Results for the sensitivity scans of these quantities are presented in figures 6.29 (a) and (b) respectively.

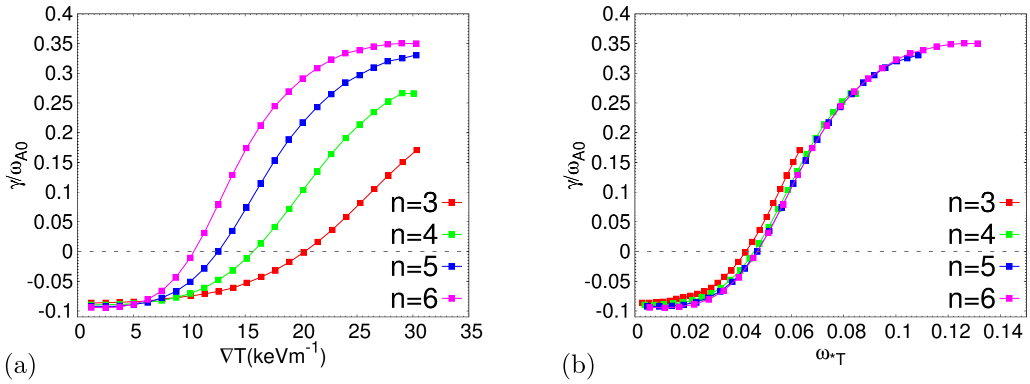

Figure 6.28. BAE continuum damping/growth rate evolution with increasing (a) background temperature gradient and (b) diamagnetic frequency.

It can be seen from figure 6.29 (a) that the acoustic Alfvén eigenmode frequency increases with ∇T at a rate proportional to the toroidal mode number n, with the CAPs with higher mode numbers associated with them having higher frequencies. It can also be seen that the frequencies of the modes begin to saturate between approximately $0.056 \leq \omega/\omega_{A0} \leq 0.062$, when the temperature gradient reaches a certain value for a given distinct toroidal eigenmode. At this point the frequency begins to decrease moderately.

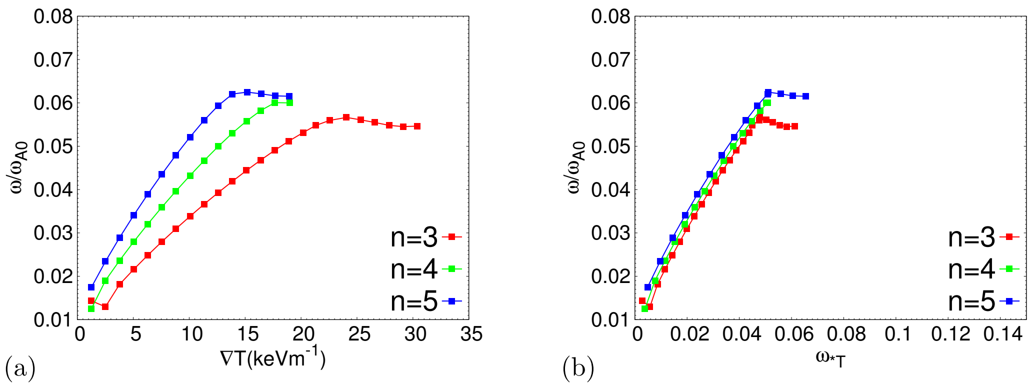

Figure 6.29. Acoustic Alfvén eigenmode frequency evolution with increasing (a) background temperature gradient and (b) diamagnetic frequency, calculated using numeric rootsolver.

The evolution of the acoustic Alfvén eigenmode damping/growth rate with increasing ∇T and ω_{*T} is presented in figures 6.30 (a) and (b) respectively. There is a sharp decrease in the damping rate at $\nabla T \approx 14\text{keVm}^{-1}$ for the $n = 5$ mode, suggesting that the acoustic Alfvén eigenmode couples to another frequency branch with much larger damping at this point.

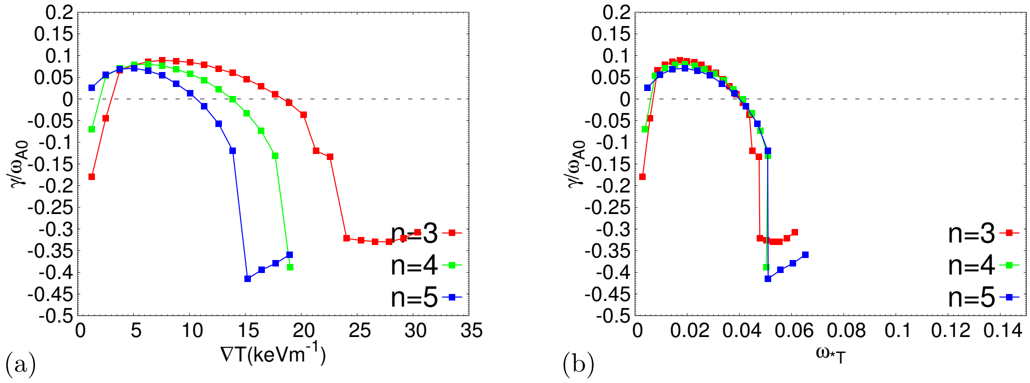

Figure 6.30. Acoustic Alfvén eigenmode damping/growth rate evolution with increasing (a) background temperature gradient and (b) diamagnetic frequency.

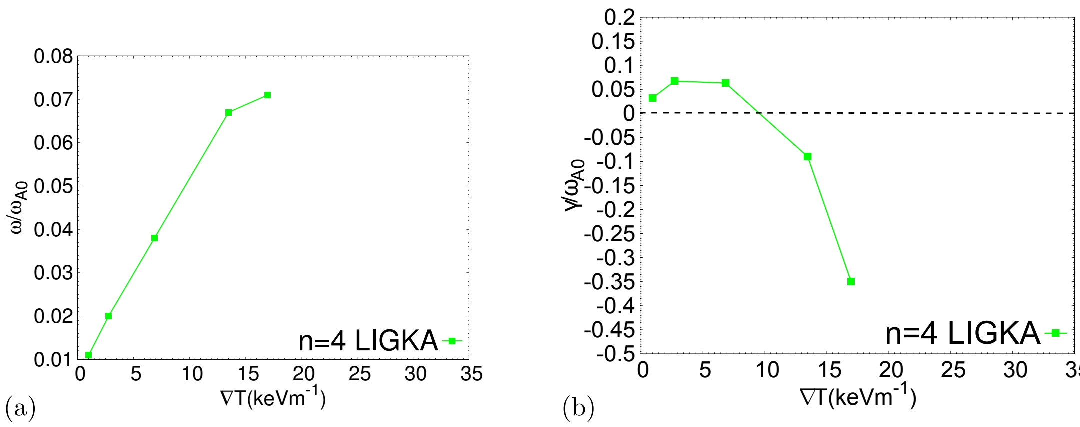

Figure 6.31. Acoustic Alfvén eigenmode (a) frequency and (b) damping/drive evolution with increasing background temperature gradient for $n = 4$, calculated using LIGKA.

This is significant as the value of ∇T is close to the experimentally observed value at the point where the acoustic Alfvén eigenmode activity ceases to a large extent during the ICRH only sawtooth periods. As such, it is proposed that this cessation in the mode activity is the result of the coupling of the acoustic Alfvén eigenmodes to another frequency branch that remains completely damped, and thus is not observed experimentally. This sharp increase in the damping rate also occurs for the $n = 3$ and 4 modes and coincides with the saturation of the mode frequency, reinforcing the conclusion that a coupling to a different frequency branch is occurring here. Figure 6.31 (a) and (b) show the evolution of the Acoustic Alfvén eigenmode frequency and damping/drive rate respectively with increasing background temperature gradient for the $n = 4$ mode, calculated using LIGKA. It can be seen that the results agree well with those obtained from the numerical root-solver, as presented in figures 6.29 and 6.30.

τ **scan** As has been mentioned previously, thus far the assumption that $T_i = T_e$ has been made for all calculations of the analysis conducted in this work. However, the parameter $\tau = T_e/T_i$ plays a prominent role in the kinetic dispersion relation 3.4.61. As such, it is instructive to investigate the impact that altering this parameter from a value of $\tau = 1$ has on the mode dynamics. Linear model electron and ion temperature profiles were again used for this purpose and the analysis is divided into two parts. Firstly, the electron and ion temperature profiles were set equal to one another. The electron temperature profile was then kept fixed and the ion temperature profile shifted incrementally downwards to simulate an increase in τ, given that $\tau = T_e/T_i$. The downward direction of the shift was based on the experimental observation that the ion temperature is typically less than the electron temperature in the core region.

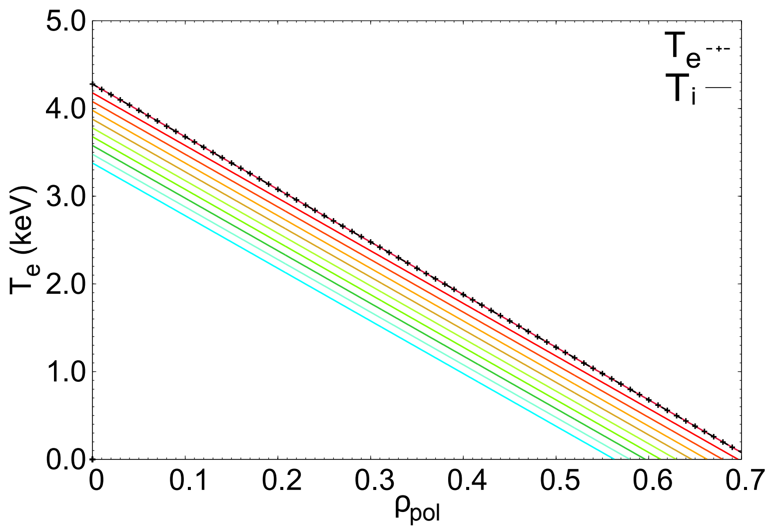

Figure 6.32. Model linear temperature profiles for determining impact of τ on the mode frequency and damping/growth rate.

The experimental value of τ is found to range from $\tau \approx 1.1 - 1.4$. The fact that only a downward translation of the ion profile was made meant that the gradient of the two profiles remained the same, allowing the effect of increasing τ to be disentangled from the effect of decreasing the ion temperature profile gradient.

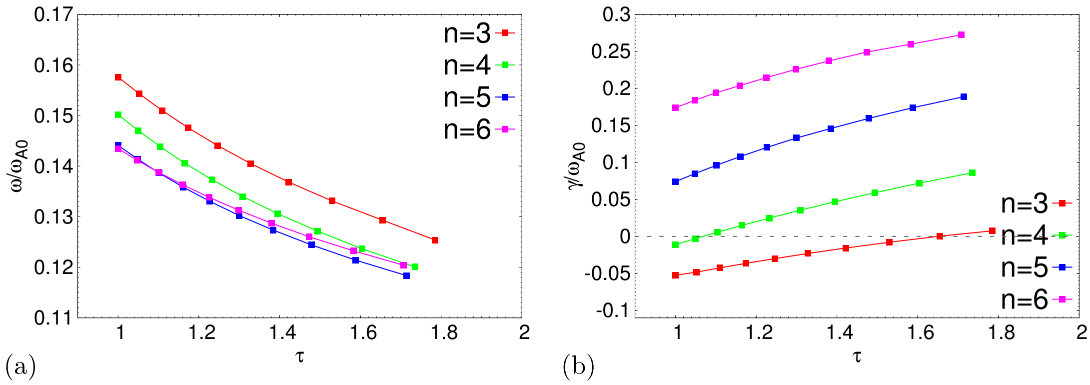

Figure 6.33. Evolution of (a) BAE CAP frequency and (b) continuum damping/growth rate with increasing τ.

Figure 6.32 presents the relative changes made between the electron and ion temperature profiles for the scan. The results for the BAE frequency evolution with τ are presented in figure 6.33 (a). The frequency of the BAE CAP is found to decrease steadily with increasing τ. From theory, a higher value of τ would be expected to result in reduced damping from acoustic branch coupling.

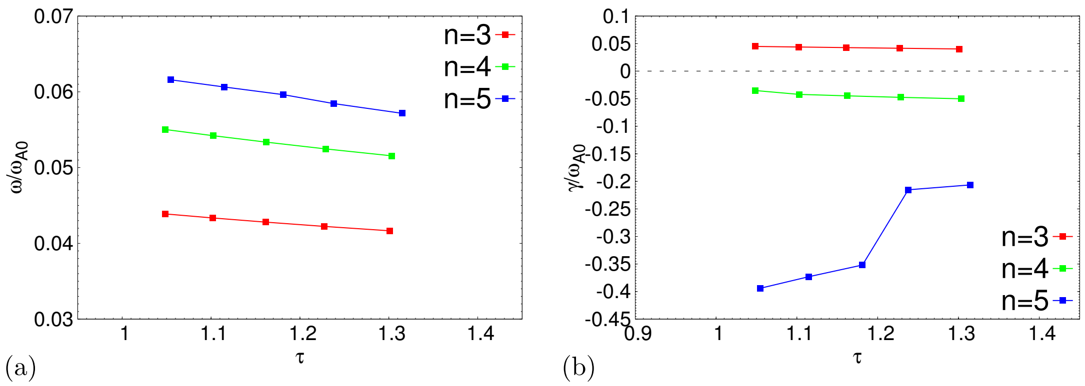

Figure 6.34. Evolution of (a) acoustic Alfvén eigenmode CAP frequency and (b) continuum damping/growth rate with increasing τ.

From figure 6.33 (b) it can be seen that this is indeed the case, with the damping rate decreasing and/or the growth rate subsequently increasing as the value of τ is increased. The same analysis was conducted for the acoustic Alfvén eigenmodes, with the results presented in figure 6.34. As in the case of the BAEs, the frequency is observed to decrease with increasing τ, albeit at a rate lower than for the BAEs. It is not clear how the damping rate of the acoustic Alfvén eigenmodes changes with increasing τ in this case.

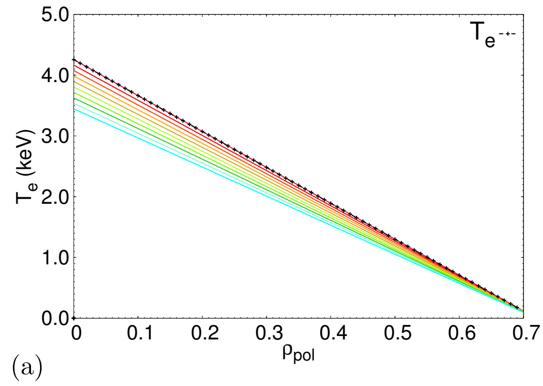

Figure 6.35. Model linear temperature profiles for determining combined impact of τ and ∇T_i on the mode frequency and damping/growth rate.

The second aspect of this section of the analysis involved determining the relative influence between changes in the value of τ and corresponding changes in the ion temperature gradient. As mentioned above, the ion temperature is typically observed experimentally to be less than the electron temperature in the core region.

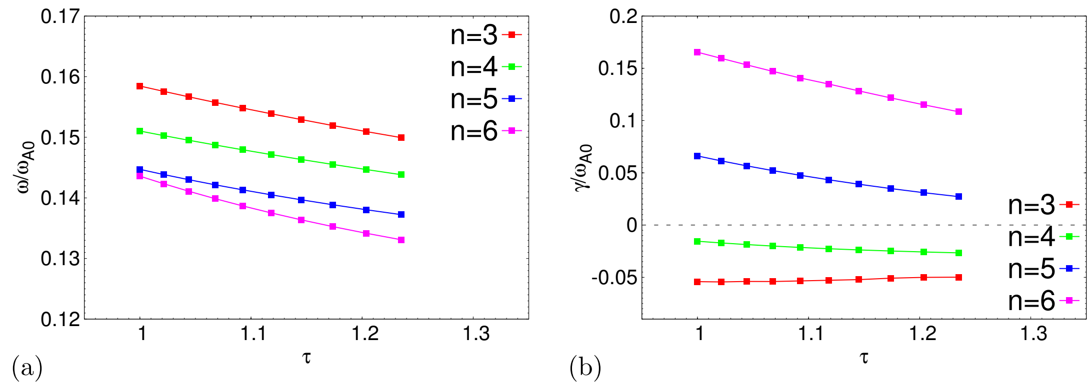

Figure 6.36. Evolution of (a) BAE CAP frequency and (b) continuum damping/growth rate with increasing τ and decreasing ∇T_i.

This generally results in the ion temperature gradient also being somewhat less than that of the electron temperature in this region. The effect that this can have on the damping/growth rate has been discussed in [59] and is expanded on here. Again, linear model profiles were employed for the electron and ion temperatures with the former kept fixed. However, in this case the slope of the model ion temperature profile was decreased incrementally.

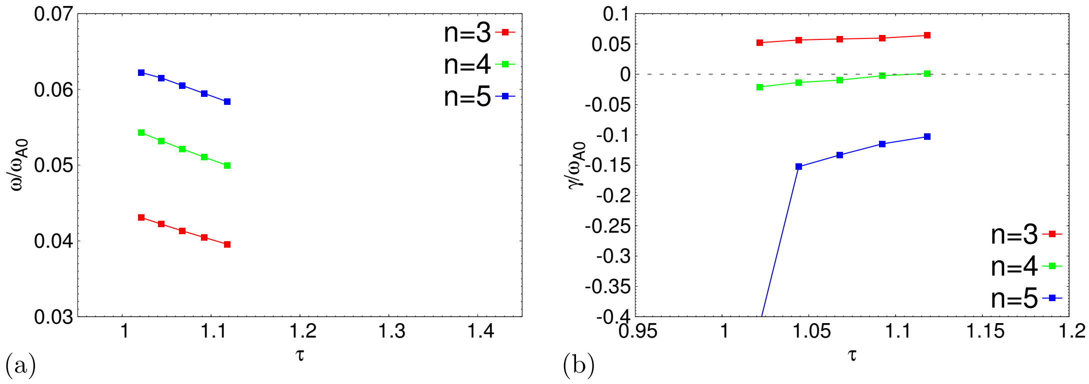

Figure 6.37. Evolution of (a) acoustic Alfvén eigenmode CAP frequency and (b) continuum damping/growth rate with increasing τ and decreasing ∇T_i.

This had the effect of both increasing τ and lowering the ion temperature gradient. The evolution of the temperature profiles and gradients are presented in figures 6.35 (a) and (b) respectively. As in the case where the gradients were kept fixed, the BAE frequency is observed to be shifted downwards with increasing τ. However, the rate at which this occurs at is less in this case. This is due to the reduced ion temperature gradient that results from the form of the model T_i profile utilised. As the gradient decreases, so does ω_{*T}, meaning that the frequency is not shifted downwards to as large an extent. The effect that this has on the damping/growth rate can be seen in figure 6.36 (b). Whereas in figure 6.33 (b) the damping rate decreased with increasing τ, the reduction in the ion temperature gradient results in a decreased coupling to the kinetic ballooning mode branch through the ω_{*T} term. This compensates for the decrease in damping from increasing τ and results in a decrease in mode drive and increased damping rate.

The same analysis was conducted for the acoustic Alfvén eigenmode case. Again, the frequency was observed to decrease with increasing τ. However, in this case the reduced ω_{*T} resulted in an increase in the mode drive. This would be expected as it has been shown in sections 5.4.4 and 5.4.4 that increasing ω_{*T} increases the damping rate of the acoustic Alfvén eigenmodes.

6.4 Conclusion

The aim of the analysis conducted in this chapter was to investigate the behaviour of low-frequency Alfvén eigenmodes during periods of both ICRH and ECRH. Observations of the BAEs were not as distinct as those during the ICRH only phase, with the frequency separation between distinct toroidal eigenmodes of this period essentially absent. The addition of ECRH was observed to cause the distinct toroidal eigenmodes to be much more closely spaced. In addition, the acoustic Alfvén modes were found to be more highly damped, with behaviour inverted when compared to the ICRH only phase, occurring only during the central phase of each sawtooth period.
A number of different parameter sensitivity scans were conducted in section 6.3. This was done to investigate how BAEs and acoustic Alfvén eigenmodes would behave during parameter regimes outside of those observed experimentally. In the case of the BAEs, it was found that the decrease in mode frequency brought about by increasing the diamagnetic frequency ceases at a certain threshold. From that point onwards an increase in the diamagnetic frequency results in the BAE frequency shifting back upwards. It was also found that increasing the diamagnetic frequency sufficiently results in the acoustic Alfvén eigenmode coupling to another frequency branch with a significantly higher damping rate than that of the acoustic Alfvén eigenmodes. This explains further the absence of acoustic Alfvén eigenmode activity during the central phase of the sawtooth period, when the gradients are highest. Increasing the parameter $\tau = T_e/T_i$ was found to shift the BAE and acoustic Alfvén eigenmode frequencies downwards and to decrease the BAE continuum damping rate.

Chapter 7

Investigation of eITB-driven modes, BAE-like modes and edge-TAEs during discharges heated primarily via ECRH

7.1 Introduction and motivation

7.1.1 Overview of modes and relation to low-frequency Alfvén eigenmode analysis

Several distinct types of mode activity in the BAE/BAAE and TAE frequency regimes have been observed at ASDEX Upgrade, where these regimes are typically from $f \approx 10 - 80$kHz and $f \geq 150$kHz respectively. These modes have been observed during certain discharges externally heated primarily via ECRH, with short NBI beam blips employed to provide ion temperature and plasma rotation data. The observed modes can be divided into two categories. The first occur during the early phase of the discharges in question, when high levels of ECRH power are applied. The electron density during this phase is observed to be very low, with core values typically less than $n_{e0} \approx 2.0 \times 10^{19}\text{m}^{-3}$. These modes, an example of which is presented in figure 7.1 (a), arc in frequency at the beginning of these high ECRH power phases, typically reaching maximum frequencies well over 300kHz, before falling again in frequency once the level of the ECRH power is reduced. It is observed that these modes coincide with the occurrence an electron internal transport barrier (eITB) in the plasma, and it is proposed that they their development is mediated by the presence of the eITB. Thus, they will be referred to as eITB-driven modes during this work.

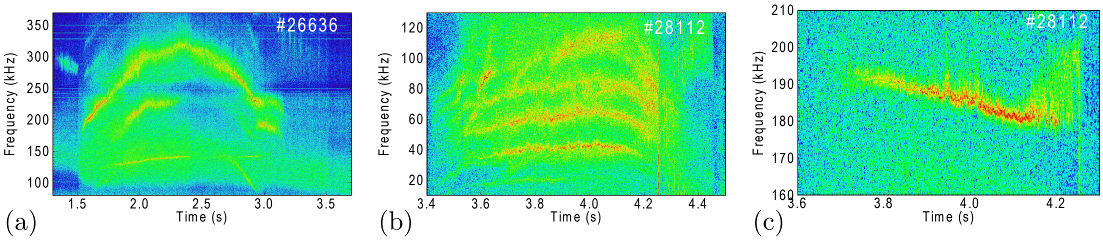

Figure 7.1. Observations of (a) eITB-driven modes, (b) BAE-like modes and (c) edge-TAEs, measured using coil B31-14 of the Mirnov coil disgnostic during discharges 26636 and 28112, with $nfft = 8192$ and $nstp = 2048$.

The second category of modes are observed during the ELM-free H-mode phase that frequently occurs during the latter stage of these discharges. By this time, the input ECRH power has been reduced substantially, while the electron density has typically been ramped up to a value of $n_{e0} \approx 3.0 - 4.0 \times 10^{19}\text{m}^{-3}$, with the objective of transitioning the plasma into a H-mode phase. The first of these modes is observed to occur in and around the BAAE/BAE frequency range, from $f \approx 10 - 80$kHz at ASDEX Upgrade, and an example of an observation of the mode during discharge 28112 is presented in figure 7.1 (b). These modes exhibit an inverted mode number ordering, suggesting that they are related to the beta-induced Alfvén eigenmode (BAE), this behaviour being a prominent feature of BAEs. On account of this, as well as their spanning of the BAE frequency range, they will be referred to as BAE-like modes during this work.

The second type of mode encountered during the H-mode phase of the discharges exhibits frequency characteristics similar to those of the TAE, with a relatively high frequency, changing from $f \approx 195 - 180$kHz, and is only observed clearly during one of the discharges considered - #28112. Experimental observations indicate that it occurs towards the plasma edge and as such will be referred to as edge-TAEs during this work. Figure 7.1 (c) presents an observation of this edge-TAE from $t \approx 3.7 - 4.2$s during discharge 28112.

From initial considerations, the discharges described above appear unrelated to those considered in chapters 5 and 6. Indeed, the densities measured during the initial phase of discharges such as 28112 are much lower than those typically observed during discharge 25546. In addition, no ICRH is employed during the discharges considered during this chapter, while the BAEs observed during discharge 25546 occurred primarily in conjunction with ICRH. The link between the two analyses stems from two related considerations. The first is the experimental characteristics shared by these modes, the BAEs and the TAEs, which suggests that the application of an analysis procedure similar to that employed in chapters 5 and 6 is valid.

The second consideration arises from the nature of the heating method employed during these discharges. The primary objective of the previous BAE and acoustic Alfvén eigenmode analysis was to demonstrate that low to medium frequency Alfvénic mode dynamics were strongly influenced by the presence of appreciable gradients in the background temperature and density profiles. As such, utilising discharges heated almost exclusively by ECRH for this analysis means that any observed Alfvénic modes are potentially driven by background profile gradients alone, owing to the almost total absence of energetic particles in these plasmas.

It has been demonstrated that radially adjacent low-frequency Alfvénic modes in different frequency regimes have the ability to couple, and thereby facilitate the outward redistribution of the energetic particle population [63]. The possibility that these types of modes could be excited in the absence of energetic particles would have important consequences as it would mean that energetic particles introduced subsequently to the plasma could be subject to immediate and deleterious outward transport caused by these pre-existing low-frequency Alfvénic modes. This potential for modes to be excited exclusively by high background temperature gradients is a primary focus of the analysis in this chapter.

As will be detailed in the sections that follow, the modes described above each exhibit similarities to the Alfvén eigenmodes discussed in chapters 5 and 6. However, the observations of the modes are much less clear and do not possess the same defined frequencies of the previously analysed Alfvén eigenmodes. This suggests that the modes cannot be described purely by the linear model described in chapter 3 and that additional non-linear mechanisms are at work. This will be discussed further in the conclusion and outlook of this chapter.

7.1.2 Characterisation of discharges investigated

During this section, observations of the main experimental parameters of the discharges investigated are presented. As has been discussed in section 7.1.1, several discharges with similar plasma parameters exhibit the mode activity described in that section, including discharges #26573, #26635 – 26639, #28110 – 28112 and #28200 – 28201.

Discharge	I_p (MA)	B_t (T)	$q_{95,max}$	n_e (m^{-3})	P_{ECRH} (MW)
26573	0.600	-2.392	-6.771	4.18×10^{19}	2.260
26635	0.600	-2.506	-6.769	5.08×10^{19}	0.910
26636	0.600	-2.508	-6.806	3.85×10^{19}	2.505
26637	0.600	-2.408	-6.598	3.80×10^{19}	2.466
26638	0.600	-2.633	-6.762	4.00×10^{19}	2.480
26639	0.600	-2.632	-6.717	3.96×10^{19}	1.604
28110	0.600	-2.383	-7.024	5.53×10^{19}	2.796
28111	0.600	-2.383	-7.034	4.59×10^{19}	2.591
28112	0.600	-2.383	-7.035	5.58×10^{19}	3.370
28200	0.600	-2.400	-6.726	3.83×10^{19}	2.659
28201	0.600	-2.402	-6.756	4.81×10^{19}	2.686

Table 7.1. Main global parameters during discharges exhibiting eITB driven, BAE-like and edge TAE mode activity.

Table 7.1 presents the main global parameters observed during these discharges. While broadly similar, these discharges possess certain differences in the parameters that allow inferences to be drawn about the impact that changes in the plasma parameters have on the observed mode activity. A number of initial observations can be made about the discharges from table 7.1 that should be taken into account in when considering the observed mode behaviour. Firstly, all eleven discharges possess a plasma current of $I_p \approx 0.600$MA and a safety factor profile value close to the edge ranging from $q_{95} = 6.598-7.035$. This suggests little variation in the plasma current, and hence the q-profile, close to the plasma edge between the different discharges and indicates that these factors are not likely to account for significant differences in mode activity observed between different discharges. The on-axis toroidal magnetic field varies from $|B_t| \approx 2.383 - 2.633$T between the different discharges.

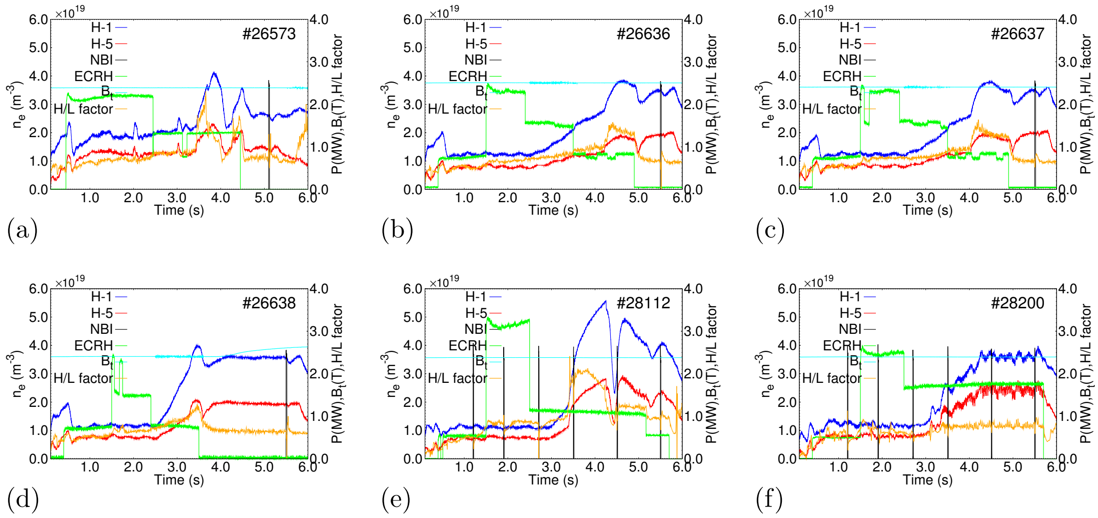

Figure 7.2. Time-traces of main experimental parameters measured during the high ECRH power phase and the ELM-free H-mode phase of the discharges under investigation.

This will impact the ECRH resonant layer position, and result in variations in the maximum heating power delivered at a given radial location over different discharges of differing B_t. Likewise, the maximum input ECRH power varies from $P_{ECRH} \approx 0.910 - 3.370$MW. It will be demonstrated that this has an impact on whether and in what manner a mode is excited at a given time, but is not the sole determining factor. Finally, the peak core electron density varies from $n_{e0} \approx 3.80 - 5.58 \times 10^{19}\text{m}^{-3}$, but possesses a much lower value during the initial phase of the discharges, as mentioned previously. Later, it will be seen that this appears to have an impact on whether the plasma is capable of sustaining eITB-driven modes at a given time. Figure 7.2 presents time-traces of the global parameters of six of the discharges under investigation, chosen either for the prominence of the observed mode activity or for its conspicuous absence, for purposes of comparison. It can be seen that each of the discharges exhibits broadly similar behaviour, with densities that remain exceptionally low for the first $\sim 2.5 - 3.0$s before ramping steadily upwards to much higher values during the latter stages of each discharge. This early low-density phase is accompanied in most cases by a period of maximum input ECRH power, typically commencing at $t \approx 1.5$s and usually lasting for approximately 0.9s. The ECRH power is then typically decreased in steps during the periods preceding and accompanying the high density phase later in the discharges.

7.2 eITB driven modes

7.2.1 Overview of eITB driven modes

The first type of mode considered is the eITB-driven mode. As has been introduced in section 7.1, this mode is observed during the L-mode phase, early in the discharges in question, when high levels of ECRH power are applied.

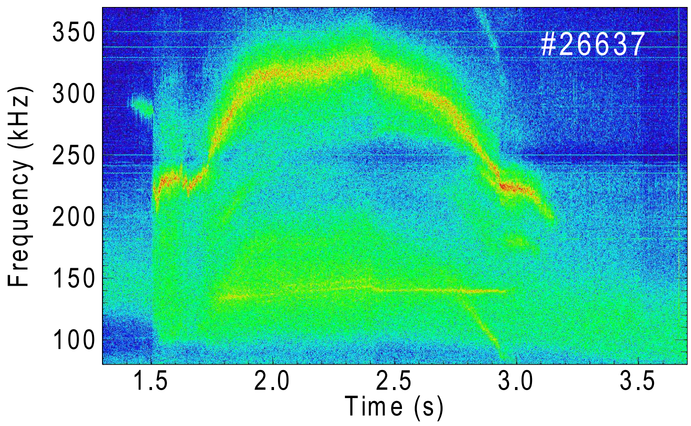

Figure 7.3. eITB-driven mode activity, measured by coil B31-14 of the Mirnov coil diagnostic, with $nfft = 8192$ and $nstp = 2048$, during discharge 26637.

Figure 7.3 shows an observation of this type of mode, made using the $B31-14$ coil of the Mirnov coil diagnostic, during discharge 26637. While the precise frequency of the eITB driven mode is difficult to identify due to the diffuse nature of the frequency observations, an arcing frequency trajectory is clearly visible with the frequency increasing from $f \approx 223 - 318$kHz during $t \approx 1.51 - 2.00$s. It then remains quite steady, with $f \approx 318 - 325$kHz, during $t \approx 2.00 - 2.40$s, attaining its highest frequency during this period of maximum input ECRH power, before dropping in frequency to $f \approx 199$kHz by $t \approx 3.15$s.

7.2.2 eITB-driven mode experimental analysis

In this section, the observed relationship between the eITB-driven mode behaviour and different plasma parameters is investigated. In addition, estimates of the radial localisation of the modes are made using the soft x-ray diagnostic.

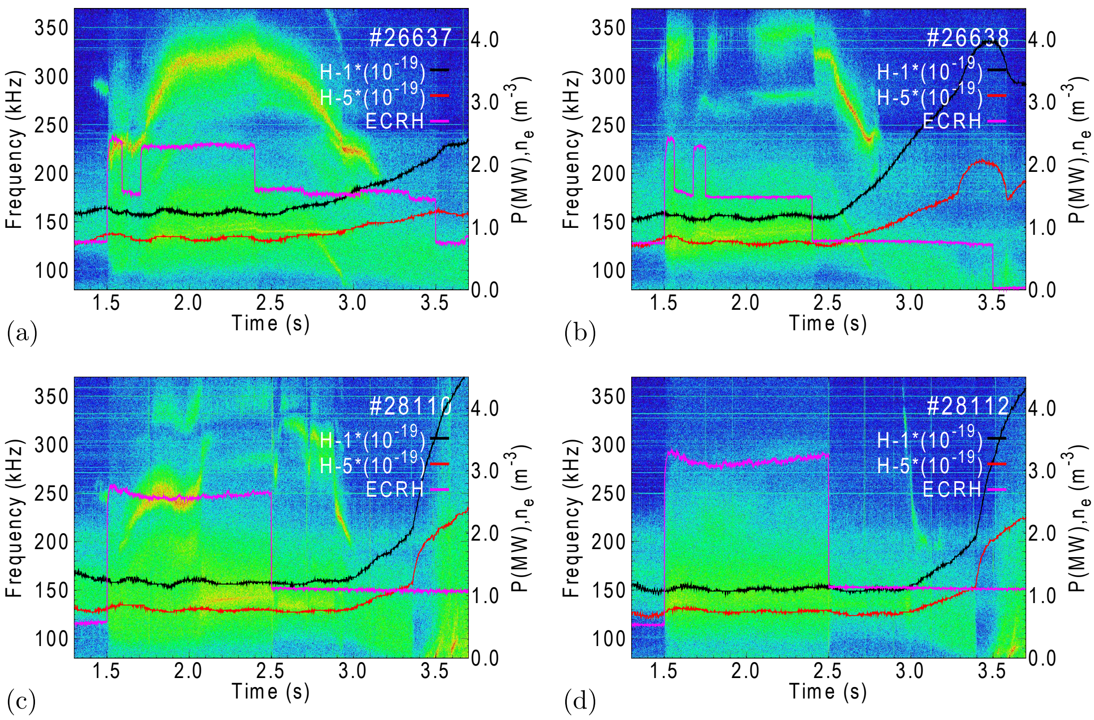

Figure 7.4. eITB-driven mode frequency evolution during discharges 26637, 26638, 28110 and 28112, measured by coil B31-14 of the Mirnov coil diagnostic, with $nfft = 8192$ and $nstp = 2048$, along with time-traces of ECRH power and core and edge densities.

As stated in section 7.1, the eITB driven modes are observed to occur during phases of high input ECRH power, typically when the ECRH power exceeds $P_{ECRH} \approx 2.2$MW. However, despite the fact that several of the discharges considered in table 7.1 possess peak ECRH heating powers ranging from $P_{ECRH} \approx 2.26 - 3.37$MW, the eITB driven modes are not observed in most cases. This can be seen by comparing the observed plasma parameters and corresponding mode behaviour during the periods of discharges 26637, 26638, 28110 and 28112 from $t = 1.3 - 3.7$s, as is done in figure 7.4. The global parameters are observed to be similar in each case, with very low values for the measured core electron density, ranging from $n_{e0} \approx 1.01 - 1.33 \times 10^{19}\text{m}^{-3}$ during the initial periods of observed mode behaviour from $t \approx 1.5 - 2.5$s. The peak ECRH powers during this period of the four discharges are $P_{ECRH} \approx 2.46$MW, 2.46MW, 2.80MW and 3.37MW respectively. The on-axis toroidal magnetic field strengths of discharges 26637, 28110 and 28112 are $B_t \approx -2.408$T,-2.383T and -2.383T respectively, while that of discharge 26638 is $B_t \approx -2.633$T. In each case, when high frequency mode activity is first observed, it accompanies the introduction of higher levels of ECRH power at $t \approx 1.5$s, as seen in figure 7.4.

Discharge	eITB cut-off time (s)	$H-1$ (m^{-3})	$H-5$ (m^{-3})
26636	3.15	1.71×10^{19}	1.01×10^{19}
26637	3.15	1.70×10^{19}	1.07×10^{19}
26638	2.78	1.67×10^{19}	0.96×10^{19}

Table 7.2. Times at which eITB driven mode activity is observed to cease and the corresponding core and edge densities at these times during discharges 26636, 26637 and 26638.

Despite these similarities, the observed mode behaviour varies significantly from discharge to discharge. Discharge 26637 displays the most persistent mode activity, continuing essentially uninterrupted until $t \approx 3.15$s. The mode frequency begins its rise at $t \approx 1.5$s, with the introduction of additional ECRH power, and reaches its peak frequency during this period of high ECRH power from $t \approx 2.0 - 2.4$s. The mode begins to decrease in frequency immediately once the input power is reduced from $P_{ECRH} \approx 2.29 - 1.57$MW at $t \approx 2.4$s, decreasing steadily until $t \approx 3.15$s after which time the mode activity is no longer observed.

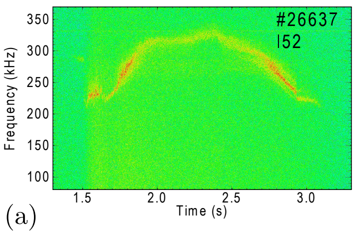

(a)

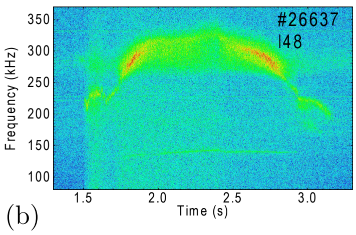

(b)

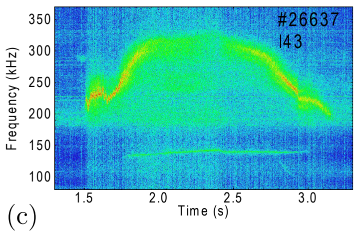

(c)

Figure 7.5. eITB driven mode activity observed using channels I52, I48 and I43 of the soft x-ray diagnostic, with $nfft = 8192$ and $nstp = 2048$, with tangency radii of $\rho_{pol} \approx 0.20, 0.57$ and 0.86 respectively.

Discharge 26638 exhibits some intermittent mode activity in the same frequency range as that observed during discharge 26637. However, it lacks the same arcing in frequency between $t \approx 1.5 - 2.5$s observed in the latter discharge. The downward frequency evolution beginning at $t \approx 1.4$s is present, though with a steeper frequency slope in time than was observed during discharge 26637. As can be seen by comparing figures 7.4 (a) and (b), the density ramp beginning at

$t \approx 2.5$s is also much steeper for discharge 26638 than for 26637. This suggests a relationship between the mode frequency evolution and that of the density. Further evidence supporting this arises when one considers the cut-off frequency of the modes at the end of this downward sweeping frequency phase. For discharges 26636, 26637 and 26638, this occurs at $t \approx 3.15$s, 3.15s and 2.78s respectively. For all three discharges the densities are very similar at these times, suggesting the existence of a cut-off density above which these modes are not supported by the plasma. Table 7.2 presents the times after which the modes are no longer observed during discharges 26636, 26627 and 26638 as well as the core and edge densities at these times, as measured using interferometry.

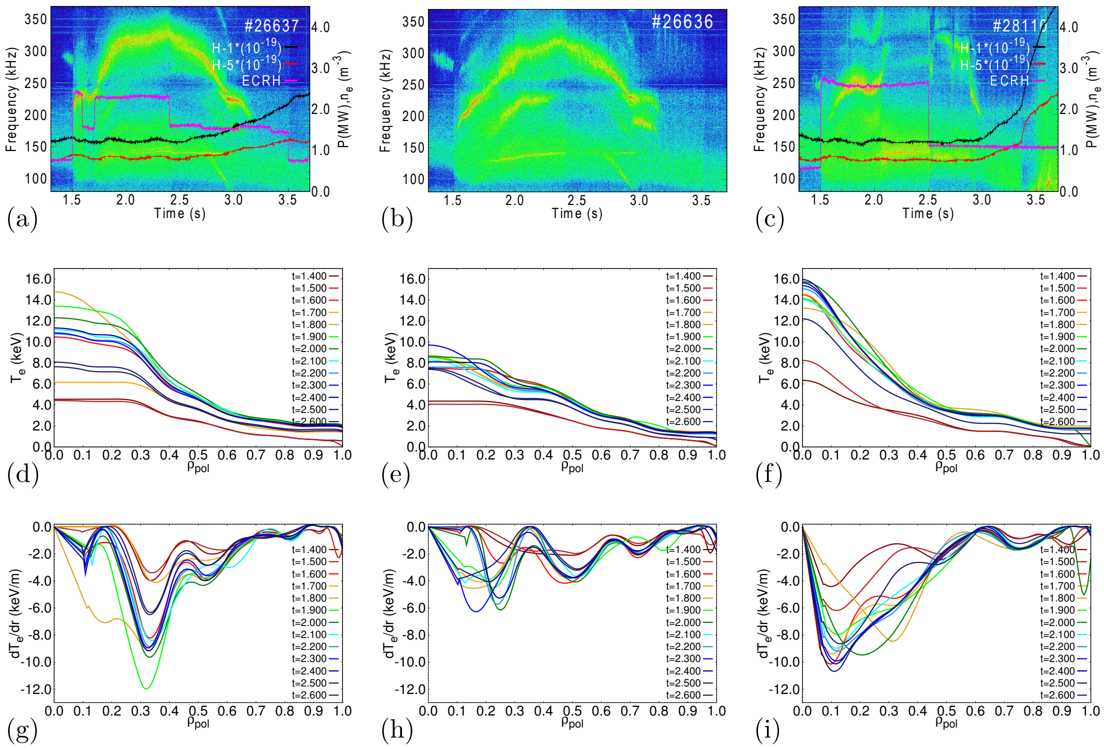

Figure 7.6. eITB driven mode activity during discharges 26637, 26636 and 28110, observed using the B31-14 coil of the Mirnov coil disgnostic, with $nfft = 8192$ and $nstp = 2048$, as well as the evolution of the background electron temperature profile and its corresponding gradient.

Observations of eITB driven mode activity made using three different channels of the soft x-ray diagnostic are presented in figure 7.5. These have tangency radii of $\rho_{pol} \approx 0.20, 0.57$ and 0.86 respectively. The fact that the eITB driven mode activity is still clearly visible for all three channels, despite their greatly different tangency radii, makes it difficult to determine the precise radial location.

This suggests that the modes could have a very large radial extent. Alternatively, they could be localised very close to the plasma edge, with a part of their signal still measured by the soft x-ray channels observing the core whose lines of sight pass through the edge region. Based on these initial observations of eITB-driven modes during discharges 26635-26639, a further series of discharges, dedicated in part to reproducing the eITB driven mode behaviour and investigating its radial structure using ECE imaging, were conducted at ASDEX Upgrade. These were unsuccessful in reproducing the desired eITB-driven mode activity but nonetheless provided additional information regarding the conditions under which these modes are excited.

It was observed that the position of the resonant layer of the input ECRH power appeared to play a role in determining whether these modes were present or not, with an eITB only forming in certain cases. As such, a potential explanation for the disparities in mode observations between the different discharges described above becomes apparent when one considers the background temperature profiles during the high power ECRH phase. These are presented for discharges 26637, 26636 and 28110 in figure 7.6. Figures 7.6 (d) and (g) show the evolution of the electron temperature profile and its corresponding gradient from the IDA diagnostic during the period from $t = 1.400 - 2.600$s of discharge 26637. It is immediately evident that an eITB is present in the plasma, with an extremely large electron temperature gradient present in the region centred on $\rho_{pol} \approx 0.32$ and a flattening of the electron temperature profile inside this region. The gradient starts with a relatively modest value of $\nabla T_e \approx 4$keV/m at $t = 1.40$s, before approximately doubling by $t = 1.60$s. It then increases rapidly, reaching an approximate peak value of $\nabla T_e \approx 12$keV/m at $t = 1.90$s. The exception to this trend is the large drop in the gradient that occurs at $t = 1.70$s, which can be accounted for by the temporary drop in ECRH power evident from $t \approx 1.591 - 1.705$s evident in figure 7.6 (a). The electron temperature gradient hovers between $\nabla T_e \approx 8 - 10$keV/m from $t = 2.00 - 2.40$s before dropping to $\nabla T_e \approx 6$keV/m at $t = 2.60$s with the lowering of ECRH power at $t = 2.50$s.

The rise in ∇T_e from $t = 1.50 - 1.90$s coincides with the period of mode frequency growth from $f \approx 223 - 318$kHz, while the stagnation in the gradient evolution is mirrored by a steadying of the frequency evolution. Finally, the removal of heating power and resultant decrease in the electron temperature gradient starting at $t \approx 2.50$s results in a corresponding drop in the mode frequency. Thus, it is concluded that some type of relationship exists between the two quantities. This is explored further by comparing observations from discharge 26637 with those from discharges 26636 and 28110.

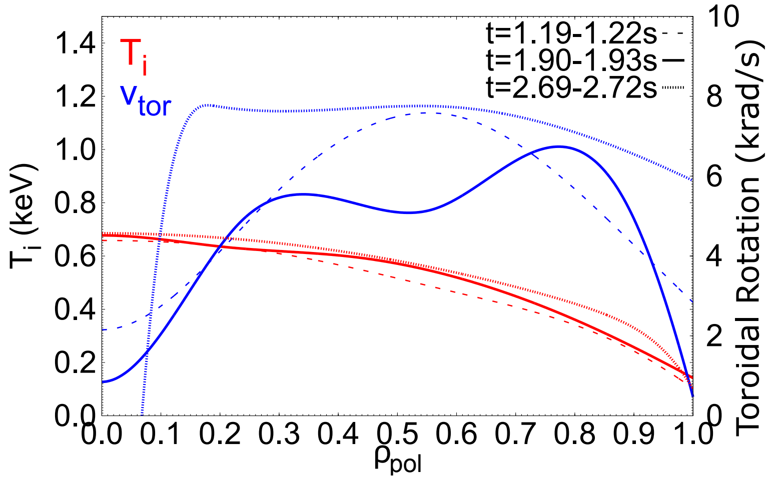

Figure 7.7. Fitted ion temperature and toroidal rotation profiles, from data measured before, during and after period of peak input heating power from $t \approx 1.5 - 2.4$s during discharge 28112.

Similar eITB driven mode activity is observed during discharge 26636, though with a lower amplitude during the phase from $t \approx 2.0 - 2.4$s. Considering the electron temperature profile and its gradient during this discharge, as presented in figures 7.6 (e) and (h) respectively, the presence of an eITB is also observed, though not as prominent as in discharge 26637. This suggests that it is primarily the presence of the eITB itself and not necessarily the magnitude of the temperature or gradient that gives rise to the mode. Weight is lent to this assertion by considering observation during discharge 28110 in figures 7.6 (c), (f) and (i). While extremely high levels of ECRH power are applied in this case, with steep electron temperature gradients in the core, no eITB is observed to be formed. As such, the persistent eITB driven mode behaviour observed during discharges 26636 and 26637 is likewise absent.

The slope of the frequency change in time from $t \approx 1.5 - 2.0$s is shallower during discharge 26636 than for the corresponding period of discharge 26637. This appears to be attributable to the fact that the plasma is heated steadily during this period of discharge 26636, while the heating in 26637 is subject to a temporary decrease from $t \approx 1.591 - 1.705$s, with the increase in frequency recommencing at a higher rate from $t \approx 1.7 - 2.0$s.

While no ion temperature data was available for discharges 26636-26638, CXRS measurements at a number of time-points throughout discharges 28112 provided an estimate for the ion temperature and the toroidal rotation velocity of the plasma during the former three discharges.

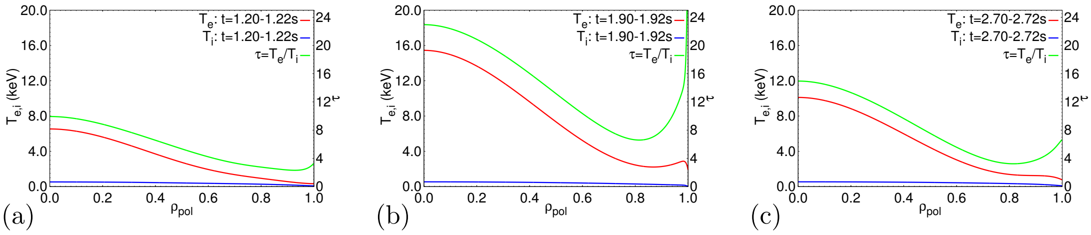

Figure 7.8. τ profile for time slices from (a) $t = 1.20 - 1.22$s, (b) $t = 1.90 - 1.92$s and $t = 2.70 - 2.72$s during discharge 28112, with the corresponding electron and ion temperature profiles.

This assumption was justified based on the similarity in the parameters of the discharges, as demonstrated in figure 7.2, with observations of the ion temperature for discharge 28112 presented in figure 7.7, along with observations of the plasma toroidal rotation velocity. As would be expected based on the absence of ICRH or extended periods of NBI heating, the ion temperature was observed to be very low, with an on-axis value of $T_i \approx 0.7$keV. In addition, the ion temperature does not vary much between the three measurements before, during and after the period of high ECRH power from $t \approx 1.5 - 2.4$s. Similarly, the toroidal rotation velocity is quite low and does not vary substantially over the three measurements. This would discount it as a potential cause of the large changes in frequency observed throughout the course of the eITB driven modes.

While the ion temperature itself is quite low, it could still play a substantial role in the eITB driven mode evolution if they are Alfvénic in nature and governed by the kinetic dispersion relation 3.4.61. This would come about through this equations dependence on the equations dependence on the ratio between the electron and ion temperatures $\tau = T_e/T_i$, which would be extremely high during the discharges considered here. The effect that this can have on low-frequency Alfvén eigenmodes has been discussed in section 6.3.1, where it is found that moderate changes in the value of τ can result in substantial shifts in the BAE and acoustic Alfvén eigenmode frequencies. The τ profile for three different time slices during discharge 28112 is plotted in figure 7.8, along with the corresponding electron and ion temperature profiles.

7.3 BAE-like modes

7.3.1 Overview of BAE-like modes

BAE-like modes are observed clearly during the ELM free H-mode phases of discharges 26573, 28110-28112, and weakly in a number of discharges of the series 26635-26639 and 28200-28201. They are observed in and around the BAAE/BAE frequency regime, from $f \approx 20 - 100$kHz at ASDEX Upgrade, and exhibit an inverted mode number ordering, with toroidal mode numbers $n = 1 - 5$ ranging from lowest to highest in order of decreasing frequency. These observations suggest that the modes are similar in nature to BAEs, this type of behaviour being characteristic of the latter type of mode. Figure 7.9 (a) shows an observation of the BAE-like modes, made using the Mirnov coil diagnostic during discharge 28112, while figure 7.9 (b) presents an estimate of the corresponding toroidal mode numbers from magnetics measurements.

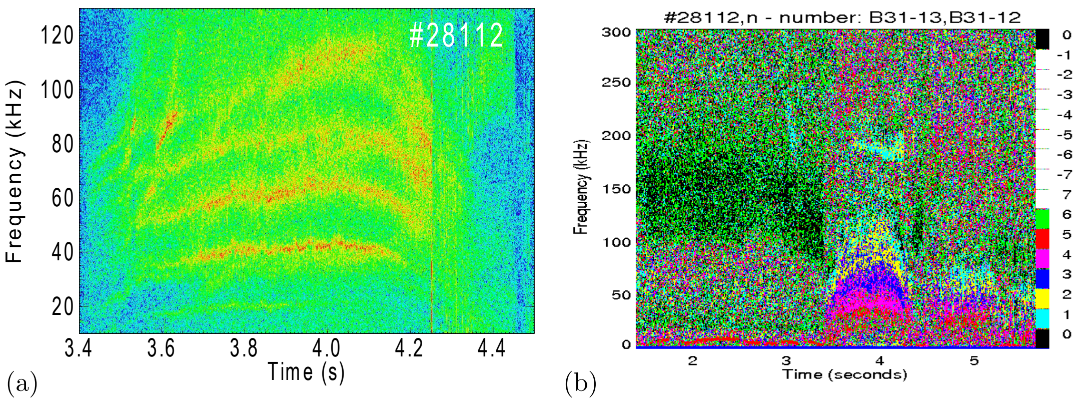

Figure 7.9. (a) BAE-like mode activity observed with MHA B31-14, with $nfft = 8192$ and $nstp = 2048$, during high β_{pol} phase from $t \approx 3.4 - 4.5$s of discharge 28112. (b) Estimated toroidal mode numbers of observed modes.

7.3.2 BAE-like mode experimental analysis

In this section, the behaviour of the main plasma parameters during discharges 26573, 28110, 28112 and 28201 will be investigated in an effort to gauge their relationship to the observed BAE-like mode activity. These discharges possess similar global parameters, with the toroidal magnetic field varying from $B_t \approx -2.383\text{T}$ to -2.402T and a plasma current of $I_p \approx 0.600\text{MA}$. Each exhibits varying degrees of mode activity in the frequency range from $f \approx 20 - 100\text{kHz}$, overlapping with the BAAE/BAE frequency regimes.

Observations during periods of highest amplitude Figure 7.10 presents examples of the BAE-like mode activity during discharges 26573, 28110, 28112 and 28201, with time-traces of the main plasma parameters also plotted.

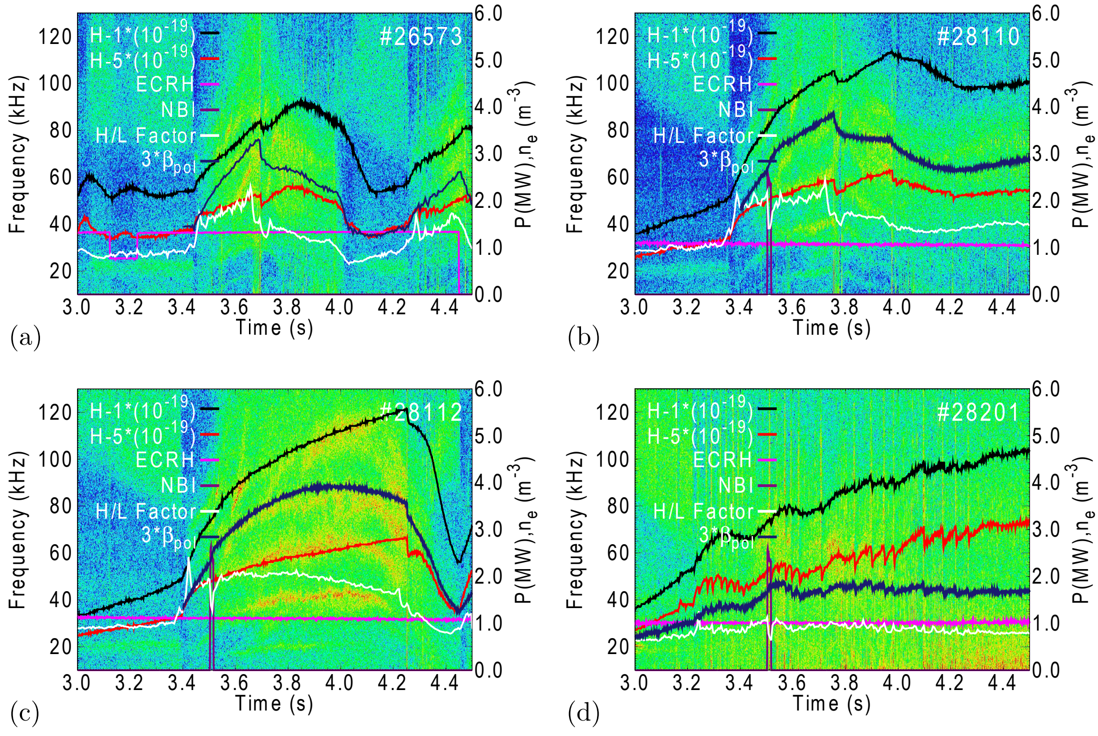

Figure 7.10. Observations of BAE-like mode activity, from coil B31-14 of the Mirnov coil diagnostic, with $nfft = 8192$ and $nstp = 2048$, during discharges (a) 26573, (b) 28110, (c) 28112 and (d) 28201, with time-traces of the main plasma parameters also plotted.

During the period in question, from $t = 3.0 - 4.5\text{s}$, it is observed that the ECRH power remains approximately constant at just over $P_{ECRH} \approx 1.3\text{MW}$ for discharge 26573. This is slightly lower for discharges 28110, 28112 and 28201, remaining approximately constant at $P_{ECRH} \approx 1.1\text{MW}$. The BAE-like modes are only clearly observed during the H-mode phases of the discharges, with observations beginning shortly after the L/H-factor, which provides as estimate for which confinement regime the plasma is in, rises above a value of one. Discharges 28110 and 28112 are each observed to enter an H-mode phase at $t \approx 3.36$s while for discharge 26573 it occurs at $t \approx 3.42$s. This transition is accompanied by rapid increases in the core and edge electron densities and, of more interest in the context of this analysis, a rapid increase in the poloidal beta β_{pol}. The exception to this behaviour is discharge 28201, which doesn't exhibit an obvious transition to H-mode and lacks the distinct BAE-like mode activity of the other three discharges.

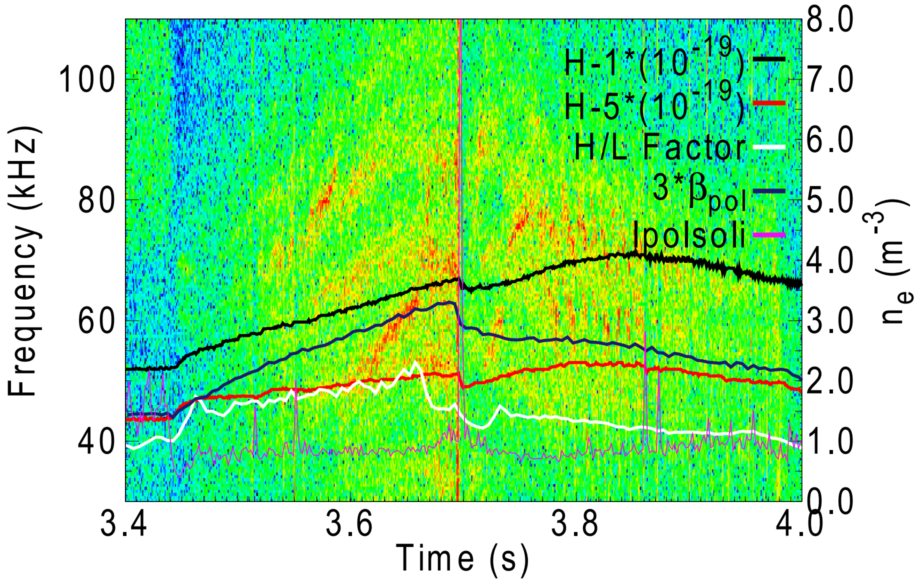

Figure 7.11. Observations of BAE-like mode activity, from coil B31-14 of the Mirnov coil diagnostic, with $nfft = 4096$ and $nstp = 2048$, during discharge 26573, with time-traces of the main plasma parameters also plotted.

Each of the discharges presented in figures 7.10 (a)-(c) differ somewhat from one another with regard to the precise nature and duration of the observed BAE-like mode activity. For discharge 26573, frequency separations between distinct toroidal eigenmodes which increase gradually in frequency are evident from $t \approx 3.50 - 3.69$s in the frequency range from $f \approx 40 - 90$kHz, as demonstrated in figure 7.11. More prominent mode activity which increases more rapidly in frequency is also observed from $t \approx 3.560 - 3.585$s and $t \approx 3.600 - 3.660$s, with initial frequencies of $f \approx 75$kHz and $f \approx 47$kHz respectively. It is not clear whether this activity differs from the more diffuse frequency separations between distinct toroidal eigenmodes also observed. β_{pol} and the core and edge densities are observed to increase steadily during the period from $t = 3.500 - 3.695$s along with the mode frequency. From ECE measurements, the core electron temperature is observed to decrease gradually over this time period. The electron temperature also appears to exhibit moderate sawtoothing activity, suggesting the presence of a $q = 1$ surface in the plasma. This particular period of mode activity ceases at $t \approx 3.695$s, with the occurrence of a large ELM.

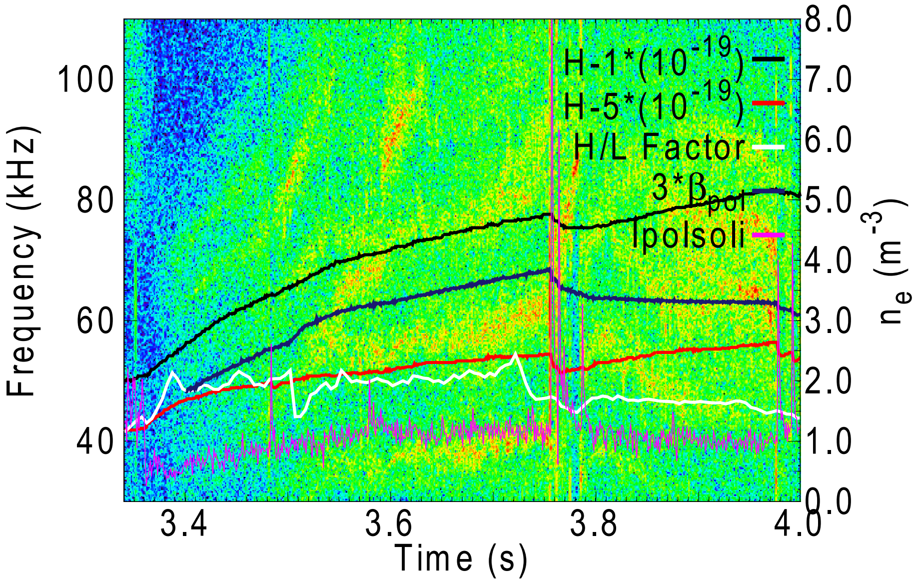

Figure 7.12. Observations of BAE-like mode activity, from coil B31-14 of the Mirnov coil diagnostic, with $nfft = 8192$ and $nstp = 2048$, during discharge 28110, with time-traces of the main plasma parameters also plotted.

This ELM activity is accompanied by a moderate drop in β_{pol}, while the plasma appears to remain in H-mode despite a large drop in confinement which begins slightly earlier at $t \approx 3.657$s. β_{pol} then begins to decrease in time while the core and edge densities, after dropping as a result of the ELM, continue to increase before peaking at $t \approx 3.85$s. In the period that follows from $t \approx 3.70 - 3.98$s, low-frequency mode activity is again observed, exhibiting intermittent downward sweeping behaviour, whose initial frequency decreases gradually over time. The exception to this is the upward sweeping mode activity observed from $t = 3.715 - 3.735$s, beginning at $f \approx 52$kHz, and that from $t = 3.735 - 3.755$s, beginning at $f \approx 72$kHz. The cessation of pronounced mode activity at $t = 3.86$s coincides with the onset of moderate levels of ELM activity, whereas the final cessation of all activity during this period approximately coincides with a large peak in the total radiated power at $t \approx 4.00$s and a substantial drop in the core electron temperature. The plasma drops out of H-mode at $t \approx 3.98$s and exhibits another large drop in β_{pol}.

Very similar behaviour is observed during discharge 28110, as presented in figure 7.12. Diffuse BAE-like frequency separations between distinct toroidal eigenmodes with increasing frequency are again observed from $t \approx 3.50 - 3.78$s with more prominent modes observed in the range from $f \approx 75 - 105$kHz starting at $t \approx 3.49$s and $t \approx 3.59$s. There is an NBI beam-blip at $t \approx 3.50$s which may initially excite this prominent mode activity. However, the effects of this would be expected to end after a few hundred milliseconds, after which time the BAE-like modes are still observed, pointing to another source of mode excitation.

The increase in frequency of the BAE-like modes is accompanied by corresponding increases in β_{pol} and the core and edge densities. This time-period is relatively quiescent with little ELM activity and decreases in the core electron temperature and gradients. Two ELMs in quick succession at $t = 3.757$s and $t = 3.764$s result in moderate drops in β_{pol} and core and edge electron densities. There is a sharp drop in confinement which begins at $t \approx 3.722$s but the discharge remains in H-mode. Following this, the mode frequency begins to decrease overall as was the case in discharge 26573. While β_{pol} begins to decrease slowly, the density continues its upward trend, suggesting that the mode frequency does not follow the density evolution directly.

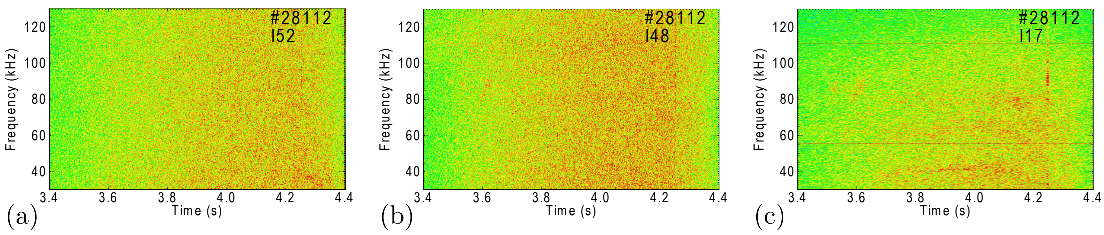

Figure 7.13. BAE-like mode activity observed using channels I52 and I48, with $nfft = 8192$ and $nstp = 2048$, and I17, with $nfft = 8192$ and $nstp = 512$, of the soft x-ray diagnostic, with tangency radii of $\rho_{pol} \approx 0.20, 0.55$ and 0.94 respectively.

Figure 7.14 shows BAE-like mode activity, observed with the Mirnov coil diagnostic, during discharge 28112. In this case the density is slightly lower at the H-mode transition and the discharge exhibits low-frequency mode behaviour from $t \approx 3.40 - 4.35$s. This period of the BAE-like mode activity is punctuated by the transition to H-mode at $t \approx 3.36$s and a large ELM at $t = 4.253$s.

The evolution of the mode frequency in time, at least for the two central frequency distinct toroidal eigenmodes, appears to follow quite closely that of β_{pol}, which reaches a local maximum at $t \approx 3.95$s. By comparison, the two central frequency distinct toroidal eigenmodes reach their maximum frequencies at $t \approx 4.02$s. The agreement is not as close for the highest frequency distinct toroidal eigenmodes, which reaches its local maximum frequency at $t \approx 4.05$s.

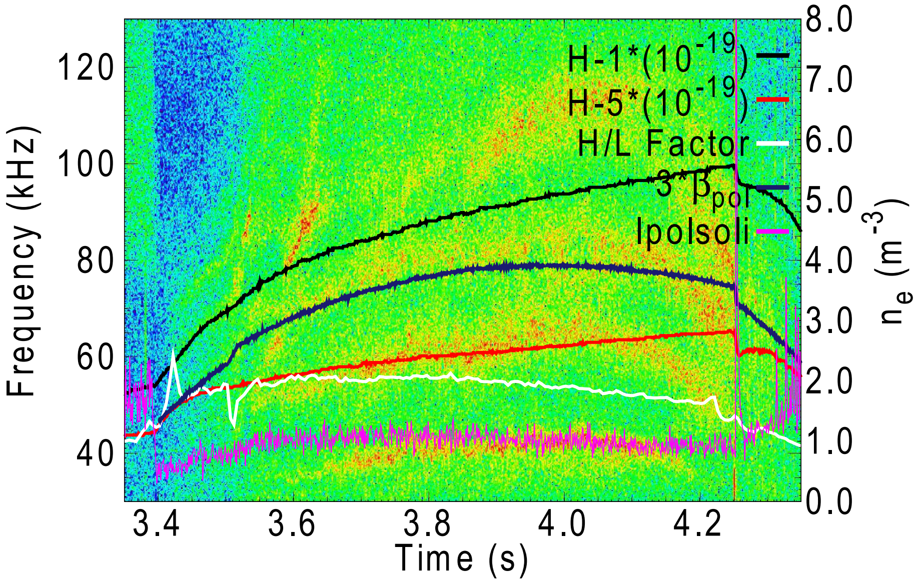

Figure 7.14. Observations of BAE-like mode activity, from coil B31-14 of the Mirnov coil diagnostic, with $nfft = 8192$ and $nstp = 2048$, during discharge 28112, with time-traces of the main plasma parameters also plotted.

Mode evolution with βpol It has been demonstrated how the BAE-like mode frequency is observed to be related to the evolution of β_{pol} during the initial H-mode phase of the discharges under consideration. We now extend these observations to investigate how this relationship develops throughout the remaining periods of discharges 26573 and 28110. As seen in figure 7.15, BAE-like mode activity re-emerges intermittently throughout the latter periods of discharges 26573 and 28110. During the former discharge it essentially ceases from $t \approx 3.98 - 4.26$s as the plasma drops out of H-mode and β_{pol} drops significantly. During this period, the core electron temperature rises substantially and peaks as faint low-frequency mode activity recommences at $t \approx 4.26$s. This is accompanied by intermittent moderate ELM activity until $t \approx 4.39$s, after which time higher amplitude BAE-like mode activity is again observed. This resembles the BAE-like mode activity first observed in the period $t = 3.50 - 3.69$s, with distinct frequency separations between distinct toroidal eigenmodes and a gradual increase in frequency. The core and edge densities increase during this period, with β_{pol} also increasing steadily until $t \approx 4.454$s. This period is again ended by a large ELM at $t = 4.478$s, as was the case for the first period of low-frequency mode activity from $t \approx 3.50 - 3.69$s. While the electron temperature drops rapidly as ECRH power is removed at $t = 4.45$s, the electron density continues to increase until $t \approx 4.50$s. Similar observations for discharge 28110 are presented in figure 7.15 (b).

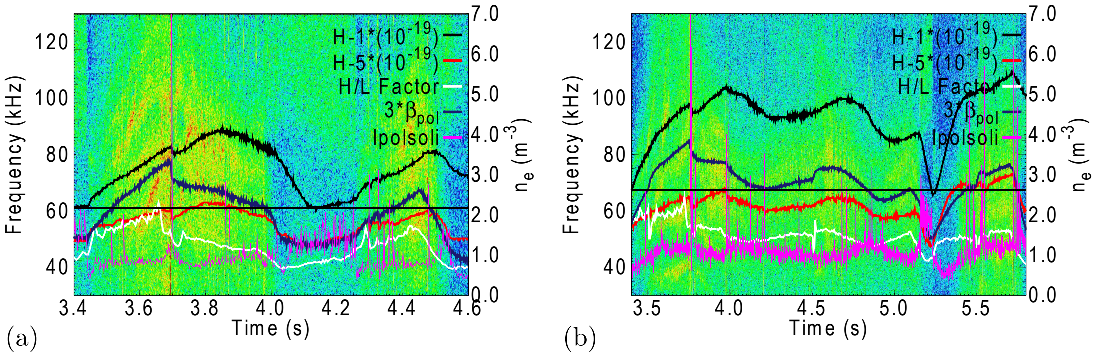

Figure 7.15. Time-traces of main experimental parameters during BAE-like mode activity phase of discharges 26573 and 28110, measured using coil B31-14 of the Mirnov coil diagnostic, with $nfft = 8192$ and $nstp = 2048$.

Some insight into the relationship between the BAE-like modes and β_{pol} can be gained by comparing the behaviour of β_{pol} during periods of mode activity and also when this activity is absent, as is done in figure 7.15. The black horizontal lines represent the value of β_{pol} when the BAE-like mode activity is first observed. It can be seen that the mode activity is observed most clearly during the times when β_{pol} rises approximately above this initial value and decreases when it is below it. This behaviour is also observed for discharges 28111 and 28112, suggesting the existence of a β_{pol} limit, below which the BAE-like modes are not excited. A consequence of this apparent dependence on β_{pol} is the fact that significant ELM activity, which degrades confinement and β_{pol}, can remove the drive necessary for these modes to be excited. Figure 7.16 shows the temperature and density components of the electron and ion diamagnetic profiles at $t \approx 4.08$s during discharge 28112. It can be seen that the ion diamagnetic frequency is extremely small due to the low flat ion temperature profile.

The electron diamagnetic frequency is also quite small in the region close to the $q = 1$ surface and continuum accumulation point at $\rho_{pol} \approx 0.48$. When one compares these observations with the experimental observations in figure 7.14, it is clear that some factor other than the diamagnetic frequency is required to explain the experimental behaviour of the BAE-like modes. Based on the low-amplitude soft x-ray observations in figure 7.13, it also appears that the BAE-like modes are localised towards the plasma edge.

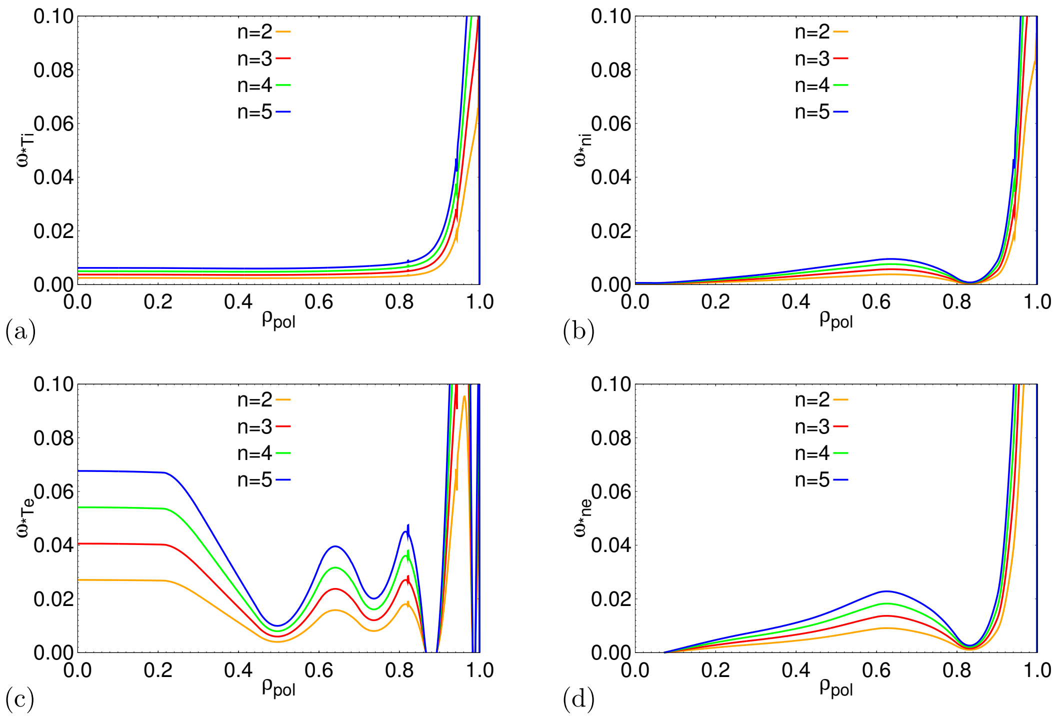

Figure 7.16. Diamagnetic frequency profiles at $t \approx 4.08$s during discharge 28112.

7.4 Edge-TAEs

7.4.1 Overview of edge-TAEs

Mode activity in the TAE frequency regime has been observed during the ELM free H-mode phase of discharge 28112, an example of which is presented in figure 7.17. This mode activity has a higher amplitude than the BAE-like modes observed during the same period and decreases in frequency from $f \approx 195$kHz to $f \approx 175$kHz from $t \approx 3.72 - 4.24$s. These modes are observed towards the plasma edge, as will be discussed later in this section, and as such will be called edge-TAEs for the duration of this work. As has been demonstrated in figure 7.9, the edge-TAE is found to have a toroidal mode number of $n = 1$. However, it was not possible to obtain an estimate for the poloidal mode number m.

7.4.2 Edge-TAE experimental analysis

Figure 7.17 (a) shows an observation of TAE-like mode activity from $t \approx 3.72 - 4.24$s during discharge 28112 made using coil B31-14 of the Mirnov coil diagnostic, with time traces of the main plasma parameters also plotted. Discharge 28112 is observed to be in H-mode for the duration of the observed TAE-like mode activity, which ceases with the occurrence of an ELM at $t \approx 4.252$s.

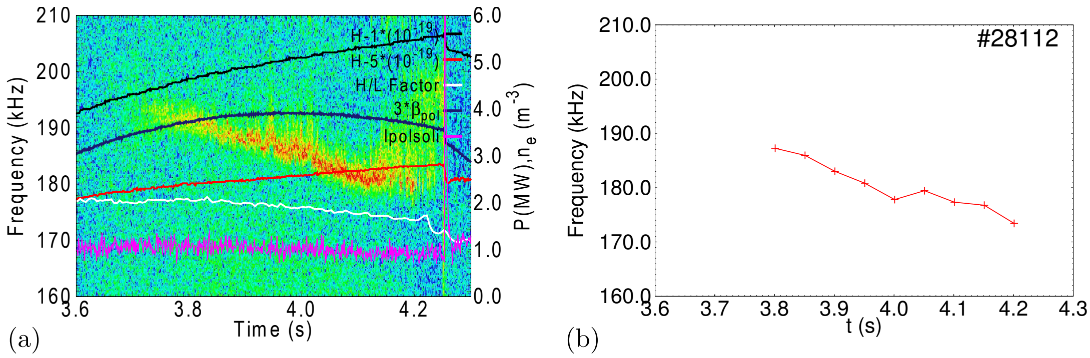

(a) (b)

Figure 7.17. (a) Observation of TAE-like mode activity from $t \approx 3.72 - 4.24$s during discharge 28112 made using coil B31-14 of the Mirnov coil diagnostic, with $nfft = 8192$ and $nstp = 2048$, with time traces of the main plasma parameters also plotted. (b) Theoretical TAE frequency evolution at the estimated gap location at $\rho_{pol} = 0.70$, calculated from $f = \upsilon_A/(4\pi qR_0)$.

The core and edge densities increase during this period, while the mode frequency decreases, which would be expected for a TAE-like mode. β_{pol} exhibits an arcing evolution, which does not appear to influence the edge TAE-like frequency as it did for the BAE-like modes. This frequency behaviour, coupled with the frequency range in which it is observed provide tentative evidence that this mode is somewhat Alfvénic in nature, possibly a TAE. This is supported by calculations of the theoretical TAE frequency evolution, calculated using $f = \upsilon_A/(4\pi qR_0)$, as seen in figure 7.17 (b). No observations for Z_{eff} are available for this discharge so an estimate of $Z_{eff} = 1.6$ was utilised. It can be seen that the theoretical and experimental behaviour agree quite well both qualitatively and quantitatively, with the frequencies of both decreasing steadily in time. An estimate of the radial localisation of the mode is made using the soft x-ray and fast ECE diagnostics, as well as through a determination of the radial displacement eigenfunction (RDE) of the modes, via the methods described in section 4.3.2. Figure 7.18 shows measurements from four channels of the soft x-ray diagnostic with tangency radii of $\rho_{pol} \approx 0.15, 0.47, 0.73$ and 0.93 respectively.

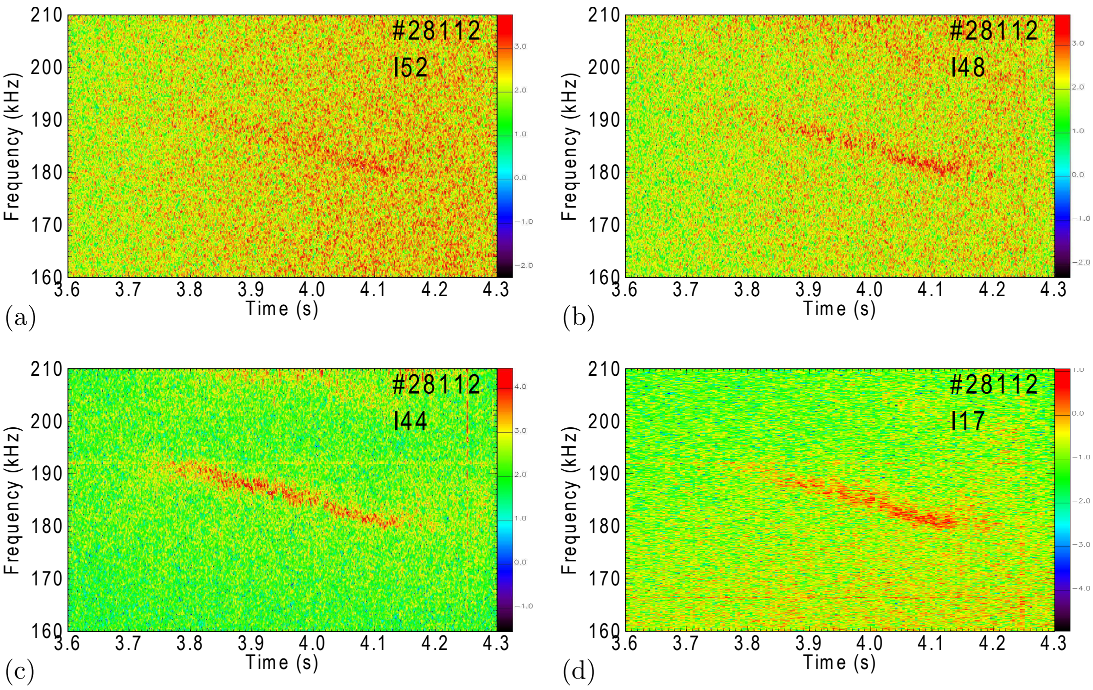

Figure 7.18. Edge-TAE mode activity observed using channels I52, I48, I44 and I17 of the soft x-ray diagnostic, with $nfft = 8192$ and $nstp = 2048$, with tangency radii of $\rho_{pol} \approx 0.15, 0.47, 0.73$ and 0.93 respectively.

It can be seen that while the edge-TAEs are visible across most of the plasma radius, they are most clearly observed by more edge localised channels. Figure 7.19 shows RDEs calculated for the I and F cameras for three 10ms time-slices during the observed edge-TAE activity. It is observed that the modes appear to exhibit the greatest displacement in the region from $\rho_{pol} \approx 0.40 - 0.95$, with the most prominent peaking in the RDEs occurring from $\rho_{pol} \approx 0.65 - 0.80$. Taking into account the soft x-ray observations from figure 7.18 and the RDE calculations from figure 7.19, it can be stated with reasonable certainty that the mode activity observed in figure 7.17 is radially localised towards the edge of the plasma.

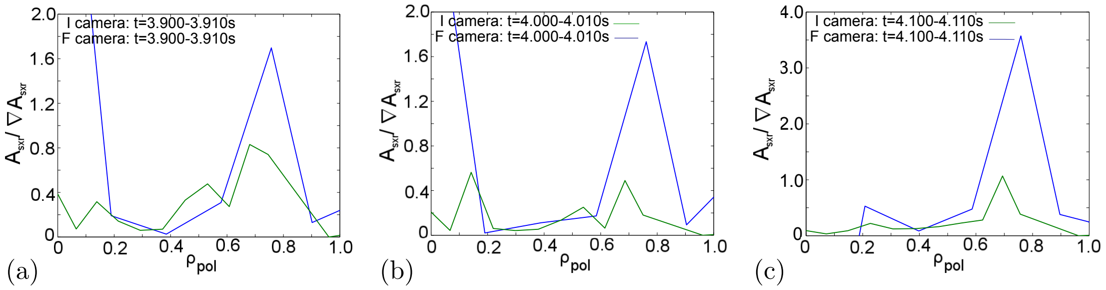

Figure 7.19. RDEs calculated from I and F cameras for TAE-like mode during different time-slices of discharge 28112.

7.4.3 Edge-TAE numerical analysis

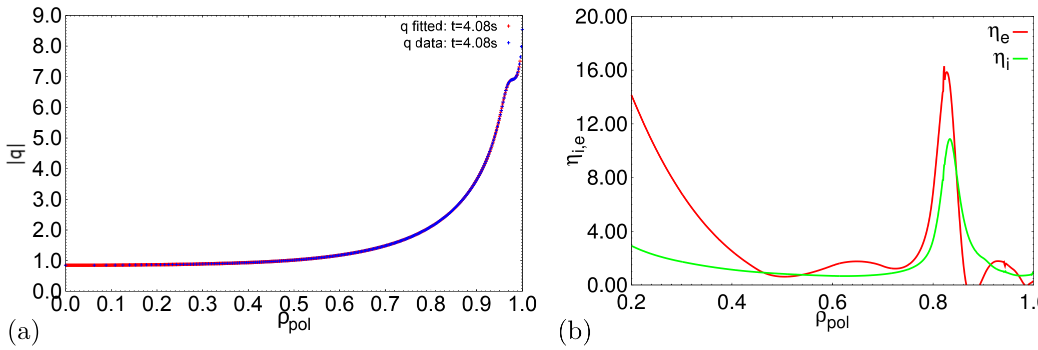

Figure 7.20. (a) q-profile recovered from CLISTE equilibrium reconstruction at $t = 4.08$s for discharge 28112. (b) η_e and η_i profiles at $t = 4.08$s for discharge 28112.

In order to further investigate the edge-TAEs, a numerical analysis has been carried out using the CLISTE and LIGKA codes. An equilibrium reconstruction was calculated using CLISTE utilising, among others, an estimate for the $q = 1$ surface and background temperature and density profile data as input sources. Due to the fact that no estimates for the poloidal mode number was available for this discharge, a value of $m = 4$ was assumed at the radial location where the RDE peak is typically observed. Thus, the numerical analysis serves more as a modelling exercise with realistic input profiles rather than a definitive comparison with experiment. The q-profile recovered from CLISTE is presented in figure 7.20 (a).

Figure 7.21 presents results for the shear Alfvén continuum, calculated numerically using LIGKA, for a case where kinetic effects are excluded and one where they are included for $n = 1 - 3$. From figure 7.21 (b) it can be seen that a minimum in the $n = 1$ continuum exists at $f \approx 200$kHz and $\rho_{pol} \approx 0.96$. This would be broadly in agreement with the experimentally observed frequency of the edge-TAE modes, if somewhat closer to the plasma edge than the experimental estimates would suggest. From figure 7.21 (c) it can be seen that this minimum in the continuum is accompanied by an eigenfunction of quite narrow radial extent at approximately the same radial location.

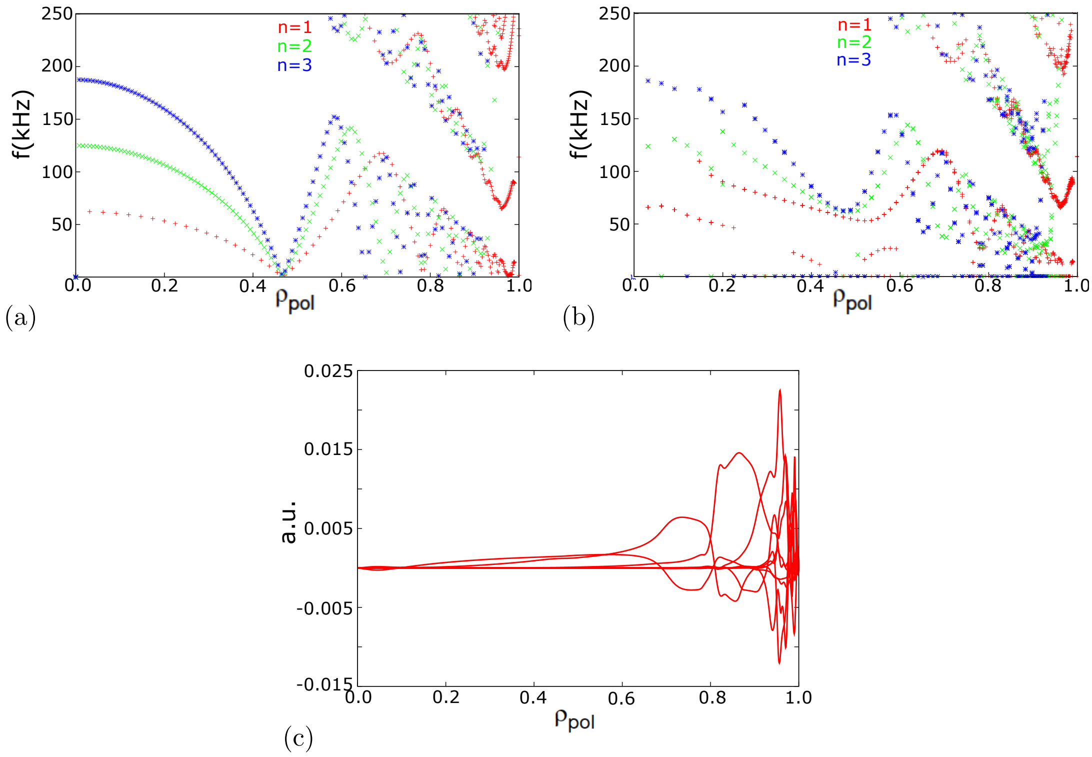

Figure 7.21. Alfvén continuum (a) excluding and (b) including kinetic effects and (c) Eigenfunctions calculated by LIGKA for discharge 28112 at $t = 4.08$s.

Likewise, a maximum in the $n = 1$ continuum is observed at $f \approx 170$kHz and $\rho_{pol} \approx 0.85$. This is also accompanied by an eigenfunction at approximately the same radial location, but which is broader. While the structure of the continuum would preclude excitation of these modes from core localised background gradients due to continuum damping, it has been suggested that turbulence could drive a mode such as this close to the plasma edge [89]. A second minimum in the $n = 1$ continuum is evident at approximately the same frequency as the first but located at $\rho_{pol} \approx 0.70$. A mode excited beneath this continuum minimum would not be subject to the same damping due to the opening up of the continuum structure for $\rho_{pol} < 0.70$ at this frequency. This continuum minimum is accompanied by a broader eigenfunction which peaks at approximately the same radial location as the minimum.

The term $\eta = \frac{\nabla T}{T} / \frac{\nabla n}{n}$ is an important mechanism for driving certain modes, according to turbulence theory. Figure 7.20 (b) presents the electron and ion η profiles at $t = 4.08$s. It should be noted that the ion temperature profile is taken from the closest CXRS measurement at $t \approx 3.51$s, though it is not expected to vary much in the intervening period, as has been demonstrated in figure 7.8. The hypothesis that the edge TAE modes could be driven by turbulence is strengthened by the strong peaking in η that occurs at $\rho_{pol} \approx 0.82 - 0.84$. This overlaps approximately with the RDE measurements shown in figure 7.19 and occurs in a position that would allow it to provide turbulent drive to the modes identified in figure 7.21 [89].

7.5 Conclusion

Three different types of mode have been investigated in this chapter; the eITB driven mode, BAE-like mode and edge TAE mode. It was speculated in the introduction that these modes could be at Alfvénic in nature due to the various characteristics that they share with BAEs and TAEs such as their mode number and the frequency regimes where they are observed. It has been demonstrated that although these modes exhibit many of the characteristics of Alfvénic modes, they cannot be explained purely using linear Alfvén theory, as described in chapter 3. Estimates of the radial localisation of the modes via experimental observations and numerical calculations, in conjunction with the background temperature and density profiles, suggest they are at least partially turbulence driven. The edge-TAE in particular exhibits Alfvénic frequency behaviour but occurs in a region that appears to lack the background gradient necessary to drive such a mode. The frequency observations are also quite diffuse, lacking definite harmonics. These observations, in conjunction with the peaking of the turbulence relevant parameter η in the region close to where the edge TAE and BAE like modes appear to occur offers strong evidence that these modes are explained by a combination of turbulence and Alfvénic physics [89]. However, further work is required in order to ascertain the nature of these modes definitively.

Chapter 8

Conclusion and outlook

Low-frequency Alfvén eigenmodes may play a central role in determining the stability of future fusion reactors such as ITER and DEMO. Their ability to redistribute energetic particle populations has the potential to reduce confinement to a sufficient degree to prevent the attainment of a viable burning plasma. In addition, these modes are capable of expelling fast particles from the plasma, potentially resulting in damage to the vacuum vessel surrounding the plasma. As such, it has become clear that a detailed understanding of the properties of these modes is necessary in order to mitigate the scenarios described above.

This thesis focuses primarily on two of the above mentioned low-frequency Alfvén eigenmodes, namely BAEs and acoustic Alfvén eigenmodes. These exist at frequencies lower than the TAE but can become important due to the potential coupling between modes at different radial positions and frequencies. Thus, these low-frequency modes can interact with TAEs to facilitate the radial redistribution of energetic particles. The investigation in this work has focussed on the impact that background temperature and density profiles can have on the dynamics of BAEs and acoustic Alfvén eigenmodes during periods of sawtooth activity when the plasma is heated exclusively by ICRH. As presented in section 5.3, these modes were observed to exhibit a distinct frequency evolution in time, dependent on the background temperature and density gradients. By considering observations from the soft x-ray diagnostic as well as estimates of the coherence between the soft x-ray and Mirnov coil diagnostics, the BAEs were determined to be located in the plasma core.

The character of the safety factor during discharge 25546 was investigated in section 5.4.2, in particular the existence and position of the $q = 1$ surface. This was achieved by reconstructing the plasma equilibrium using the CLISTE code, using various plasma parameters as constraints, in particular the $q = 1$ surface location estimate from the sawtooth inversion radius. As expected, during the appearance of the sawtooth instability, a $q = 1$ rational surface in the core region of the plasma was recovered. The location of this rational surface was typically found to overlap with regions exhibiting high background temperature gradients.
The evolution of the BAEs was investigated numerically in section 5.4.3. It was found that the modes occur close to the $q = 1$ surface location and that their frequency evolution and damping/growth rates are determined primarily by the diamagnetic frequency. These observations have important implications for the form of q-profile that will be chosen for future reactors, as they indicate that BAEs could be driven unstable if the $q = 1$ surface occurs too close to regions of high background gradient.
The behaviour of acoustic Alfvén eigenmodes during the sawtooth cycle was investigated in section 5.4.4. These were observed during periods of ICRH heating to be present at the beginning and end of a sawtooth period, but absent during the central phase. It was determined numerically that the mode damping increases during the central phase of the sawtooth period in conjunction with the background temperature gradient. To a certain extent, this would account for the observed mode activity during the initial and central phases of the sawtooth period, if not during the end phase.
The behaviour of low-frequency Alfvén eigenmodes during periods of both ICRH and ECRH was investigated in section 6.2. Observations of the BAEs were not as distinct as those during the ICRH only phase, with the frequency separations between distinct toroidal eigenmodes of this period essentially absent. It was found numerically that these eigenmodes are much more closely spaced with the addition of ECRH. This phase also differed from the ICRH only phase in that the acoustic Alfvén eigenmodes were much more damped. Experimentally, these modes were observed to invert their behaviour compared to the ICRH only phase, only occurring during the central phase of each sawtooth period.

A series of parameter sensitivity scans were conducted in section 6.3 in order to investigate the behaviour of BAEs and acoustic Alfvén eigenmodes during different parameter regimes. In the case of the BAEs, it was found that the decrease in mode frequency brought about by increasing the diamagnetic frequency ceases at a certain threshold. After this point, an increase in the diamagnetic frequency results in the BAE frequency shifting back upwards. It was also found that increasing the diamagnetic frequency sufficiently results in the acoustic Alfvén eigenmode coupling to another frequency branch, with a significantly higher damping rate. This contributes further to explaining the absence of acoustic Alfvén eigenmode activity during the central phase of the sawtooth period when the gradients are highest. Varying the parameter $\tau = T_e/T_i$ was found to shift the BAE and acoustic Alfvén eigenmode frequencies and change the continuum damping/growth rates.

Three different types of modes that are observed during discharges heated almost exclusively by ECRH were investigated in chapter 7. These modes included the eITB driven mode, which was observed to coincide with the occurrence of an electron internal transport barrier in the plasma, the BAE-like mode that exhibits characteristics similar to those of the BAE and the edge TAE, that exhibits frequency characteristics similar to the TAE. It was proposed that these modes could potentially be governed solely by the kinetic dispersion relation 3.4.61. However, after investigating these modes it was concluded that they are not governed by linear shear Alfvén physics alone, and appear to require the inclusion of nonlinear turbulence physics in order to fully explain them [89].

Following on from the investigation conducted here, there are further questions that remain to be addressed in future work. Additional experiments are required to provide more comprehensive experimental measurements such as the ion temperature and toroidal rotation for use in the analysis. It also remains to further investigate the physics occurring towards the end of the sawtooth cycle, to better understand the low-frequency mode behaviour occurring during this period. The inclusion of the full analytical expression for the kinetic dispersion relation with the effects of trapped particles and particles with finite $v_\perp$ taken into account is also important for future work. Finally, further work is required to fully understand the physics underlying the modes described in chapter 7 and to determine whether it is Alfvénic physics, turbulence or a combination of both mechanisms that drive these modes, as discussed above [89].

Bibliography

[1] Wesson J *Tokamaks Third Edition* Oxford University Press (2004)

[2] Population Division of the Department of Economic and Social Affairs of the United Nations Secretariat, World Population Prospects: The 2012 Revision

[3] Fitzpatrick R, Plasma Physics Notes: http://farside.ph.utexas.edu/teaching/plasma/

[4] EFDA website https://www.efda.org/2011/09/tokamak-principle-2/

[5] ASDEX Upgrade website http://www.aug.ipp.mpg.de

[6] Herrmann A and Gruber O 2003 *Fusion Science and Technology* **44** 569

[7] Chu M S et al 1992 *Phys. Fluids B* **4** (11) 3713

[8] Freidberg J P 1982 *Reviews of Modern Physics* **54** 801

[9] Bellan P *Fundamentals of Plasma Physics, California Institute of Technology, Cambridge Press 2006*

[10] Hugo J. de Blanc *Guiding centre motion* Private correspondences

[11] Nguyen C *Magnetohydrodynamics activity and energetic particles: Application to beta Alfvén eigenmodes* Ph.D. Thesis, Ecole Polytechnique (2009)

[12] Mc Carthy P J 1999 *Phys. Plasmas* **6** 3554

[13] Shafranov V D 1958 *Sov. Phys. JETP* **6** 545

[14] Grad H and Rubin H 1958 *Proceedings of the Second United Nations Conference on the Peaceful uses of Atomic Energy* (United Nations, Geneva), **21** 190

[15] Gerhard J 1992 *IPP Report* 1/262

[16] Igochine V et al 2010 *IPP Report* 1/338

[17] Suttrop W and Peeters A G 1997 *IPP Report* 1/306

[18] Classen I G J et al 2011 *Rev. Sci. Instrum.* **81** 10D929

[19] Mylnek A et al 2010 *Rev. Sci. Instrum.* **81** 033507

[20] Kurzan B et al 2001 *Rev. Sci. Instrum.* **72** 1111

[21] Fiedler S et al 1999 *Journal of Nuclear Materials* **269** 1279

[22] Schneider P *Characterization and scaling of the tokamak edge transport barrier* Ph.D thesis LMU 2012

[23] Fischer R et al 2010 *Fusion Science Technology* **58** 2 675

[24] Viezzer E et al 2012 *Rev. Sci. Instrum* **83** 103501

[25] Igochine V et al 2010 *Phys. Plasmas* **17** 122506

[26] Kadomtsev B B 1975 *Sov. J. Plasma Phys.* **1** 710

[27] Pinches S D *Non-linear interaction of fast particles with Alfvén waves in tokamaks* Ph.D. Thesis, University of Nottingham (1996)

[28] Kramer N F *Physics of Alfvén Waves* Wiley-VCH (2001)

[29] Tataronis J and Grossman W 1973 *Z. Physik* 261 203

[30] Chen L and Hasegawa A 1974 *Phys. Fluids* **17** (7) 1399

[31] Heidbrink W W 2008 *Phys. Plasmas* **15** 55501

[32] K. Appert, R. Gruber, F. Troyon and J. Vaclavik 1982 *Plasma Physics* **24** (9)

[33] D. W. Ross, G. L. Chen and S. M. Mahajan 1982 *Phys. Fluids* **25** (4)

[34] Hazeltine and Meiss *Plasma Confinement* Dover (1992)

[35] Cheng C Z and Chance M S 1986 *Phys. Fluids* **29** (11) 3695

[36] Fu G Y and Van Dam J W 1989 *Phys. Fluids B1* (10) 1949

[37] Gorelenkov N N et al 2007 *Phys. Letters A* **370** 70-77

[38] Turnbull A D et al 1993 *Phys. Fluids B* **5** (7) 2546

[39] Zonca F et al 2010 *J. Phys. Conf. Ser.* **260** 012022

[40] Biancalani A 2012 Private correspondences

[41] Chavdarovski I *Kinetic theory of low frequency Alfvén waves in burning plasmas* Ph.D. Thesis, University of Tor Vergata (2009)

[42] Zonca F et al 1996 *Plasma Phys. Control. Fusion* **38** 2011

[43] Freimann E A and Chen L 1982 *Phys. Fluids* **25** (3)

[44] Biglari H and Chen L 1991 *Phys. Rev. Lett.* **67**

[45] Tsai S T and Chen L 1993 *Phys. Fluids B* **5** 3284

[46] Qin H et al 1998 *Phys. Plasmas* **5** (4) 1035

[47] Qin H et al 1999 *Phys. Plasmas* **6** (6) 2544

[48] Lauber Ph et al 2009 *Plasma Phys. Control. Fusion* **51** 124009

[49] Berk H L et al 1993 *Phys Fluids B* (5) 3969

[50] Mett et al 1992 *Phys Fluids B* (4) 2885

[51] Lauber Ph et al 2007 *Journal of Computational Physics* 226

[52] Lauber Ph and Berk H L *Kinetic BAEs and GAMs* Private correspondences

[53] Antonsen T M and Lane B 1980 *Phys. Fluids* **23** (6) 1205

[54] Lauber Ph *Linear gyrokinetic description of fast particles effects on the MHD stability in tokamaks* Ph.D. Thesis, Technische Universitaet Muenchen (2002)

[55] Gao Z et al 2009 *Nucl. Fusion* **49** 045014

[56] Catto P J, Tang W M and Baldwin D E 1981 *Plasma Phys.* **23** 639

[57] Heidbrink W W et al 1993 *Phys. Rev. Letters* **71** 855

[58] Elfimov A G et al 2011 *Plasma Phys. Control. Fusion* **53** 025006

[59] Curran D et al 2012 *Plasma Phys. Control. Fusion* **54** 055001

[60] Hahm T S, Lee W W and Brizard A 1988 *Phys. Fluids* **31** 1940

[61] Bytschkow D *Investigation of MHD mode rotation in ASDEX Upgrade* Master Thesis, Technische Universitaet Muenchen (2010)

[62] Igochine V, Private correspondences/Matlab script for calculating RDEs

[63] Lauber Ph et al 2010 *Proc. of the 23rd IAEA Fusion Energy Conference, Daejon, Korea Rep. of (IAEA, Vienna)* **Vol. IAEA-CN-180** THW/2-2Ra

[64] Piovesan P 2008 *Nucl. Fusion* **48** 065001

[65] Igochine V *Investigation of MHD instabilities in conventional and advanced tokamak scenarios on ASDEX Upgrade* Ph.D. Thesis, Technische Universitaet Muenchen (2002)

[66] Conway G D and Elliot L A 1987 *J. Phys. E: Sci. Instrum.* **20** 1341

[67] Shumway R Stoffer D *Time Series Analysis and Its Applications* http://www.stat.pitt.edu/stoffer/tsa3/tsa3ez.pdf

[68] da Graça et al 2007 *Plasma Phys. Control. Fusion* **49** 1849

[69] Conway G D Private correspondences

[70] da Graça S, Private correspondences

[71] Sharapov S E et al 2007 *Phys. Plasmas* **9** 2027

[72] da Graça et al 2012 *Plasma Phys. Control. Fusion* **54** 095014

[73] Pietrzyk Z A et al 1999 *Nucl. Fusion* **18** 587

[74] Hastie R J 1998 *Astrophysics and Space Science* **256** 177

[75] Bock A *Correlation analysis methods for real time localization* Diploma Thesis, Technische Universitaet Muenchen (2012)

[76] Sassenberg K *Improved analysis of measured MHD activity and the use of toroidicity induced Alfvén eigenmodes to constrain current density profile reconstruction in the ASDEX Upgrade tokamak* Ph.D. Thesis, University College Cork (2009)

[77] Sauter O, Angioni C and Lin-Liu Y R 1999 *Phys. Plasmas* **6** 2834

[78] Mc Carthy P J 2012 *Plasma Phys. Control. Fusion* **54** 015010

[79] Mc Carthy P J et al 1999 IPP Report 5/85

[80] Sassenberg K et al 2009 *Plasma Phys. Control. Fusion* **51** 065003

[81] Classen I G J et al 2011 *Plasma Phys. Control. Fusion* **53** 124018

[82] Brunner S *Private communication*

[83] Davies B 1986 *Journal of Comp. Physics* **66** 36

[84] Rathgeber S K et al 2010 *Plasma Phys. Control. Fusion* **52** 095008

[85] Furth H P, Rutherford P H and Selberg H 1973 *Phys. Fluids* **16** 1054

[86] Rutherford P H 1973 *Phys. Fluids* **16** 1903

[87] Buttery R J et al 2000 *Plasma Phys. Control. Fusion* **42** B61

[88] La Haye R J 2005 *Phys. Plasmas* **13** 055501

[89] Biancalani et al *40th EPS Conference on Plasma Physics* P1.157

Appendix A

Experimental observations during discharge 25546

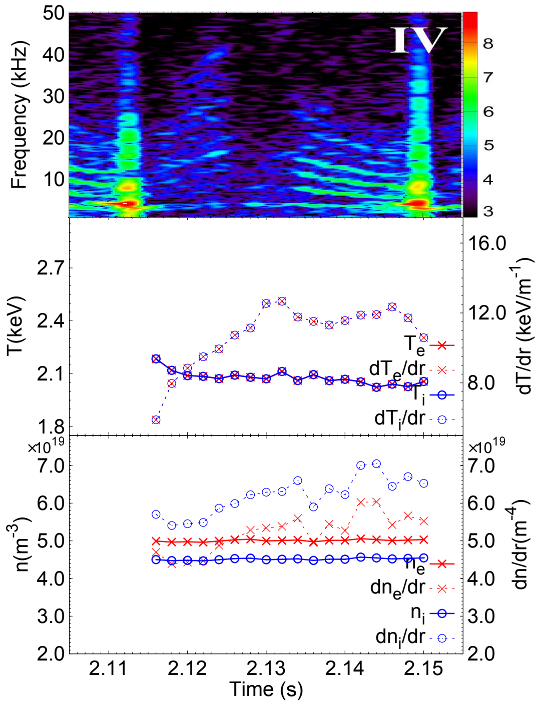

Figure A.1. Acoustic Alfvén eigenmode frequency evolution from $t = 2.105 - 2.155$s during discharge 25546, measured using line of sight $I5I$ of the soft x-ray diagnostic, with $nfft = 8192$ and $nstp = 512$, with a tangency radius of $\rho_{pol} \approx 0.24$ and the corresponding evolution in the background profiles at the $q = 1$ surface. Note that $T_i = T_e$ is assumed in this case.

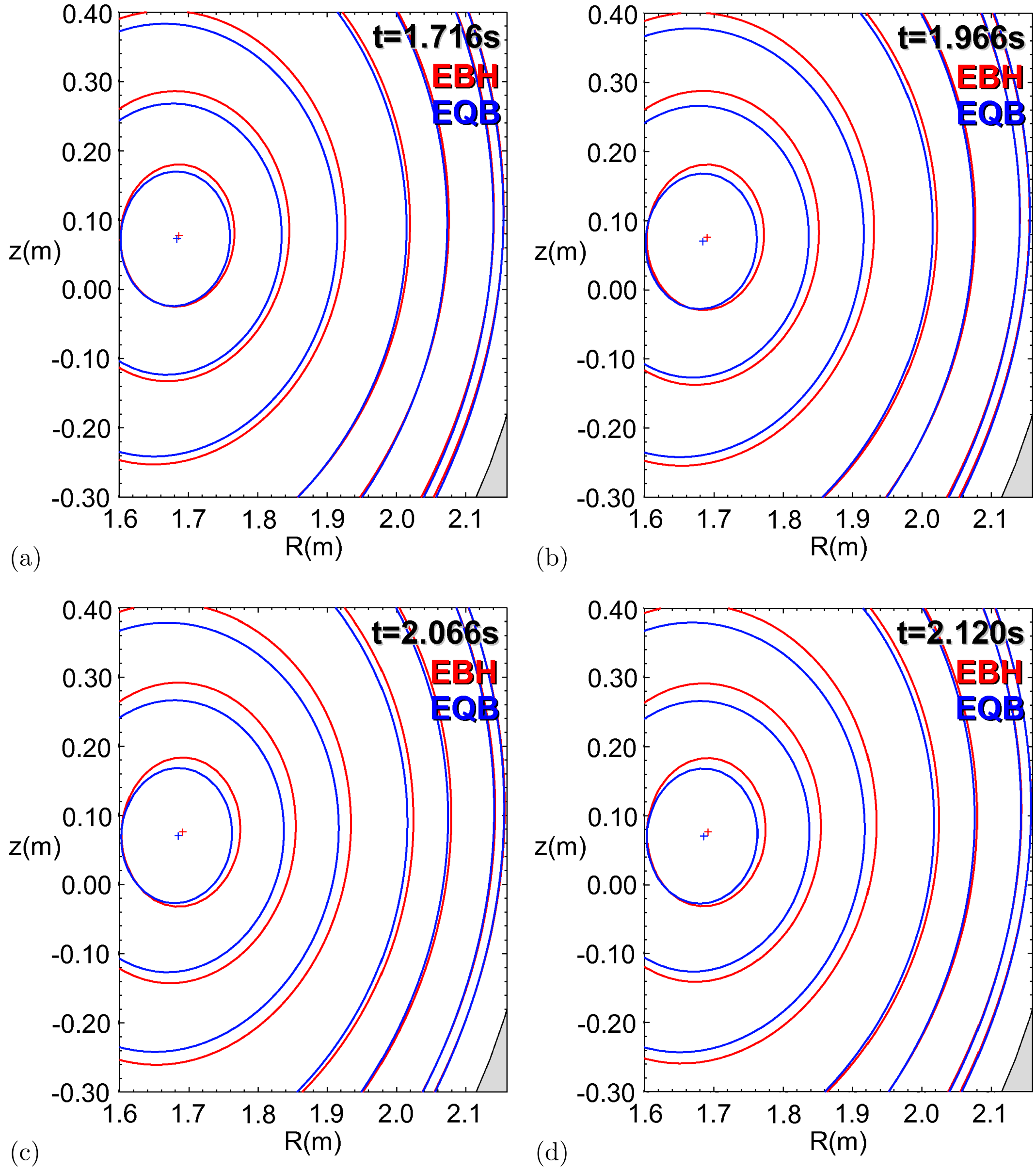

Figure A.2. Comparison between equilibrium reconstructions using magnetic and coil current data only (EQH) and with the addition of background kinetic profile and a rational surface constraint (EQB) for discharge 25546.

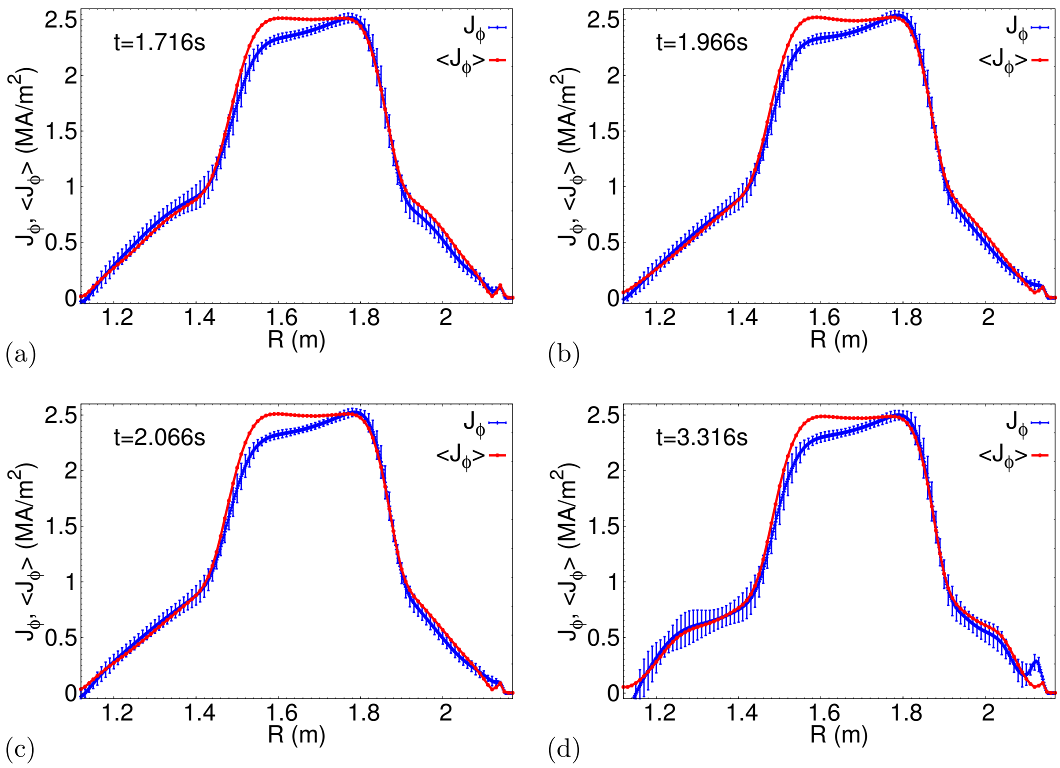

Figure A.3. Output local $J_\phi(R)$ and flux surface averaged $\langle J_\Phi(R)\rangle$ toroidal current density profiles for CLISTE equilibrium reconstructions during discharge 25546.

Appendix B

Numerical results for ICRH phase

B.1 BAEs during discharge 25549

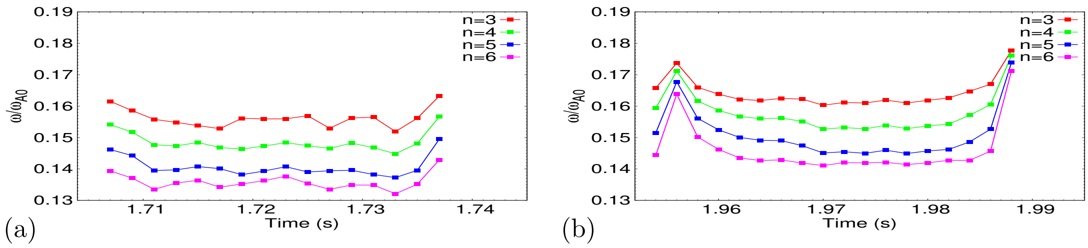

Figure B.1. Evolution of numerically calculated BAE continuum accumulation point frequency for toroidal mode numbers $n = 3 - 6$ during sawtooth periods I-II of discharge 25549.

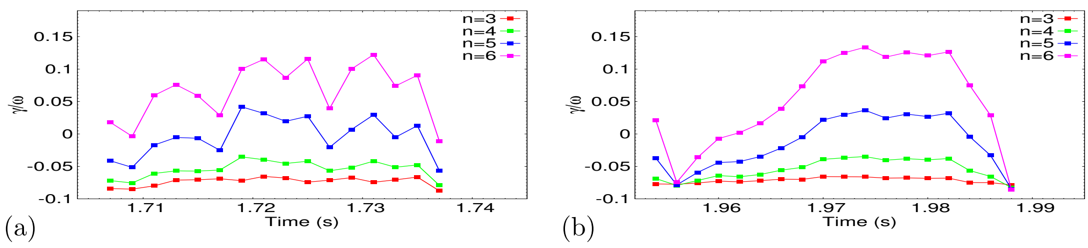

Figure B.2. Evolution of numerically calculated BAE damping/growth rate at $\rho_{pol}(CAP)$ for toroidal mode numbers $n = 3 - 6$ during sawtooth periods I-II of discharge 25549.

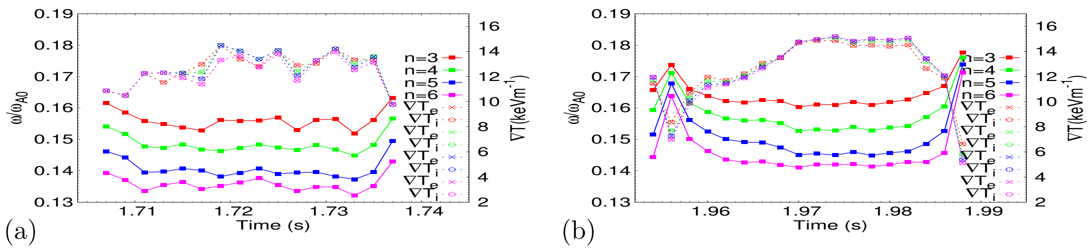

Figure B.3. Evolution of numerically calculated BAE frequency and damping/growth rate with the background ion and at electron density gradients at $\rho_{pol}(CAP)$ during sawtooth periods I-II of discharge 25549.

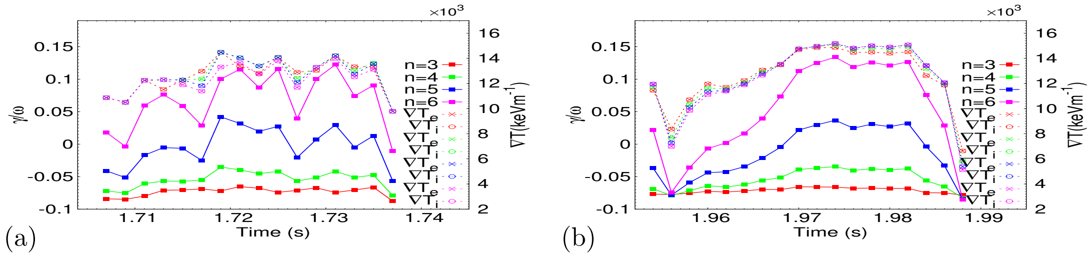

Figure B.4. Evolution of numerically calculated BAE frequency and damping/growth rate with the background ion and at electron density gradients at $\rho_{pol}(CAP)$ during sawtooth periods I-II of discharge 25549.

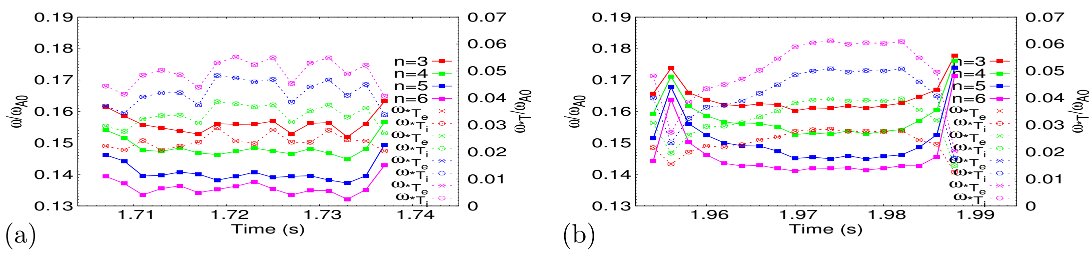

Figure B.5. Evolution of numerically calculated BAE CAP frequency for toroidal mode numbers $n = 3 - 6$ with the temperature component of the electron and ion diamagnetic frequencies at $\rho_{pol}(CAP)$ during sawtooth periods I-II of discharge 25549.

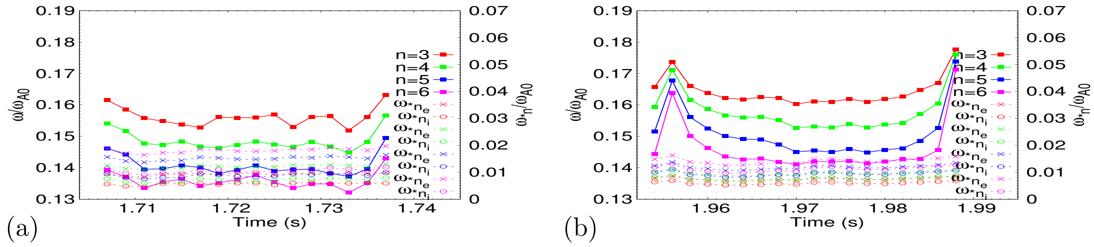

Figure B.6. Evolution of numerically calculated BAE CAP frequency for toroidal mode numbers $n = 3 - 6$ with the density component of the electron and ion diamagnetic frequencies at $\rho_{pol}(CAP)$ during sawtooth periods I-II of discharge 25549.

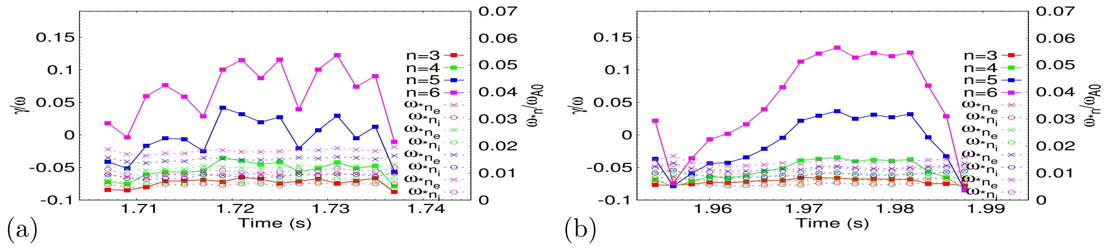

Figure B.7. Evolution of numerically calculated BAE CAP frequency for toroidal mode numbers $n = 3 - 6$ with the density component of the electron and ion diamagnetic frequencies at $\rho_{pol}(CAP)$ during sawtooth periods I-II of discharge 25549.

B.2 BAEs during discharge 25546

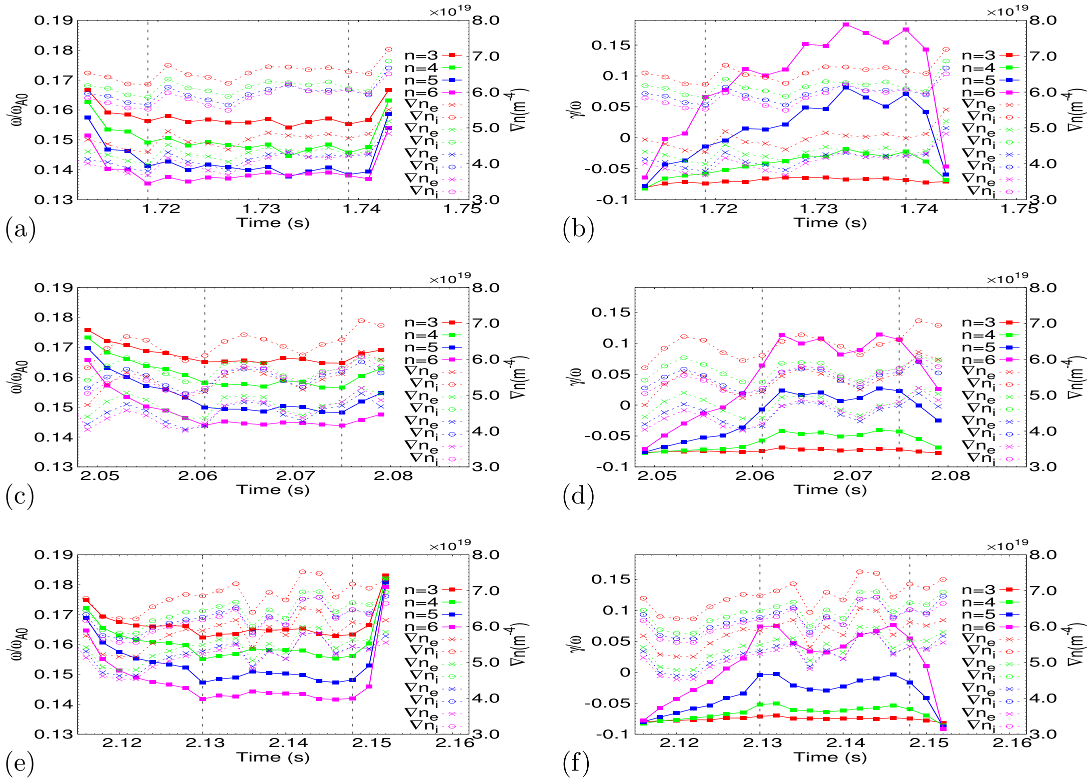

Figure B.8. Evolution of numerically calculated BAE frequency and damping/growth rate with the background ion and at electron density gradients at $\rho_{pol}(CAP)$ during sawtooth periods I-IV of discharge 25546.

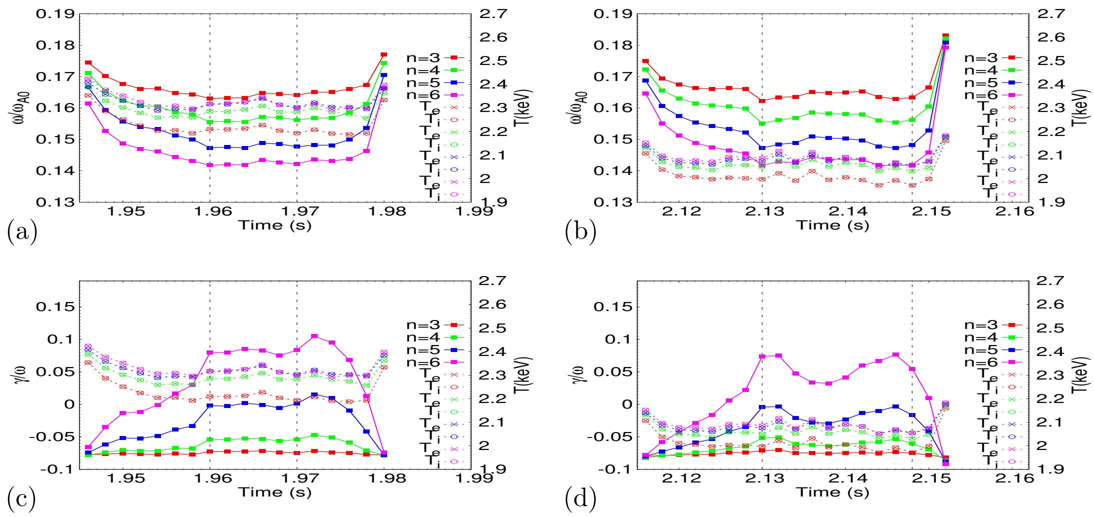

Figure B.9. Evolution of numerically calculated BAE CAP frequency for toroidal mode numbers $n = 3 - 6$ with the electron and ion temperatures at $\rho_{pol}(CAP)$ during sawtooth periods I-IV of discharge 25546.

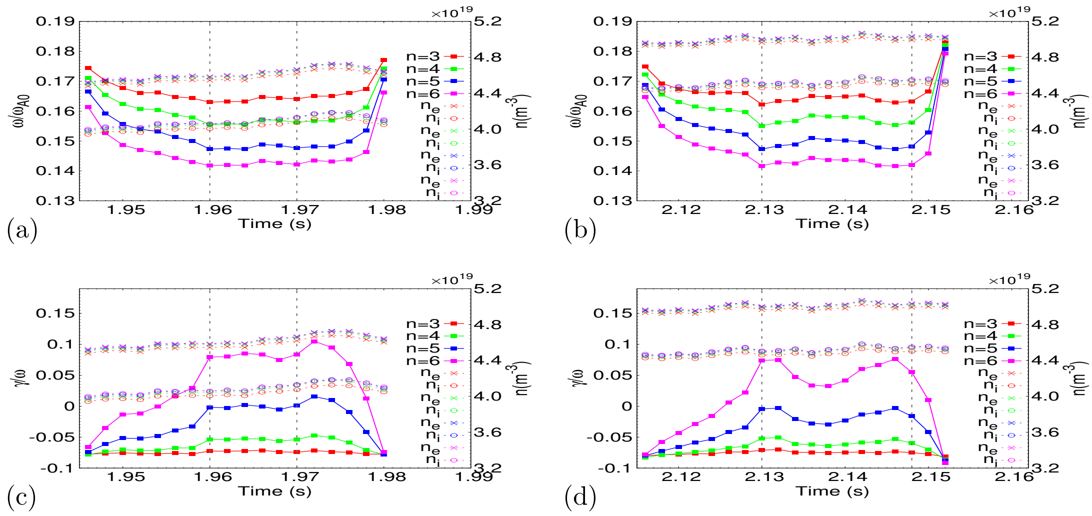

Figure B.10. Evolution of numerically calculated BAE CAP frequency for toroidal mode numbers $n = 3 - 6$ with the electron and ion densities at $\rho_{pol}(CAP)$ during sawtooth periods I-IV of discharge 25546.

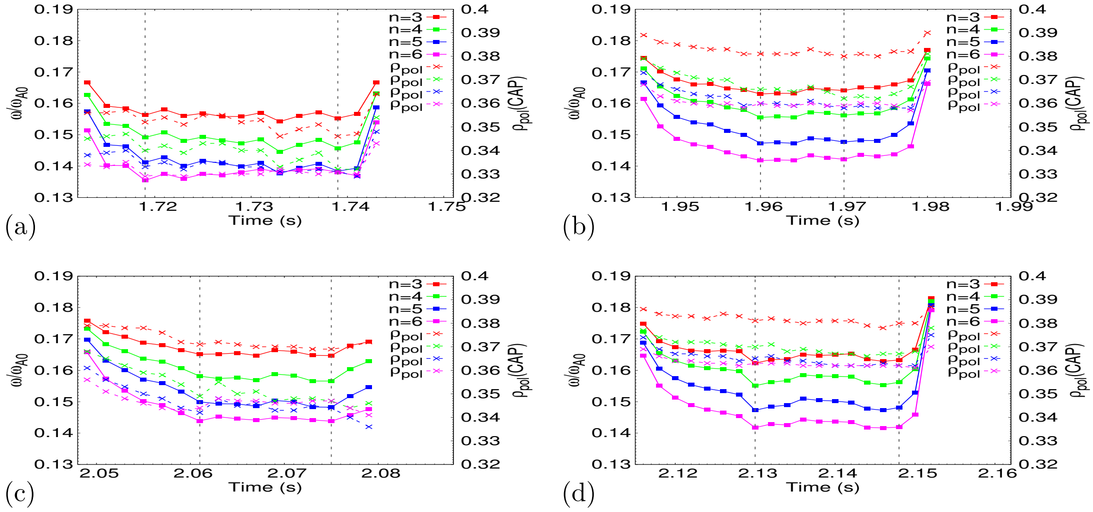

Figure B.11. Evolution of numerically calculated BAE CAP frequency for toroidal mode numbers $n = 3 - 6$ and the corresponding $\rho_{pol}(CAP)$ evolution for sawtooth periods I-IV during discharge 25546.

B.3 Acoustic Alfvén eigenmodes during discharge 25546

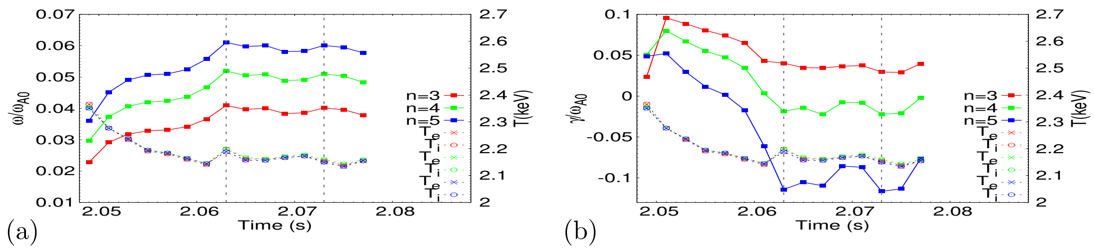

Figure B.12. Evolution of numerically calculated acoustic Alfvén CAP frequency and damping/growth rate for $n = 3 - 5$ with the electron and ion temperatures at $\rho_{pol}(CAP)$ for sawtooth periods II-IV during discharge 25546.

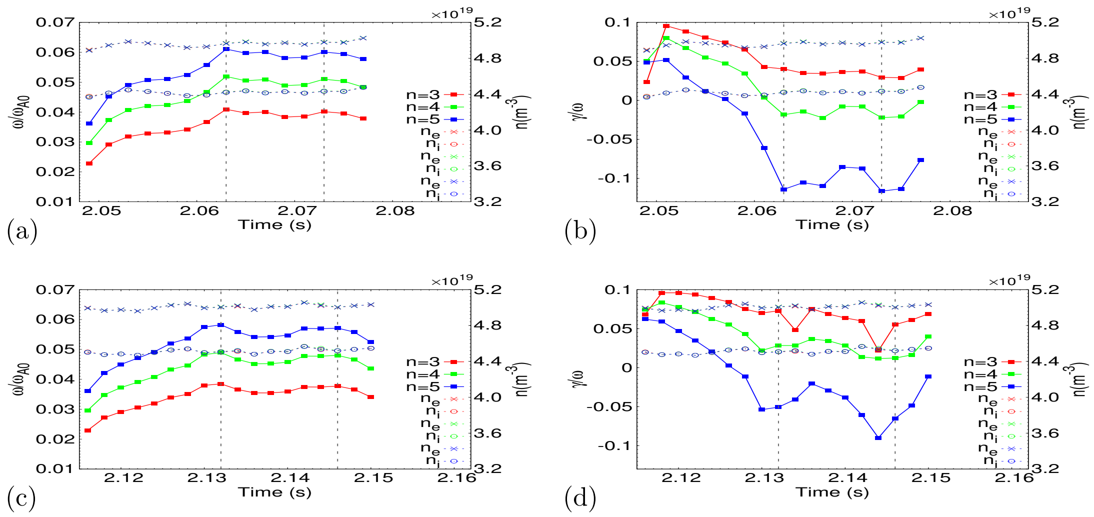

Figure B.13. Evolution of numerically calculated acoustic Alfvén CAP frequency and damping/growth rate for $n = 3 - 5$ with the electron and ion temperatures at $\rho_{pol}(CAP)$ for sawtooth periods II-IV during discharge 25546.

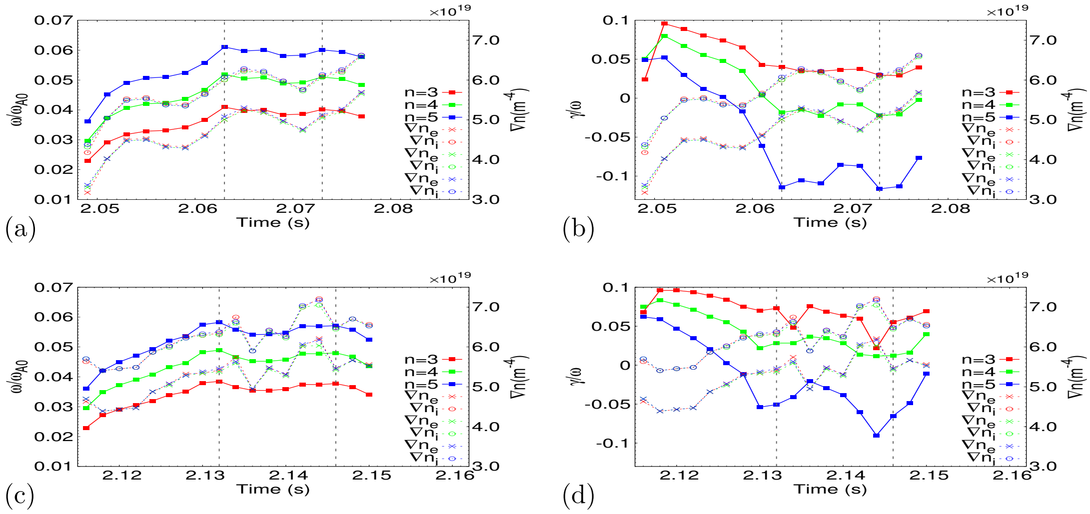

Figure B.14. Evolution of numerically calculated acoustic Alfvén CAP frequency and damping/growth rate for $n = 3-5$ with the electron and ion temperatures at $\rho_{pol}(CAP)$ for sawtooth periods II-IV during discharge 25546.

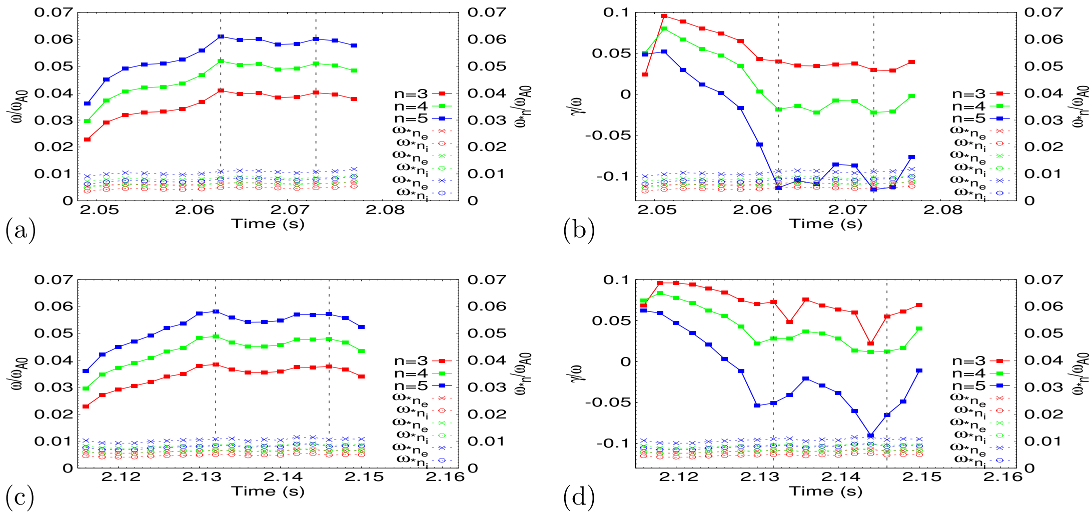

Figure B.15. Evolution of numerically calculated acoustic Alfvén CAP frequency and damping/growth rate for $n = 3-5$ with the electron and ion temperatures at $\rho_{pol}(CAP)$ for sawtooth periods II-IV during discharge 25546.

Appendix C

Numerical results for ICRH/ECRH phase

C.1 BAEs during discharge 25546

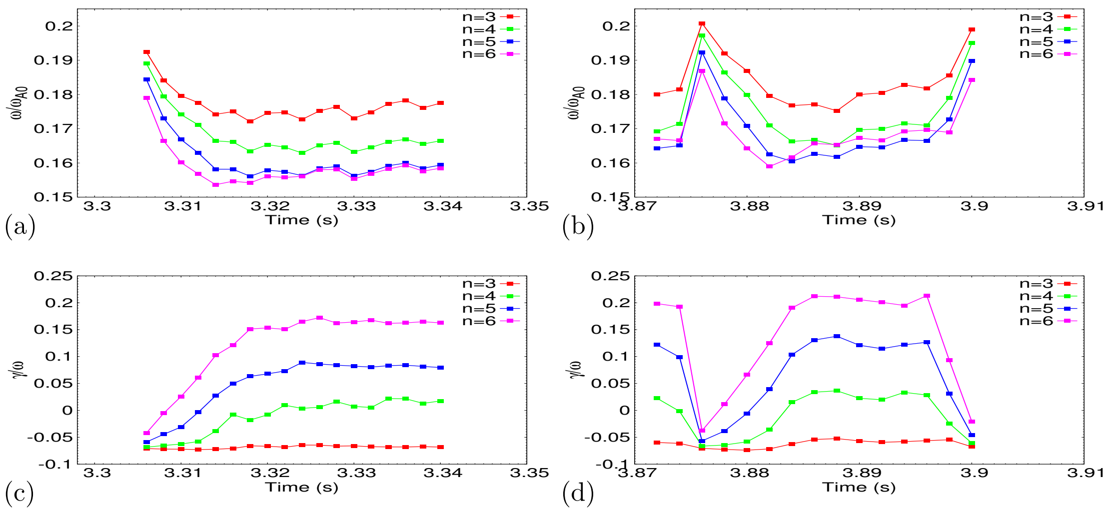

Figure C.1. Evolution of numerically calculated BAE continuum accumulation point frequency for toroidal mode numbers $n = 3 - 6$ during sawtooth periods I and II of ECRH phase of discharge 25546.

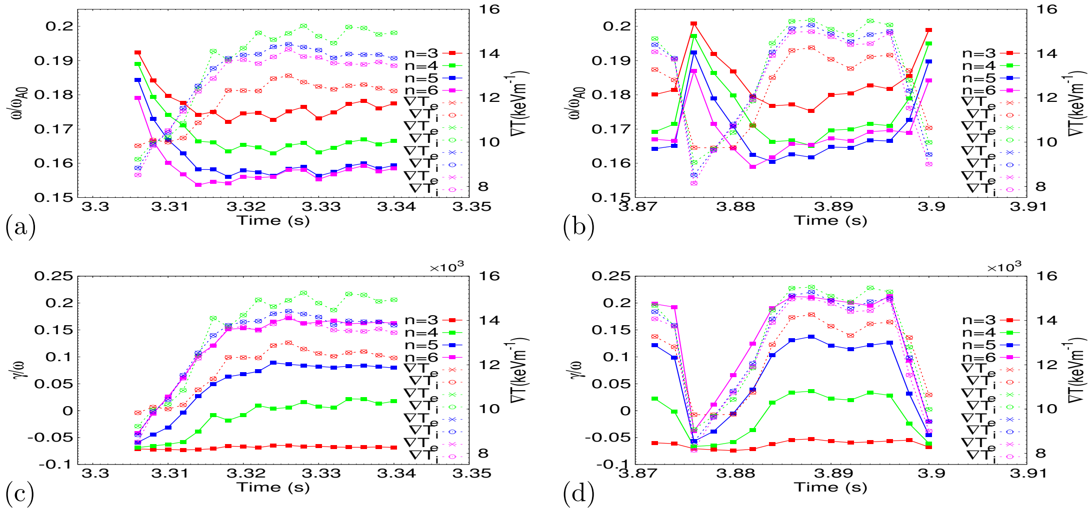

Figure C.2. Evolution of numerically calculated BAE CAP frequency for $n = 3 - 6$ with the electron and ion temperature gradients at $\rho_{pol}(CAP)$ during sawtooth periods I and II of ECRH phase of discharge 25546.

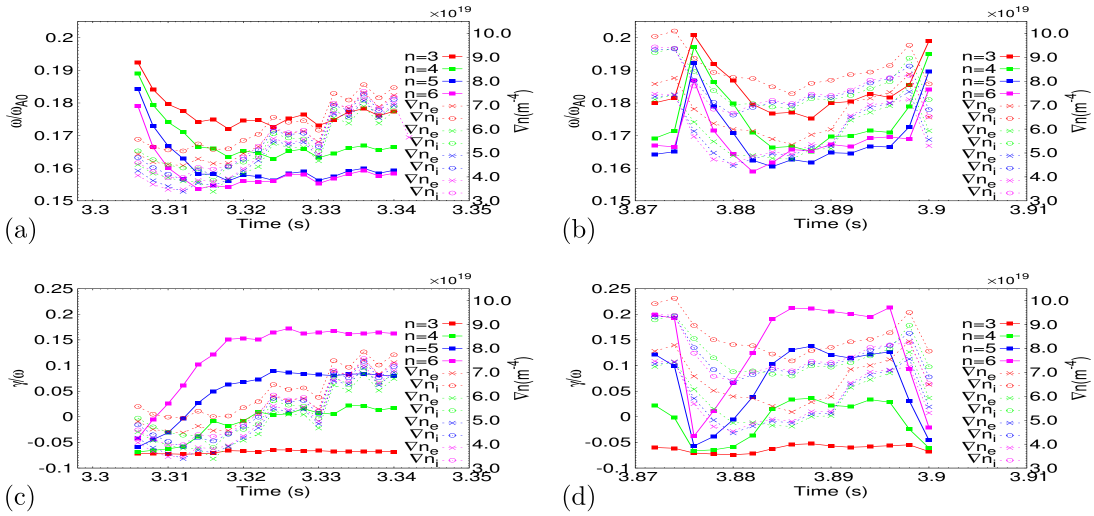

Figure C.3. Evolution of numerically calculated BAE frequency and damping/growth rate with the background ion and at electron density gradients at $\rho_{pol}(CAP)$ during sawtooth periods I and II of discharge 25546.

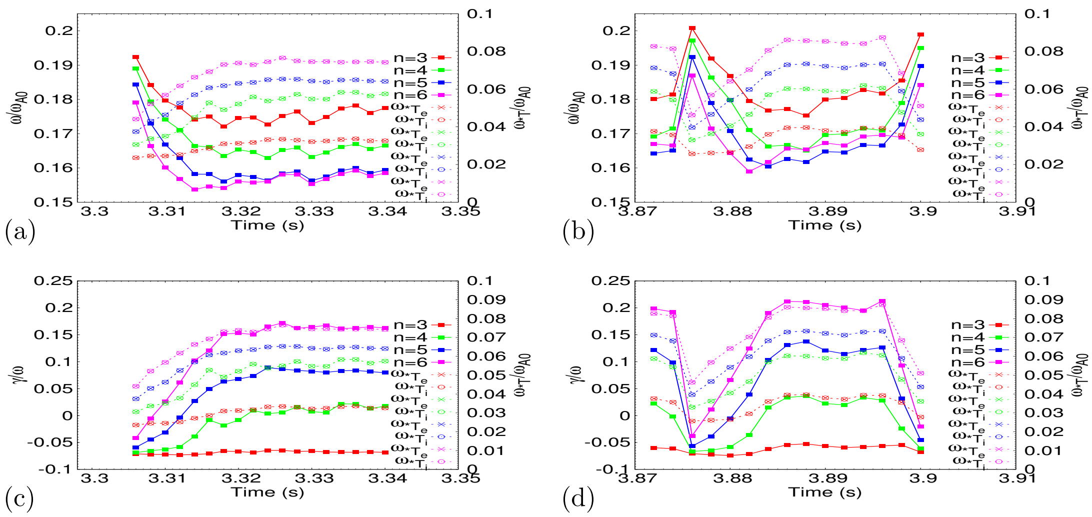

Figure C.4. Evolution of numerically calculated BAE CAP frequency for toroidal mode numbers $n = 3 - 6$ with the temperature component of the electron and ion diamagnetic frequencies at $\rho_{pol}(CAP)$ during sawtooth periods I and II of ECRH phase of discharge 25546.

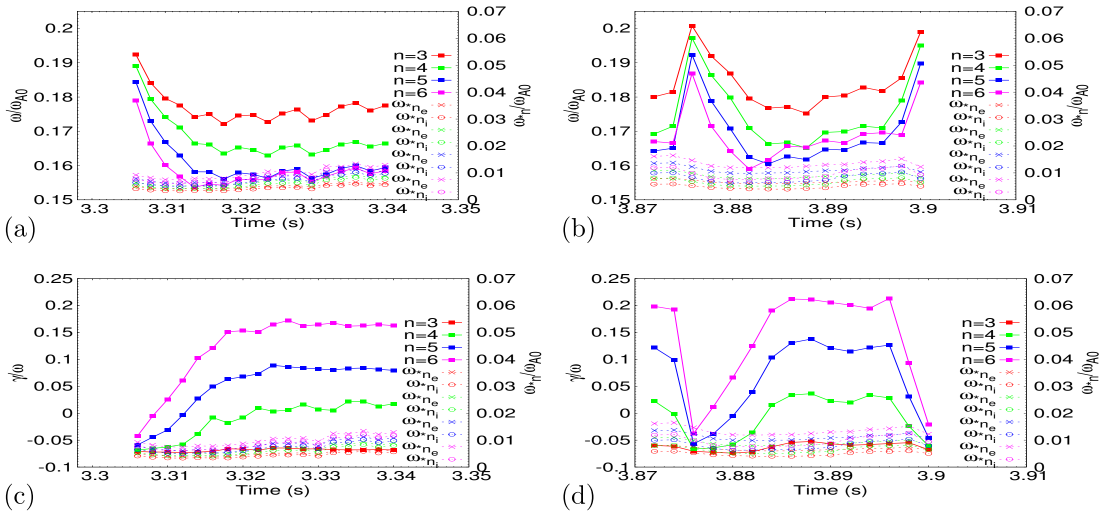

Figure C.5. Evolution of numerically calculated BAE CAP frequency for toroidal mode number $n = 3 - 6$ with the density components of the electron and ion diamagnetic frequencies at $\rho_{pol}(CAP)$ during sawtooth periods I and II of ECRH phase of discharge 25546.

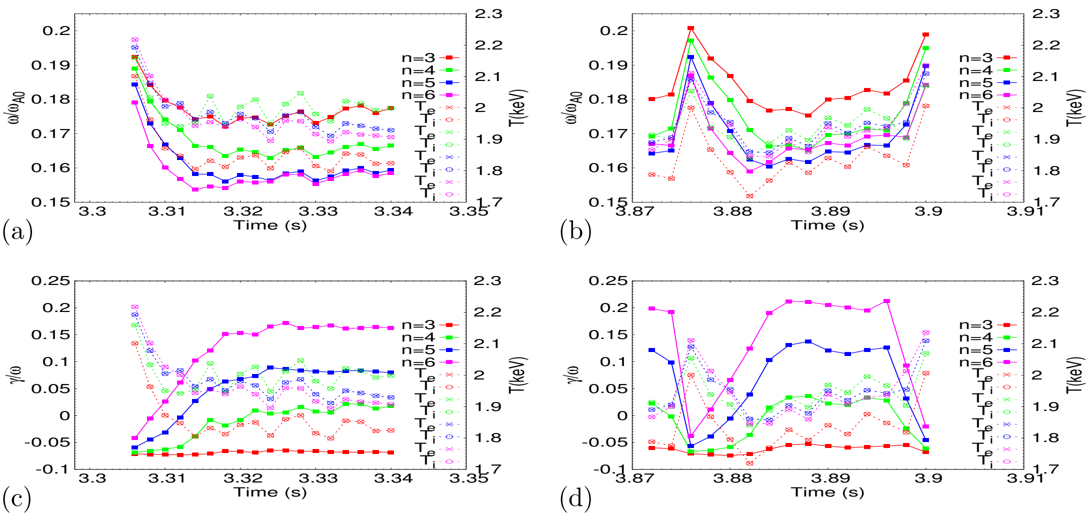

Figure C.6. Evolution of numerically calculated BAE CAP frequency for toroidal mode numbers $n = 3 - 6$ with the electron and ion temperatures at $\rho_{pol}(CAP)$ during sawtooth periods I and II of ECRH phase of discharge 25546.

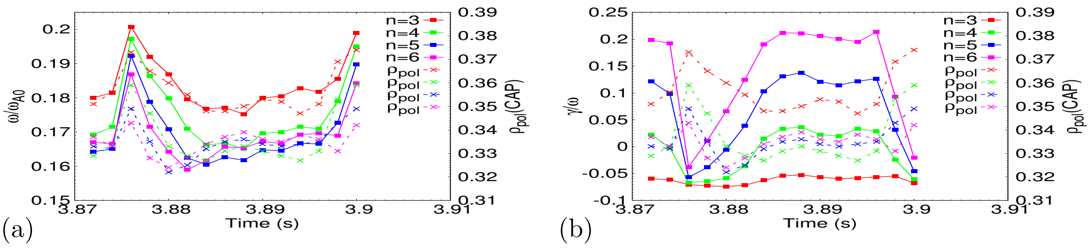

Figure C.7. Evolution of numerically calculated BAE CAP frequency for toroidal mode numbers $n = 3 - 6$ and the corresponding $\rho_{pol}(CAP)$ evolution for sawtooth period II during the ECRH phase of discharge 25546.

List of acronyms

AC	Alfvén Cascade
AE	Alfvén Eigenmode
ASDEX	Axially Symmetric Divertor EXperiment
AUG	ASDEX Upgrade
BAAE	Beta-induced Acoustic Alfvén Eigenmode
BAE	Beta-induced Alfvén Eigenmode
DCN	Deuterium-Cyanide-Nitrogen laser
ECE	Electron Cyclotron Emission
ECRH	Electron Cyclotron Resonance Heating
eITB	Electron Internal Transport Barrier
ELM	Edge Localised Mode
FLR	Finite Larmor Radius
H-mode	High confinement mode
ICRH	Ion Cyclotron Resonance Heating
ITER	International Thermonuclear Experimental Reactor
KBM	Kinetic Ballooning Mode
LHS	Left Hand Side
LIB	Lithium Beam
L-mode	Low confinement mode
MHD	Magnetohydrodynamics
NBI	Neutral Beam Injection
RHS	Right Hand Side
RSAE	Reverse Shear Alfvén Eigenmode
SAW	Shear Alfvén Wave
SMA	Slow Magnetoacoustic Wave
SSW	Slow Sound Wave
SXR	Soft x-ray
TAE	Toroidicity-induced Alfvén Eigenmode

Acknowledgements

This work was made possible by the support of many people. Firstly, I would like to thank my academic supervisor Dr. Patrick J. McCarthy for all of the support and patience over the course of my Ph.D. Whatever issue I had you were always available to talk and to give me as much time and help as I required. Thank you for giving me the opportunity to spend some truly memorable years in Munich.

I would also like to thank my supervisor at the IPP Dr. Philipp Lauber for making me feel welcome in Garching and for his guidance during my time there. I learned a great deal from you and your door was always open to me for any questions that I had.

I would like to thank Dr. Valentin Igochine, Dr. Alessandro Biancalani and Dr. Sylvia da Graça for always being available to clarify any questions that I had about the physics of Alfvén eigenmodes or about any other topic. My thanks also go the ASDEX Upgrade Team without whom this work would not have been possible. My special thanks go to Dr. Marc Marashek, Dr. Thomas Pütterich and Dr. Ivo Classen for their help in designing my discharges. I would also like to thank the administrative staff in UCC and the IPP: Margaret Bunce, Alice O'Leary, Gabriele Dörsch, Anja Bauer and Petra Jordan.

Thanks also go to Dr. Andreas Bergmann, Dr. David Coster, Dr. Hajo Klingshirn, Dr. Christian Konz, Dr. Tiago Ribeiro and Dr. Bruce Scott for making me feel welcome at the IPP when I first arrived and for many interesting chats over a Friday afternoon coffee.

During my time at the IPP I had the pleasure of meeting a lot of great people, many of whom I am now lucky enough to call my close friends: Dr. Leena Aho-Mantila, Dr. Andreas Burckhart, Dr. Tim Happel, Dr. Philip Schneider and Dr. Christian Vorpahl. Thank you all for making my time in Munich so much fun.

A special thanks goes to a good friend, Dr. Mike Dunne. I could always count on you to watch the rugby with me or to go for a chat over a coffee.

I am especially grateful to Maria Cozocea. Your optimism and support never wavered and I can't thank you enough for that.

To my friends here in Ireland. I never lacked for a place to stay and a great welcome on my trips home and I thank you all for that.

Finally, to my family. You have always been there for me and have supported every decision that I have made in my life without question. I would never be where I am today without you. Thank you so much for being exactly who you are.